SCIENTIFIC VALIDATION OF STANDARDS FOR TIDAL CURRENT ENERGY RESOURCE ASSESSMENT

Mathieu Toupin

Submitted under the supervision of

Dr. Ioan Nistor
Dr. Andrew Cornett

In partial fulfillment of the requirements for the degree of

Master of Applied Science in Civil Engineering

Department of Civil Engineering
University of Ottawa
August 2015

uOttawa

Acknowledgements

Many thanks are owed and I'll do my best to remember the many deserving people here. First of all, a thank you to my supervisors Dr. Ioan Nistor and Dr. Andrew Cornett for the help, patience, guidance, and swift kicks in the rear they provided as needed (and they were). I'm especially grateful to Dr. Nistor for his mentorship and for the many opportunities he's given me, from summer internships in the hydraulics lab, to Japan, to his backing for my medical school applications. There is every likelihood that I would not be where I am without his support.

I want to express my gratitude to Prof. Tomoya Shibayama for being an excellent host during my stay in Japan and to his students for making me feel welcome. That summer was, in a word, singular.

There's no way to get through this without thanking my friends and fellow coastal engineers who helped the past two years fly by: Steffanie, Derek, Alexandra and Marta. I wouldn't have found tidal energy without Derek's schemes, in a way this thesis began as our undergraduate Capstone project.

Big thanks to Steffanie for sharing an office, productive (and unproductive) discussions, and for her edits, advice, and comments. Lastly, my deep and sincere thanks go out to my family for the love and support they showed throughout all the hard work that went into my thesis. There's no doubt that this accomplishment would have been impossible without them.

Remerciements

Je dois de nombreux remerciements et je vais faire de mon mieux pour les offrir ici. Tout d'abord, un gros merci à mes superviseurs Dr. Ioan Nistor et Dr. Andrew Cornett pour l'aide, la patience, les conseils, et les coups de pied qu'ils ont fourni au besoin (j'en avais besoin). Je suis particulièrement reconnaissant envers Dr. Nistor pour son mentorat et pour les riches opportunités qu'il m'a données : les stages d'été dans le labo d'hydraulique, le Japon, et son soutien pour mes applications à l'école de médecine. Sans son appui, je ne serais probablement jamais parvenu où j'en suis aujourd'hui.

Je tiens à exprimer ma gratitude envers Prof. Tomoya Shibayama pour avoir été un excellent hôte pendant mon séjour au Japon et à ses étudiants pour m'avoir fait senti le bienvenu. Cet été fût, en un mot, singulier.

Pas moyen de faire mes remerciements sans une mention pour mes amis et collègues en génie côtier qui firent passer si vite ces deux dernières années : Steffanie, Derek, Alexandra et Marta. Je n'aurais jamais découvert l'énergie marémotrice sans les idées de Derek, d'une manière cette thèse a commencé au premier cycle avec notre projet Capstone.

Un grand merci à Steffanie pour avoir partagé un bureau avec moi, pour les discussions productives (et improductives), et pour ses révisions, conseils et commentaires. Enfin, mes remerciements profonds et sincères vont à ma famille pour l'amour et le soutien qu'ils ont démontré tout au long du travail et de la rédaction ci-jointe. Il n'y a aucun doute que cette réussite aurait été impossible sans eux.

Abstract

The tidal current energy resource is challenging to assess with accuracy and precision. An accepted standard methodology is lacking, which in turn perpetuates uncertainty and hinders the industry's development. Technical Committee 114 of the International Electro-technical Commission (IEC-TC-114) is working to develop a standard for emerging tidal energy conversion systems. The draft standard prescribes methods for determining, objectively and reliably, the scale and character of tidal current energy resources at a site. The IEC-TC-114 draft standard for tidal energy resource assessment and characterisation has not yet been tested in a real world case study. Hence, it is not yet known whether the proposed methods will yield the desired outcome.

This research has adopted the Fundy Ocean Research Center for Energy (FORCE) project in Minas Passage, Nova Scotia, for pilot application of the draft standard on tidal current resource assessment. The Bay of Fundy, located on the Atlantic coast of North America between the Canadian provinces of New Brunswick and Nova Scotia, is known for having the highest tidal range in the world and has long been recognised as an ideal stage for tidal energy development.

The thesis is presented in three main parts. Firstly, the latest peer-reviewed scientific literature is summarised and the standard is reviewed in view of lessons learned. The aim of this exercise is to establish a scientific basis for and to develop suggestions towards improving and extending future revisions of the standard. Secondly, a comprehensive assessment of the tidal current energy resource at the FORCE project site is conducted in a manner that is consistent with IEC-TC-114 protocol based on available measurements from static current profiler surveys and a two-dimensional hydrodynamic model of the upper Bay of Fundy developed for this study. Thirdly, a sensitivity analysis is performed to determine the main sources of error and uncertainty affecting resource assessment, a topic which has yet to be addressed in the literature.

Keywords: Tidal current resource, Tidal energy, Renewable energy, Numerical model, Bay of Fundy, 2D Hydrodynamic model, Resource assessment

Table of contents

Acknowledgements ii
Remerciements iii
Abstract iv
Table of contents v
List of figures viii
List of tables xi
List of symbols xii
Latin symbols xii
Greek symbols xv
List of abbreviations xvi
1. Introduction 1
1.1. Significance of the study 1
1.2. Objectives 3
1.3. Novelty 3
1.4. Thesis outline 4
1.5. Tidal power 5
1.5.1. A brief history 5
1.5.2. Tidal barrages 6
1.5.3. Tidal lagoons 8
1.5.4. Tidal turbines 9
2. Literature review 14
2.1. Kinetic energy 14
2.2. Desktop studies 16
2.3. Direct measurement 18
2.4. Analytical models 20
2.5. Numerical models 23
2.5.1. KE flux method 23
2.5.2. Augmented drag method 25
2.5.3. 'Per-generator' method 26
2.5.4. Farm method 28
2.5.5. Sensitivity to numerical parameters 32

2.6. Spatial and temporal variability 33
2.7. Wave interactions 36
2.8. Array interactions 37
2.9. Site selection 39
3. Review of the draft standard 40
3.1. Methodology overview 41
3.2. Modelling requirements 42
3.3. Discussion 44
3.4. Summary 52
4. Field study 54
4.1. The Bay of Fundy 54
4.1.1. Hydrodynamic modelling 54
4.1.2. The Minas Passage 57
4.2. Stationary tidal current surveys 60
4.3. Data correction 64
4.4. Tidal characteristics 68
4.5. Harmonic analysis 71
4.6. Discussion 75
5. Hydrodynamic modelling 79
5.1. Model development 79
5.1.1. Description of the numerical model 79
5.1.2. Strickler's law 80
5.1.3. Coriolis force 81
5.1.4. Modelling turbulence 82
5.1.4.1. Constant viscosity model 82
5.1.4.2. Elder model 82
5.1.4.3. K-epsilon model 82
5.1.4.4. Smagorinsky model 83
5.1.5. Model grid 84
5.1.6. Topography / Bathymetry 86
5.1.7. Boundary conditions 87
5.2. Model calibration and validation 89
5.2.1. Friction domains 90

5.2.2. Frequency-domain calibration 92
5.2.3. Time-domain calibration 95
5.2.4. Frequency-domain validation 97
5.2.5. Time-domain validation 99
5.3. Flow structures 105
5.4. Harmonic analysis 108
5.5. Discussion 109
6. Resource assessment 114
6.1. Annual Energy Flux 114
6.2. Annual Energy Production 115
6.3. Discussion 118
7. Sensitivity analysis 121
7.1. Harmonic analysis 121
7.2. Boundary specification (tidal amplitude) 129
7.3. Spatial resolution 133
7.4. Coriolis force 140
7.5. Bathymetry resolution 140
7.6. Turbulence model 144
7.7. Boundary specification (tidal database) 146
7.8. Uncertainty 148
7.9. Discussion 149
8. Conclusions 156
9. Recommendations for future work 159
10. References 161
Appendices 167
A. Theory of tides 167
B. Field study 174
C. Simulation log 190

List of figures

Figure 1.1. Atlantis Resources 1 MW AR1000 tidal turbine 2
Figure 1.2. OpenHydro 2 MW Open-Centre tidal turbine 2
Figure 1.3. Marine Current Turbines 1.2 MW SeaGen tidal turbine 2
Figure 1.4. Black Rock Tidal Power 2.5 MW tidal turbine 2
Figure 1.5. Number of publications retrieved annually by Web of Science on the topic of "tidal power" 6
Figure 1.6. Aerial photograph of the Rance Tidal Power Station 7
Figure 1.7. Artist's impression of an offshore tidal lagoon, left, and a coastal tidal lagoon, right 8
Figure 1.8. Example of turbine systems 10
Figure 1.9. Life cycle carbon intensities of energy generating technologies 12
Figure 1.10. OpenHydro 1 MW tidal turbine deployed in the Bay of Fundy 12
Figure 1.11. Biofouling of Clean Current tidal turbine after 3 years at Race Rocks, BC 12
Figure 2.1. Piezometric and velocity head variation for flow through a venturi section 16
Figure 2.2. Comparison of theoretical spring (left) and neap (right) tidal speed profiles 19
Figure 2.3. Available power and electrical power output for the Evopod and Gorlov turbines 27
Figure 2.4. Power curve of the Evopod turbine 27
Figure 2.5. Flowchart of resource estimation methodology 28
Figure 2.6. Comparison of the Alas Strait tidal array configuration 31
Figure 2.7. Simulated depth-averaged tidal current velocities with spring-neap ratios 34
Figure 2.8. Mean spring peak velocity plotted against annual practical power 34
Figure 2.9. The difference in the net power available over a tidal cycle when the simulated tidal velocities are modified by waves for tidal velocities exceeding 1.5 m/s 37
Figure 3.1. Flowchart of the IEC-TC-114 methodology 40
Figure 4.1. The Bay of Fundy, shown on the east coast of North America 56
Figure 4.2. The Minas Channel 56
Figure 4.3. Model-predicted currents: (a) peak ebb; (b) 2 h after the peak ebb; (c) 3 h after the peak ebb; (d) 4 h after the peak ebb 57
Figure 4.4. (Top) A comparison of simulated [red] and observed [blue] tidal currents 58
Figure 4.5. The Minas Passage and Crown Lease Area 59
Figure 4.6. Minas Passage bathymetry 59
Figure 4.7. ADCP survey locations 60
Figure 4.8. High-resolution (5 m) bathymetry of the CLA and surroundings 61
Figure 4.9. Vertical bin processing scheme 62
Figure 4.10. Separation of ebb and flood records 63
Figure 4.11. Separation of slack tide 64
Figure 4.12. Correction of invalid data at Site A, before (left) and after (right). 65
Figure 4.13. Correction of rotated data at Site A, before (left) and after (right) 66
Figure 4.14. Angular correction 67
Figure 4.15. Correction of a shift in MSL at Site D, before (left) and after (right). 67
Figure 4.16. Observed pulse at the beginning of ebb 69
Figure 4.17. Typical spring and neap currents (Site C) 70
Figure 4.18. Observed flow through the Crown Lease Area 74
Figure 5.1. The standard mesh of the upper Bay of Fundy 84
Figure 5.2. The standard mesh without a submesh 85
Figure 5.3. Minas Passage 150 m submesh 85
Figure 5.4. DEM data sources (Cousineau 2012) 86
Figure 5.5. Minas Channel 5 m bathymetry survey 87

Figure 5.6. Strickler's coefficient in the computational domain 91
Figure 5.7. CHS boundary and calibration stations 91
Figure 5.8. Scatterplot of the observed and modelled amplitude and phase at Parrsboro 94
Figure 5.9. Observed and modelled tidal height at Cape Sharp, Parrsobor, and Port Greville 96
Figure 5.10. Scatterplot of the observed and modelled amplitude and phase at Site C 98
Figure 5.11. Tidal height, currents, and tidal ellipse at Site A 101
Figure 5.12. Tidal height, currents, and tidal ellipse at Site B 102
Figure 5.13. Tidal height, currents, and tidal ellipse at Site C 103
Figure 5.14. Tidal height, currents, and tidal ellipse at Site D 104
Figure 5.15. Tidal currents and tidal ellipse at Site F 105
Figure 5.16. Modelled pulse at the beginning of ebb 106
Figure 5.17. Modelled pulse at the beginning of ebb at 7:15, 7:30 and 7:45 AM on 30/09/2011 107
Figure 5.18. Modelled eddies off Cape Split and Cape Sharp 108
Figure 6.1. Current predictions for Jan 1-7 2015 (Site C) 115
Figure 6.2. Kinetic energy flux for Jan 1-7 2015 (Site C) 115
Figure 6.3. Exceedance curve of tidal currents for 2015 (Site C) 116
Figure 6.4. The measured power curve of the SeaGen S tidal turbine 116
Figure 6.5. Tidal current histograms for Site C and SeaGen power curve 117
Figure 7.1. Tidal height constituents of amplitude and phase for M2 versus record length 123
Figure 7.2. Tidal height constituents of amplitude and phase for N2, S2 and K1 versus record length 124
Figure 7.3. Tidal current constituents for M2 versus record length 125
Figure 7.4. Tidal height constituents of amplitude and phase for M2 versus record length and analysed constituents 126
Figure 7.5. Tidal height constituents for M2, N2, S2 and K1 versus sampling interval 126
Figure 7.6. Tidal current constituents for M2, N2, S2 and K1 versus sampling interval 127
Figure 7.7. Annual Energy Flux as a function of the tidal amplitude modelled at the open boundary 129
Figure 7.8. Fraction of the Annual Energy Flux modelled versus number of modelled constituents (Sites A, B and D) 131
Figure 7.9. Fraction of the Annual Energy Flux modelled versus number of modelled constituents (Site C) 131
Figure 7.10. 20 m submesh 134
Figure 7.11. 100 m submesh 134
Figure 7.12. 250 m submesh 135
Figure 7.13. 500 m submesh 135
Figure 7.14. Annual Energy Flux as a function of local mesh resolution (Site B) 136
Figure 7.15. Relative error in Annual Energy Flux as a function of local mesh resolution (Sites A, C and D) 136
Figure 7.16. Computational time versus minimum mesh resolution 137
Figure 7.17. Tidal current speed probability of exceedance at 500, 200 and 20 m resolution (Site C) 138
Figure 7.18. Observed (blue) and modelled (red) tidal ellipse at 500, 400, 200 and 20 m resolution (Site D) 139
Figure 7.19. Resampled 5, 40 and 80 m bathymetric data 141
Figure 7.20. Resampled 20, 80 and 150 m bathymetric data mapped onto the 20 m mesh 142
Figure 7.21. Annual Energy Flux as a function of local bathymetric resolution (Site A, B and D) 143
Figure 7.22. Relative error in Annual Energy Flux as a function of local bathymetric resolution (Site C) 143
Figure 7.23. Tidal height prediction at Dipper Harbour West on 1st Jan. 2015 146
Figure 7.24. Tidal height prediction at the ocean boundary on 1st January 2015 147
Figure A.1. Equilibrium tide 168
Figure A.2. Spring and neap tide 169
Figure A.3. Daily inequality 169
Figure A.4. M2 for Saint John NB, March 1-28, 1990 171
Figure A.5. M2 + S2 for Saint John NB, March 1-28, 1990 171

Figure A.6. M2 + K1 for Saint John NB, March 1-28, 1990 172
Figure A.7. M2 + N2 for Saint John NB, March 1-28, 1990 172
Figure B.1. East-west, north-south, and vertical velocities (Site A) 174
Figure B.2. Current speed, direction, and water elevation (Site A) 175
Figure B.3. Tidal ellipse (Site A) 176
Figure B.4. Temperature and salinity depth profiles (Site A) 176
Figure B.5. Average ebb and flood current profiles (Site A) 177
Figure B.6. East-west, north-south, and vertical velocities (Site B) 178
Figure B.7. Current speed, direction, and water elevation (Site B) 179
Figure B.8. Tidal ellipse (Site B) 180
Figure B.9. Temperature and salinity depth profiles (Site B) 180
Figure B.10. Average ebb and flood current profiles (Site B) 181
Figure B.11. East-west, north-south, and vertical velocities (Site C) 182
Figure B.12. Current speed, direction, and water elevation (Site C) 183
Figure B.13. Tidal ellipse (Site C) 184
Figure B.14. Temperature and salinity depth profiles (Site C) 184
Figure B.15. Average ebb and flood current profiles (Site C) 185
Figure B.16. East-west, north-south, and vertical velocities (Site D) 186
Figure B.17. Current speed, direction, and water elevation (Site D) 187
Figure B.18. Tidal ellipse (Site D) 188
Figure B.19. Temperature and salinity depth profiles (Site D) 188
Figure B.20. Average ebb and flood current profiles (Site D) 189

List of tables

Table 3.1. Resource assessment stages 41
Table 3.2. Validation from recent tidal current energy resource assessments 50
Table 4.1. Location of five ADCPs in the Minas Passage and their installation period 60
Table 4.2. ADCP survey characteristics 62
Table 4.3. Summary of corrections to the observed data 68
Table 4.4. Summary of observed tidal characteristics 71
Table 4.5. Tidal height harmonics of amplitude (m) and phase (°) (observed) 71
Table 4.6. East-west tidal current harmonics of amplitude (m) and phase (°) (observed) 72
Table 4.7. North-south tidal current harmonics of amplitude (m) and phase (°) (observed) 72
Table 4.8. IOS and T_TIDE (tidal height harmonics of amplitude, m, and phase, deg) 73
Table 4.9. IOS and T_TIDE (east-west tidal current harmonics of amplitude, m, and phase, deg) 73
Table 4.10. IOS and T_TIDE (north-south tidal current harmonics of amplitude, m, and phase, deg) 73
Table 5.1. CHS Tidal height constituents at Dipper Harbour West and Deep Cove 88
Table 5.2. CHS boundary and calibration stations 90
Table 5.3. Observed and modelled tidal height harmonics for M2 at CHS stations 92
Table 5.4. Observed and modelled tidal height harmonics for N2 at CHS stations 93
Table 5.5. Observed and modelled tidal height harmonics for S2 at CHS stations 93
Table 5.6. Relative error and phase difference of high and low tides at the CHS stations 95
Table 5.7. Observed and modelled tidal height harmonics for M2 at FORCE berths 97
Table 5.8. Observed and modelled tidal height harmonics for N2 at FORCE berths 97
Table 5.9. Observed and modelled tidal height harmonics for S2 at FORCE berths 97
Table 5.10. Relative error and phase difference of high and low tides at the FORCE berths 99
Table 5.11. Statistical comparison of observed and modelled parameters at the FORCE berths 99
Table 5.12. East-west tidal current harmonics of amplitude (m) and phase (°) (modelled) 108
Table 5.13. North-south tidal current harmonics of amplitude (m) and phase (°) (modelled) 109
Table 6.1.Annual Energy Flux for 2015 from observed and modelled tidal constituents 114
Table 6.2. Annual Energy Production for 2015 from observed and modelled tidal constituents 117
Table 7.1. Number of constituents extracted based on record length 122
Table 7.2. Annual Energy Flux versus numerical output time step 128
Table 7.3. Contribution of each constituent to the Annual Energy Flux at Site A 130
Table 7.4. Average Annual Energy Flux contributed by 7 constituents at the FORCE berths 132
Table 7.5. Annual Energy Flux predicted by 7 key constituents compared to the maximum of 20 132
Table 7.6. Properties of the developed grids 133
Table 7.7. Relative error in Annual Energy Flux for the four turbulence models (150 m mesh) 144
Table 7.8. Relative error in Annual Energy Flux for the four turbulence models (50 m mesh) 144
Table 7.9. Relative error in Annual Energy Flux for the four turbulence models (20 m mesh) 145
Table 7.10. Ratio of simulated to real time in the turbulence model simulations 145
Table 7.11. Relative computational efficiency of the turbulence models 145
Table 7.12. Relative error in Annual Energy Flux for the five tidal databases 147
Table A.1. Important tidal constituents 170

List of symbols

Latin symbols

a_0	Mean sea level [m]
a_i	Tidal constituent amplitude [m]
$c_{1\varepsilon}$	Constant of the k-ε model [-]
$c_{2\varepsilon}$	Constant of the k-ε model [-]
e	Relative error [-]
$f_i(U_i)$	Time occurrence likelihood of a velocity in each bin [-]
f	Coriolis parameter [s^{-1}]
g	Gravitational acceleration [m/s^2]
h	Water depth [m]
k	Turbulent kinetic energy [m^2/s^2]
t	Time [s]
u	Depth-averaged velocity in x-direction [m/s]
u_0	Velocity of the flow [m/s]
u^*	Shear velocity [m/s]
v	Depth-averaged velocity in y-direction [m/s]
w	Vertical velocity [m/s]
x	Space coordinate in x-direction [m]
y	Space coordinate in y-direction [m]
A	Sweep area of the turbine [m^2]
A_c	Cross-sectional area of the channel [m^2]
C	Chézy coefficient [-]

C_f	Friction coefficient [-]
C_F^{Peak}	Farm's optimal drag coefficient [-]
C_k	Constant of the k-ε model [-]
C_P	Power coefficient [-]
C_s	Smagorinsky coefficient [-]
C_ε	Constant of the k-ε model [-]
C_μ	Constant of the k-ε model [-]
$\bar{E}$	Mean of the error [-]
E_i	Difference between modelled and observed value [-]
E_k	Kinetic energy [J]
F_x^c	Coriolis force in x-direction [N]
F_y^c	Coriolis force in y-direction [N]
F_x^f	Bottom shear force in x-direction [N]
F_y^f	Bottom shear force in y-direction [N]
H_i	Bin size [m]
K	Strickler's coefficient [$m^{1/3}/s$]
K_l	Longitudinal eddy viscosity [m^2/s]
K_n	Spring neap factor [-]
K_s	Velocity shape factor [-]
K_t	Transverse eddy viscosity [m^2/s]
L	Characteristic length of the flow field [m]
N_B	Number of velocity bins [-]
N_h	Number of hours in the simulated year [h]
P	Power generated [W]
P_0	Power available [W]

$P_{\varepsilon v}$	Production term of the k-ε model [m^2/s^3]
P_f	Power flux [W/m^2]
P_{kv}	Production term of the k-ε model [m^2/s^4]
$\bar{P}_{max}$	Maximum average extractable power [W]
P_{mean}	Mean power flux [W/m^2]
$P_i(U_i)$	Power generated by the ith velocity bin of the TEC power curve [kW]
Q_{max}	Peak volume transport in the undisturbed channel [m^3/s]
R	Spring neap ratio [-]
Ro	Rossby number [-]
S_h	Source or sink of fluid [m/s]
S_x	Source or sink of momentum in x-direction [m/s^2]
S_y	Source or sink of momentum in y-direction [m/s^2]
U	Characteristic velocity of the flow field [m/s]
U_i	Mean current velocity of the ith bin of the TEC power curve [m/s]
U_{peak}	Peak spring tide velocity [m/s]
$\bar{V}$	Depth-averaged velocity [m/s]
$\bar{V}_{ebb}$	Mean depth-averaged ebb velocity [m/s]
$\bar{V}_{flood}$	Mean depth-averaged flood velocity [m/s]
V_i	Bin velocity [m/s]
X_i	Observed value [-]
Y_i	Modelled value [-]
Z	Free surface elevation [m]

Greek symbols

α	Angle of the bottom slope [rad]
α_i	Tidal constituent phase angle [rad]
γ	Channel dynamical balance coefficient [-]
Δ	Grid size [m]
ε	Turbulent dissipation [m^2/s^3]
ζ_0	Amplitude of the water level difference between the ends of the channel [m]
η_0	Amplitude of the dominant tidal constituent in the ocean [m]
η	Water level [m]
θ_{ebb}	Mean ebb direction [rad]
θ_{flood}	Mean flood direction [rad]
λ	Latitude [rad]
ν_t	Eddy viscosity [m^2/s]
ρ	Water density [kg/m^3]
σ_ε	Constant of the k-ε model [-]
σ_k	Constant of the k-ε model [-]
τ_{xz}	Bottom shear stress in the x-z plane [Pa]
τ_{yz}	Bottom shear stress in the y-z plane [Pa]
ω	Angular velocity of the Earth [rad/s]
ω_i	Angular frequency of the tide generator [s^{-1}]

List of abbreviations

2D	Two-dimensional
3D	Three-dimensional
ADCP	Acoustic Doppler Current Profiler
AEF	Annual Energy Flux
AEP	Annual Energy Production
AF	Availability Factor
BoF	Bay of Fundy
CHS	Canadian Hydrographic Service
CF	Capacity Factor
CFD	Computational Fluid Dynamics
CLA	Crown Lease Area
DEM	Digital Elevation Model
EPRI	Electric Power Research Institute
FES	Finite Element Solution
FORCE	Fundy Ocean Research Center for Energy
GoM	Gulf of Maine
HAT	Highest Astronomical Tide
IEC	International Electro-technical Commission
IOS	Institute of Ocean Sciences
KE	Kinetic Energy
LAT	Lowest Astronomical Tide
LCA	Life Cycle Assessment
LES	Large Eddie Simulation
MCEC	Marine Current Energy Converter

MCT	Marine Current Turbine
MSL	Mean Sea Level
NAD	North American Datum
NAVD	North American Vertical Datum
NRCan	Natural Resources Canada
ORPC	Ocean Renewable Power Company
RANS	Reynolds Averaged Navier-Stokes
R&D	Research and Development
RITE	Roosevelt Island Tidal Energy
RMAE	Relative Mean Absolute Error
RMS	Root-Mean-Square
RMSE	Root-Mean-Square Error
SERG	Sustainable Energy Research Group
SGS	Subgrid-scale
SI	Scatter Index
SIF	Significant Impact Factor
TC	Technical Committee
TEC	Tidal Energy Converter
TISEC	Tidal In-Stream Energy Converter
TKE	Turbulent Kinetic Energy
TPXO	TOPEX/Poseidon
TSG	Tidal Stream Generator
TSE	Tidal Stream Exploitability
TST	Tidal Stream Turbine
UTM	Universal Transverse Mercator
WCT	Water Current Turbine

1. Introduction

1.1. Significance of the study

Promising new technologies are emerging for the exploitation of tidal currents – a freely available, renewable, and reliable resource. In the coming years, the ever-increasing demand for energy in tandem with growing awareness of anthropogenic influence on climate change will drive the proliferation of these technologies. Reliable information on tidal energy resources is critical at many stages of the development cycle for any tidal energy project: when selecting a location for the project, for detailed design of the equipment and infrastructure, for predicting power output and variability, for evaluating alternative development options, and for predicting return on investment. Technical Committee 114 of the International Electro-technical Commission (IEC-TC-114) is working to develop a standard for the nascent field of tidal energy systems. The draft standard prescribes methods and procedures for determining, objectively and reliably, the scale and character of tidal energy resources in a region. The proposed methods are complex and involve sophisticated numerical modelling of tidal circulation validated by field measurements. The draft standard has not yet been trialed, tested, nor assessed in a real world case study. Hence, it is not yet known whether the proposed methods can be applied successfully in Canada or elsewhere, nor is it known whether the proposed methods will yield the desired outcomes.

Many diverse stakeholders including project developers, financiers, device developers, regulators, utilities, and insurers all have a common interest in ensuring that marine energy resources are assessed using recognised standards and best practice guidelines. By following recognised standards and procedures, stakeholders can have greater confidence in the quality and accuracy of the resource assessments, reducing risk for everyone. This research has adopted the Fundy Ocean Research Center for Energy (FORCE) project in Minas Passage, Nova Scotia, for pilot application of the draft standard on tidal flow resource assessment. The FORCE project site provides technology developers with the electrical infrastructure to connect devices to the grid and environmental monitoring at four deployment berths. Atlantis Resources, Marine Current Turbines, OpenHydro, and Black Rock Tidal Power (Figures 1.1 to 1.4) have been awarded rights to test their devices at FORCE. This study is intended to benefit the Canadian marine energy sector as a whole through the development and promotion of technical standards.

Figure 1.1. Atlantis Resources 1 MW AR1000 tidal turbine
(source: Atlantis Resources Ltd.)

Figure 1.2. OpenHydro 2 MW Open-Centre tidal turbine
(source: OpenHydro Group Ltd.)

Figure 1.3. Marine Current Turbines 1.2 MW SeaGen tidal turbine
(source: Marine Current Turbines Ltd.)

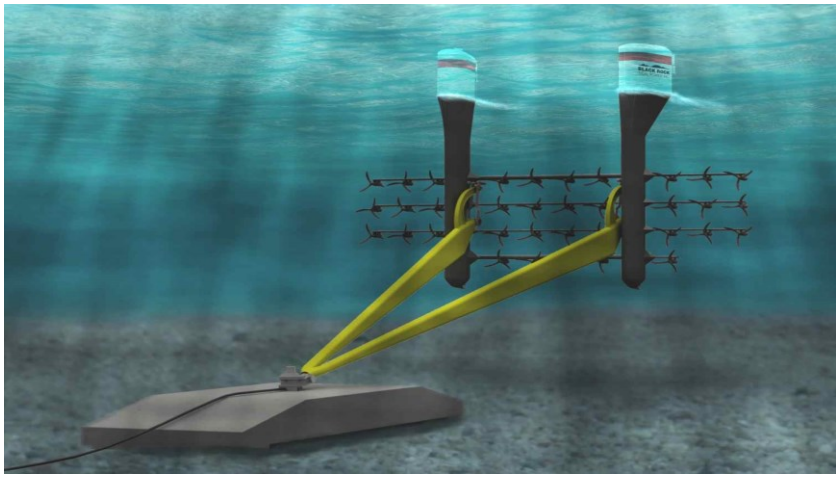

Figure 1.4. Black Rock Tidal Power 2.5 MW tidal turbine
(source: Black Rock Tidal Power Inc.)

Canada's marine renewable energy sector has the potential to become highly competitive in the global marketplace – serving domestic and global power needs. The Bay of Fundy, situated on the Atlantic coast of North America between the Canadian provinces of New Brunswick and Nova Scotia, is known for having the highest tidal range in the world and has long been recognised as an ideal stage for tidal power development. Marine energy projects, both domestic and international, will create employment opportunities for Canadians in design, construction, deployment, monitoring and decommissioning of devices and systems. Increased expertise in this domain will enable Canadian firms to become leaders in development of marine energy systems and projects. Long-term outcomes are widespread acceptance and use of the IEC standard in Canada and internationally, leading to further investments in the marine energy sector within Canada and abroad. The intended ultimate outcome is environmental, social, and economic benefits for Canada from the advancement of a clean energy technology for export and domestic use.

1.2. Objectives

The purpose of this study is pilot application of the IEC-TC-114 draft standard for tidal energy resource assessment and characterisation at the FORCE project site. The aims of piloting are:

1. To establish a firm scientific basis for the standard
2. To develop suggestions for improving and extending future revisions of the standard
3. To conduct a comprehensive assessment of the tidal current energy resource across the FORCE project site that is consistent with IEC-TC-114 protocols
4. To conduct a sensitivity analysis to determine the main sources of error and uncertainty affecting tidal current energy resource assessment

1.3. Novelty

Tidal energy systems are an emerging technology for which standards exist as yet only in draft phase. The IEC standard for assessment of tidal current resources has never been trialed in a real world context. This research attempts to evaluate and assess the performance of the new standard by applying the methods prescribed to predict and characterise the tidal resource at the FORCE deployment berths. Lessons learned from this work will inform and improve future development of the draft standard.

1.4. Thesis outline

This thesis is organised into ten chapters.

Chapter 1 introduces the topic of interest, the significant and novel aspects of the study, and outlines the main objectives.

Chapter 2 is a review of the state of the art in tidal current energy resource assessment. Publications are reviewed and discussed.

Chapter 3 is a dedicated review of the IEC-TC-114 draft standard for tidal current energy resource assessment and characterisation.

Chapter 4 presents an overview of hydrodynamics in the Bay of Fundy and Minas Passage and proceeds with analysis of available field measurements.

Chapter 5 describes the development, calibration, and validation of a hydrodynamic model of the upper Bay of Fundy.

Chapter 6 calculates the observed and modelled tidal current energy resource in a manner consistent with IEC-TC-114 protocol.

Chapter 7 carries out a sensitivity analysis to determine the main sources of error and uncertainty affecting resource assessment.

Chapter 8 summarises the main research findings and provides conclusions.

Chapter 9 provides recommendations for future investigations into this topic.

Chapter 10 enumerates all references consulted for the purpose of this thesis.

1.5. Tidal power

1.5.1. A brief history

The concept of energy from the tides is not novel. As early as the Classical era, tidal mills harnessed the power of the tides on the Tiber River in Rome (Charlier and Finkl 2009). Tidal barrages, akin to traditional hydroelectric installations, have been around for decades: the world's first and – until recently – largest tidal barrage was built in 1966 on the Rance River in France. After 45 years of operation the 240 MW Rance Tidal Power Station was surpassed by the 254 MW Sihwa Lake Tidal Power Station in South Korea. Smaller-scale projects have been constructed around the world in Canada, China, and Russia (Hammons 1993), but only small steps have been taken towards wider implementation. The 20 MW Annapolis Royal Generating Station in Canada remains the only tidal generating station in North America. Meanwhile, the proposed Severn Barrage in the United Kingdom has been debated for the better part of a century (Nature 1933). Alternate schemes have recently been proposed to exploit tidal energy, for example the tidal lagoon, tidal fence, and tidal turbine. The present decade has seen more R&D initiatives in tidal power than any before (Khan *et al.* 2009) (Figure 1.5).

All of these technologies share a number of pros and cons. Tidal energy is clean, without emission of greenhouse gases during normal operation, and reliable; the tides depend on the movements of astronomical objects and are thus predictable years ahead. Tidal is one of the few renewables to allow a finite amount of daily supply to be reliably contracted (Johnstone *et al.* 2013). On the other hand electricity generation is intermittent, following the ebb and flood, creating problems in power delivery and hindering the economic feasibility of projects. Recent publications (Grabbe *et al.* 2009) have proposed that the problem of intermittency could be mitigated by developing sites that are phase shifted relative to each other. Esteban *et al.* (2011) showed that the problem of intermittency is partly alleviated in countries with a diverse portfolio of renewables, as unfavourable conditions in one location for one renewable source might be compensated by better conditions for a different renewable at the same location or elsewhere. Technology for generating electricity from tidal energy is relatively new and burdened with the added risk and cost of emerging generation technology. However, capital and operational costs are expected to fall with maturity; the cost of tidal energy is projected to become competitive with other forms of electricity production in the next decade (Esteban and Leary 2012; Johnstone *et al.* 2013).

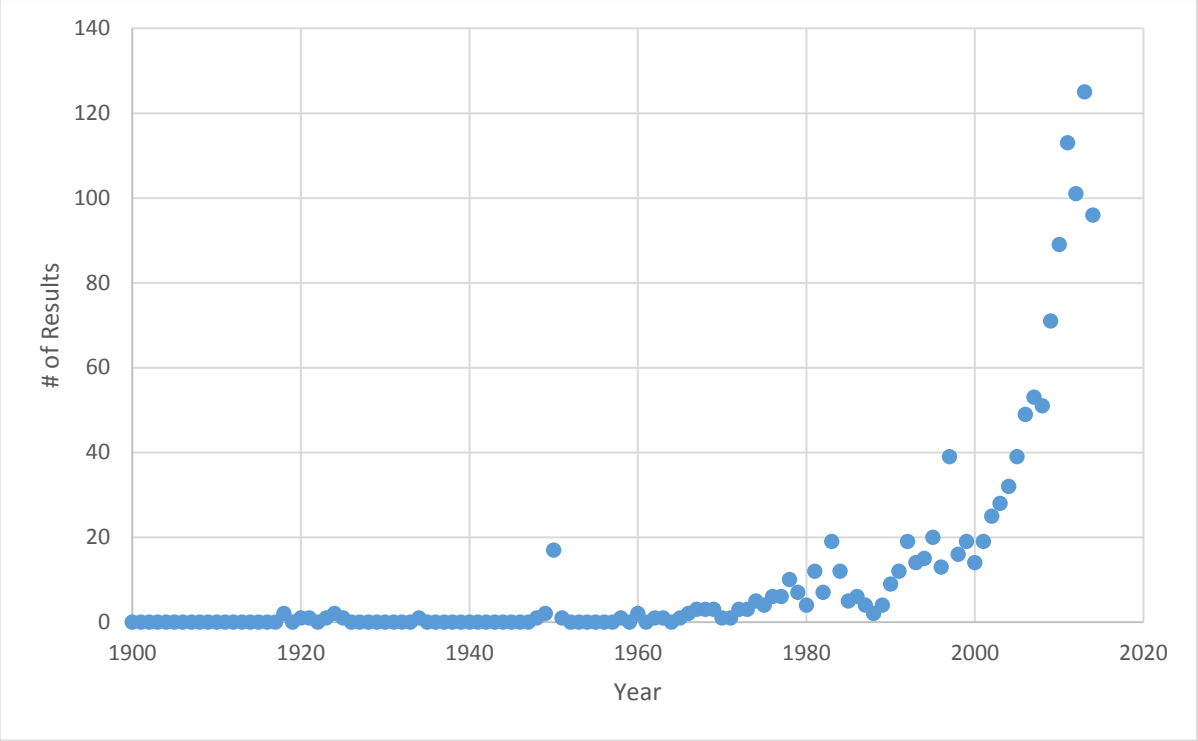

Figure 1.5. Number of publications retrieved annually by Web of Science on the topic of "tidal power" or "tidal energy"

1.5.2. Tidal barrages

The conventional method of harnessing tidal energy is analogous to run-of-the-river hydroelectricity: by constructing a barrier fitted out with sluices and turbines across a river, estuary, or bay with a high tidal range. There are three modes of operation for generating electricity within a single basin: ebb generation, flood generation, and two-way generation. The most common is ebb generation, described as follows. As the tide comes in the sea level rises, the basin floods and a large amount of potential energy is captured. As the tide then ebbs, the hydraulic head between the flooded basin and the receding sea level is used to drive water through low-head hydraulic turbines. A pumping system increases average output levels and improves flexibility of the scheme. This in turn leads to improved economic efficiency as power delivery can be tuned to match energy cost levels, though the turbines and electrical system are more costly (Hammons 1993). Additional schemes and modes of operation are described by Clark (2007).

The world's first tidal power station, *La Rance*, began operating in 1966 on the estuary of the Rance River in Brittany, France (Figure 1.6) (Charlier 2007). *La Rance* is a single-basin, two-way generating station with pumped storage and an installed capacity of 240 MW. The station supplies 0.12% of France's power requirements. The only tidal generating station in North America opened in 1984.

Figure 1.6. Aerial photograph of the Rance Tidal Power Station (source: Wikipedia)

The 20 MW Annapolis Royal Generating Station operates in a sub-basin of the Bay of Fundy. Plans to develop the vast, accessible resource of the Bay of Fundy by way of large-scale tidal barrages have never passed the feasibility stage despite enduring ambition (Lawton 1972). More recently the feasibility of constructing one or more tidal lagoons in the upper Bay of Fundy has been investigated (Cousineau *et al.* 2012). See Section 2.3.3 Tidal lagoons.

Tidal barrages have the benefit of using established technology, but they require extensive civil works. Cost of materials and construction has been a key factor in studies looking at the economic viability of tidal barrages. The number of suitable locations is a different challenge. According to the U.S. Department of Energy, tidal barrages require a tidal range of at least 5 m to pass feasibility, of which there exist some 40 sites worldwide (Etemadi *et al.* 2011). Lastly, the local environmental impact is considerable and has time and again proven to be an insurmountable obstacle for these projects. Many of the ecological impacts are shared with traditional hydropower, *e.g.* altered hydrology and interrupted fish migration. The basin experiences reduced tidal flushing, affecting turbidity, salinity, and sediment transport (Retiere 1994). Changes in sediment transport are not all negative: marine life may flourish as a result of increased light penetration (Garrett 1984). There is a mortality risk for fish or other animals attempting to pass through turbines. The tidal barrage is also an impediment to

maritime traffic, though locks may be included. Many studies have documented the far-field hydrodynamic impacts of barriers in the Bay of Fundy and Gulf of Maine (Greenberg 1979; Garrett 1974; Sucsy *et al.* 1993). Sucsy *et al.* (1993) predicted an increase of tidal amplitude in the Gulf of Maine of 30 - 50 cm when an impermeable barrier was placed across the Minas Channel.

1.5.3. Tidal lagoons

A recent alternative is the *offshore tidal lagoon*. Rather than blocking off a river, estuary, or bay, a retaining wall in a closed shape is built offshore, creating an artificial lagoon, with turbines placed on the seaward side. The *coastal tidal lagoon* is a variant of the tidal lagoon. In this case the lagoon is connected to shore and incorporates the shoreline into the retaining structure (Figure 1.7). Tidal lagoons operate in the same manner as a tidal barrage, though they remain at the conceptual stage and there are no constructed examples anywhere in the world.

With no case studies to look to, any discussion of the challenges and impacts of tidal lagoons has to extrapolate from existing technology. Tidal lagoons, as a design option, add to the number of sites suitable for tidal power development. On the other hand, the scale and cost of civil works would be greater than in the case of a tidal barrage. Tidal lagoons do not block a natural channel and thus side-step some of the environmental impacts of tidal barrages, *e.g.* interrupted fish migration and maritime traffic. Blade strike on fish or other animals is still a concern, as are changes in sedimentation processes and flow patterns. Cousineau *et al.* (2012) predicted a 4 cm tidal range increase at Boston for a coastal tidal lagoon constructed in Minas Basin with an output of 500 MW.

Figure 1.7. Artist's impression of an offshore tidal lagoon, left, and a coastal tidal lagoon, right (source: Tidal Electric Inc.)

1.5.4. Tidal turbines

The last decade has seen a veritable *renaissance* of tidal power with unprecedented scientific inquiry into the *tidal turbine* at its centre. Analogous to a wind turbine, tidal turbines exploit the kinetic energy of tidal currents to produce electricity. It's striking to note that a book written on tidal power only 8 years ago makes no mention of the concept (Clark 2007). The sheer number of synonyms for these devices tells the story of an industry in its infancy: *tidal in-stream energy converters* (TISEC) (Gooch *et al*. 2009), *marine current turbines* (MCT) (Grabbe *et al.* 2009), *water current turbines* (WCT) (Güney and Kaygusuz 2010), *marine current energy converters* (MCEC) (Bahaj and Myers 2004), *tidal stream generators* (TSG) (Tousif and Taslim 2011), *tidal stream turbines* (TST) (Evans *et al.* 2015) and *tidal energy converters* (TEC) (IEC-TC-114) are found in the published literature.

The design of tidal turbines is currently as diverse as the growing number of institutions pioneering their development: in a recent technology survey, Khan *et al.* (2009) identified a total of sixty-two different devices and schemes (Figure 1.8). With few exceptions, these technologies are at the proof-of-concept or part-system stage. The most common turbine designs are horizontal and vertical axis, the rotational axis of the former being parallel to the direction of current and the latter perpendicular to the direction of current. In addition, there are a number of novel non-turbine conversion schemes, *e.g.* flutter vane, piezoelectric, oscillating hydrofoil, and sails.

There are three main support structure options for tidal energy converters (Rourke *et al.* 2010). The first option is a piled structure pinned to the seabed with one or more steel or concrete beams. The second option is a gravity structure which consists of a large mass of steel and concrete attached to the base of the structure to achieve stability. The third option is a floating structure moored to the seabed using chains or wire.

According to Khan *et al.* (2009) turbine development and duct augmentation go hand in hand: 33% of horizontal axis and 48% of vertical axis turbines are being considered for duct augmentation. There are numerous practical advantages to duct augmentation (Kirke 2005): in areas where there is a danger of divers, floating debris (*e.g.* ice), fish or other animals being drawn into the turbine, a mesh could be placed to reduce danger to life and to the equipment; the turbine is shielded from direct sunlight thereby reducing biofouling; the duct improves efficiency by eliminating tip losses on horizontal axis turbine blades; by concentrating a large flow area containing a large amount of energy into a smaller area a more economical turbine can be used for a given power output.

DeltaStream, UK (source: Tidal Energy Ltd.)
Horizontal axis

Evopod, UK (source: Oceanflow Energy Ltd.)
Horizontal axis. Floating structure.

Kobold, Italy (source: Ponte di Archimede)
Vertical axis. Floating structure.

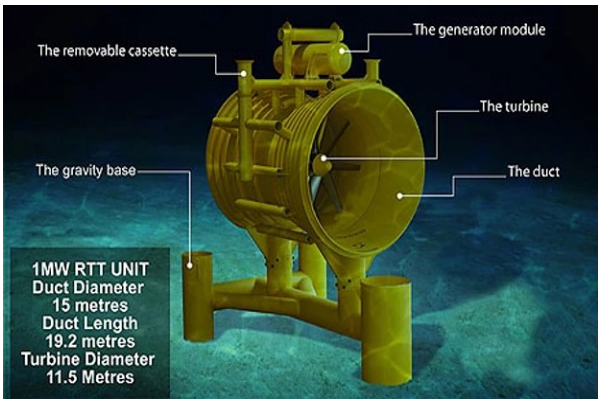

Lunar Tidal Turbine, UK (source: Lunar Energy Power Ltd.)
Horizontal axis

Gorlov Helical Turbine, US (source: GCK Technology Inc.)
Vertical axis

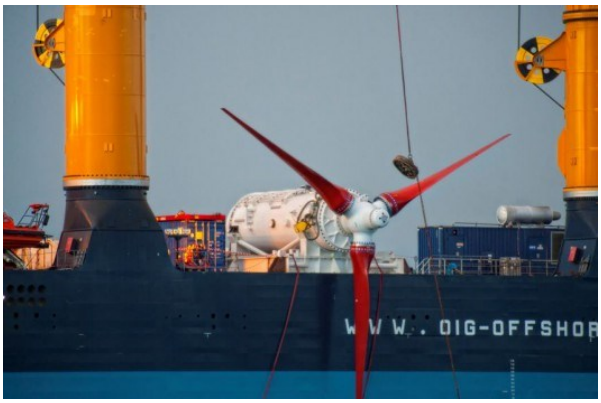

HS1000, Norway (source: Andritz Hydro Hammerfest)
Horizontal axis

Figure 1.8. Example of turbine systems

According to Güney and Kaygusuz (2010) more than 300 hydrokinetic projects are already underway around the world. SeaGen, the world's first commercial-scale tidal turbine is deployed, operational and connected to the grid in Strangford Lough, UK (Fraenkel 2007). The 1.2 MW SeaGen turbine is mounted on a cantilever tower tall enough to permanently project above the surface of the sea and facilitate maintenance. Andritz Hydro Hammerfest is experimenting with the HS1000 axial turbine in Norway (Grabbe *et al.* 2009), in Italy, Ponte di Archimede is developing the floating vertical axis Kobold turbine (Elghali *et al.* 2007), and in France, Sabella is assembling the D10 for demonstration. In the United States, Verdant Power has deployed six turbines in the East River in New York as part of the Roosevelt Island Tidal Energy (RITE) Project (Verdant Power 2010). While it is widely believed that commercial deployments of TECs will occur in arrays, not standalone devices, at present there are no such arrays in commercial operation.

Tidal energy converters hold many advantages over other forms of tidal power. Tidal turbines are submerged and hence *unobtrusive*. The solution is *modular*, turbines can be designed with different support structures and augmentations to fit local conditions; and *scalable*, turbines can be deployed in ones, twos, or in vast arrays. Whereas barrages and lagoons need a large tidal range, tidal turbines simply need a strong current: the basic requirements for cost-effective TECs are a mean spring peak velocity > 2.25 - 2.5 m/s in a 30 - 40 m depth of water (Douglas *et al.* 2008), hence a wider range of sites can be exploited. By avoiding dams and large reservoirs, the capital cost of civil works is eliminated. At the same time, disruption to ecosystems and maritime traffic is minimised. Despite the early stage of development, Douglas *et al.* (2008) show in a life cycle assessment (LCA) that the SeaGen turbine compares favourably with large wind turbines regarding carbon intensity and energy payback period (Figure 1.9).

There are also many challenges ahead for tidal energy converters. Tidal turbines are, by necessity, deployed at sites with strong tidal currents. Under these conditions, with only a few minutes of slack time between tides, constructing a foundation, installation and maintenance are no easy task. After installation, powerful currents coupled with dense seawater apply exceptional forces on TECs, many times larger than those acting on wind turbines of a similar output. The first turbine deployed by OpenHydro in the Bay of Fundy had its blades destroyed by powerful currents in less than three weeks (Figure 1.10). In addition to physical forces, the turbines, support structures, and moorings are all subject to biofouling and corrosion, affecting the efficacy and survivability of the device (Figure 1.11). Bahaj and Myers (2003) provide a review of barriers to TEC development.

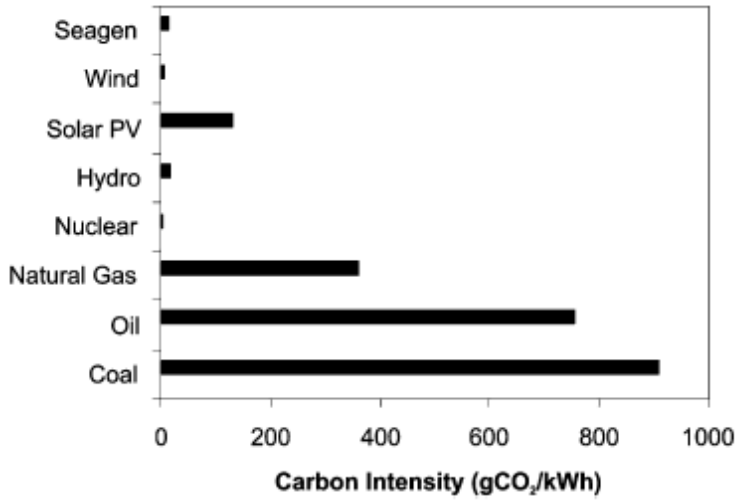

Figure 1.9. Life cycle carbon intensities of energy generating technologies (Douglas *et al.* 2008)

Figure 1.10. OpenHydro 1 MW tidal turbine deployed in the Bay of Fundy (source: OpenHydro Group Ltd.)

Figure 1.11. Biofouling of Clean Current tidal turbine after 3 years at Race Rocks, BC (source: racerocks.ca)

Among the major forms of tidal power generation, TECs are seen as the most environment-friendly. Authors commonly describe the environmental impact of TECs as 'minimal' and 'benign' in comparison to tidal barrages (Khan *et al.* 2009; Rourke *et al*. 2010; Atwater and Lawrence 2011). Minimal is not a synonym of negligible; benign is not a bill of good health; and enthusiasm for tidal power does not warrant disregard for the inevitable disruption of the natural environment that comes with any anthropogenic interference. A dramatic increase in the number of studies dealing with renewable energy these past years has seen only a small percentage deal with environmental effects (Gill 2005). The knowledge gaps have been identified (Boehlert and Gill 2010), but research has lagged behind development. Potential environmental impacts include: changes to water levels, tidal currents, water quality, and sediment transport; blade-strike of fish or other marine animals; short- and long-term exposure of marine organisms to anthropogenic noise; exposure of marine organisms to electromagnetic fields; and contamination of the habitat, *e.g.* due to antifouling or anti-corrosion measures. At this point in time, the availability of scientific literature on the environmental impacts of tidal energy converters is limited by the small number of full-size devices that have been deployed in natural environments for prolonged periods of time. In addition, environmental effects are likely to be technology, scale, and site-specific. The environmental monitoring reports available for SeaGen (Haskoning 2011) and the Cobscook Bay Tidal Energy Project (ORPC 2013) are an invaluable supplement to the literature. Reviews have been published by Gill (2005), Langhamer *et al.* (2010), Boehlert and Gill (2010), and Frid *et al.* (2012).

2. Literature review

The purpose of this section is to review the literature on tidal current energy resource assessment. In other words, this section will answer the question: how have interested parties assessed the tidal current resource up to now. To that end, desktop studies, analytical and numerical models are reviewed and discussed with an eye towards identifying best practice. Lessons learned here will provide a framework for the review and pilot application of the IEC-TC-114 draft standard. Note that there is often considerable overlap between the methodologies, the author has merely tried to categorise them so as to highlight key differences or to group similar approaches. Basic theory of tides is applied throughout this work – uninitiated readers are directed to Appendix A.

2.1. Kinetic energy

A current of speed u_0 has a kinetic energy (J) of

$$E_k = \frac{1}{2}\rho u_0^2 \tag{2.1}$$

per unit volume, where ρ (kg/m^3) is the density of the water. The energy flux (W/m^2)

$$P_f = \frac{1}{2}\rho u_0^3 \tag{2.2}$$

provides a useful metric for the power that might be available per unit cross section of a turbine. Energy flux, power flux, and power density are used interchangeably. The total kinetic power (W) in a tidal turbine is governed by the following equation

$$P_0 = \frac{1}{2}\rho A u_0^3 \tag{2.3}$$

where ρ (kg/m^3) is the density of seawater, A (m^2) is the sweep area of the turbine, and u_0 (m/s) is the fluid velocity. As can be seen from (2.3), power is proportional to the cube of the current speed; therefore, the power generated is highly sensitive to fluctuations in the tidal currents. The power of the flow is also proportional to the fluid density which for seawater is between 1020 and 1030 kg/m^3 (about 800 times that of air). As a result, the energy flux of a tidal flow at 2 m/s is about 9 times greater than that for wind at a speed of 9 m/s. Hagerman and Polagye (2006) provide a comparison between tidal and wind power.

A tidal energy converter or tidal turbine can only harness a fraction of this power due to losses and (2.3) is modified as follows

$$P = \frac{1}{2} C_P \rho A u_0^3 \tag{2.4}$$

where C_P is known as the power coefficient and governs the fraction of power that can be extracted from a fluid stream after hydrodynamic, mechanical, and electrical losses. The power coefficient has typical values in the range of 0.25 - 0.30 for wind turbines (Elghali *et al.* 2007) and 0.35 - 0.50 for tidal energy converters (Blunden 2009).

In a classic analysis, Albert Betz estimated that the maximum power that can be extracted by a single horizontal axis wind turbine in an unconstrained flow is the fraction 16/27 or 59.3 per cent of the kinetic energy flux through the sweep area of the turbine. The derivation of the so-called 'Betz Limit' can be found in many textbooks and other publications on fluid mechanics (Ragheb and Ragheb 2011). The classic analysis also applies to the case of a similar turbine in a tidal stream provided that the channel is wide and deep compared with the sweep area of the turbine and that there is only a small change in free surface across the turbine. However, the assumption of unconstrained flow is not always justified for tidal turbines, where the fluid is bounded by the free surface and the seabed. Many of the most appealing sites for tidal current energy development rely on local constraints that give rise to strong currents, *e.g.* narrow channels and inlets. Hence, a different theoretical upper limit will apply for each installation. For example, Garrett and Cummins (2007) showed that the Betz limit for an isolated turbine increases by $(1 - A/A_c)^{-2}$ for a turbine of cross-sectional area A in a channel of cross-sectional area A_c because the confining effect of the channel boundaries increases the pressure drop that can occur. However, the analytical model of Garrett and Cummins makes many assumptions (see Section 2.4).

The Betz limit can be circumvented, in a manner of speaking, by placing a turbine in a shroud or duct. Duct augmentation induces sub-atmospheric pressure about the rotor (Figure 2.1), which increases flow velocity and power capture (recall that power is proportional to the cube of the flow speed). In actual fact, the Betz limit still applies: the power coefficient is calculated with the largest cross-section of the duct instead of the sweep area of the turbine. In a recent technology survey Khan *et al.* (2009) reported a maximum velocity increase factor of 1.67 among tidal energy converters, in other words the power coefficient increased 4.63 times. Kirke (2005) achieved a power coefficient as high as 1.69 in physical experiments with tidal turbines.

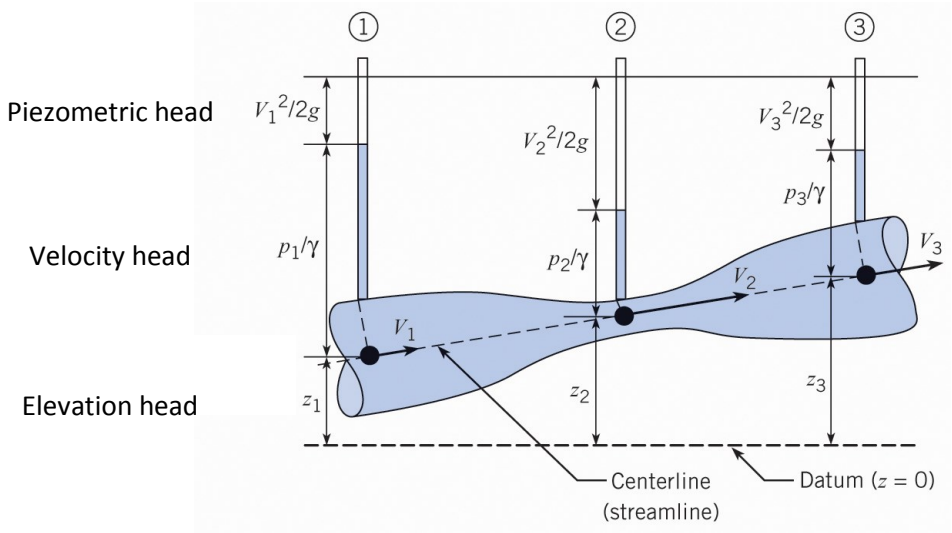

Figure 2.1. Piezometric and velocity head variation for flow through a venturi section (Crowe *et al.* 2009)

2.2. Desktop studies

Early attempts at tidal current resource assessment called for a cookie-cutter methodology that could be implemented for all sites (Blunden and Bahaj 2007). The purpose of these desktop studies was to provide government and industry with a preliminary estimate of the potential from a large number of sites to aid in decision-making with respect to policy or future investments in tidal energy. Hence, in most cases, the kinetic energy flux through the channel cross-section was used as a metric for the available power despite the limits and flaws of that method (see Section 2.4).

Hagerman and Polagye (2006) describe the methodology used by the Electric Power Research Institute (EPRI) to calculate the mean annual tidal current energy resource. Screening identifies promising sites based on the speed of the tidal currents and the channel cross-sectional area. Proximity to an existing grid connection, seabed geology, and ease of inspection, maintenance, and repair are secondary factors. The velocity time series is determined at each site from tidal current tables or a tidal prediction program (*e.g.* WebTide). Values are corrected to account for the depth profile by assuming a $1/10^{th}$ power law and values are taken as constant across the width of the channel. The time-varying cross-sectional area is estimated from bathymetric charts and tidal elevation forecasts. The theoretical tidal current energy resource is the product of the mean annual depth- and width- averaged power density and the mean channel cross-section. The extractable resource is limited either by channel geometry (the maximum number of turbines that could be physically placed within the channel) or by environmental concerns (local policy dictates allowable changes to flow properties). The authors assume that environmental factors limit the extractable

power to 15 per cent of the theoretical resource as per the significant impact factor (SIF) method. Physical constraints are verified by calculating annual energy production with a generic power curve, velocity time series, and conventional device spacing.

The significant impact factor was defined by Black and Veatch (2004) in a tidal current resource assessment for the UK. The SIF is the proportion of the kinetic energy flux in a site that can be extracted without significant impact. Based on the model of a simple channel connecting two large bodies of water by Bryden *et al.* (2004), the significant impact was defined in terms of an acceptable percent decrease in upstream flowrate after energy extraction was applied. Values of 10 to 20% have been applied in the literature (Hagerman and Polagye 2006). What constitutes acceptable social and environmental restrictions and whether a blanket factor is appropriate is up for discussion.

Grabbe *et al*. (2009) reviewed two published tidal current resource assessments of Norway and compared the results with their own. The methodology used in these assessments is similar to that described by Hagerman and Polagye (2006). All three assessments are based on the same data: current speeds gathered from pilot books and width and depth estimated from digital sea charts. Only the interpretation of the materials differs: the three studies differ in the resource they assess (*i.e.* theoretical, extractable, practical), the significant impact factor, device efficiency and availability, and site selection. Based on the peak spring current speed and the cross-sectional area at a site the kinetic energy flux is calculated. The annual resource is extrapolated with factors accounting for the relationship between spring and neap tide and the velocity profile. This review illustrates the subjective character of desktop studies: the two reviewed studies found an extractable resource on the order of 1 TWh, while Grabbe *et al.* (2009) calculated a theoretical resource of about 17 TWh. As the authors readily state, all three studies suffer from other shortcomings besides the input data. The cost of deployment at different depths and distance to the nearest grid connection could be pivotal in the economic assessment of a site. Furthermore, the appearance of current speeds in pilot books suggests that the channel sees maritime traffic and highlights the need to consider user conflict in the course of site screening.

There is considerable skepticism with regard to these desktop studies as they are mainly based on secondary material meant for other uses than tidal current energy resource assessment. A study by Black and Veatch (2005) found disagreements of as much as 2 m/s at a site using different tidal atlases. The problem is subsequently amplified when the velocity is cubed to calculate the energy flux.

What is more, these assessments ignore the change in flow conditions due to the back effect of the generating devices. At best the results of a desktop study could give a rough indication of the distribution of the tidal current energy resource.

2.3. Direct measurement

Measurements are required in the first instance to understand the resource; in the second instance, to allow for future model validation. For example, by characterising the velocity profile resource assessments can be tailored to specific turbine designs (*e.g.* floating, gravity, or monopile). Bottom- and ship-mounted acoustic Doppler current profiler (ADCP) surveys are both useful in tidal current resource assessment: the former offers high temporal resolution but comparatively limited spatial resolution and the latter vice versa.

Fairley *et al.* (2013) used ADCP transects to characterise the tidal current resource in three channels in the Ramsey Sound region of Pembrokeshire, United Kingdom. Vennell (2011) presented a simple method for estimating the potential of currents in tidal channels to produce power (see Section 2.5). The method only requires measurement of the peak tidal volume transport through the channel. Following Vennell, the transect data was used to calculate the theoretical maximum extractable power and this was compared to the measured kinetic energy flux. The maximum extractable power ranged from 7.2 to 21.8 MW. These values are about ¼ of the average flux through the channels over a spring tidal cycle, which ranged from 39 to 84 MW.

In a case study of two sites along the west coast of Ireland, O'Rourke *et al.* (2014) used bottom-mounted ADCP surveys to assess the tidal current resource. The site in the Shannon Estuary sees maximum mid-depth speeds > 2 m/s whereas the site in the Bulls Mouth experiences maximum speeds of about 1 m/s. The power density at each location was calculated by taking the mean of the distribution of instantaneous power densities, yielding values of 521 and 10 W/m^2 at the Shannon Estuary and the Bulls Mouth, respectively. Measured currents were used in conjunction with the technical specs of the SERG (Sustainable Energy Research Group) turbine to calculate the annual energy output. Values of 137.4 and 2.2 MWh were found for the Shannon Estuary and the Bulls Mouth, respectively. Note how the disparity between the sites is amplified as the assessment progresses from current speed, to power density, to power output.

The authors compared theoretical tidal current velocity profiles with measured data at both sites. While most tidal current resource assessments adopt a $1/7^{th}$ power law, O'Rourke concluded that a

1/4th power law provided a better fit in the Shannon Estuary and the Bulls Mouth (Figure 2.2). In another study, Coles *et al.* (2013) showed that the velocity profile changed throughout the tidal cycle in Strangford Lough and that a 1/10th power law often provided the best fit. The unpredictable nature of the velocity profile in energetic tidal channels makes power predictions challenging and may be a significant source of error due to the sensitivity of power calculations to current speed.

Evans *et al*. (2015) analysed measurements of tidal velocity in Ramsey Sound to gauge the effect of depth-averaging tidal velocity data across the entire water column instead of over the depth span of the turbine on tidal current energy assessment. As would be expected, there is little difference in the power flux when vertically-averaging the data over the depth span of the turbine compared to across the entire water column in the shallower regions of the Sound. However, in the deeper regions, a power flux of 27.4 and 3.5 kW/m^2 is calculated at flood and ebb, respectively, with depth-averaged velocity over the depth span of the turbine compared to 22.2 and 2.1 kW/m^2 with depth-averaged velocity across the entire water column. That represents a relative error of 23.4 and 12.9 per cent, respectively. The depth-averaged velocities only deviated by 8.6 and 5.6 per cent at flood and ebb, respectively, exemplifying the error magnification that occurs as a result of the cubic velocity term. Although depth-averaging tidal data over the entire water column is common practice in tidal applications (Ramos and Iglesias 2013), it can mask important flow characteristics in these dynamic tidal regions, resulting in either an under- or an overestimation of the tidal current energy resource. The authors argue based on these findings that 2D depth-averaged numerical models should be eschewed in favour of 3D modelling in dynamic tidal regions.

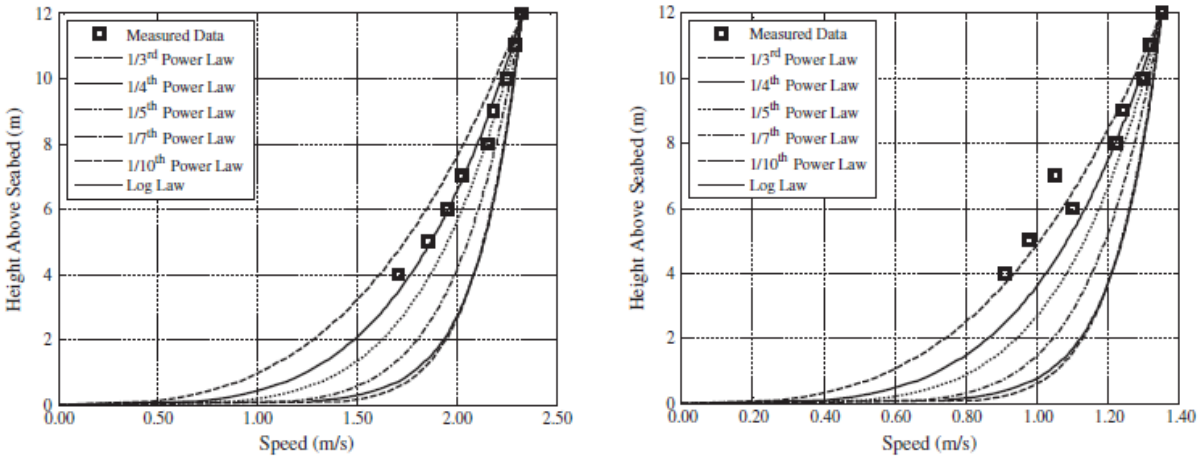

Figure 2.2. Comparison of theoretical spring (left) and neap (right) tidal speed profiles with measured data at a site in the Shannon Estuary (O'Rourke *et al.* 2014)

2.4. Analytical models

Simplified analytical models have been developed to try and establish relationships between the power extracted and the changes in flow conditions. Many of these are concerned with estimating the maximum extractable power from a site with a certain characteristic geometry, for instance a channel connecting a bay to a large basin, a channel split by an island into two sub-channels, or a channel with a varying-cross section linking two large bodies of water. Initially, the average extractable power for electricity generation increases as turbines are added to the tidal stream; too many turbines, however, will diminish the flowrate excessively and reduce the extractable power.

Bryden *et al.* (2004) looked at the case of a simple rectangular channel connecting two large bodies of water where the flow is driven by a static head difference. The act of power extraction is modeled as an added roughness (an approach that will be repeated time and again). A substantial head drop accompanied by local flow acceleration is observed across the extraction point, along with a global reduction in flow speed. Although the simulation represents the withdrawal of 10 per cent of the kinetic energy flux in the channel, the alteration of the hydraulic regime caused by the turbine (*i.e.* added roughness) means that the extraction represents only 8.4% of the kinetic energy flux in the undisturbed channel. It's important to recognise that calculations based on the kinetic energy flux don't account for the back effect of energy extraction. Removing energy from tidal currents increases drag and slows flow, limiting the power that can be extracted. Consequently, power generation falls below the metric of kinetic energy flux. The authors note that extracting 10% of the undisturbed energy flux results in a speed reduction of < 3% while greater extraction yields diminishing returns on the energy produced. Bryden *et al.* (2004) suggest based on these findings that extraction of 10% of the apparent kinetic energy flux could serve as a 'rule of thumb' for the environmental limit.

Garrett and Cummins (2004) considered the case of power generation at the mouth of an enclosed bay subject to sinusoidal tides. The authors compared the maximum average power extracted by a tidal barrage with ebb generation to a scheme with tidal energy converters. The turbines were modeled with a quadratic drag force applied uniformly across the mouth of the bay, which would require turbines to be deployed as a tidal fence intercepting all the flow. The tidal fence scheme is capable of extracting 76% of the maximum average power generated by the tidal barrage while maintaining the tidal range within the bay at 74% of the natural state. When the power extracted by the fence decreases to 67% the tidal range inside the bay increases to 90% of the natural state. The authors argue that a tidal fence at the entrance to a bay could generate power comparable to a

tidal barrage with a fraction of the environmental impact. However, it's worth noting that the analysis neglected any energy losses at the mouth of the bay apart from turbine drag.

Garrett and Cummins (2005) extended their analysis to a channel of variable cross-section connecting two large bodies of water with a sinusoidal head difference. The authors developed a practical formula $\gamma\rho g\zeta_0 Q_{max}$ for the maximum average extractable power where Q_{max} denotes the peak volume flowrate through the undisturbed channel and ζ_0 is the amplitude of the difference in surface elevation between the ends of the channel. Across the range of possible channel dynamical balances γ varies between 0.21 and 0.24. As a result, the solution may be estimated with an accuracy of 10% using $0.22\rho g\zeta_0 Q_{max}$. However, the analysis neglects losses associated with turbine operation. Garrett and Cummins show that the relationship between mean kinetic energy flux and maximum average extractable power is dependent on the flow speed, not simply on the physical characteristics of the channel. From this, the authors argue that the mean kinetic energy flux is not a useful metric for the extractable power, as there's no simple relationship between the two.

The analytical model developed by Garrett and Cummins (2005) was subsequently verified by a numerical modelling study of Johnstone Strait, British Columbia. Sutherland *et al.* (2007) estimated the maximum tidal power potential of the channel using a two-dimensional finite element model by increasing the drag in certain regions to simulate turbines. The numerical and analytical models agree reasonably well, with estimates of 886 and 826 MW, respectively. The numerical model is able to simulate the impact of maximum energy extraction: the current is reduced to between 57 and 58% of the natural state, close to the 58% predicted by the analytic theory (Atwater and Lawrence 2011).

Blanchfield *et al.* (2008a) adapted the formula developed by Garrett and Cummins (2005) to the case of a channel linking a bay to the open ocean by defining η_0 as the magnitude of the dominant tidal constituent in the open ocean just outside the channel and increasing the range of γ to 0.19 - 0.26. The maximum average power available may be estimated with an accuracy of 15% by $0.22\rho g\eta_0 Q_{max}$ for any bay geometry. Blanchfield *et al.* (2008b) then presented a case study of the tidal current energy resource for Masset Sound, a channel in Haida Gwaii, British Columbia, which links Masset Inlet to the Pacific Ocean. The maximum average extractable power is estimated at 79 MW when only the dominant M2 tidal constituent is included in the analysis. The value increases by 9% to 87 MW when the three dominant constituents are included. If the maximum available power is extracted, the tidal range within the bay and the maximum tidal flowrate are reduced to 58% of their undisturbed values. The tidal regime may be preserved at 90% of the natural state by extracting

37 MW at the most. As in the case of Garrett and Cummins (2005), the model excludes hydrodynamic, mechanical, and electrical losses. The authors draw attention to the fact that Haida Gwaii has a peak demand of about 10 MW, thus a significant fraction of its electricity demand could be met by tidal power while maintaining a nearly undisturbed tidal regime.

Garrett and Cummins (2007) expanded their model from (2005) to allow for turbines that occupy only a fraction of the channel cross-section. The authors showed that energy is lost as water moving slowly in the wake of the turbines merges with faster flow in the free stream. Consequently, the maximum tidal power potential of a partial fence is always a fraction of the potential of a complete fence. The fraction is 2/3 if the turbines occupy a small part of the channel cross-section and decreases to 1/3 if they occupy most of the section (*i.e.* the blockage ratio increases from zero to close to unity). Note that the actual, rather than fractional, power still increases as the blockage ratio increases. Again, the model neglects losses associated with turbine operation.

The drawback of the approach by Garrett and Cummins (2005) is that calculating the extractable power necessitates measurements of the water level at both ends of the channel. Vennell (2011) adapted the equation to calculate the maximum average extractable power using only the peak tidal flowrate through the undisturbed channel, the cross-sectional area, and a drag coefficient:

$$\bar{P}_{max} = \frac{4}{3\pi} \frac{\rho C_F^{Peak}}{A^2} (Q_{max})^3 \tag{2.5}$$

Estimating the maximum extractable power following Vennell (2011) or Garrett and Cummins (2005) requires the peak tidal flowrate through the natural channel, which is conveniently measured via ADCP transect (see Section 2.4).

Cummins (2013) recently looked at the case of a tidal channel split by an island into two sub-channels. A tidal fence is deployed in one of the sub-channels, while the second is left free for navigation or other purposes, as local policy may require. The free sub-channel allows for flow to be diverted away from the obstructed sub-channel, which leads to a reduction in the available power. The author approaches the problem with an electric circuit analogue to develop an analytic expression for the maximum extractable power and for the modification of the flow regime. The model is limited to linear frictional drag, which the author concedes is not realistic. On the other hand, the model is versatile and can be generalised to allow for multiple branching channels. When the maximum power is extracted, the flowrate in the impeded channel is reduced to between 50 and 71 percent of the

undisturbed value. The author notes that these are the same limits as in the single channel case. A sample calculation is presented where the maximum average power from the impeded sub-channel is 25 MW compared to 124 MW for the single channel case with similar dimensions. Flowrate is reduced in the impeded sub-channel to 52% of its magnitude in the natural state, while the flow in the free sub-channel increases by 28%. Notably, total transport is essentially unchanged. Again, the model neglects losses associated with turbine operation.

An important lesson to take away from this section concerns the kinetic energy flux. For an isolated turbine in a large channel, the extractable power is proportional to the turbine cross-section, water density, and the local kinetic energy flux. However, the *maximum extractable power* from a tidal stream in a channel is *not* proportional to the kinetic energy flux through the whole cross-section in the undisturbed state. The literature concurs that there is no simple relationship between the maximum extractable power from a channel and the mean kinetic energy flux (*e.g.* Vennell 2011; Garrett and Cummins 2005; Atwater and Lawrence 2011). The relationship is site-specific. Thus, tidal current resource assessments based on this metric are likely to under- or overestimate the tidal power potential. The analytic solutions presented here provide quick and easy methodologies to estimate the maximum extractable power for a number of typical geometries. Given the assumptions inherent to these solutions, their ideal role may be as an upper bound to help decide whether more sophisticated methodologies are worth applying. Assessing the tidal current resource in more realistic scenarios calls for numerical modelling.

2.5. Numerical models

2.5.1. KE flux method

Numerical tidal current energy resource assessments in the literature differ immensely in the methods that they implement. For the purpose of this review assessments will be categorised into: (2.5.1) kinetic energy flux, (2.5.2) augmented drag, (2.5.3) 'per-generator' and (2.5.4) farm methods. In spite of the limits and flaws brought up in Section 2.4, methods based on the kinetic energy flux have a place in the preliminary assessment of tidal current resources.

Carballo *et al*. (2009) adopted the power flux method to assess the tidal current energy resource at Ria de Muros, Spain. For their assessment a 2D hydrodynamic model was developed capable of accounting for horizontal density gradients. Although most studies opt for a constant water density, the authors considered the modelling critical because water density varies in time and space between

1008 and 1020 kg/m^3 in the estuary. Tidal, wind, and river forcing were additionally accounted for. The model's predictions were validated against one week of depth-averaged tidal current measurements yielding a correlation coefficient of R = 0.71. Having been validated, the model was used to forecast tidal currents for a spring-neap cycle. For these simulations, the model was run without wind forcing. The corresponding power density time series was calculated using Eq. (2.2). The authors selected two locations with high power densities to further characterise the tidal current resource. Numerical integration of the predicted power density at Sites A and B yields energy outputs of 205 and 81 kWh/m^2 and extrapolation yields annual figures of 5344 and 2114 kWh/m^2 respectively. The authors assumed a power coefficient of 0.33 and a turbine aperture of 750 m^2 (representing a swept area $\sim$2 times that of SeaGen) to estimate an annual energy production of 1.32 x 10^3 and 0.52 x 10^3 MWh, respectively. There are many assumptions inherent to this approach, for example, the back effect of energy extraction is neglected, and use of a power coefficient doesn't account for the cut-in, rated, and cut-out velocities of a genuine turbine. However, Carballo *et al*. (2009) represents the quintessential KE flux methodology.

Brooks (2006) followed a similar methodology in the Passamaquoddy-Cobscook Bay archipelago, located near the entrance to the Bay of Fundy. A 3D hydrodynamic model was developed capable of resolving temperature and salinity gradients. Tidal forcing was applied at the open boundary in the form of the M2 constituent (while Carballo *et al.* specified 7 constituents) and freshwater inflows were specified at river mouths. Predicted tidal currents were used to calculate the kinetic energy flux with Eq. (2.2). The highest power densities on the flood tide of > 10 kW/m^2 were found in constricted passages around the Lubec Narrows and Letete Passage, where peak tidal currents exceeded 3 m/s. Under mean tidal conditions, with an assumed power coefficient of 0.33 and a turbine aperture of 600 m^2 the model predicts an annual energy production of about 10^4 MWh.

The preceding studies exemplify how resource assessments can differ even when they adopt the same methodology. Choices such as two versus three dimensions, the number of constituents for modelling the driving boundary, the inclusion of meteorological phenomena, how to extrapolate to annual energy production, the specifications of tidal energy converters, and validation standards are usually up to the modeller. Although not without their flaws, these two studies suggest that there may be a role for the KE flux method in identifying sites which could benefit from a more detailed assessment informed by field measurements or grid refinement.

2.5.2. Augmented drag method

The augmented drag method has already been presented by Sutherland *et al.* (2007) in their case study of the Johnstone Strait (see Section 2.4). Turbines are modelled by increasing the drag over specified regions of the domain. At the start, the average extractable power for electricity generation increases as drag is added to the tidal stream; too much drag, however, diminishes the flowrate excessively and reduces the extractable power. The augmented drag method represents the maximum physically extractable power including any and all losses, *e.g.* due to drag on support structures, downstream wake mixing and conversion losses. The augmented drag method has also been applied to the Minas Passage locale.

Karsten *et al.* (2008) developed a 2D hydrodynamic model of the Bay of Fundy-Gulf of Maine system to validate theoretical estimates of the tidal current energy resource and to examine far-field effects of power extraction. The ocean boundary was forced with the M2 tide and the modelled amplitude and phase were compared to observations at 37 tidal stations scattered throughout the domain. The root-mean-square error was within 8 cm in amplitude and 3.1° in phase. The authors adapted the formula previously derived by Garrett and Cummins (2005) and later Blanchfield *et al.* (2008a) to the Minas Passage to estimate the maximum average extractable power and the change in local tides in response to the turbines. The *theoretical* maximum power that could be extracted is between 6.65 and 8.75 GW and, at maximum extraction, the tidal range in the Minas Basin is reduced to between 58 and 71% of the undisturbed value and the phase lag is 51 degrees. Turbines were modelled by increasing the drag over the entire Minas Passage in an approximation of a turbine farm or tidal fence. The *modelled* maximum power of 6.79 GW occurs when Minas Basin tides have been reduced to 64% and the phase lag is 55 degrees, which is in very good agreement with the theoretical estimate. Moreover, about 50% of the maximum extractable power can be reached with only a 7.5% reduction in the basin tides. These estimates of the maximum extractable power are more than 3 times greater than previous estimates based on the energy flux. In a desktop study by Triton Consultants (2006), the resource was estimated at about 1.9 GW in the Minas Basin. As discussed by Blanchfield *et al.* (2008a) and Garrett and Cummins (2005), the additional power above and beyond the kinetic energy comes from the potential energy forcing the tidal flows. The flux method does not account for such a back effect. Recall also that the inclusion of additional tidal constituents can increase the power significantly, by as much as 9% (Blanchfield *et al.* 2008a).

Sensitivity tests were carried out by Karsten *et al.* (2008) to see whether the same results would be obtained with smaller regions of increased drag – a more genuine representation of a turbine farm. Simulations were run where turbines (*i.e.* increased drag) were only placed along a quarter of the total length of Minas Passage. To obtain the same net drag over a reduced surface area the drag coefficient of the turbines was increased, *i.e.* each turbine has to work harder. The thinner strip of increased roughness gave nearly identical results to the original simulations, suggesting that the maximum power extraction can be achieved with a single tidal fence.

2.5.3. 'Per-generator' method

The 'per-generator' method of resource assessment relies on calculating the output of a more-or-less realistic generator under the operating conditions of the undisturbed flow field. Therefore, the tidal current resource is the velocity probability distribution transformed by a device's power curve. Consequently, the results of the 'per-generator' method are sensitive to the specifications of an actual or presumed device.

Ramos and Iglesias (2013) employed parametric comparison and a 'per-generator' assessment to select the optimal tidal energy converter for a site in the Ria de Arousa. The methodology is based on four parameters: the capacity factor, availability factor, site-specific turbine efficiency and the annual energy production. The capacity factor (CF) of a turbine is the ratio of its actual power output over a period of time to its potential output if it were to operate at rated capacity continuously over the same period of time. The availability factor (AF) is the amount of time that a turbine is able to produce electricity over a certain period (*i.e.* the amount of time the flow velocity is between cut-in and cut-out velocities), divided by the amount of time in that period. In a manner of speaking, the capacity and availability factors represent how effectively a turbine is being exploited at a given location. The site-specific turbine efficiency is a parameter defined by the authors as the ratio of the electrical energy output of the turbine to the available energy at the site based on the kinetic energy flux over a reference time period (Figure 2.3). The electrical energy output is calculated from modelled velocity time series during the reference period and the device-specific power curve which accounts for cut-in, rated and cut-out velocities (Figure 2.4).

The authors compared two tidal energy converters, the Evopod and the Gorlov turbine, for a site in the Ria de Arousa, Spain. A 2D hydrodynamic model was developed including wind, river and tidal forcing with seven constituents derived from the TPXO7.2 Global Tide Solution. The model was used

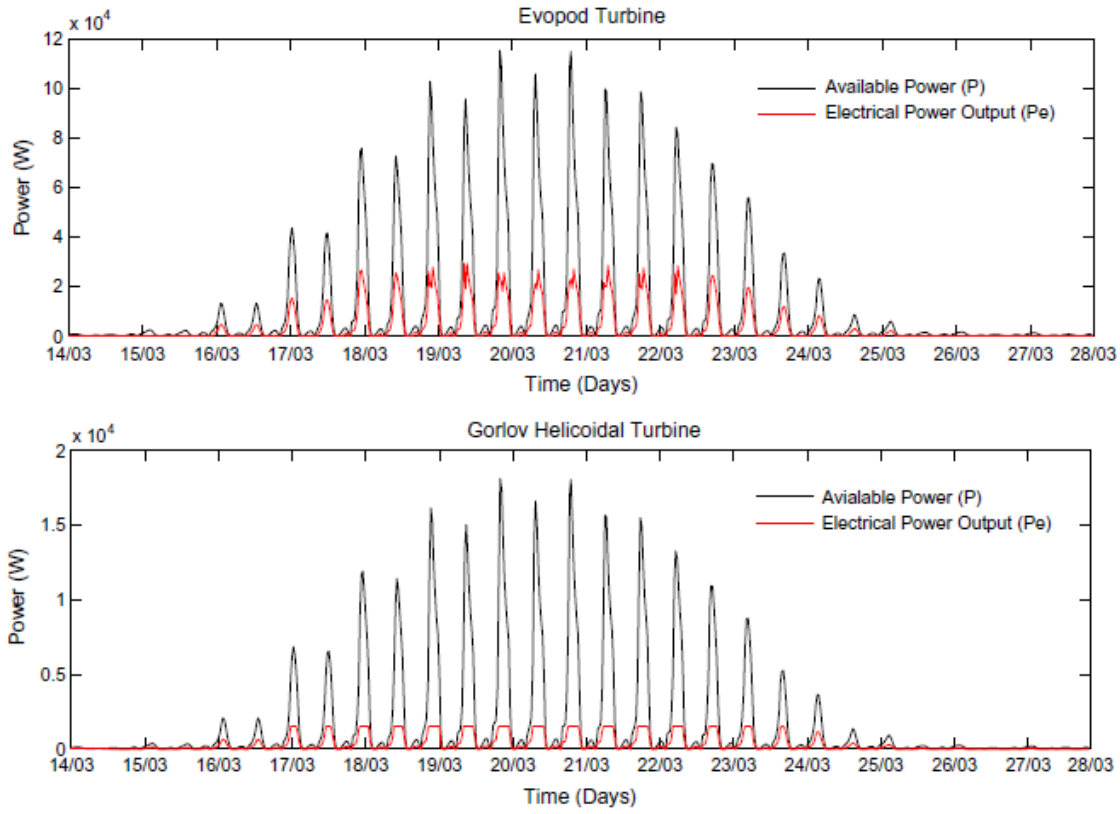

Figure 2.3. Available power and electrical power output for the Evopod and Gorlov turbines (Ramos and Iglesias 2013)

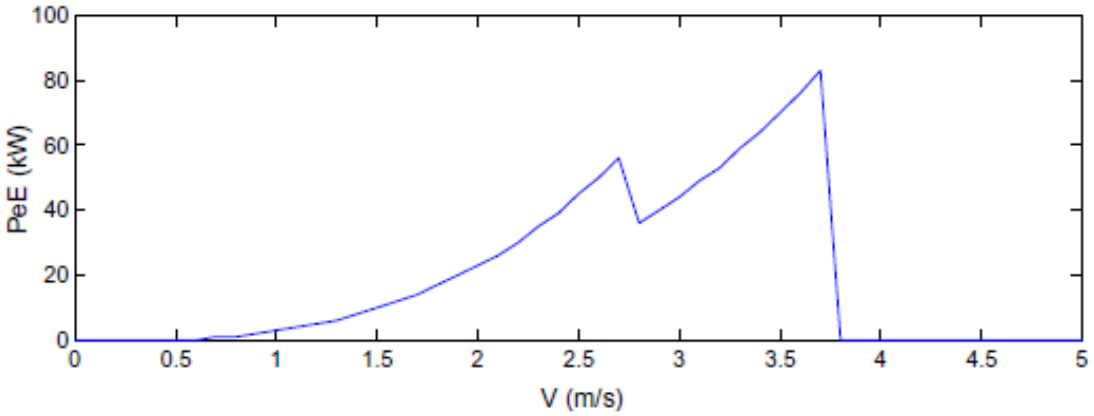

Figure 2.4. Power curve of the Evopod turbine (Ramos and Iglesias 2013)

to simulate tidal velocities for a spring-neap cycle. The site for the performance assessment was selected with the help of the tidal stream exploitability (TSE) index previously developed by the authors which incorporates water depth, mid-ebb and mid-flood velocity data. The Gorlov turbine was found to have higher availability and capacity factors. Extrapolating from the reference period, the Gorlov would be operational 4730 hours and the Evopod 3241 hours. Similarly, the Gorlov would operate at rated capacity for an equivalent of 3241 hours versus 1051 for the Evopod. Conversely,

the Evopod has a higher site-specific efficiency and energy output. Extrapolating to a year, the annual energy output is estimated at 30.6 and 5.2 MWh for the Evopod and Gorlov, respectively. Despite the uneven results in terms of annual energy production, the greater availability of the Gorlov machine reduces intermittency which affects the value of energy produced. The authors propose that based on these parameters and a 'per-generator' assessment, potential developers could carry out a cost-benefit analysis to choose the optimal device to deploy.

2.5.4. Farm method

The farm method calculates the output of a more-or-less realistic generator under the operating conditions of the undisturbed flow field and scales the output by the expected number of generator units in a region (Figure 2.5).

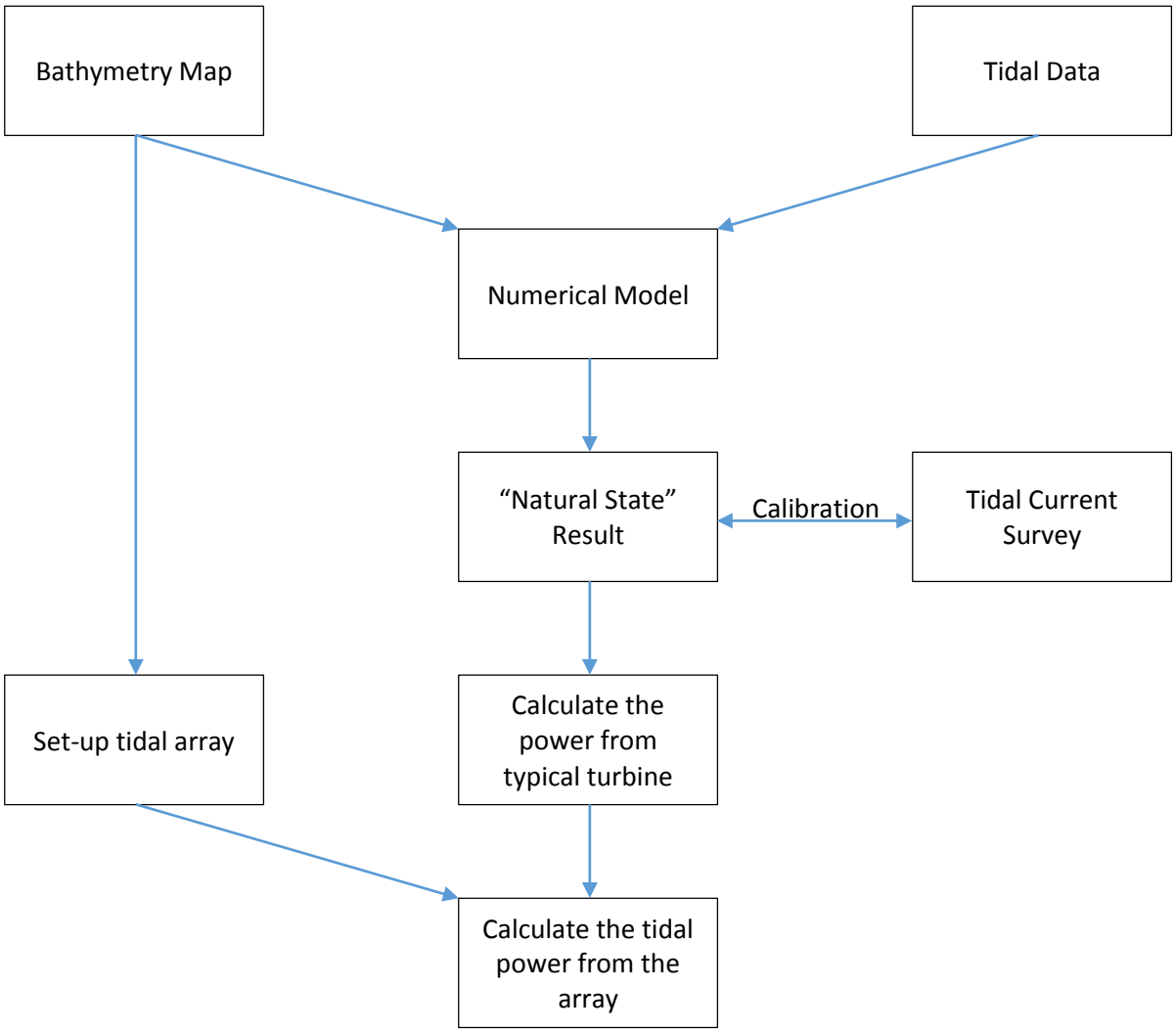

Figure 2.5. Flowchart of the farm method (Blunden *et al.* 2013)

Evans (1987) first established the farm method in a doctoral thesis. Evans developed a two-dimensional finite difference model to simulate tidal heights and currents from the M2 tide in the sea around the Channel Islands. The model was used to select suitable development sites by selecting grid squares based on minimum depth and mean kinetic energy flux over a spring-neap cycle. The power output of each grid square was calculated as the product of the mean kinetic energy flux, the swept area of the turbine, an assumed number of generators per unit surface area, the surface area of the grid square, and a power coefficient. The total tidal current energy resource could be computed as the sum of the power output of the grid squares. Since then, many have applied the farm method or variants thereof.

Lewis *et al.* (2015) developed a 3D hydrodynamic model of the Irish Sea to compare the present and future potential of tidal current energy resources. The ocean boundary of the model was forced with FES2012 data for 10 tidal constituents. The spring-neap cycle tidal heights showed a root-mean-square error of ∼10 cm and tidal currents were accurate within about 8 - 11 percent. In their initial assessment the authors assume first generation TEC technology, which requires water depths of 25 - 50 m and peak spring tidal velocities > 2.5 m/s. Two additional scenarios were investigated: second and third generation technologies, defined as capable of exploiting currents with peak spring tidal velocities > 2 m/s and > 1.5 m/s respectively. Second and third generation technologies were also presumed capable of exploiting deeper sites: depths > 25 m were considered with no upper limit.

The authors quantified the tidal current resource in three phases. Firstly, the maximum potential sea space for development was calculated. Secondly, the mean kinetic energy flux for a spring-neap cycle is calculated. Thirdly, the practical power available at each model grid cell is calculated by applying the measured power curve of the SeaGen turbine to the pure spring-neap tidal current time-series at all applicable locations and assuming two devices per fine resolution model grid cell (∼278 km^2). Based on the criteria outlined above, a surface area of about 90 km^2 was found suitable for development of first generation sites. Likewise for first generation sites, the undisturbed kinetic energy flux was estimated at 4 TJ, yielding an annual practical power output of approximately 24 GWh. Some 800 and 6000 km^2 were suitable for second and third generation technologies, respectively. The undisturbed kinetic energy increases by factors of 7 and 37, respectively, when upgrading from first to second and second to third generation technology. The practical annual resource increases by a factor of 8 between first and third generation with the majority of this increase occurring at the jump from first to second generation.

Farm method assessments tend to ignore the effects of upstream on downstream either by assuming conservative spacing between devices or by reducing resource estimates by a blanket factor. Blunden *et al.* (2013) investigated the tidal current energy resource in Alas Strait, Indonesia, while taking into account the reduction of incident flow speed based on the number of rows deep into the array. In this way, the authors try to account for the effects of array shape in the numerical model without including computationally expensive parameterisation of turbines. The 3D hydrodynamic model was driven by 8 harmonics and validated against tidal velocity measurements. The authors began by identifying suitable grid cells based on water depth. Two scenarios were considered: with and without a maximum depth restriction of 40 m (Figure 2.6). Each suitable grid cell was assigned a sub-array of 16 - 28 devices (depending on the rotor diameter) arranged in a pair of rows facing the principal flow direction. To account for downstream flow reduction in a tidal array, the direction of flow relative to the array is determined and a factor of 0.9 is applied to the tidal currents from the undisturbed state numerical model results in every row past the first. The authors based the attenuation factor on data from large wind farms, which indicate that the majority of the velocity reduction occurs between the first two rows, before the mean wind velocity profile adjusts to the increased momentum transfer. The annual energy production is calculated by assuming TEC parameters similar to SeaGen and adding the contribution of each sub-array. The depth-limited scenario yielded an annual resource of 330 GWh and the unlimited scenario 640 GWh.

The most recent tidal current energy resource assessment for Ireland was put together in a report by Sustainable Energy Ireland (2004). The assessment employed a 2D hydrodynamic model of the Irish Sea to assess the theoretical resource and with the introduction of constraints and limitations the technical, practical, accessible and viable resources were obtained. O'Rourke *et al.* (2010) published a comprehensive review of the assessment.

First, the theoretical tidal current energy resource was calculated. The authors defined this as the undisturbed energy flux of the tidal currents in a strip encircling Ireland, between the 10 m depth contour line and the 12 nautical mile territorial limit. Within this strip the modelled peak spring tide velocity was used to determine the mean power flux:

$$P_{mean} = \frac{1}{2}\rho K_s K_n U_{peak}^3 \tag{2.6}$$

where K_s is the velocity shape factor (0.424 for sinusoidal flow), K_n is a neap/spring factor (0.57) and U_{peak} is the peak spring tide velocity. Fraenkel (2002) describes the equation in further detail.

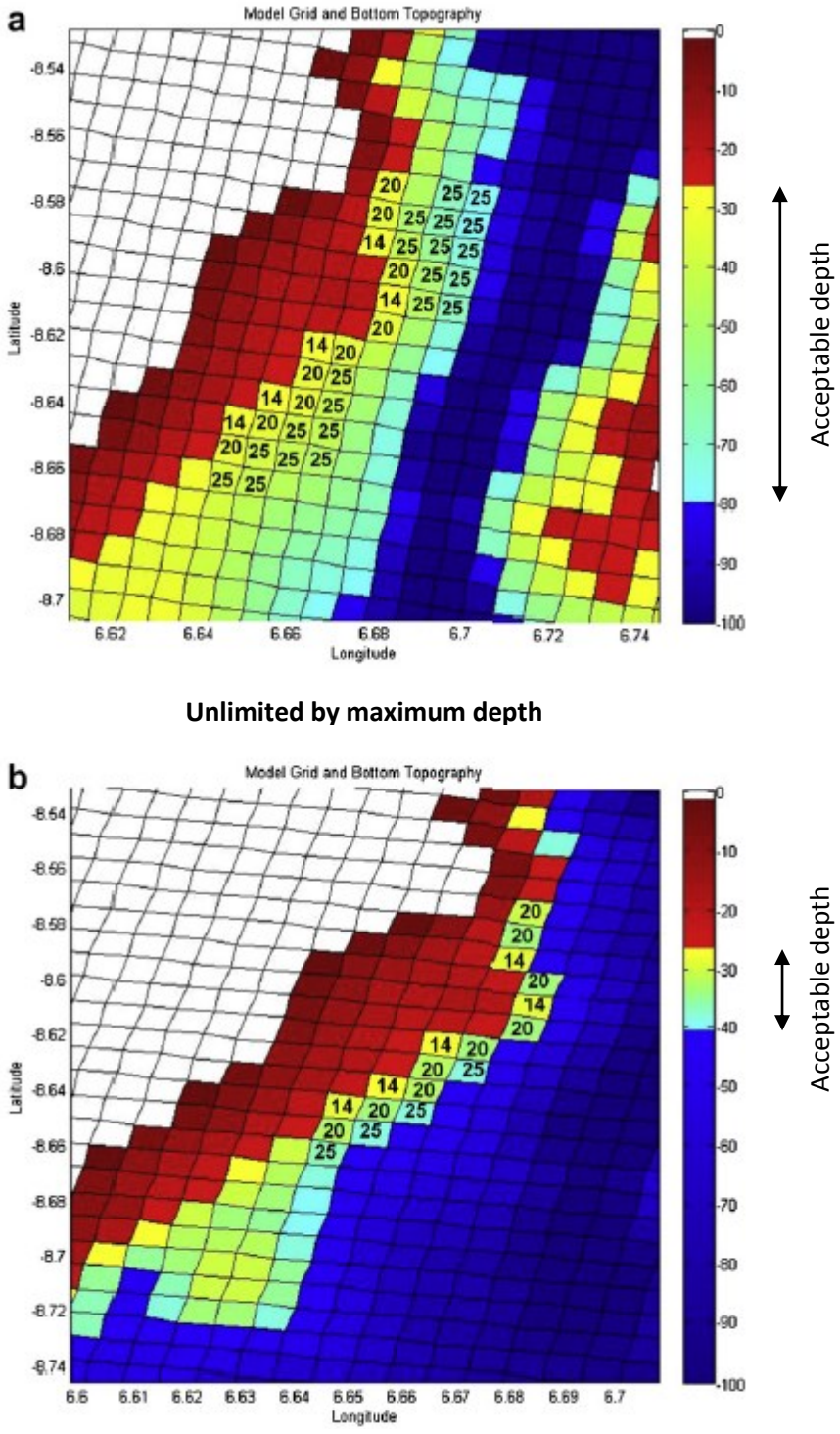

Figure 2.6. Comparison of the Alas Strait tidal array configuration between depth-limited scenario and moored/gravity-based scenario. Numbers in grid cells indicate the maximum diameter of tidal turbine that could be installed at that location (Blunden *et al*. 2013)

The *theoretical extractable* resource was calculated at 230 TWh by assuming a power coefficient of 0.59 (*i.e.* the Betz limit), lateral spacing of five diameters, upstream/downstream spacing of 10 - 20 diameters and a turbine aperture of 0.7 times the depth. The *technical* resource was calculated by applying technical limitations to the theoretical estimate. Existing tidal energy conversion technology is limited by turbine efficiency and tidal current speeds. Thus, by applying an efficiency factor of 0.39 and by excluding tidal current speeds < 1.5 m/s the technical resource was calculated at 10.46 TWh per year. The *practical* resource was calculated by applying practical limitations to the technical resource. Only sites with a water depth between 20 and 40 m were included in the assessment. The maximum water depth for tidal energy converter installation using a jack-up barge and piled construction is generally cited as 40 m (Blunden *et al.* 2013). In addition, shipping lanes and restricted areas (*e.g.* submarine pipe and cable routes) were excluded. After applying these limitations only 11 sites remained and the practical resource amounted to 2.633 TWh per year. The *accessible* resource was calculated by applying accessibility limitations to the practical resource. Accessibility limitations are restrictions imposed by regulatory institutions, *e.g.* environmental effects, health and safety. The practical resource was unaffected by these limitations, hence the accessible resource is 2.633 TWh per year. The *viable* resource is obtained by applying commercial restrictions to the accessible resource, such as infrastructure cost. To calculate the viable resource an economic model developed by Marine Current Turbines Ltd was applied. In addition, only sites with peak spring tide velocities > 2 m/s were included as economically viable. The viable resource was calculated at 0.915 TWh/y.

The farm method has become popular in tidal current energy resource assessment but it has its flaws. The methodology is rooted in the 'per-generator' approach and thus results are sensitive to the selected device specifications. A different device and power curve applied to these assessments would lead to different results. Furthermore, the assessments presented have each adopted different values for array density. For example, in a study by Robins *et al.* (2015) the farm method assumes one device per model cell, but the authors state that the annual energy production could be scaled-up from the reported values by a factor of about 15 with a more aggressive array configuration, neglecting any device feedbacks.

2.5.5. Sensitivity to numerical parameters

Lewis *et al.* (2015) additionally investigated some uncertainties in tidal current energy resource assessment that have not currently been addressed, such as the impact of hydrodynamic model spatial resolution and the assumption of rectilinear flow (see Section 2.6). To investigate the effect

of spatial resolution, three model resolutions were developed: Coarse (~1.1 km), Medium (~0.6 km), and Fine (~0.3 km) – each with 10 vertical layers. The authors concluded that horizontal resolution had no impact on the first generation resource, hence ~1.1 km resolution was sufficient, but that ~500 m resolution was required for the second and third generation resource.

2.6. Spatial and temporal variability

Tidal energy development has placed emphasis on tidal current magnitude and not on its spatial and temporal variability, and the resultant net power. For instance, a site with a low peak spring tidal velocity may in fact have a greater net resource if the velocities are more consistent or more symmetrical between the ebb and flood. Robins *et al.* (2015) investigated the impact of the neap-spring ratio, diurnal inequalities, and tidal asymmetries on the tidal current energy resource of the northwest European shelf seas. A 3D hydrodynamic model was developed to calculate annual energy production based on model-predicted depth-averaged velocities and the SeaGen power curve, assuming one device per model cell.

According to Robins *et al.* (2015), a large neap-spring ratio (*i.e.* similar spring and neap tidal currents) will generate a more stable energy yield over the spring-neap cycle and minimise intermittency – a recognised limitation of tidal power exploitation. In locations where there is a relatively large difference between the spring and neap tidal current amplitudes (*i.e.* a small neap-spring ratio), sub-optimal power will be generated during neap tides when, for the majority of the time, currents do not attain the cut-in velocity (Figure 2.7). Robins *et al.* compared two sites with similar peak spring tidal velocities: a site near Alderney in the English Channel and another in the Pentland Firth, Orkney. Significantly less practical power is calculated in the Pentland Firth at neap tide compared to the Alderney site. When extrapolated to a year, the annual energy production is 4.35 GWh at Alderney compared to 3.97 GWh in the Pentland Firth (representing an annual difference of 387 MWh, or 10%). Examining all potential first and second generation development sites over the northwest European shelf seas, the authors show that more practical power can be extracted where the neap-spring ratio is greater (Figure 2.8).

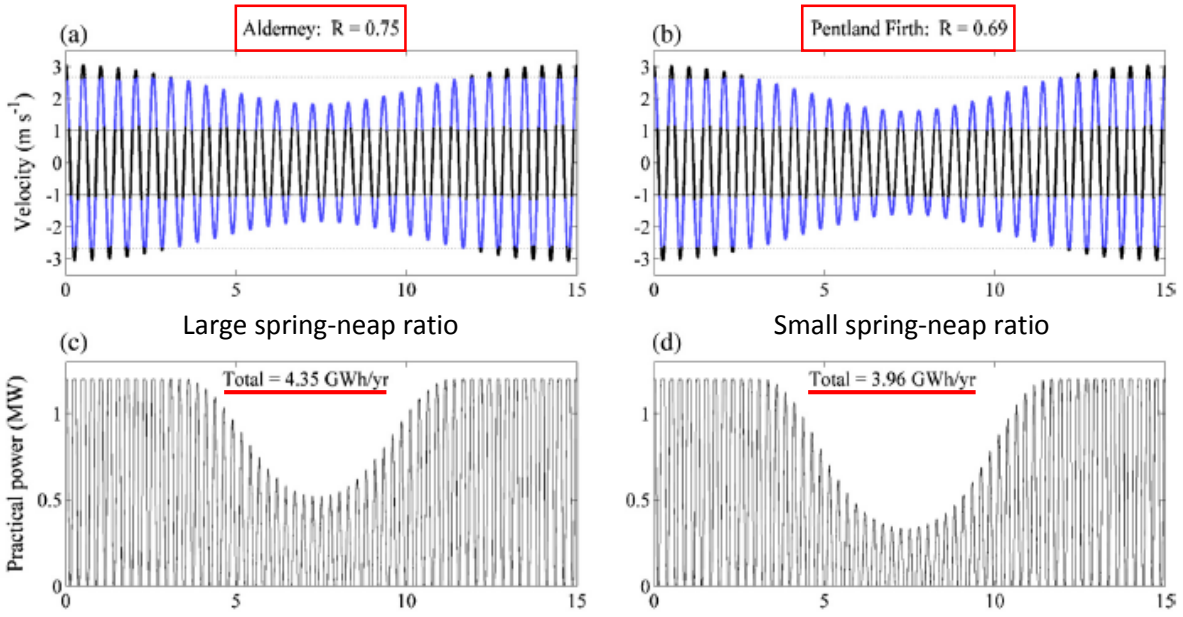

Figure 2.7. Simulated depth-averaged tidal current velocities with spring-neap ratios that are (a) large and (b) small. The blue curves indicate velocities which generate power, based on the measured Seagen-S power curve, and black curves indicate when velocities are either too small (below cut-in speeds) or exceed rated velocities and hence do not contribute to the practical power. Panels (c) and (d) represent the corresponding practical power generated from (a) and (b), respectively, where total power output per year is also shown (Robins *et al.* 2015)

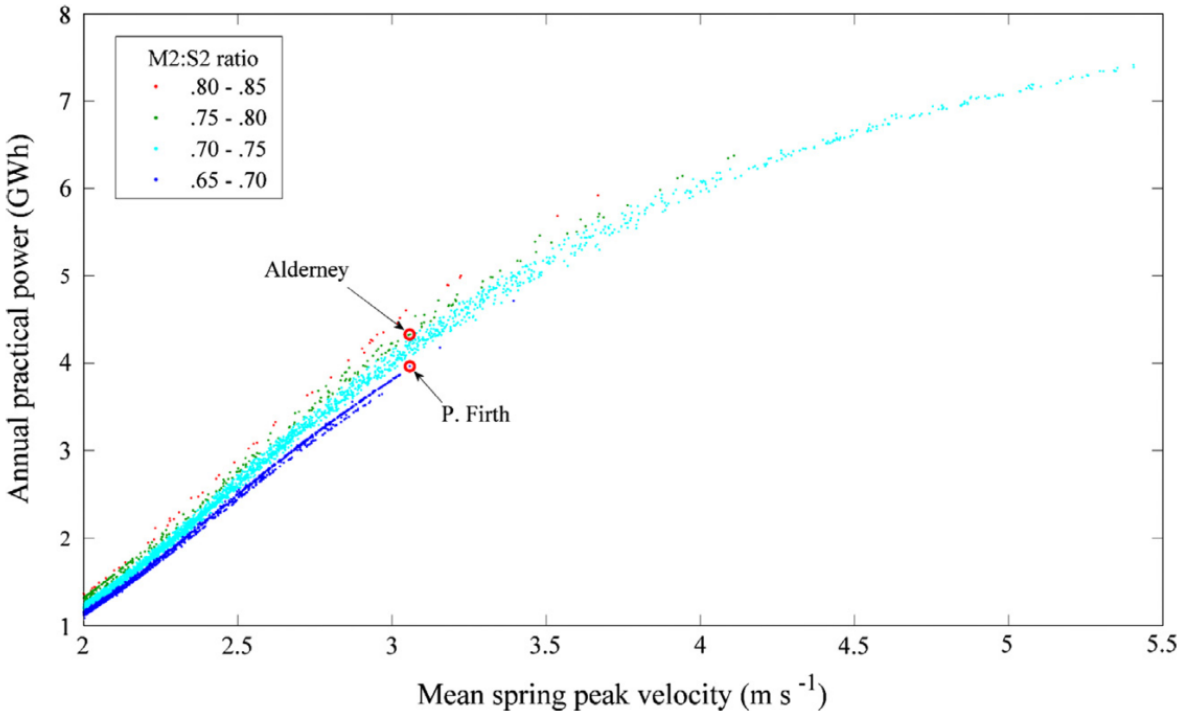

Figure 2.8. Mean spring peak velocity plotted against annual practical power, for all potential TEC sites. Sites are coloured corresponding to their spring-neap ratio, showing that, for any given peak flow, sites with a higher spring-neap ratio produce more practical power (Robins *et al*. 2015)

There also exists a relationship between the daily inequality in tidal currents and annual energy production. If the tide is strongly semi-diurnal, then equal amounts of power will be generated on two consecutive tides. As the daily inequality becomes more pronounced, sub-optimal power will be generated for one of the daily tides, leading to intermittency in peak power production. Robins *et al.* (2015) show that a greater diurnal inequality, defined by the form ratio, leads to the production of significantly less practical power. For sites with peak spring tidal velocities of about 3 m/s the annual practical power varies from 2.5 GWh (high form ratio) to 4.1 GWh (low form ratio), which represents a change of about 40%.

Another factor not routinely considered in tidal energy development is tidal asymmetry, *i.e.* variations between the ebb and flood. Where significant tidal asymmetry exists, optimal power generation may occur once per tidal cycle rather than twice, leading to reduced power output compared to the symmetrical case. Over the course of their field measurements in Ramsey Sound, Fairley *et al.* (2013) and Evans *et al.* (2015) made note of a flood-dominated tidal asymmetry, observing that cost-effective electricity generation ideally requires parity between generation on the ebb and flood. Although previous assessments had suggested that Ramsey Sound is a promising site for tidal development, these two studies conclude that the spatial and temporal variability of the flow field may render much of the sea space unsuitable for TEC deployment. In their case study, Robins *et al.* (2015) found that a shift from tidal symmetry to tidal asymmetry represents a reduction in practical power of 55 MWh per year, even though peak velocities increase.

At many sites considered attractive for tidal energy development there is considerable misalignment between ebb and flood current directions, which may reduce the practical resource. Tidal current energy resource assessments generally assume that tidal flows are completely exploitable, either assuming that tidal currents are rectilinear or that devices have yawing capability. Lewis *et al.* (2015) have conducted the only assessment to date to account for ebb-flood tidal current misalignment. By applying an average misalignment to a large-scale resource assessment the authors concluded that first generation estimates based on the undisturbed kinetic energy may overestimate the resource by $\sim$6% unless devices at such locations can yaw. At second and third generation sites, misalignment was found to have a negligible effect on the undisturbed kinetic energy.

Spatial and temporal variability are, fundamentally, a matter of tidal constituents. Robins *et al.* (2015) calculate that the contribution from M2 and S2 accounts for 75% or more, with an average contribution of 93%, of the annual practical power at first and second generation development sites.

The remaining 25% or less of annual practical power is produced by the remaining tidal constituents. Robins *et al.* (2015) conclude that, for strongly semi-diurnal tidal environments, the first step in resource assessment should consider the M2 and S2 tides. As a second step, more accurate resource assessment should consider lower current amplitude constituents. Finally, to account for the full range of spatial and temporal variability in the tidal current resource, even preliminary assessments should be based on mean annual power density.

2.7. Wave interactions

Although it has been acknowledged that the local wave climate may render some tidal energy sites inefficient, the impact of waves and wave-tide misalignment on the tidal current energy resource has not generally been considered in resource assessments. Previous observations from flume experiments and CFD models have shown an increase in upper water-column velocities when waves propagate against the tidal flow and a decrease when waves propagate with the tidal flow (Lewis *et al.* 2014). Hence, under specific circumstances, the tidal current energy resource could be augmented by wave-tide interactions. Because tidal current energy is a function of velocity cubed, even small changes in the velocity profile can have a significant effect on the resource.

Lewis *et al.* (2014) investigated the effect of realistic wave conditions on the tidal current energy resource for an idealised symmetrical headland. A dynamically coupled wave-tide model was applied to the domain which represented typical tide and wave conditions expected at first generation tidal current energy sites. The mean power density was calculated over a tidal cycle from the model-predicted depth-averaged velocity. The effect of wave interaction with the tidal current resource was calculated as the net change in mean power density over a tidal cycle. The study found a strong linear relationship (R^2 = 0.94) between the wave height and the net power available over a tidal cycle. The theoretical resource is reduced by about 10% for every metre increase in wave height, even for 1 - 2 m waves. Figure 2.9 shows the percentage difference in the net power available over a tidal cycle where depth-averaged tidal velocities exceed 1.5 m/s. Although the relationship requires validation, if proven correct, computationally expensive dynamically coupled wave-tide models may not be required to assess the tidal current resource if the local wave climate is known.

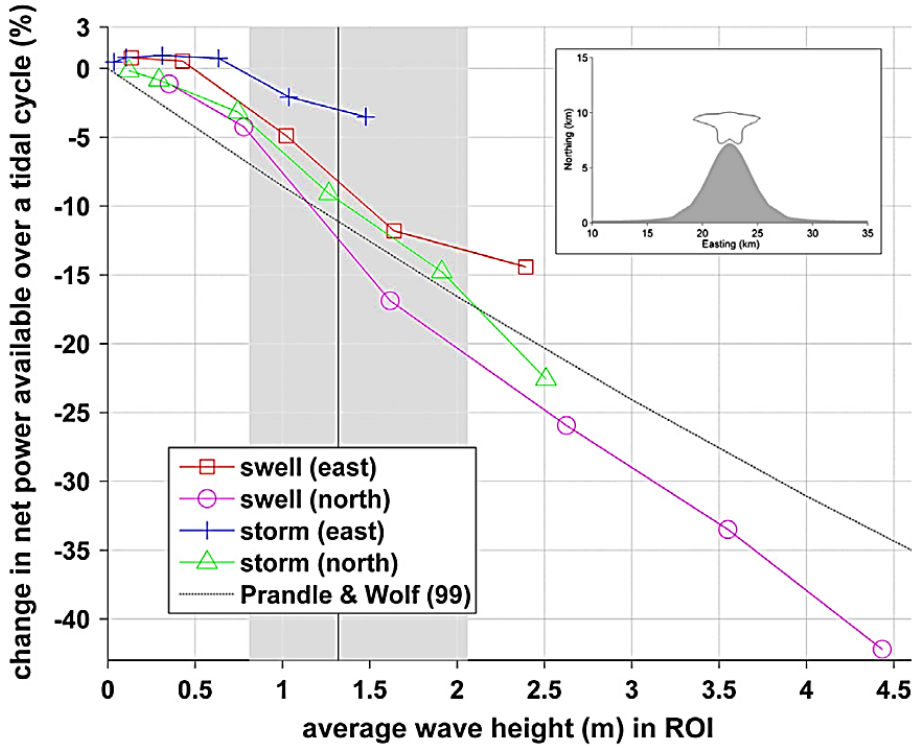

Figure 2.9. The difference in the net power available over a tidal cycle when the simulated tidal velocities are modified by waves for tidal velocities exceeding 1.5 m/s (Lewis *et al.* 2014)

Hashemi *et al.* (2015) developed a dynamically coupled wave-tide model of a proposed tidal energy converter array to investigate the effect of wave-current interactions on the tidal current energy resource as the site. The project by Marine Current Turbines Ltd would see an array consisting of 5 SeaGen S 2 MW turbines installed off the northwest coast of Anglesey, a large island located northwest of Wales. The model was forced with mean and extreme wave scenarios based on the wave statistics of the site. The effect of wave-current interactions on the tidal current resource is assessed by running the model with and without wave-current interactions, and then computing the relative difference in average tidal power. The results show that as a consequence of the combined effects of the wave radiation stresses and enhanced bottom friction, the tidal current energy resource is reduced by up to 20 and 15% for the extreme and mean winter wave scenarios, respectively. However, Hashemi *et al.* assessed a site relatively exposed to waves, and the magnitude of the effect of wave interactions will depend on the local wave climate.

2.8. Array interactions

At present, a number of pilot projects are undergoing sea trials to demonstrate the commercial viability of TEC technology. However, in order to provide meaningful quantities of electrical power to

the grid, it's believed that commercial deployments of tidal turbines will occur in the form of arrays. Array configuration strategies are largely unknown and site-specific, making predictions of tidal current energy resources challenging. Details such as the vertical current profile, turbine wake effects and blockage effects, turbine optimisation within an array, and array-array interactions between neighbouring sites must be accurately incorporated into models for accurate predictions of the tidal current energy resource.

Three methods have been used to simulate array interactions numerically. The first is the augmented drag approach, whereby the tidal energy dissipation associated with the presence of tidal turbines is approximated by increasing the bottom friction (*e.g.* Coles *et al.* 2013). The second is the momentum sink approach, in which the loss of momentum due to tidal energy extraction is incorporated into the momentum equations (*e.g.* Chen *et al.* 2014; Serhadlıoğlu *et al.* 2013). The third is the blade element actuator disk approach, which couples a blade element model with a three-dimensional Navier Stokes model (*e.g.* Bai *et al.* 2013). In the field of physical modelling, the porous disk method has been applied (*e.g.* Myers and Bahaj 2012). With no operational arrays of tidal turbines, these methods lack validation and have not been incorporated into tidal current resource assessment methodologies.

As an example of the type of approach that can be applied at a later design stage, let's consider Adcock *et al.* (2015). The purpose of their work was to calculate an upper bound on the power available from the Pentland Firth using a tidal array to assess the magnitude of the resource. A depth-averaged hydrodynamic model was developed and validated against field measurements. Tidal turbines are represented in the model as a line discontinuity in water level. This method relates the water level downstream of a uniform row of turbines to the water level upstream, and describes a momentum sink representative of the force applied by the turbines to the tidal flow. The available power generated by the device producing this force is estimated using actuator disk theory, which accounts for energy lost due to mixing in the wake of the turbine (but not other hydrodynamic, mechanical and electrical losses). Rows of tidal turbines are introduced numerically, and the turbine properties are adjusted within each row to maximise the power available. Different numbers of rows with different blockage ratios are considered. To determine whether or not an additional row of turbines is feasible in practice, the authors use the metric of time-averaged power per swept area of turbine. Taking the largest viable blockage as 0.4 and the minimum incremental power per swept area as 1 kW/m^2 (equivalent to an offshore wind turbine), it's concluded that three rows of turbines extending across

the entire width of the Pentland Firth can generate a maximum average extractable power of 1.9 GW over a spring-neap cycle.

2.9. Site selection

A resource assessment, according to Blunden and Bahaj (2007), is an iterative process that begins at site selection. Site selection, many publications will say (*e.g.* Blunden and Bahaj 2007), is constrained primarily by the mean cube tidal velocity. As kinetic energy flux varies as the cube of velocity, there are obvious advantages to selecting the most energetic sites. However, this has resulted in a preoccupation in the industry with seeking the highest peak spring tide velocities with the implication that this value is sustainable, and that the value covers the entire region. This is false, and leads to an overestimation of the available resource. There are myriad other important factors to consider, of which the following is not an exhaustive list: water depth, bed slope, spatial and temporal variability (*e.g.* neap-spring ratio, daily inequality, tidal asymmetry), proximity to an existing grid connection, velocity profile, competition (*e.g.* shipping lanes, fishing aquaculture), availability of data, installation and maintenance, environmental impact (*e.g.* permitted flow reduction, sediment transport), regulations (*e.g.* permits and permissions), and wave climate.

Additionally, many of these factors call for device-by-device consideration (Bryden *et al.* 1998). For example, Evans *et al.* (2015) showed that only 2 percent of Ramsey Sound meets the requirements of 2 m/s depth-averaged velocities over a 15 m diameter turbine, a maximum bed slope of 5 degrees and a minimum water depth of 30 m (values based on the DeltaStream turbine).

According to Couch and Bryden (2006) the most important factors are: water depth, distance to the nearest useable grid connection and “an energetic and persistent resource.” Water depth determines the maximum turbine size: as a rule of thumb it’s suggested that turbine diameter should be no more than 50% of the water depth and the hub should be at the midwater point (Bryden *et al.* 1998). For an immature industry, the economics of tidal current energy extraction demand easy access to a nearby grid connection with spare capacity, otherwise the capital cost cannot be viably recovered across the life cycle of the project. The importance of a persistent resource has already been shown by Robins *et al.* (2015).

All things considered, how exactly to go about site selection is up to the individual developer. Several methodologies have been presented here: a decision matrix (Blunden *et al.* 2013), phasing solution techniques (Sustainable Energy Ireland 2004), and parametric optimisation (Ramos and Iglesias 2013).

3. Review of the draft standard

The purpose of this section is to review the tidal current energy resource assessment methodology proposed by IEC-TC-114. A simplified flowchart illustrating the process is shown below (Figure 3.1). With the help of the preceding literature review, Chapter 3 addresses two objectives of the thesis: establishing and confirming a solid scientific basis for the IEC-TC-114 standard and developing suggestions for improving and extending future revisions of the standard.

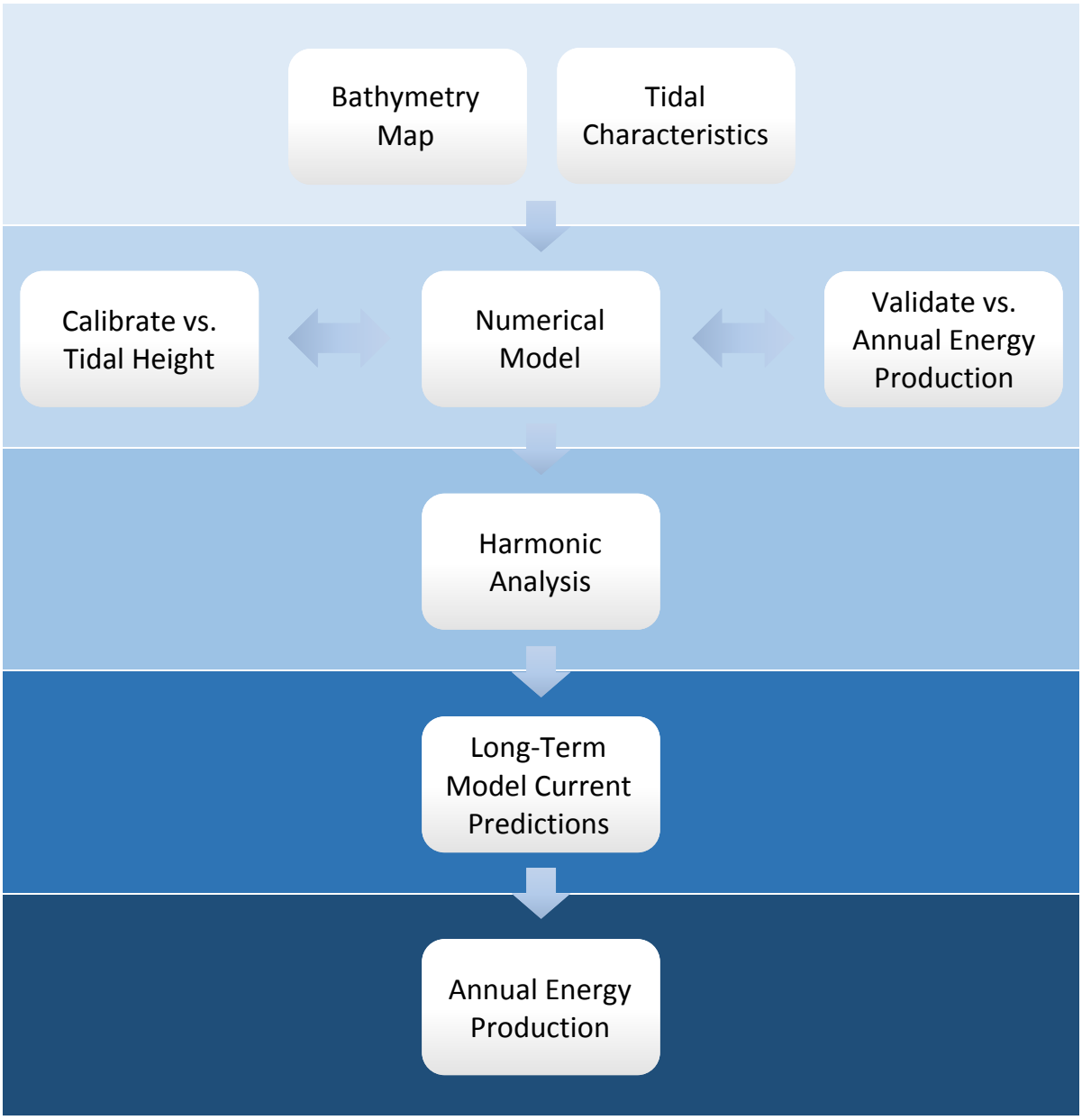

Figure 3.1. Flowchart of the IEC-TC-114 methodology

3.1. Methodology overview

The purpose of the IEC-TC-114 draft standard is to provide a uniform methodology that will ensure consistency and accuracy in tidal current energy resource assessment. In the context of the standard, the tidal energy resource is defined as the velocity probability distribution. For projects over 10 MW the velocity probability distribution is calculated using a hydrodynamic model validated using measured data. For projects below 10 MW, an alternate method which uses measured data at each TEC location may be used to define the resource. The overall objective of the methodology is to calculate the Annual Energy Production (AEP) of a Tidal Energy Converter (TEC) or of an array of TECs.

The standard is intended to be applied at various stages of the project life cycle to provide increasingly accurate estimates of the velocity probability distribution for computing Annual Energy Production. The methodology proposes two distinct types of studies: Feasibility and Layout Design (Table 3.1). These studies differ in terms of scope, scale, accuracy, and data collection/modelling requirements. Whereas the Feasibility stage is focused on investigating the scale and characteristics of the tidal current energy resource in a large area, Layout Design aims to generate detailed and accurate information on the tidal current resource at a specific site to support the layout design of an array. A key distinction is that the Stage 2 study should incorporate energy extraction and consider the technology to be installed and locations of TEC deployments in order to estimate AEP with lower uncertainty. For Stage 1, the "natural state" model output may be used to produce the velocity probability distribution for AEP calculation. For Stage 2, the model should be run with energy extraction in order to accurately specify the velocity probability distribution for AEP calculations.

Table 3.1. Tidal current energy resource assessment staging (IEC-TC-114)

Stage	**Stage 1**	**Stage 2**
Aim	Feasibility	Layout Design
Area	Whole estuary, channel	Development site
Level of Uncertainty	Medium	Low
Minimum number of harmonic constituents for modelling driving boundary	4 - 8	8 - 12
Minimum grid resolution at the area(s) of interest	< 500 m	< 50 m

Harmonic analysis is performed on the model output to generate long-term model current predictions, for periods of a year or more. For Feasibility studies, the depth-averaged currents should be predicted and for Layout Design, currents at specific depths related to TEC deployment should be predicted. A histogram analysis for the tidal current speed and direction is carried out using the results from the tidal analysis. The velocity distribution or exceedance curve is plotted with data from the model (and static measurements for comparison).

The mean Annual Energy Production for each individual TEC within an array is estimated by combining an appropriate *power curve* with the *velocity probability distribution* at the intended deployment site. The mean AEP (kWh) of every TEC is calculated by:

$$TEC\ AEP = N_h \cdot TECA \cdot \sum_{i=1}^{N_B} P_i(U_i) \cdot f_i(U_i) \tag{3.1}$$

where N_h is the number of hours in the simulated year, $TECA$ describes the expected TEC availability, N_B is the total number of velocity bins in the device power curve, $P_i(U_i)$ describes the power in kW generated by the ith velocity bin of the TEC power curve and $f_i(U_i)$ describes the proportion of time for which the mean current velocity occupies a value within the ith bin of the TEC power curve. Depth-averaged velocities output from 2D models should be converted to the velocity at the depth of the TECs for AEP calculations. It is recommended that the assessment be performed for both *hub height* velocity and *area-weighted* velocity. Area-weighted velocity is the predicted velocity at each vertical bin weighted by the fraction of the rotor-swept area in each bin.

3.2. Modelling requirements

For projects using a hydrodynamic model for AEP calculation, tidal height data is required for model calibration and validation, and to define the model boundary conditions. Tidal height may be measured, acquired from existing long-term datasets (*e.g.* Canadian Hydrographic Service), or from appropriate satellite databases (*e.g.* TPXO). The standard prescribes a requisite minimum of direct measurement. For Feasibility studies, a minimum of one static current profiler is to be deployed for a substantial period of time at the intended development site. The pre-requisite of extracting 20 tidal constituents from the data can be achieved with a minimum of a 35 day dataset. For Layout Design, a number of short-term deployments of > 35 days across the region of the intended TEC array are required. It is recommended that data should be collected over a 12 month period and the frequency

of data acquisition should be higher than during Stage 1. Mobile surveys using ship-mounted current profilers are recommended for all proposed TEC sites at Stage 1.

For Stage 1 resource assessments the model may be either 2D or 3D and at Stage 2, the vertical dimension must be resolved in the model. The model domain is determined by the Stage of the resource assessment (Table 3.1), the requirements for far-field environmental impact assessment, and the availability and location of appropriate data for specifying boundary conditions. For far-field environmental impact assessment, model coverage out to deep ocean water depths beyond the continental shelf break is considered to be current best practice. The recommended grid resolution for each Stage is provided in Table 3.1. For Stage 1, minimum grid resolution at the area of interest should be < 500 m, and refined to 200 m in regions of bathymetric complexity. For Stage 2, the model cell resolution should be as fine as reasonably practical with an upper bound limit of 50 m at the area of interest. Bathymetric data should approximately match the intended grid resolution. Model boundary conditions should be constructed from time series simulated from available tidal constituents. Sources of boundary data include tidal stations (*e.g.* Canadian Hydrographic Services), larger-scale tidal circulation models (*e.g.* Webtide), and satellite databases (*e.g.* TOPEX/Poseidon). Because fewer constituents are significant in deep water, the accuracy of satellite-derived data is increased. In addition, any shallow water effects that develop as the tidal wave propagates onto the continental shelf will similarly develop in a numerical simulation.

Meteorological phenomena, such as wind and atmospheric pressure, and the wave climate may affect the tidal current energy resource. The impact of these factors should be assessed by comparing the modelled flow properties with and without their inclusion. If these are found to significantly influence flow dynamics at the project site – for example a 5% change in tidal current velocity across the TEC – the phenomena should be included in the modelling. Similarly, the decision of whether or not to include the modelling of temperature and salinity transport or suspended sediment load is left up to the individual modeller, but should be reported and justified. The impact of turbulence on tidal current energy resource assessment is indicated as an area of ongoing research.

Model calibration is achieved by adjusting bottom friction and turbulence parameters so that model-predicted tidal heights provide the most accurate match to measured data. Modelled and measured tidal height are compared on the basis of harmonic constituents of amplitude and phase for all the major modelled tidal constituents, or compared to the time series directly if harmonic analysis is deemed insufficient. The model should also be calibrated against tidal height data measured at the

site during the mobile or static surveys. Calibration to tidal height ensures that the model accurately simulates flow continuity, however it does not verify whether the model is able to accurately simulate momentum/advection processes important to accurately replicate tidal currents. Therefore, the standard recommends additional statistical comparisons between model-predicted tidal currents and measured field data to determine whether the model is capable of accurately simulating currents at the project site and whether grid refinement is adequate to replicate the observed flow dynamics. Model validation is achieved with quantitative comparisons between the modelled and measured Annual Energy Production. Additional statistical comparisons of modelled and measured tidal height and currents are recommended by the standard.

The resource assessment should include the modelling of energy extraction if the installed capacity of the project exceeds 10 MW or if the proposed energy extraction exceeds 2% of the theoretical tidal current energy resource, based on analytical models such as those presented in Section 2.4 of the literature review. Technical resource assessment (*i.e.* including the modelling of energy extraction) is only required for Stage 2 and then only if the conditions indicated above are met. In order to successfully model energy extraction, the standard suggests that an additional term is needed in the governing equations. In 2D models using the shallow-water equations, this may be achieved with an augmented drag approach. However, in 3D models, this is not appropriate. A common solution can be achieved with the introduction of an additional term in the momentum equations and the inclusion of an additional source of turbulent kinetic energy. The momentum term should describe a friction-like force where the level of energy extraction is related to the local flow velocity and TEC specifications. With the exception of these general guidelines, the standard refers readers to the latest peer-reviewed literature for the modelling of energy extraction noting that the existing methodologies are a “work in progress” and require validation against appropriate field data.

3.3. Discussion

The purpose of this section is to discuss the strengths and weaknesses of the IEC-TC-114 methodology in view of the preceding literature review. The suggested procedure follows a ‘per-generator’ method as described in Section 2.5.3. The tidal current resource is therefore effectively the velocity probability distribution transformed by an appropriate power curve. There are a number of advantages to the ‘per-generator’ method, for example, if the velocity distribution is accurate the calculated Annual Energy Production should reflect the output of an isolated device, including losses. The velocity probability distribution is computed from long-term model current predictions,

for periods of a year or more. Therefore, provided that enough harmonic constituents are modelled, the resource assessment should account for the spatial and temporal variability of the resource in a typical year. In other words, the neap-spring ratio, daily inequality, and tidal asymmetry are all accounted for (Robins *et al.* 2015). The resulting estimate is more accurate than the conventional approach where tidal currents are simulated for a spring-neap cycle and annual energy production is extrapolated (*e.g.* Carballo *et al.* 2009; Lewis *et al.* 2015). The issues afflicting the draft standard are not to do with the methodology itself, but either areas of ongoing research or a lack of specificity in the requirements set out that lead to uncertainty.

At present, the standard is only appropriate for individual or sparsely arrayed TECs extracting a relatively minor fraction of the theoretical extractable resource. And yet, it's believed that commercial deployments of tidal turbines will occur in arrays, where application of the standard may be ill-advised. The reason is that the proposed method for assessing Annual Energy Production in an array is by summation of the individual TEC AEP. However, turbine wake effects and blockage effects, turbine optimisation within an array, and array-array interactions are (critically) not addressed by the standard. It's understandable why: energy extraction and its consequences are areas of ongoing research. The fact remains that the scope of the standard is narrowed as a result. Energy extraction and the back effect to the tidal stream are necessary to model the additional power that comes from the potential energy forcing tidal flows. Thus, in order to assess the tidal current energy resource for more than an isolated turbine, the standard needs to include a comprehensive solution for the modelling of energy extraction. The two pages of the standard allocated to a methodology for incorporating energy extraction simply suggest that an additional term should be included in the governing equations, with little to no practical guidance. In 2D models, solutions could be based on the augmented drag method implemented by Sutherland *et al.* (2007) and Karsten *et al.* (2008), however, this approach is not appropriate in 3D.

If a tangible procedure is not implemented for the modelling of energy extraction, the standard could propose appropriate values for device spacing. At present, each study applying the farm method adopts its own 'conservative' spacing. Blunden *et al.* (2013) assigned 16 - 28 devices per suitable ∼1 km cell, Lewis *et al.* (2015) allocated two devices per ∼300 m cell by assuming minimum lateral spacing of 3 device widths and minimum upstream/downstream spacing of 10 device widths, Sustainable Energy Ireland (2004) assumed minimum lateral spacing of 5 diameters and upstream/downstream spacing of 10 - 20 diameters, Robins *et al.* (2015) considered one device per

~1 km cell but assert that their resource assessment could be scaled up by a factor of 15 neglecting any device feedbacks.

Recent studies have shown that the local wave climate may have a significant impact on the tidal current energy resource at exposed sites (Lewis *et al.* 2014; Hashemi *et al.* 2015). The standard recommends that users compare flow properties with and without the modelling of wave-current interactions and, if these are found to impact flow dynamics at the project site significantly, the phenomenon should be included in the modelling. However, the standard does not specify a threshold to judge the significance of these interactions (*e.g.* 5% change in tidal current velocity). The study by Lewis *et al.* (2014) suggests a strong linear relationship between average wave height and the change in net power available over a tidal cycle. The standard could implement a simplified procedure for the inclusion of wave-current interactions by reducing the Annual Energy Production by a factor derived from Figure 2.9, thereby avoiding computationally expensive dynamically coupled wave-tide models. However, research into the impact of wave-current interaction on the tidal current energy resource is ongoing and the findings of Lewis *et al.* (2014) require validation. Both of the studies referenced above relied on depth-averaged values, but the effect of wave-current interaction processes varies throughout the water column. In addition, the impact was assessed by the change in kinetic energy flux over a tidal cycle. Future studies should look at the phenomenon in 3D and consider the effect on Annual Energy Production.

Language, it has already been said (see Section 1.5.4), is a divisive issue in the tidal power industry. Every source defines the tidal potential in its own terms, adding to unnecessary confusion and uncertainty. For example, the resource is sometimes given as theoretical, extractable, technical, practical or viable, but these terms have no commonly accepted definition. Grabbe *et al.* (2009) defined the theoretical resource as the kinetic energy available in the entire cross-sectional area, and the amount of energy that could be extracted was labelled the extractable resource. Quite frequently, however, concerns for environmental, social or economic factors are included in assessments of the extractable power. Hagerman and Polagye (2006), for instance, assume that environmental concerns limit the extractable resource to 15% of the mean annual kinetic power. According to Grabbe *et al.* (2009), the calculation of the extractable power should include the back effect of energy extraction. On the other hand, the IEC-TC-114 draft standard only incorporates the modelling of energy extraction for what it calls the technical resource. The practical power is defined by some (*e.g.* Lewis *et al.* 2015) as the resource estimated by applying the farm method with a suitable

power curve. In their report, Sustainable Energy Ireland (2004) calculated the theoretical, technical, practical, accessible and viable resources by applying the Betz limit, technical, practical, accessibility and commercial limitations, respectively. The distinction between a technical, practical, accessibility or commercial limitation is subjective and defining the resource in such a way does not seem useful. Terms and definitions should be assigned a specific meaning within the IEC-TC-114 standard so as to promote normalisation in the tidal power industry. In the author's opinion, the theoretical resource should be based on the total kinetic energy, the extractable resource should be the maximum physically extractable power (defined by an analytical model or through augmented drag method), and the practical resource should account for any and all practical, technical, environmental, social, accessibility or commercial limitations that are site-specific.

The question of whether to resort to 3D modelling is important in tidal current resource assessment. Depth-averaged models are, after all, very common in these studies (*e.g.* Ramos and Iglesias 2013). The methodology proposed by IEC-TC-114 only requires that the vertical dimension be resolved in the model at Stage 2, however, depth-averaged velocities output from 2D models need to be converted to the velocity at the depth of the TECs for AEP calculations. Extrapolation from 2D results is not an insignificant assumption. Studies have shown considerable uncertainty with regard to the velocity profile in dynamic tidal regions. For example, Coles *et al.* (2013) showed that the characteristics of the velocity profile change throughout the tidal cycle. An empirical law could be adopted, but depending on the location and timing different laws may apply. Although $1/7^{th}$ power laws are commonly applied, Coles *et al.* (2013) and O'Rourke *et al.* (2014) determined that $1/10^{th}$ and $1/4^{th}$ power laws provided a better fit in their studies, respectively. Based on these findings, simply using depth-averaged velocity may be better than introducing additional error into the AEP calculation. The standard recommends using velocity profile data from a static survey to assist in defining a characteristic depth profile, but that assumption requires validation. There is pressing need for a comparison of Annual Energy Production calculated from direct measurements, 2D and 3D model output with various empirical laws assumed in 2D to establish a best current practice. In addition, the draft standard recommends calculating AEP with both hub height and area-weighted velocity. However, many examples in the literature support the use of depth-averaged velocity across the rotor-swept area (Bryden *et al.* 2007). Evans *et al.* (2015) compared different methods of depth-averaging tidal velocity and found relative errors of 23.4 and 12.9% in the kinetic energy flux as a result of averaging over the entire water column. Based on these findings, Evans *et al.* argued that 3D modelling is preferable over 2D in resource assessment. It should be fair to say that for Layout Design

assessments the recommendation of 3D modelling is appropriate, whereas for Feasibility studies 2D modelling is adequate with or without extrapolation to a specific depth given the uncertainty of that assumption and the required level of accuracy at Stage 1.

The recommended minimum of 4 - 8 harmonic constituents for modelling the driving boundary at Stage 1 and 8 - 12 at Stage 2 may be too stringent according to the literature. Robins *et al.* (2015) found that the contribution from M2 and S2 accounts for 75% or more of the annual practical power predicted by the 5 primary tidal constituents, with an average contribution of 93%. Sutherland *et al.* (2007) found that by including the 8 major constituents for the Johnstone Strait, the power estimates from the M2 tide are multiplied by 1.12. Similarly, Blanchfield *et al.* (2008b) showed that by including the 3 dominant constituents in Haida Gwaii the extractable power increased by 9%. As recommended by Robins *et al.* (2015), it would be reasonable for Feasibility studies to model only M2 and S2, adding more constituents at later stages. Note that 93% is the average contribution and thus including M2 and S2 should model 93% of Annual Energy Production. On the other hand, their contribution may be as low as 75% at any given time. Hence, if the objective of the modelling exercise is not strictly to calculate AEP more constituents may be required. A major advantage of tidal power over other renewables is its predictable nature. Those predictions are only as accurate as the tidal constituents driving the model. Layout Design studies should consider the importance of resource assessment at different scales than Annual Energy Production. Accurate predictions on a daily, weekly or monthly basis far into the future necessitates modelling of long-term constituents of lesser amplitude.

Minimum grid resolution at the area of interest is provided at each Stage (Table 3.1), but these values are not justified by the standard. Model grid resolution differs greatly from study to study in the literature, and there is considerable uncertainty with regard to the sensitivity of tidal current energy resource assessment to numerical parameters. Lewis *et al.* (2015) looked at the importance of spatial resolution in the only sensitivity analysis of tidal resource assessment to date. According to the draft standard, minimum grid resolution at the area of interest should be < 500 m for Feasibility studies, refined to 200 m in regions of bathymetric complexity. For Layout Design, minimum grid resolution should be as fine as reasonably practical with an upper bound of 50 m at the area of interest. Conversely, Lewis *et al.* concluded that coarse spatial resolution > 1 km is sufficient for first generation resource assessment and that ∼500 m resolution is required for assessment of the second or third generation resource. However, these results should be interpreted cautiously. Three model grids were developed: Coarse (∼1.1 km), Medium (∼0.6 km), and Fine (∼0.3 km). The resource was

evaluated in three phases for first, second and third generation technology: (1) the maximum potential sea space for development, (2) the mean kinetic energy flux at all applicable grid cells, and (3) the practical power at all applicable grid cells assuming two devices per fine resolution model cell. The farm method is inappropriate for a sensitivity analysis because only slight differences would be expected from better discretisation. A coarse cell represents an average of the finer cells, therefore the available sea space and mean kinetic energy flux should not change. Similarly, two devices per fine resolution model cell are always assumed, hence the practical power would remain approximately the same. The trends reported in available area, mean kinetic energy and annual practical power do not seem significant. Moreover, the trends at times contradict each other: for the third generation resource the available sea space and mean kinetic energy decrease slightly while the annual practical power increases slightly. Lastly, the SeaGen power curve was applied to calculate practical power and thus the trends are dependent on that device. The importance of spatial resolution has been underestimated before. O'Rourke *et al.* (2010) reported that the tidal current energy resource assessment for Strangford Lough and SeaGen were underestimated, with inadequate spatial resolution in the 2D hydrodynamic model most likely at fault.

On a similar note, the standard does not provide any guidance regarding bathymetric data quality and resolution beyond that it should relate to the desired model grid set-up. In contrast, the IEC-TC-114 standard on wave energy resource assessment and characterisation provides specific values at each Stage for maximum horizontal spacing of bathymetric data as a function of water depth. This lack of specificity with regard to numerical parameters is a recurring theme in the draft standard. The reason for this may be a lack of evidence to support more specific guidance: in that case, the standard could provide a review of typical values in published resource assessments.

According to the standard, model calibration is accomplished by adjusting bottom friction and turbulence parameters so that model results provide the most accurate match to tidal height measurements with respect to tidal constituents of amplitude and phase. Validation of model simulations is achieved with quantitative comparisons between the Annual Energy Production computed from the static surveys of the measured current and from model simulations. However, the standard needs to set out specific calibration and validation targets. It's important for users of the standard to have an objective in these procedures, and values differ greatly from study to study. Table 3.2 summarises the validation of recent tidal current energy resource assessments included in the literature review. Most commonly, studies report the root-mean-square error (RMSE) achieved

for the M2 tide in amplitude and phase. At times, S2 or another dominant constituent are reported as well. The studies shown typically have an RMSE within 10 cm and 10° in M2 amplitude and phase, respectively. Other reported metrics include the mean absolute error (MAE) and relative error. Note that these studies look at different domains and approach validation differently. The model may be validated against tidal stations, current profiler surveys, or published data from another source. Similarly, the number of sites included in the validation exercise ranges from 37 (Karsten *et al.* 2008), to 20 (Robins *et al.* 2015), to 7 (Lewis *et al.* 2015). Validation with respect to tidal currents is infrequently reported. Hashemi *et al.* (2015) reported a mean absolute error of < 0.20 m/s in depth-averaged tidal currents. Robins *et al.* (2015) reported an RMSE of 0.046 and 0.016 m/s in amplitude and 12° in phase for M2 and S2, respectively. All of this highlights the necessity for standardisation in calibration and validation targets and in the reporting of accuracy. For example, an RMSE of < 10 cm in amplitude and < 10° in phase for M2 at a minimum number of sites could be specified, along with similar targets for other dominant harmonics such as S2. Alternatively, the standard could implement a validation procedure similar to Gunn and Stock-Williams (2013) which makes use of the 95% confidence intervals for tidal constituents provided by T_TIDE. As previously stated, if there is a lack of sufficient evidence to recommend specific targets, the standard could provide a review of typical values in published resource assessments (Table 3.2).

Table 3.2. Validation from recent tidal current energy resource assessments

Study	Validation			
	Tide	**Error**	**Amp. (cm)**	**Phase (°)**
Karsten *et al.* (2008)	M2	RMSE	8	3
Adcock *et al.* (2015)	M2	RMSE	2	2
Lewis *et al.* (2015)	M2	RMSE	11	4
	S2	RMSE	8	1
Robins *et al.* (2015)	M2	RMSE	15	12
	S2	RMSE	5	10
Neill *et al.* (2014) Regional model	M2	RMSE	8.3	6.8
	S2	RMSE	3.7	7.5
Neill *et al.* (2014) High resolution model	M2	RMSE	2.7	5.0
	S2	RMSE	1.7	5.5
Hashemi *et al.* (2015)	M2	MAE	5	2
	S2	MAE	8	1

Misalignment between ebb and flood current directions is not presently addressed in the draft standard, *i.e.* the methodology assumes that tidal currents are rectilinear or that TECs can yaw. In a resource assessment of the Irish Sea, Lewis *et al.* (2015) concluded that estimates based on the undisturbed kinetic energy flux may overestimate the resource by ∼6% unless devices can yaw. Although a histogram analysis for the tidal current direction is carried out using the results from the long-term current predictions following IEC-TC-114 protocol, the purpose of the analysis is to determine the optimum TEC orientation. Future revisions of the standard will need to incorporate tidal current direction into Annual Energy Production calculations. This may not be necessary for Feasibility assessments, but the accuracy required for Layout Design demands consideration of ebb-flood tidal current direction misalignment.

Although a footnote references a number of analytical models, these should feature more prominently in the standard as a means of preliminary tidal current energy resource assessment. Many such models have been successfully validated (Sutherland *et al.* 2007; Karsten *et al.* 2008; Fairley *et al.* 2013) and make use of data available early in the resource assessment process, *e.g.* vessel-mounted current profiler measurements (Vennell 2011). Analytical models are ideal for quick and easy upper bound estimates of the tidal current resource to help decide whether more sophisticated methodologies are worth applying. Calculating the theoretical maximum extractable power will additionally help anticipate the environmental impact of a project: the formula by Vennell (2011), for example, provides the reduction in flow and tidal range.

The standard assumes that an area of interest has already been identified, which may not be the case. For example, to date, only desktop assessments have been conducted in Norway (Grabbe *et al.* 2009). The standard could include a large-scale preliminary assessment Stage for the purpose of reconnaissance for less experienced users. The procedure could be simple and rapid, using the kinetic energy flux to identify promising sites and help focus the later stages of assessment.

The standard imposes an observation/simulation period of at least 35 days for the purpose of extracting the requisite 20 harmonic constituents. The literature seems to support this requirement. Robins *et al.* (2015) indicate that robust estimates of the long-term power generation potential of a site require an observation/simulation period of at least 30 days. European Marine Energy Centre guidelines indicate that for later stages of site characterisation at least 20 harmonic constituents should be resolved, which should be possible with one month of data (Legrand 2009). Based on these

numbers 35 days seems reasonable, given the spin-up needed for numerical models and the potential for bad data in field measurements.

As a closing comment, the standard is quite dense with notes and frequently references supplementary materials. This research has highlighted the need for a user-friendly, all-in-one, plain language guide to facilitate application of the IEC-TC-114 methodology if the standard is to attain wider acceptance. The guide should include example graphs and tables, clear and concise requirements for inputs and outputs, and guidance on the more practical aspects of model development, for example, commonly used models in the industry. The draft standard is generally well conceived and draws on the scientific literature. The presented flaws and limits have more to do with areas of ongoing research than any oversight on the part of IEC-TC-114.

3.4. Summary

Chapter 3 has contributed to two goals of the thesis: establishing and confirming a solid scientific basis for the IEC-TC-114 standard and developing suggestions for improving and extending future revisions of the standard. The main recommendations are summarised as follows:

- At present, the standard is only appropriate for individual or sparsely arrayed TECs extracting a relatively minor fraction of the theoretical extractable resource. A comprehensive procedure for the modelling of energy extraction is required to overcome these limitations. In two-dimensional models, Sutherland *et al.* (2007) and Karsten *et al.* (2008) among others may offer guidance.
- Turbine wake effects and blockage effects, and array-array interactions require additional consideration.
- New studies on the impact of wave-current interactions on tidal current energy resource assessment necessitate updating the relevant clause (Lewis *et al.* 2014; Hashemi *et al.* 2015). The linear relationship between kinetic energy flux and average wave height proposed by Lewis *et al.* (2014) may provide a simplified method of incorporating wave-current interactions in resource assessment.
- For meteorological phenomena (*i.e.* wind and storm surge) and wave-current interactions, a threshold should be established indicating when the effect is to be included in the modelling (*e.g.* 5% change in tidal current velocity across the TEC).

- Future revisions of the standard should include a subsection on terms and definitions. The *theoretical*, *extractable*, and *practical* resource should be among the standardised terms.
- Modelling the M2 and S2 harmonic constituents is appropriate for a Feasibility assessment. For Layout Design, or if the numerical model is intended for resource assessment at time scales finer than Annual Energy Production, more harmonic constituents are required.
- Specific requirements with regard to grid resolution and the quality and resolution of bathymetric data would attenuate uncertainty.
- Where the standard is unable to offer specific guidance, for example required accuracy in calibration or validation, a review of typical values in published resource assessments could be provided.
- Misalignment between ebb and flood current directions is not presently addressed in the draft standard, *i.e.* the methodology assumes that tidal currents are rectilinear or that TECs have yawing capability.
- Areas of ongoing research include but are not limited to: suspended sediment load, meteorological phenomena, horizontal density gradients, and turbulence. Their impact on TEC performance and AEP is unknown. Future revisions of the standard will have to continuously update the relevant clauses.
- Although a footnote references a number of analytical models, these should feature more prominently in the standard as a means of preliminary tidal current energy resource assessment. Many such models have been successfully validated (Sutherland *et al.* 2007; Karsten *et al.* 2008; Fairley *et al.* 2013).
- Specific calibration and validation targets need to be set out with regard to tidal height constituents of amplitude and phase and Annual Energy Production, respectively.
- Iteration towards a more user-friendly revision would help promote broader acceptance of the draft standard: example graphs and tables; clear and concise requirements for inputs and outputs, *et cetera*.
- The clause on model selection, features and parameterisation should include tangible recommendations based on accepted solutions in the tidal power industry. For example, TELEMAC and ROMS (Regional Ocean Modeling System) are two frequently applied models.

4. Field study

Chapter 4 begins the procedure of conducting a comprehensive assessment of the tidal current energy resource at the FORCE project site that is consistent with IEC-TC-114 protocols. Available field measurements are analysed so as to characterise the tidal properties at the site and to extract the tidal constituents. In Chapter 5, the modelled constituents are computed and in Chapter 6, the observed and modelled resource are calculated from long-term current predictions produced with the constituents.

4.1. The Bay of Fundy

The Bay of Fundy is renowned for having the world's highest tidal range. More water flows in and out of the bay in a 12.42 hour tidal cycle than the combined flow of all the rivers in the world. That's 115 billion tonnes of seawater flowing in and out of the bay twice daily. Unsurprisingly, the Guinness Book of World Records (1975) declared that Burntcoat Head, Nova Scotia has the highest tides in the world:

> "The Natural World, Greatest Tides: The greatest tides in the world occur in the Bay of Fundy… Burntcoat head in the Minas Basin, Nova Scotia, has the greatest mean spring range with 14.5 metres (47.5 feet) and an extreme range of 16.3 metres (53.5 feet)."

The Bay of Fundy is on the Atlantic coast of North America, on the north-east side of the Gulf of Maine flanked by the provinces of New Brunswick and Nova Scotia (Figure 4.1). The upper Bay of Fundy divides into Chignecto Bay in the north-east and Minas Basin in the east (Figure 4.2). Chignecto Bay divides into Cumberland Basin and Shepody Bay and the eastern part of Minas Basin is called Cobequid Bay. The shape of the bay – a long and narrow funnel – contributes to the extreme tidal range. Incidentally, it's the combination of high tidal range and narrow funneling geometry that gives the Shubenacadie River on Cobequid Bay a tidal bore (Chanson 2011).

4.1.1. Hydrodynamic modelling

Studies have frequently tried to understand the properties of the Bay of Fundy responsible for its record-setting tidal range. The accepted theory attributes these high tides to the effects of resonance. Garrett (1972) established that the Bay of Fundy and Gulf of Maine form an integral system by demonstrating that the frequency response is similar at several ports in the Bay of Fundy (BoF) and Gulf of Maine (GoM), and significantly different from that in the Atlantic. Garrett estimated the

natural period of the system to be 13.3 ± 0.4 hours by applying Platzman's numerical scheme. Consequently, the North Atlantic M2 tide with a period of 12.42 h incites a near resonant response from the BoF-GoM system and yields record-setting tides. In a further calculation with a numerical model Garret (1974) found the natural period of the system to be between 12.38 and 12.98 hours, lending further credence to the theory.

A numerical model investigation by Greenberg (1979) similarly indicates that the natural period of the BoF-GoM system is about 12.5 h. The importance of these findings is underscored by Greenberg: if alterations move the system closer to resonance with M2 – for example tidal power development – the tidal amplitude should increase, and vice versa. Greenberg confirms that assumption by simulating barriers in the upper Bay of Fundy. A reduction in tidal amplitude is seen at the barrier, and an increase in the rest of the Bay of Fundy and throughout the Gulf of Maine.

Sankaranarayanan and McCay (2003) developed a 3D hydrodynamic model of the Bay of Fundy. In contrast to the previous hydrodynamic modelling studies in the Bay of Fundy (*e.g.* Greenberg 1979), the authors included the Saint John River and Harbour region in their model grid and fresh water flows into the Bay. Five tidal constituents (M2, N2, S2, O1, K1) were modelled and mesh resolution ranged from 50 - 100 m in the Saint John Harbour to 2 - 3 km in the Bay of Fundy. The model ably reproduces a counterclockwise gyre seen in the mouth of the Bay of Fundy (Aretxabaleta *et al*. 2008) (Figure 4.3), which Greenberg (1979) was unable to replicate. The model achieved errors of < 0.2 m in amplitude and 7° in phase for M2 except in the upper Bay where errors increased to 0.3 - 0.5 m relative to an amplitude of 4.5 - 6 m. The errors in N2 (the next largest constituent) were 0.1 - 0.3 m in Minas Basin relative to an amplitude of 0.7 - 1 m with phase errors as large as 20° (~40 minute error in timing).

Dupont *et al.* (2005) developed a 2D hydrodynamic model of the upper Bay of Fundy with high resolution depiction of the extensive tidal flats in Minas Basin. The model included nine tidal constituents (M2, N2, S2, O1, K1, K2, L2, 2N2, v2) derived from TOPEX/Poseidon data and mesh resolution ranged from 5 km to 30 m. The model achieved a root-mean-square error (RMSE) of < 0.3 m in amplitude for M2 relative to a tidal amplitude of 3 m at Saint John and 5 - 6 m in Minas Basin. The errors in N2 (the next largest constituent) were < 0.05 m except at six stations where they exceeded 0.1 m, and the phases were 10 - 15° late. The total water level in Minas Basin is reproduced with an RMSE of 0.3 - 0.5 m. Overall, the model is capable of a water level accuracy of approximately 10% in Minas Basin.

Figure 4.1. The Bay of Fundy, shown on the east coast of North America

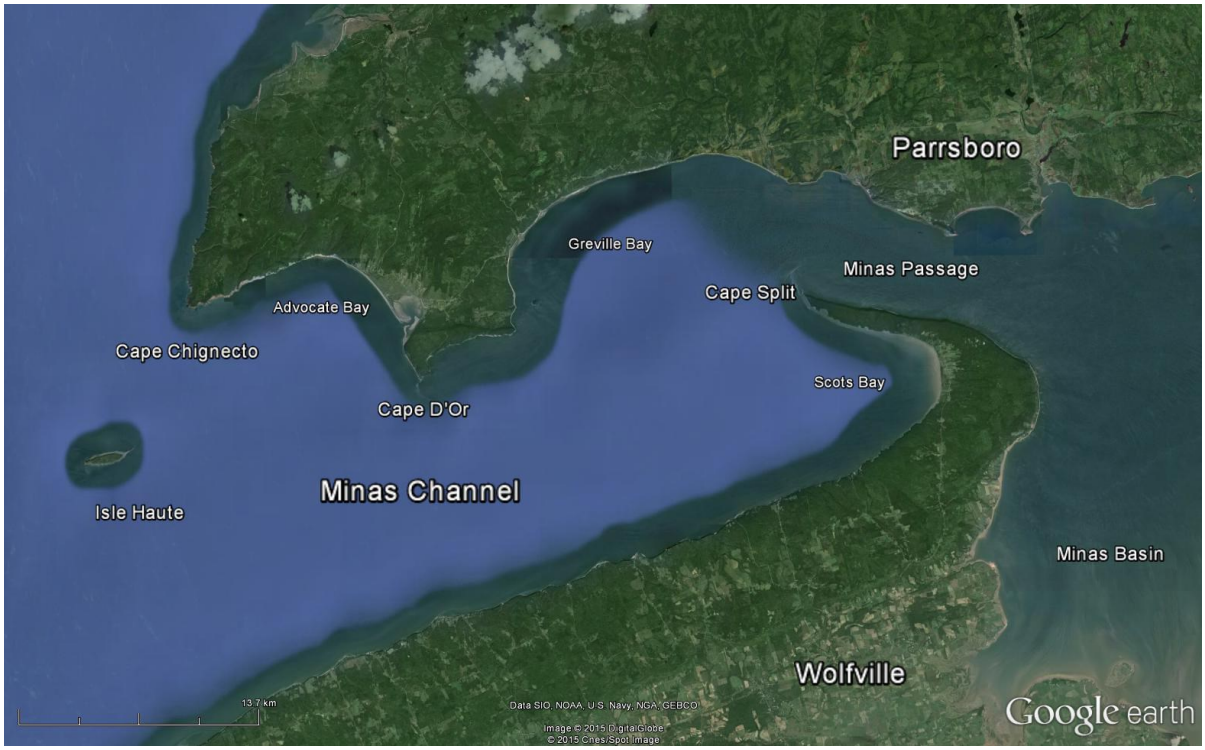

Figure 4.2. The Minas Channel

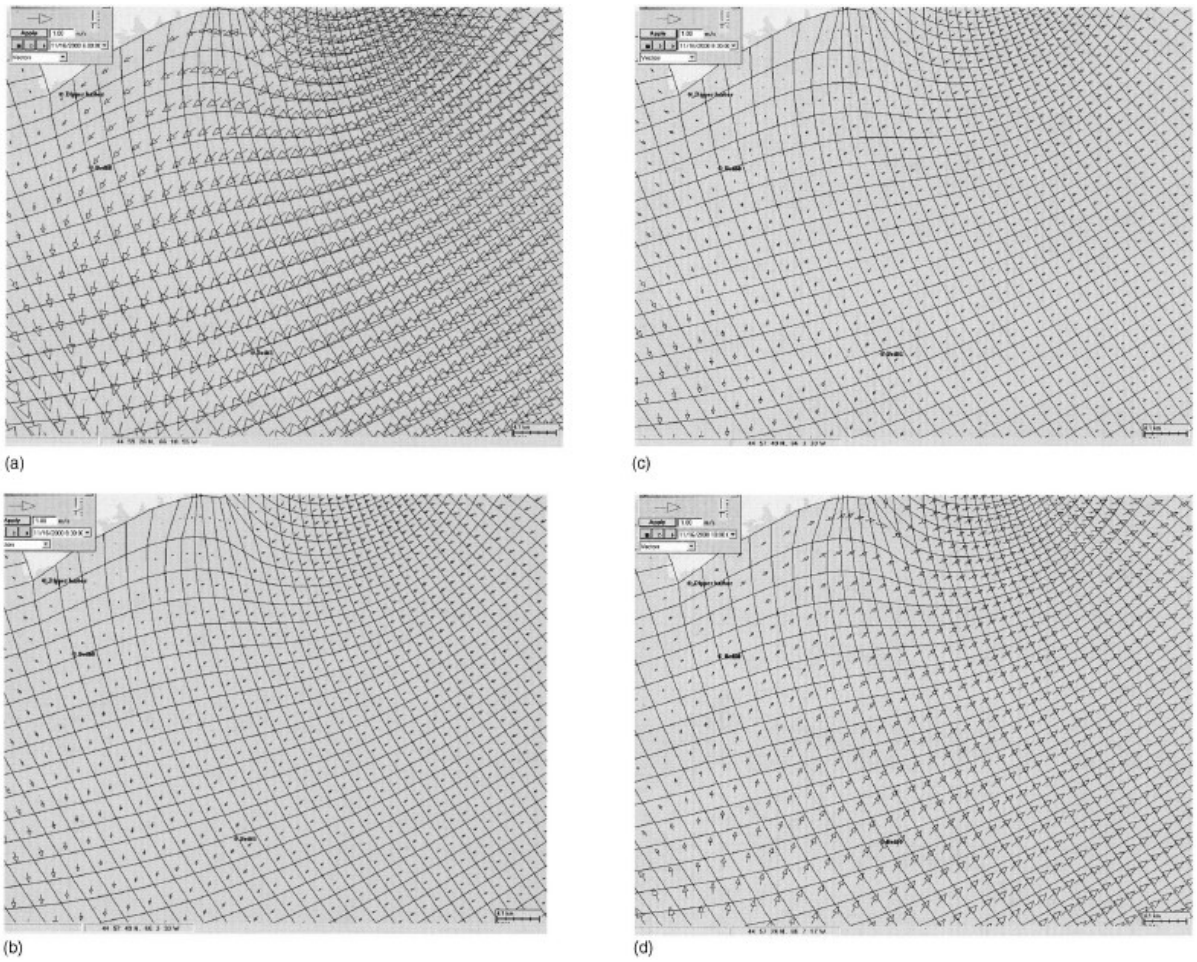

Figure 4.3. Model-predicted currents: (a) peak ebb; (b) 2 h after the peak ebb; (c) 3 h after the peak ebb; (d) 4 h after the peak ebb (Sankaranarayanan and McCay 2003)

4.1.2. The Minas Passage

Minas Basin connects with the main body of the bay through Minas Channel (Figure 4.2). To the east, Minas Channel narrows to a 5 km wide waterway known as Minas Passage, which is bounded to the south by the headland of Cape Split. Immediately south of Cape Split is Scots Bay. The Minas Passage deepens to ~170 m below mean sea level and is known for strong tidal currents exceeding 5 m/s. Figure 4.5 and Figure 4.6 show the topographical features and bathymetry of Minas Passage, respectively. Shaw *et al*. (2012) investigated the tidal scour system in Minas Passage and describe the formation of eddies. On the flood tide, a large clockwise gyre forms east of Cape Split and a lesser counterclockwise gyre develops east of Cape d'Or. On the ebb tide, a large counterclockwise gyre forms in Scots Bay and a lesser clockwise gyre forms in Advocate Bay.

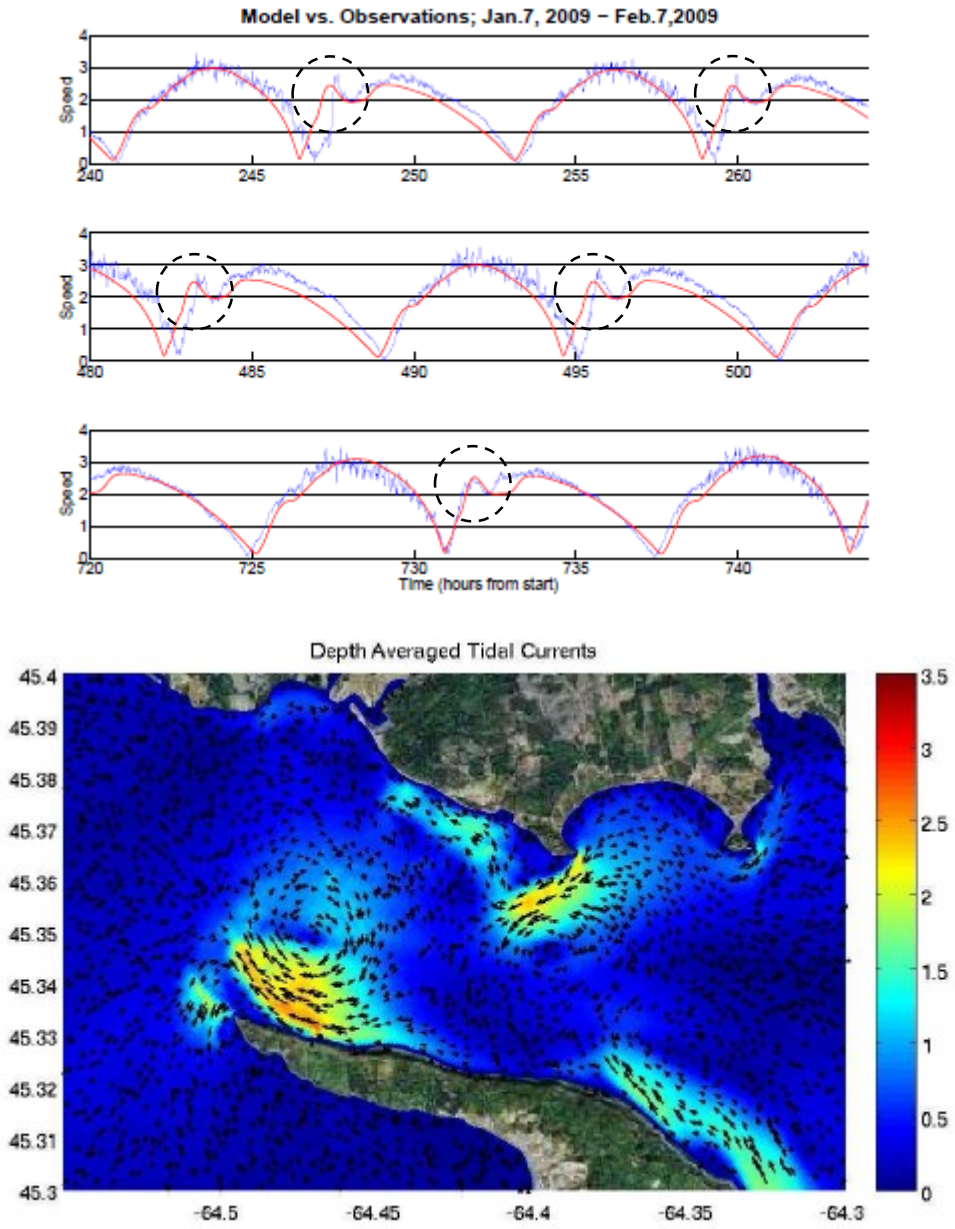

Figure 4.4. (Top) A comparison of simulated [red] and observed [blue] tidal currents. (Bottom) A snapshot of the flow through Minas Passage at the beginning of ebb tide. Note the eddy leaving West Bay that results in a pulse of high speed flow that is propagated through the FORCE test site (Karsten *et al.* 2011)

Karsten *et al*. (2011) described an asymmetry between the ebb and flood in Minas Passage. With the onset of flood tide, the flow around Cape Split results in a very strong jet in the northern half of the passage with speeds exceeding 5 m/s in proximity to the surface. On the ebb tide the flow is weaker and almost uniform across the passage. Karsten *et al*. additionally observed a pulse in flow with the onset of ebb (Figure 4.4). The hypothesis is that an eddy formed in West Bay is transported into the passage with the ebb tide and results in a pulse of high speed flow.

Figure 4.5. The Minas Passage and Crown Lease Area

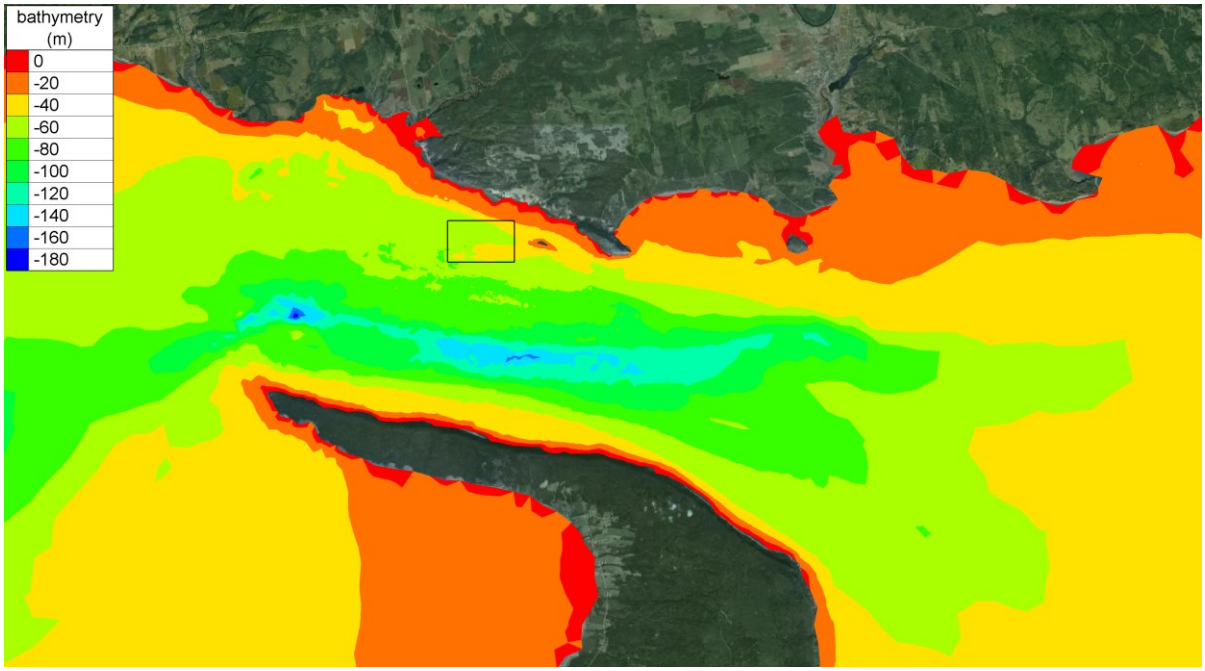

Figure 4.6. Minas Passage bathymetry

4.2. Stationary tidal current surveys

The Fundy Tidal Energy Demonstration Project consists of four submarine berths for tidal energy converters located in a Crown Lease Area, 1.6 km by 1.0 km, in Minas Passage near Black Rock Island (Figure 4.7). The region of the CLA is a rough surface of exposed bedrock ridges and some fields of ripples in gravel (Shaw *et al*. 2012). The FORCE berths are located on a shallow flat-topped ridge extending west from Black Rock Island (Figure 4.8). The four berths (A, B, C, and D) are the subject of this tidal current energy resource assessment. Data from ADCP surveys conducted between August and December 2011 was made available to the project (Table 4.1). Data from an additional ADCP survey became available at a later date, hereafter called Site F.

Table 4.1. Location of five ADCPs in the Minas Passage and their installation period

Site	Latitude (deg N)	Longitude (deg W)	Installation period
A	45.365	64.430	15th Aug. 2011 – 8th Sept. 2011 (24 days)
B	45.365	64.437	17th Sept. 2011 – 2nd Nov. 2011 (46 days)
C	45.366	64.424	2nd Nov. 2011 – 10th Dec. 2011 (38 days)
D	45.364	64.422	19th Sept. 2011 – 2nd Nov. 2011 (44 days)
F	45.357	64.404	17th Aug. 2007 – 14th Sept. 2007 (28 days)

Figure 4.7. ADCP survey locations

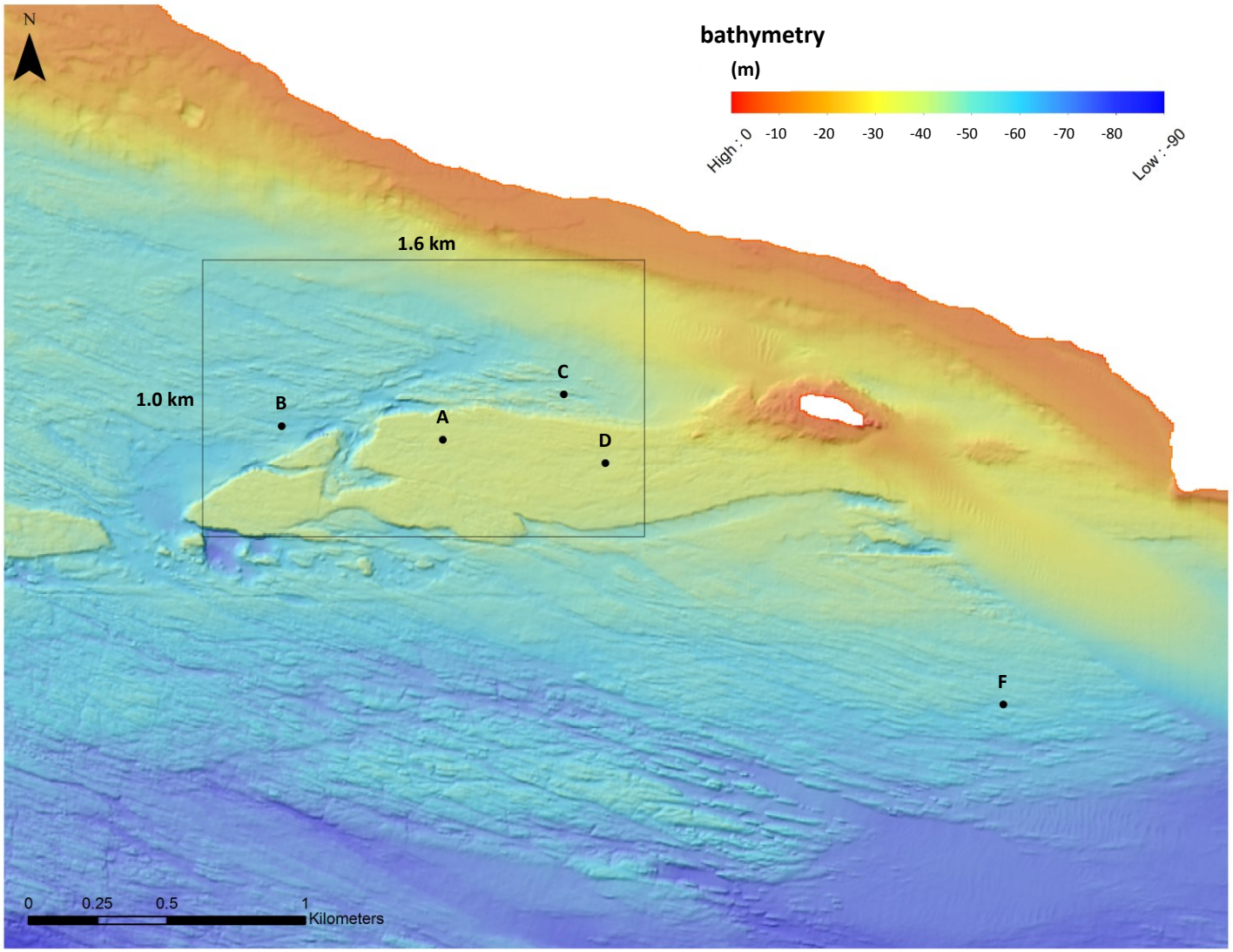

Figure 4.8. High-resolution (5 m) bathymetry of the CLA and surroundings

The data made available to the project consists of pressure and velocity time series. Pressure is given in metres at each recording interval. The directional components of velocity (u, v, w) are given in metres per second at each recording interval in vertical bins or cells. Spatial and temporal resolution are specific to the survey (Table 4.2). Note that Sites A and C had 20 and 25 minute gaps every hour, respectively. Current speed and direction are computed at each recording interval and vertical bin using the east-west, u, and north-south, v, velocity components.

Table 4.2. ADCP survey characteristics

Site	Mid-tide depth (m)	Sampling interval (min)	Bin size (m)
A	37.0	5*	1.0
B	57.0	15	2.5
C	48.7	5*	2.0
D	36.0	2	1.0
F	57.5	15	2.0

* Irregular sampling interval

Values are recorded at every vertical bin but not all of them are valid. At any given moment in time, one or more may be above the free surface. The analysis begins with the removal of any values recorded above the surface. The extent of a vertical bin must remain below the free surface for a recording to be kept as valid (Figure 4.9).

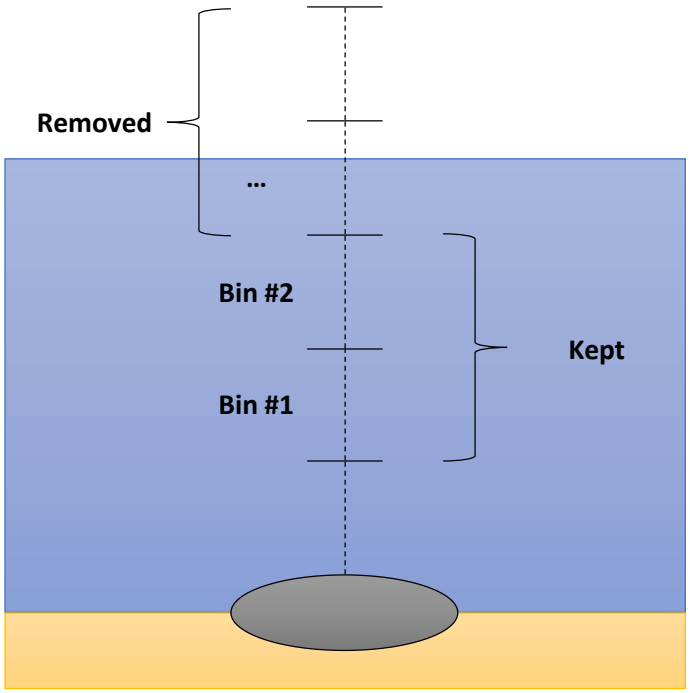

Figure 4.9. Vertical bin processing scheme

The hydrodynamic model developed for this work is two-dimensional and thus only depth-averaged velocity can be obtained. In order to compare modelled and measured velocities, the latter are depth-averaged as follows:

$$\bar{V} = \left(\sum_{i=0}^{n} V_i \cdot H_i \right) \times \frac{1}{h} \tag{4.1}$$

where V_i is bin velocity, H_i is bin height and h is water depth. The velocity at the water surface is taken as 80% that of the nearest (submerged) vertical bin. Similarly, velocity at the bed is assumed to be zero (*i.e.* no-slip condition). The preliminary results of the analysis are the depth-averaged time series of u, v, w, horizontal speed and direction, and the tidal height time series obtained from pressure readings. In addition, plots of the average ebb and flood current profiles are created by following the procedure described below:

I. Horizontal speed time series are organised into ebb and flood records (Figure 4.10)
II. Sampling intervals with depth-averaged speed <0.5 m/s are discarded (Figure 4.11)
III. Bins are time-averaged within the ebb and flood records
IV. An average ebb and flood current profile are calculated

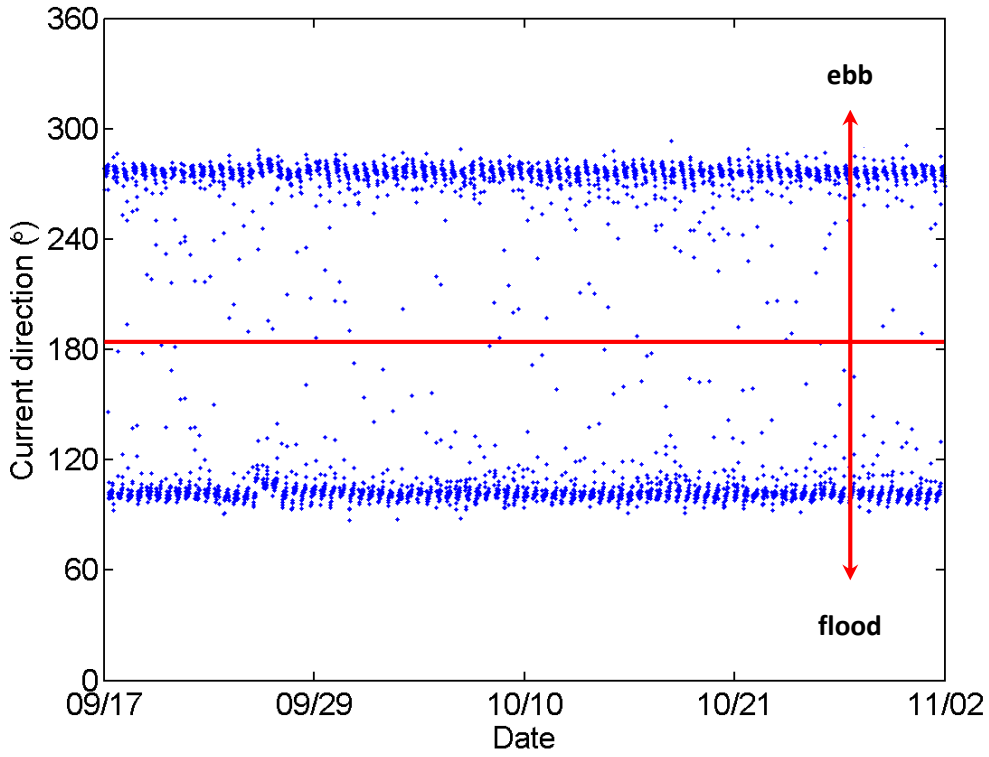

Figure 4.10. Separation of ebb and flood records

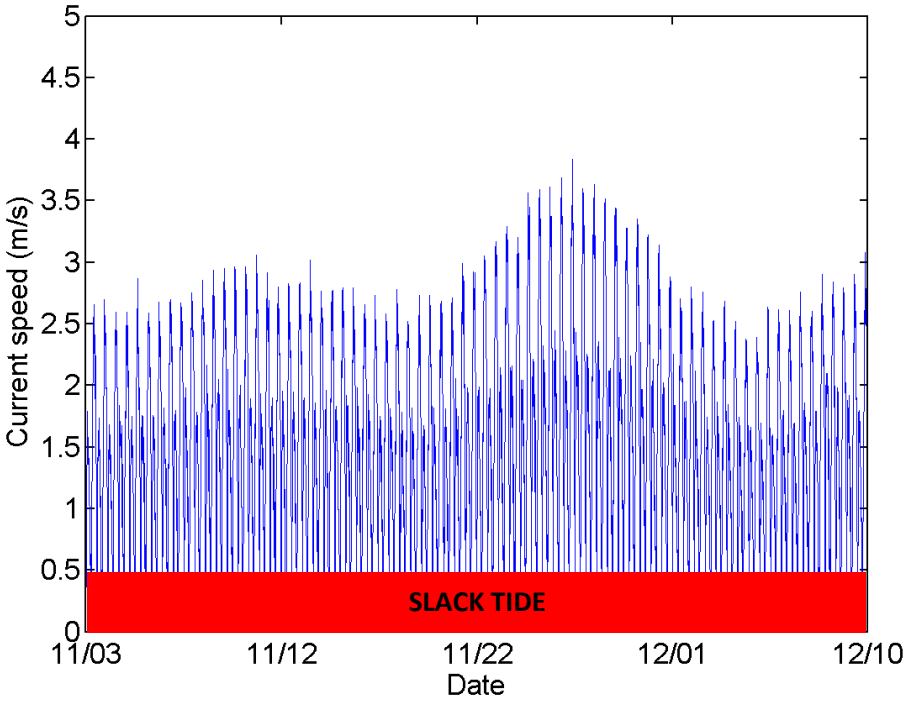

Figure 4.11. Separation of slack tide

For each survey the results of the analysis are: time-histories of u, v, w, water elevation, horizontal speed and direction; average ebb and flood current profiles; and a tidal ellipse. Depth profiles of temperature and salinity were also available.

4.3. Data correction

Plotting the results revealed significant errors in the data which had to be corrected before proceeding to harmonic analysis. Three types of error were encountered. First, invalid data was identified by a deviation from the regular tidal signal. These instances could only be resolved by discarding the erroneous data. Second, the device underwent an abrupt change in heading, pitch or roll as evidenced by a sudden and lasting change in flow direction. The solution was to calculate the change in direction using the scatterplot and apply that as a correction to the velocities in polar coordinates. Third, the water elevation time-history showed an abrupt change in mean sea level. The fix was to calculate the difference in mean sea level before and after the shift and to apply that as a correction to the water elevation. The following pages provide examples of these errors and the solutions that were applied.

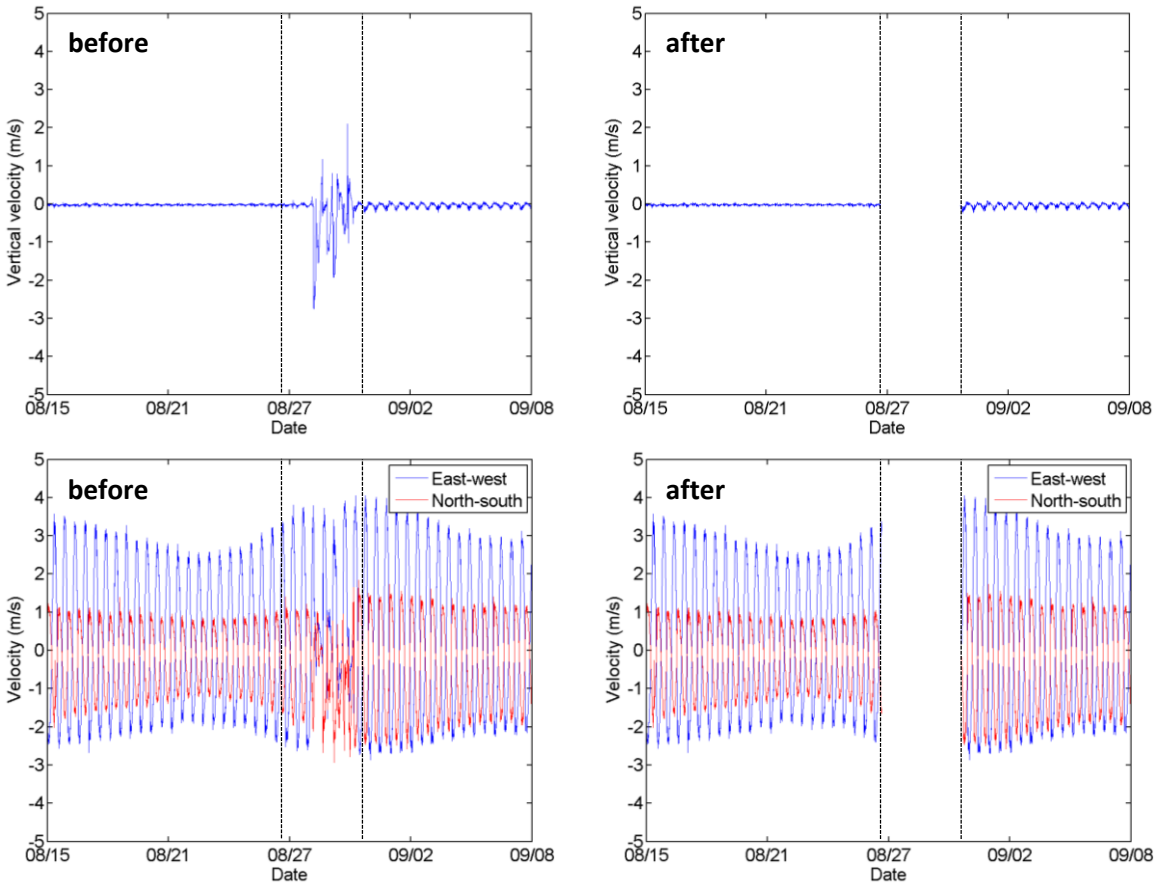

Figure 4.12. Correction of invalid data at Site A, before (left) and after (right).

Plots of depth-averaged velocity at Site A illustrate invalid data (Figure 4.12). These erratic readings differ from the smooth, regular tidal signal; most conspicuously in the case of vertical velocity where readings are ordinarily close to zero. Note that the vertical and north-south velocities are greater after the event than before. The invalid data was discarded with an added margin for error. An additional error encountered at Site A is an abrupt change in the device's heading, pitch or roll which manifests as a sudden and lasting change in flow direction (Figure 4.13) and in the relative magnitude of the velocity components u, v, and w (Figure 4.12). Without access to the heading, pitch or roll of the device to correct the readings another solution was applied. First, the least-squares line was determined before and after the event (Figure 4.14), then u and v were converted to polar coordinates and the erroneous data was rotated by the slope difference. Horizontal current direction was corrected in the same manner.

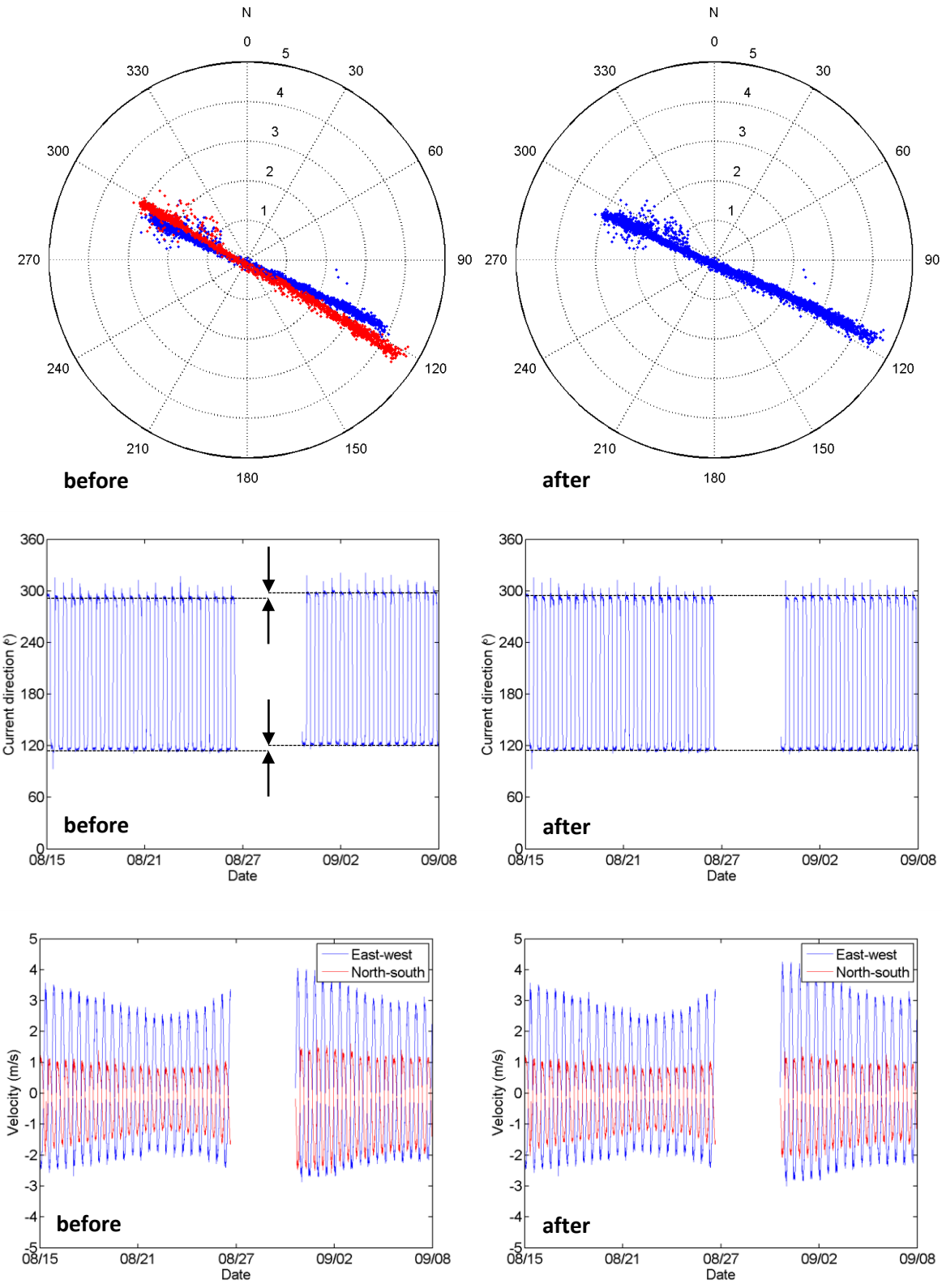

Figure 4.13. Correction of rotated data at Site A, before (left) and after (right).
The top left plot shows data before the event in [blue] and after the event in [red].

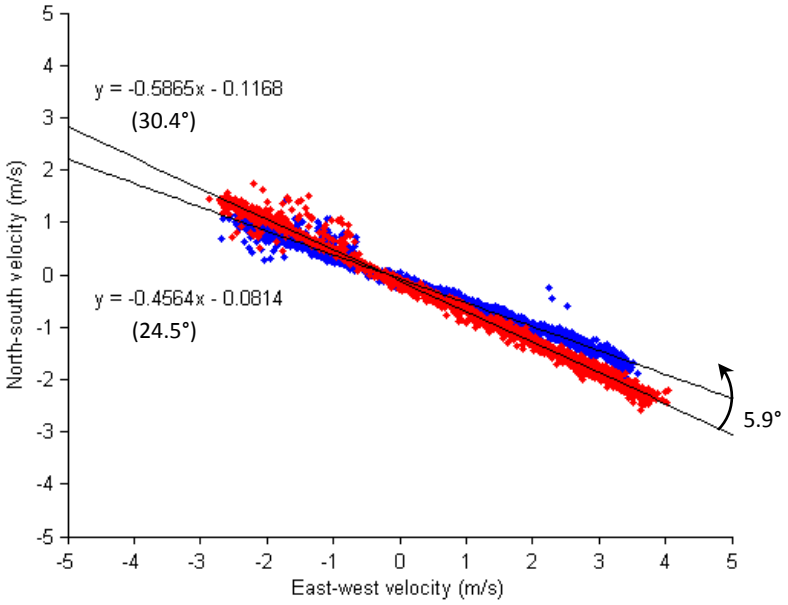

Figure 4.14. Angular correction.
The plot shows data before the event in [blue] and after the event in [red].

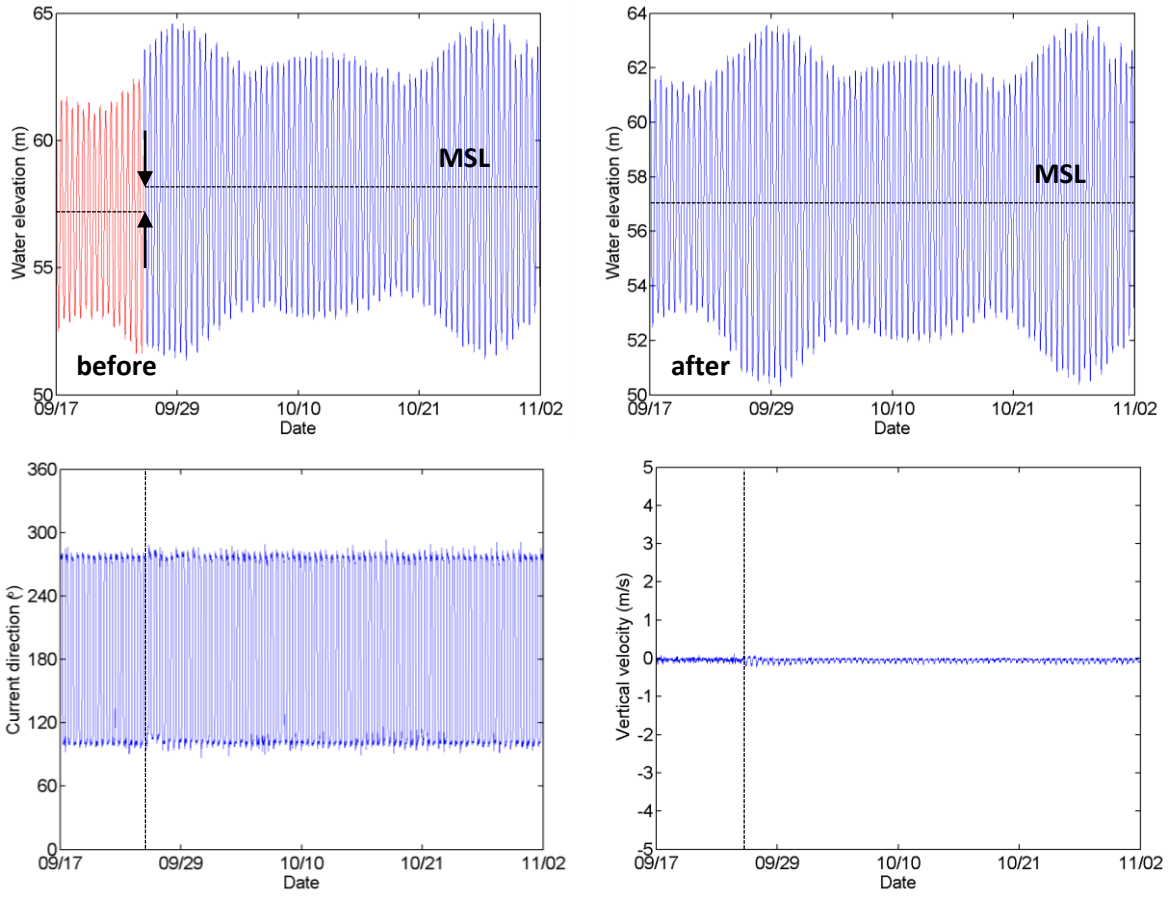

Figure 4.15. Correction of a shift in MSL at Site B, before (left) and after (right).
The top left plot shows data before the event in [blue] and after the event in [red].

The water elevation time-history at Site B exhibits an abrupt change in mean sea level (Figure 4.15). The shift is accompanied by a transient disturbance in flow direction and velocity: note the change in pattern of the vertical velocity at the same instant. The mean sea level (MSL) was calculated before and after the event and water elevations were corrected with the difference. A summary of the corrections made to the measured data is shown below (Table 4.3). Invalid data was discarded for Site A from August 27th to August 31st 2011. Sites C and D required data to be discarded for the first day of data acquisition. Directional data was rotated by 5.860° from August 31st to the end of the survey for Site A. Site B, as seen previously, had its water elevation time-series corrected by -1.044 m from September 25th until the end of the survey. Site D required the most intervention: directional data was rotated by 6.613° and the water elevation time-series was corrected by -0.661 m from September 27th until the end of the survey.

Table 4.3. Summary of corrections to the observed data

Site	A	B	C	D
Invalid data	27.08.11 – 31.08.11	N/A	02.11.11 – 03.11.11	19.09.11
Rotation	**+5.860°** 31.08.11 – 08.09.11	N/A	N/A	**+6.613°** 27.09.11 – 02.11.11
MSL	N/A	**-1.044 m** 25.09.11 – 02.11.11	N/A	**-0.661 m** 27.09.11 – 02.11.11

4.4. Tidal characteristics

Table 4.4 summarises the tidal characteristics derived from the surveys: mid-tide depth, tidal range, depth-averaged ebb and flood velocity, and tidal current misalignment. Typical spring currents are shown in Figure 4.16. The measurements were able to capture the pulse at the beginning of ebb observed by Karsten *et al*. (2011). Figure 4.17 compares typical spring and neap currents at Site C. The complete set of results at all sites is compiled in Appendix B.

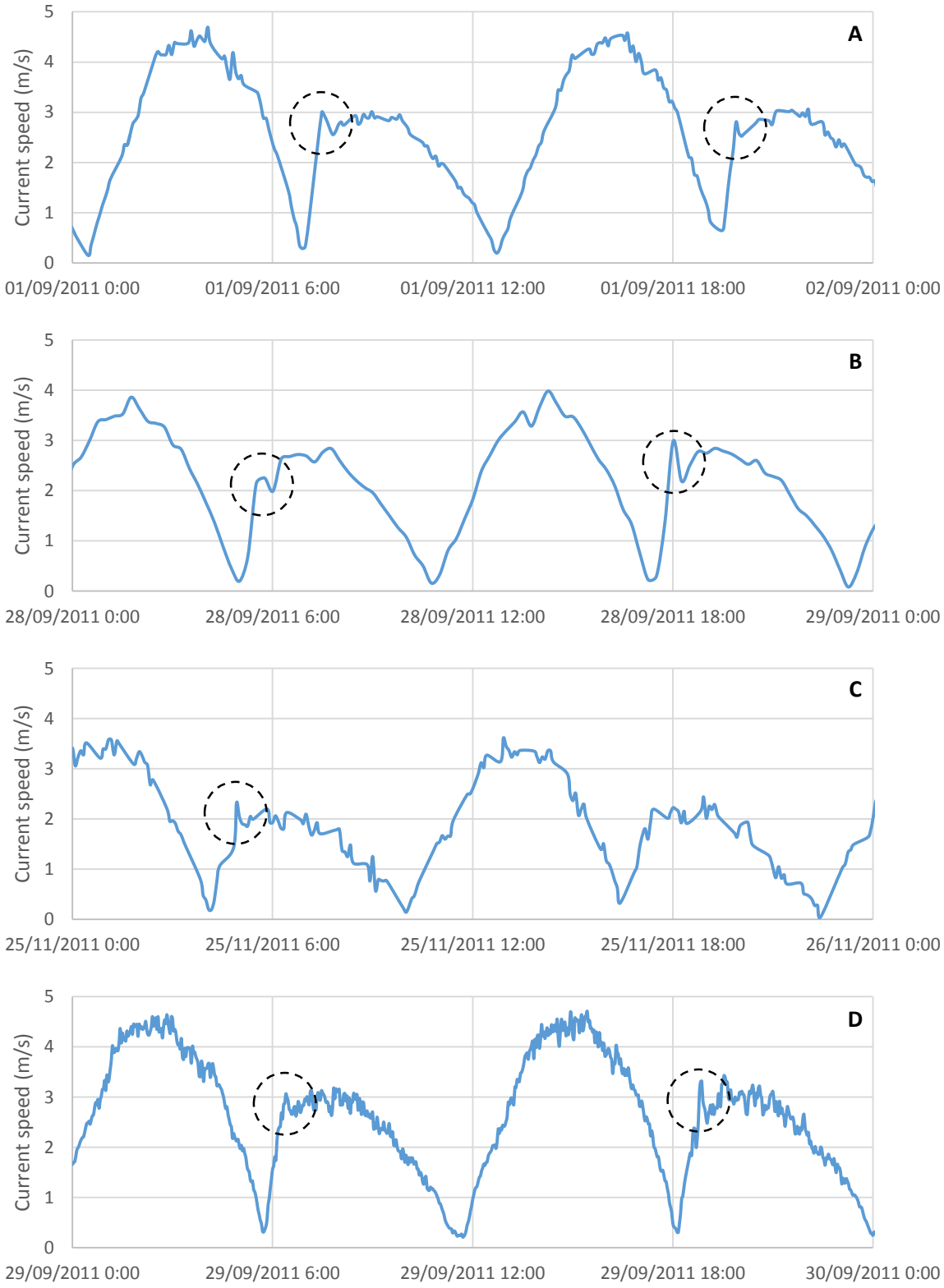

Figure 4.16. Observed pulse at the beginning of ebb

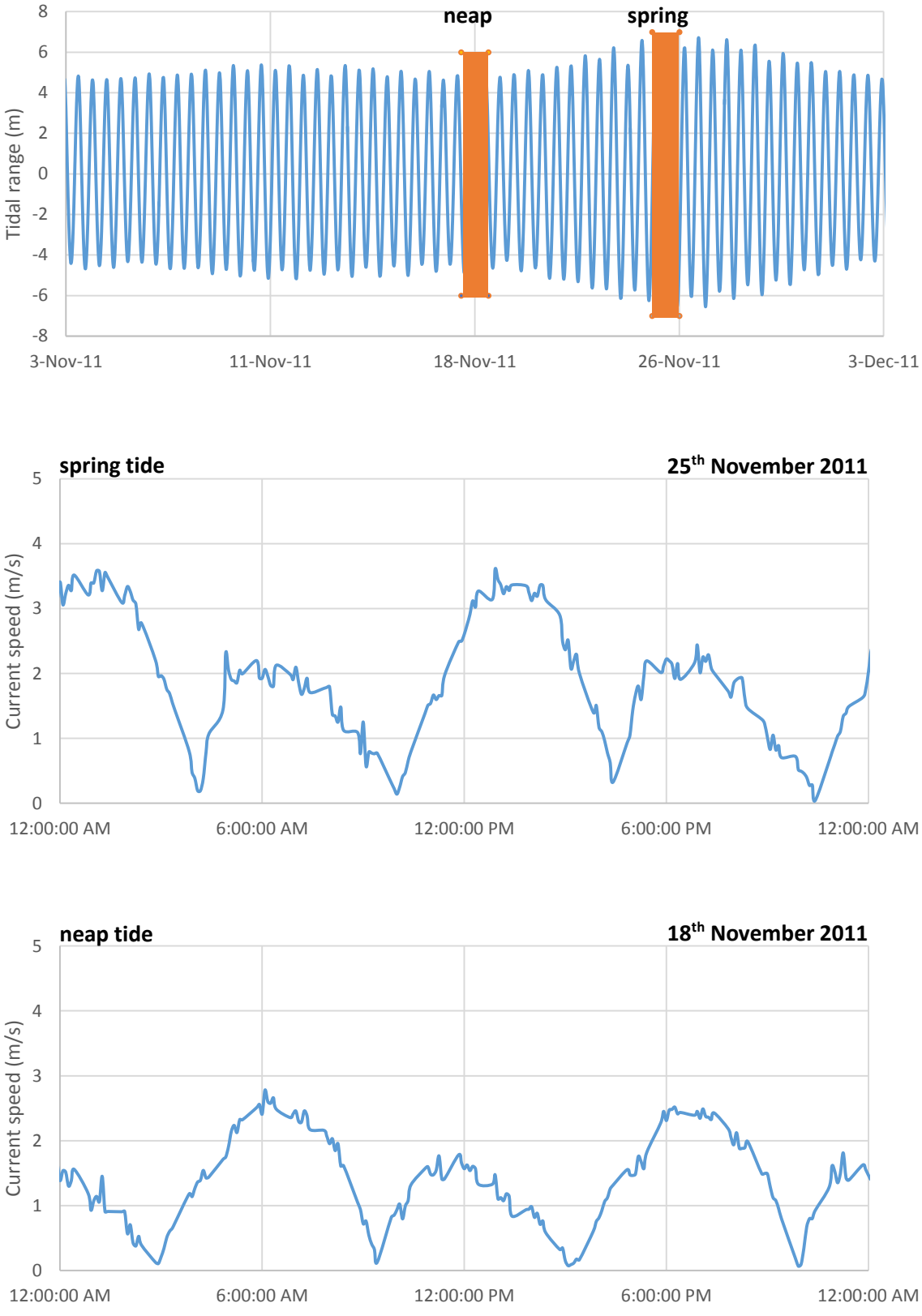

Figure 4.17. Typical spring and neap currents (Site C)

Table 4.4. Summary of observed tidal characteristics

Site	A	B	C	D
Mid-tide depth	37.0 m	57.0 m	48.7 m	36.0 m
Tidal range	9.8 m	10.3 m	10.1 m	10.3 m
$\bar{V}_{flood}$	2.43 m/s	2.09 m/s	1.96 m/s	2.54 m/s
$\bar{V}_{ebb}$	1.83 m/s	1.73 m/s	1.34 m/s	1.90 m/s
$\lvert\theta_{ebb} - \theta_{flood}\rvert$	174°	175°	175°	171°

4.5. Harmonic analysis

Harmonic analysis was performed on measured elevations and depth-averaged velocities, producing amplitudes and phases. Analyses were performed using the IOS Tidal Package (Foreman *et al.* 2009) from Fisheries and Oceans Canada. These tidal constituents are necessary for model validation and tidal current energy resource assessment. Tables 4.5, 4.6, and 4.7 show the ten most important tidal constituents for tidal height, east-west and north-south velocity, respectively.

Table 4.5. Tidal height harmonics of amplitude (m) and phase (°) (observed)

Tide	Site A		Site B		Site C		Site D	
	Amp.	Phase	Amp.	Phase	Amp.	Phase	Amp.	Phase
M2	4.877	115	4.818	116	4.913	116	4.833	118
N2	–	–	1.176	92	1.040	81	1.173	95
S2	0.579	172	0.838	149	0.736	151	0.812	152
L2	–	–	0.479	116	0.466	135	0.487	118
K1	0.151	200	0.149	194	0.208	196	0.135	187
MU2	–	–	0.099	157	0.182	185	0.117	170
M4	0.207	241	0.111	270	0.159	235	0.167	252
O1	0.093	161	0.140	185	0.120	187	0.120	185
MSF	0.133	210	0.032	179	0.094	248	0.061	210
2MN6	–	–	0.008	58	0.083	303	0.035	3

Table 4.6. East-west tidal current harmonics of amplitude (m) and phase (°) (observed)

Tide	Site A		Site B		Site C		Site D	
	Amp.	Phase	Amp.	Phase	Amp.	Phase	Amp.	Phase
M2	2.680	34	2.477	36	1.909	31	2.668	33
N2	-	-	0.594	16	0.401	356	0.632	10
S2	0.372	107	0.434	75	0.292	68	0.468	71
M4	0.283	130	0.243	150	0.234	135	0.290	132
L2	-	-	0.259	34	0.199	37	0.289	27
M6	0.155	312	0.130	333	0.107	305	0.148	306
MN4	-	–	0.118	121	0.093	93	0.132	113
MU2	-	–	0.087	93	0.078	103	0.084	88
MS4	0.035	204	0.069	188	0.067	180	0.083	170
2MN6	-	–	0.107	311	0.064	257	0.132	287

Table 4.7. North-south tidal current harmonics of amplitude (m) and phase (°) (observed)

Tide	Site A		Site B		Site C		Site D	
	Amp.	Phase	Amp.	Phase	Amp.	Phase	Amp.	Phase
M2	1.219	214	0.419	219	1.155	210	1.284	213
N2	–	–	0.106	204	0.258	180	0.299	190
S2	0.177	287	0.081	258	0.189	250	0.223	251
M4	0.152	311	0.083	321	0.182	308	0.171	308
L2	–	–	0.032	217	0.099	214	0.139	207
MN4	–	–	0.040	296	0.075	268	0.079	287
M6	0.076	134	0.023	163	0.072	123	0.083	129
MU2	–	–	0.023	267	0.059	268	0.043	272
MS4	0.015	29	0.022	356	0.055	345	0.048	343
2MN6	–	–	0.028	142	0.044	79	0.070	111

Analyses were performed using the IOS Tidal Package (Foreman *et al.* 2009) which can handle record times that are irregularly distributed (*e.g.* Sites A and C). However, in the ensuing work, model output lent itself well to harmonic analysis with T_TIDE (Pawlowicz *et al.* 2002) due to the fixed output time step. Furthermore, T_TIDE is written in MATLAB which facilitated integration into the calibration and validation codes that were developed. The error introduced into the validation process by using different tidal analysis codes for observed and modelled data has to be quantified. For that purpose, Site B data was analysed with both the IOS Tidal Package and T_TIDE. The root-mean-square error in amplitude and phase for five leading constituents is summarised in the tables below.

Table 4.8. IOS and T_TIDE comparison (tidal height harmonics of amplitude, m, and phase, deg)

Tide	IOS Tidal Package		T-Tide		Difference	
	Amp.	Phase	Amp.	Phase	Amp.	Phase
M2	4.818	116	4.837	116	0.019	0
N2	1.176	92	1.177	94	0.001	2
S2	0.838	149	0.818	151	0.020	2
L2	0.479	116	0.494	117	0.015	1
K1	0.149	194	0.138	187	0.011	7
				RMSE	**0.015**	**3.4**

Table 4.9. IOS and T_TIDE comparison (east-west tidal current harmonics of amplitude, m, and phase, deg)

Tide	IOS Tidal Package		T-Tide		Difference	
	Amp.	Phase	Amp.	Phase	Amp.	Phase
M2	2.477	36	2.477	36	0	0
N2	0.594	16	0.594	16	0	0
S2	0.434	75	0.435	75	0.001	0
L2	0.259	34	0.259	34	0	0
M4	0.243	150	0.244	151	0.001	1
				RMSE	**0.001**	**0.4**

Table 4.10. IOS and T_TIDE comparison (north-south tidal current harmonics of amplitude, m, and phase, deg)

Tide	IOS Tidal Package		T-Tide		Difference	
	Amp.	Phase	Amp.	Phase	Amp.	Phase
M2	0.419	219	0.419	219	0	0
N2	0.106	204	0.107	203	0.001	1
M4	0.083	321	0.083	322	0	1
S2	0.081	258	0.080	257	0.001	1
MN4	0.040	296	0.039	299	0.001	3
				RMSE	**0.001**	**1.7**

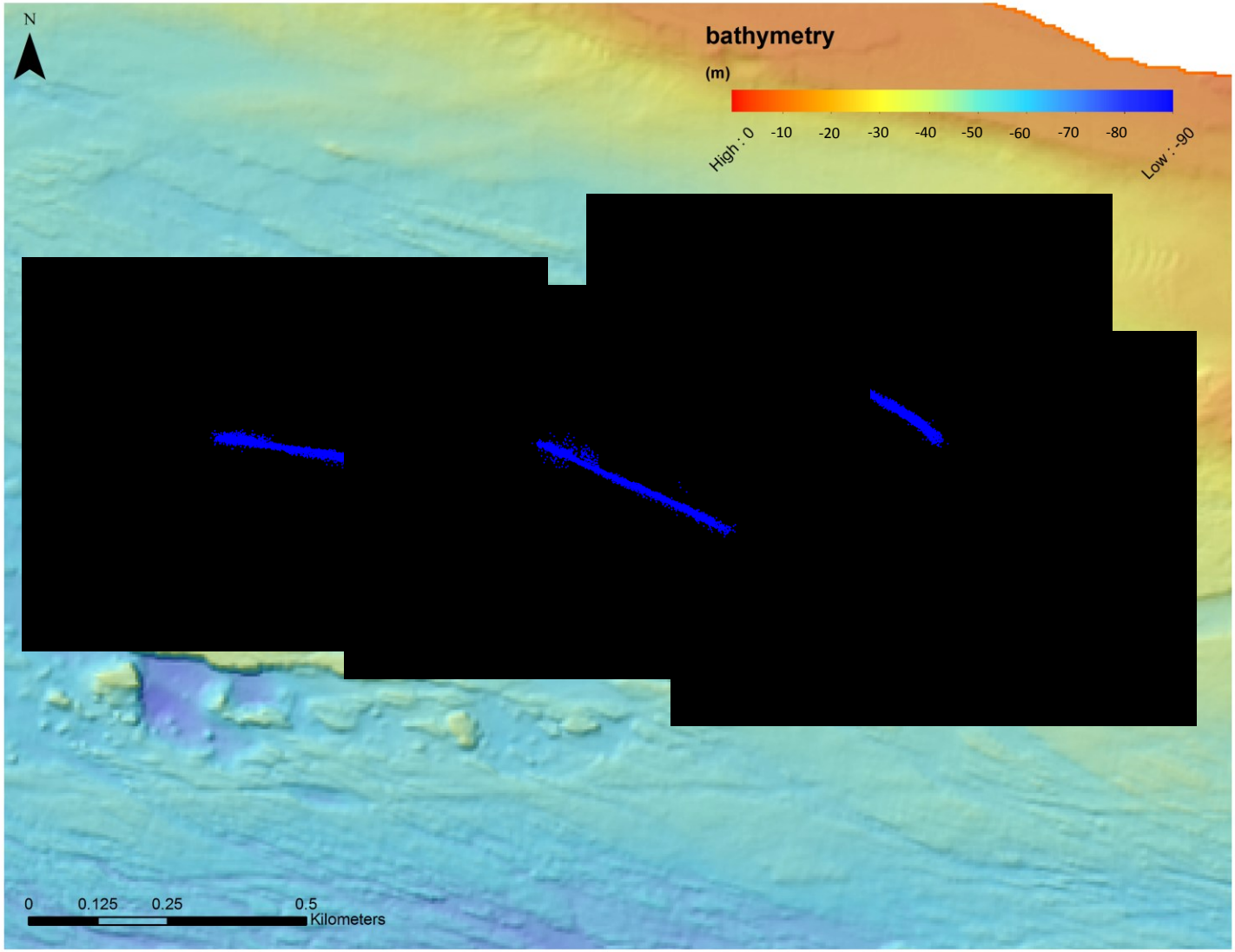

Figure 4.18. Observed flow through the Crown Lease Area

4.6. Discussion

The objective of Chapter 4 was to begin conducting a comprehensive assessment of the tidal current energy resource at the FORCE site. Available field measurements are analysed in order to characterise the tidal properties at the site and to extract the tidal constituents. In Chapter 5, the model-predicted constituents are computed and in Chapter 6, long-term current predictions are produced from the observed and modelled harmonics in order to define the velocity probability distribution and calculate Annual Energy Production as defined by the IEC-TC-114 standard.

The FORCE berths, shown on a bathymetric map in Figure 4.8, are the locations of the resource assessment. Sites A and D are located on a shallow, flat-topped ridge extending west from Black Rock Island with mid-tide depths of 37 and 36 m, respectively. Site B is located off the western edge of the shelf in the deepest part of the project site, with mid-tide depths of about 57 m. Site C is similarly set in a valley north of the shelf, closest to the shoreline, with mid-tide depths of approximately 49 m.

Data from static current profiler surveys at the four FORCE berths, Sites A, B, C and D, and from an additional survey outside the Crown Lease Area, Site F, were made available in support of this project. The deployment period of the instruments is shown in Table 4.1, note that the installation period at Site A is only 24 days, whereas instruments at Sites B, C and D were deployed more than 35 days. The raw data consists of pressure and velocity time series. The spatial and temporal resolution of each survey are tabulated in Table 4.2. Understandably, the deeper sites are accompanied by greater bin or cell sizes. The sampling interval ranges from 2 minutes at Site D to 15 minutes at Site B. Although 5 minute recording intervals are indicated at Sites A and C, it was in fact irregular, with 20 and 25 minute gaps in the data every hour, respectively. The reason for the irregularly distributed record was not provided by the supplier. The depth-averaging scheme is explained in Section 4.2 as well as the making of ebb and flood current profiles.

Plotting the depth-averaged data showed significant errors which had to be corrected before proceeding to harmonic analysis. The correction procedures are described in Section 4.3 and Table 4.3 shows the solutions that were implemented at each site. Plots of depth-averaged velocity at Site A revealed bad data (Figure 4.12). These readings differ from the smooth, regular tidal signal; most conspicuously in the case of vertical velocity where readings are ordinarily close to zero. Vertical velocity shifted erratically from -2 to 2 m/s for the span of the disruption. These fluctuations were accompanied by a sudden and lasting change in flow direction (Figure 4.13) and in the relative

magnitude of the velocity components u, v and w. Although not shown here, these changes coincide with irregularities in the water elevation time-history as well. The likely explanation is that the instrument shifted from its initial position, producing the observed change in the relative magnitude of the velocity components. Unfortunately the heading, pitch and roll of the device were not logged and the readings could not be adjusted following correct procedures. Instead, the horizontal velocity components were rotated in polar coordinates, but this is a two-dimensional solution to a three-dimensional problem. The vertical velocity is not corrected and keeps some fraction of the horizontal magnitude. As a result, the Site A survey is expected to contain errors.

The water elevation time-history at Site B exhibits an abrupt change in MSL (Figure 4.15). The shift is accompanied by a transient disturbance in flow direction and velocity: note the change in pattern of the vertical velocity at the same instant. Although not shown here, these changes coincide with irregularities in the horizontal velocity components as well. The visible issue is corrected, but the shift in pattern of the vertical velocity suggests that there may be more subtle errors in the data at Site B. At Site C, the first 24 hours of collected data were discarded due to unusual readings. Water elevation, tidal current speed and direction were erratic for the first day of recording. Site D exhibited all three of the errors encountered in the field measurements. There is an evident shift in MSL which coincides with a sudden and lasting change in flow direction and in the relative magnitude of the velocity components u, v and w – just like Site A. To close out this topic, Sites A and D demonstrate that bad data in one flow property is always accompanied by bad data in the remaining flow properties. Hence, the author has limited confidence in the Site B data where a shift in MSL coincided with subtle changes in the vertical velocity. Likewise, although the Site C survey required the least intervention, the data may not be completely reliable. These are the concerns which prompted the acquisition of the Site F survey for additional validation.

Table 4.4 summarises the tidal characteristics derived from the surveys: mid-tide depth, tidal range, depth-averaged ebb and flood velocity, and tidal current misalignment. The average tidal range at Site A is smaller because the spring peak had to be discarded. There is a conspicuous tidal asymmetry: tidal current speeds are $\sim$33% greater on the flood than on the ebb due to the eddie that forms off Cape Split (Karsten *et al.* 2008). The highest tidal velocities occur at Site D, A, B and C, in that order. The lowest velocities would be expected at Site C, which is closest to the shore and sheltered by Black Rock Island on the ebb tide. The higher velocities at Sites A and D indicate flow acceleration on top of the shallow Crown Lease Area shelf. Tidal current misalignment was calculated as the difference

between the mean ebb and flood current directions. Completely rectilinear currents would show a 180 degree difference. However, as discussed in the preceding chapters, tidal currents are rarely completely rectilinear and thus the resource assessment assumes that devices are able to yaw. In spite of the measurement errors, the surveys were able to capture the pulse at the beginning of ebb observed by Karsten *et al.* (2011) (Figure 4.16).

The complete set of results at all sites is compiled in Appendix B. Available temperature and salinity depth profiles for Sites A, B, C and D are shown in Figures B.4, B.9, B.14 and B.19, respectively. Across the water column, temperature and salinity fluctuate by 0.1°C and 0.1 Practical Salinity Units, respectively. These observations lend credence to the common assumption that the water column in strong tidal flows is well mixed due to the inherently energetic nature of the flow. Hence, tidal flows are well represented by a depth-averaged hydrodynamic model. The ebb and flood current profiles shown in Figures B.5, B.10, B.15 and B.20 also demonstrate well mixed flow. The fastest currents are seen 5 - 10 m below the surface, and velocities have a mean range of 1 m/s across the measured depth profile. The tidal ellipses are shown in Figures B.3, B.8, B.13 and B.18, and in Figure 4.18 on a bathymetric map. Figure 4.18 is a good example of the tidal asymmetry in Minas Passage: higher velocities are attained on the flood, and flow direction fluctuates more on the ebb. Tidal flows at Sites A and D are parallel, while B and C deviate.

Harmonic analysis was performed on observed tidal heights and depth-averaged currents, producing amplitudes and phases. Analyses were performed using the IOS Tidal Package due to the irregularly distributed record times at Sites A and C, as explained previously. Unfortunately, after the corrections implemented in Section 4.3, only 20 days of the original data were useable at Site A. Therefore, fewer harmonics were extractable from that record and those extracted may not be as accurate. For example, the amplitude of S2 is significantly smaller at Site A than at Sites B, C and D (Tables 4.5, 4.6 and 4.7). Readers will recall from Section 3.3 that most sources recommend a month of data to perform harmonic analysis. The harmonics at Sites B, C and D appear reasonable: amplitudes of 4.8, 0.7 and 0.9 m in M2, S2 and N2, respectively, are published at the nearby Cape Sharp CHS tidal station. Although these values aren't expected to be identical at different locations, their similarity boosts confidence in the observations.

The main objective of Chapter 4 was to begin a comprehensive assessment of the tidal current energy resource at the FORCE project site by computing the observed tidal constituents. Having obtained the observed constituents, the assessment can proceed to the numerical modelling stage. In the next

chapters, T_TIDE will be used to conduct harmonic analyses instead of the IOS Tidal Package. This should be appropriate because a comparison of their solutions shows a root-mean-square error of 1.5 cm and 3.4° in amplitude and phase, respectively, for tidal height constituents and smaller errors for tidal current harmonics (Tables 4.8, 4.9 and 4.10).

5. Hydrodynamic modelling

Chapter 5 touches on two objectives of the thesis. Firstly, to conduct a comprehensive assessment of the tidal current resource at the project site requires a validated hydrodynamic model. For that purpose, Chapter 5 presents the development of a hydrodynamic model including friction parameterisation, grid development, boundary specification, calibration and validation. Secondly, to investigate the principal sources of error and uncertainty affecting resource assessment. For that purpose, Chapter 5 describes the development of submeshes covering the project site to investigate how spatial resolution affects resource assessment.

5.1. Model development

5.1.1. Description of the numerical model

A numerical model of hydrodynamics in the upper Bay of Fundy has been developed based on the TELEMAC modelling system for free surface flow. Developed by the *Laboratoire National d'Hydraulique et Environnment*, part of the research and development group at *Électricity de France*, TELEMAC has applications in river and coastal hydraulics including: design of shipping channels, harbour structures, studies of thermal plumes, pollutant dispersion, dam breaks, coastal protection or dredging works, and tidal circulation.

The theoretical formulation of TELEMAC is described by Hervouet (2007) and its source code and manuals are available online at http://www.opentelemac.org/. TELEMAC-2D, which has been used in this study, is a finite element formulation which solves the vertically integrated equations of continuity (5.1) and momentum (5.2, 5.3) within a computational domain:

$$\frac{\partial h}{\partial t} + \vec{u} \cdot \vec{\nabla}(h) + h div(\vec{u}) = S_h \tag{5.1}$$

$$\frac{\partial u}{\partial t} + \vec{u} \cdot \vec{\nabla}(u) = -g\frac{\partial Z}{\partial x} + S_x + \frac{1}{h} div\left(h\nu_t \vec{\nabla} u\right) \tag{5.2}$$

$$\frac{\partial v}{\partial t} + \vec{u} \cdot \vec{\nabla}(v) = -g\frac{\partial Z}{\partial y} + S_y + \frac{1}{h} div\left(h\nu_t \vec{\nabla} v\right) \tag{5.3}$$

where u and v (m/s) are depth-averaged velocity components in the x and y directions, respectively, h (m) is the water depth, g (m/s^2) is gravitational acceleration, ν_t (m^2/s) is eddy viscosity,

Z (m) is free surface elevation, t (s) is time, S_h (m/s) is a source or sink of fluid, S_x and S_y (m/s^2) are sources or sinks of momentum.

TELEMAC benefits from an unstructured mesh, which allows for regions of interest to be represented with very high resolution, without the need for nesting. Accurate depiction of complex bathymetries and shorelines is possible without undue computational cost. The TELEMAC modelling system is capable of taking into account a wide range of phenomena including the propagation of long waves, bed friction, the Coriolis force, meteorological factors, turbulence, horizontal temperature and salinity gradients, and the wetting and drying of tidal flats. Additional modules allow for the simulation of three-dimensional flows (TELEMAC-3D), sediment transport and bed evolution (SISYPHE), and waves (TOMAWAC).

The developed model accounts for the wetting and drying of tidal flats, the effect of bed friction and the Coriolis effect. Strickler's formulation is adopted to model bed friction, where Strickler's coefficient is the inverse of Manning's roughness coefficient. A constant viscosity turbulence model is implemented whereby molecular viscosity is augmented with an eddy viscosity to account for increased momentum transfer in turbulent flow.

5.1.2. Strickler's law

The bottom shear stress acting on a fluid in two dimensions has the two components:

$$\tau_{xz} = -\frac{u}{2}\rho C_f\sqrt{u^2+v^2} \tag{5.4}$$

$$\tau_{yz} = -\frac{v}{2}\rho C_f\sqrt{u^2+v^2} \tag{5.5}$$

where ρ (kg/m^3) is water density, C_f is a dimensionless friction coefficient, and u and v (m/s) are depth-averaged velocity components in the x and y directions, respectively. The coefficient C_f is rarely used and is usually replaced by others, the Chézy coefficient for example:

$$C = \sqrt{\frac{2g}{C_f}} \tag{5.6}$$

Chézy's friction law for the shear force at the bottom is expressed as follows:

$$F_x^f = -\frac{u}{\cos(\alpha)}\frac{g}{hC^2}\sqrt{u^2+v^2} \tag{5.7}$$

$$F_y^f = -\frac{v}{\cos(\alpha)}\frac{g}{hC^2}\sqrt{u^2+v^2} \tag{5.8}$$

where α is the angle of the bottom slope. However, the Chézy coefficient is dependent on the bottom roughness and on the depth. The empirical law of Manning and Strickler was developed to obtain a friction coefficient independent of the depth:

$$C = Kh^{1/6} \tag{5.9}$$

where K ($m^{1/3}/s$) is the Strickler coefficient. Strickler's law follows:

$$F_x^f = -\frac{u}{\cos(\alpha)}\frac{g}{h^{4/3}K^2}\sqrt{u^2+v^2} \tag{5.10}$$

$$F_y^f = -\frac{v}{\cos(\alpha)}\frac{g}{h^{4/3}K^2}\sqrt{u^2+v^2} \tag{5.11}$$

Strickler's law is appended to the source terms S_x and S_y of the momentum equations.

5.1.3. Coriolis force

The Coriolis force is due to the rotation of the Earth on its own axis and the inertia of the mass experiencing the effect. When considering ocean dynamics, the vertical velocity is small, and the vertical component of the Coriolis acceleration is small compared to gravity. By neglecting the vertical component the Coriolis force is given by:

$$F_x^c = 2\omega\sin(\lambda)\,v = fv \tag{5.12}$$

$$F_y^c = -2\omega\sin(\lambda)\,u = -fu \tag{5.13}$$

where $f = 2\omega\sin(\lambda)$ is called the Coriolis parameter, the angular velocity of the Earth is ω = 7.292 x 10^{-5} rad/s and λ is latitude. The Coriolis parameter may be considered constant across small areas. The Rossby number describes the ratio of inertial to Coriolis force and governs the importance of Coriolis accelerations in the Navier-Stokes equations:

$$Ro = {}^{U}/_{Lf} \tag{5.14}$$

where U (m/s) and L (m) are the characteristic velocity and length scales of the flow, respectively. The Coriolis force is important only if $Ro \ll 1$. The Coriolis force includes v in the x- and u in the y-direction which implies rotation. The Earth rotates slowly (*i.e.* ω is small), thus Coriolis accelerations are small in the Navier-Stokes equations: large distances and long periods of time are required to develop the rotation. The Coriolis force equations are added to the source terms S_x and S_y of the momentum equations. In this study, the Coriolis coefficient is set to 0.0001. The effect of the Coriolis force on resource assessment is investigated in Chapter 7.

5.1.4. Modelling turbulence

Reynolds-averaging of the Navier-Stokes equations introduces unknowns in the form of Reynolds stresses. The Reynolds stresses transfer energy between the turbulence and the mean flow. Turbulence models address closure of the Reynolds Averaged Navier-Stokes (RANS) equations by specifying equations for the Reynolds stresses. In most turbulence models the Reynolds stresses are modelled according to the Boussinesq hypothesis, which postulates that the momentum transfer caused by turbulent eddies can be modelled with an eddy viscosity. Four turbulence models of differing complexity are available to TELEMAC users: constant viscosity, Elder, K-epsilon and Smagorinsky. The models presented differ by the eddy viscosity ν_t that they provide.

5.1.4.1. Constant viscosity model

The simplest model presumes that turbulent viscosity is constant, a suitable assumption when flow is governed by the pressure gradient and by advection, *e.g.* in the tide flow regime (Hervouet 2007). In this study, the model implements a viscosity coefficient (molecular + turbulent viscosity) of 0.0001. Values from 10^{-6} to 10^{0} were tried but had a negligible impact on flow statistics at the project site (see Appendix C.3). Values of ν_t provided in the literature differ wildly from 10^{-2} to 0.12 to 1500 m^2/s (Brière *et al*. 2007; Fischer 1979). Additional formulations are tested in Chapter 7 to investigate how the choice of turbulence model affects resource assessment.

5.1.4.2. Elder model

The Elder model specifies a different eddy viscosity in the longitudinal and transverse flow directions (K_l and K_t respectively). Measurements of the velocity profile in the logarithmic layer have led to:

$$K_l = 6u^* h \tag{5.15}$$

$$K_t = 0.6u^* h \tag{5.16}$$

where u^* (m/s) is the shear velocity and h (m) is the water depth.

5.1.4.3. K-epsilon model

A different approach to the RANS closure problem is to derive additional equations representing turbulence in the flow and use those to specify eddy viscosity. The most common is the k-ε model, where k is the time-averaged turbulent kinetic energy and ε is turbulent dissipation:

$$\frac{\partial k}{\partial t} + u_i \frac{\partial k}{\partial x_i} = \frac{1}{h} div\left(h \frac{\nu_t}{\sigma_k} \vec{\nabla} k\right) + P - \varepsilon + P_{kv} \tag{5.17}$$

$$\frac{\partial \varepsilon}{\partial t} + u_i \frac{\partial \varepsilon}{\partial x_i} = \frac{1}{h} div\left(h \frac{\nu_t}{\sigma_\varepsilon} \vec{\nabla} \varepsilon\right) + \frac{\varepsilon}{k}[c_{1\varepsilon} P - c_{2\varepsilon} \varepsilon] + P_{\varepsilon v} \tag{5.18}$$

P is the term for the production of turbulent energy:

$$P = \nu_t \left(\frac{\partial u_i}{\partial x_j} + \frac{\partial u_j}{\partial x_i}\right) \frac{\partial u_i}{\partial x_j} \tag{5.19}$$

P_{kv} and $P_{\varepsilon v}$ are due to the shear force of flow along the vertical:

$$P_{kv} = C_k \, {u_*^3}/{h} \tag{5.20}$$

$$P_{\varepsilon v} = C_\varepsilon \, {u_*^4}/{h^2} \tag{5.21}$$

Knowing k and ε the eddy viscosity is deduced from:

$$\nu_t = C_\mu \frac{k^2}{\varepsilon} \tag{5.22}$$

The constants for the k-ε model have been arrived at by data fitting for a range of turbulent flows.

5.1.4.4. Smagorinsky model

Whereas the preceding are RANS-based turbulence models, the Smagorinsky subgrid-scale (SGS) model belongs to the Large Eddy Simulation (LES) class. The idea behind the RANS equations is Reynolds decomposition, whereby an instantaneous quantity is decomposed into its time-averaged and fluctuating quantities, *i.e.*, the RANS equations give approximate time-averaged solutions to the Navier-Stokes equations.

Large Eddie Simulation, on the other hand, is based on spatial filtering of the Navier-Stokes equations. All flow scales larger than the filter (grid) size are exactly calculated and the scales smaller than the filter (grid) size are modelled by a SGS model and the effects are thus accounted in the solution. In LES the results are grid-dependent while in RANS they are independent of grid resolution. Smagorinsky models the eddy viscosity as:

$$\nu_t = C_s^2 \Delta^2 \sqrt{\left(\frac{\partial u}{\partial x}\right)^2 + \left(\frac{\partial v}{\partial y}\right)^2 + \frac{1}{2}\left(\frac{\partial u}{\partial y} + \frac{\partial v}{\partial x}\right)^2} \tag{5.23}$$

where C_s is the Smagorinsky coefficient and Δ the local grid size. The values of C_s typically range from 0.1 to 0.2.

5.1.5. Model grid

The region of interest is the Bay of Fundy, more specifically, the FORCE project site in Minas Passage. Accuracy and computational cost are proportional to grid size and density, therefore, to optimise the model grid a high resolution was adopted in Minas Passage with the size of elements increasing towards the ocean boundary. The recommendations of the IEC-TC-114 standard with respect to grid resolution are < 500 m for a Feasiblity stage assessment, refined to 200 m in regions of bathymetric complexity or < 50 m for Layout Design. In this study, elements of 500 m were specified at the shoreline except in Minas Passage, the region of interest, where elements were refined to 150 m (Figure 5.1). The triangular elements increase in size by a factor of 1.20 up to a maximum 3 km.

An objective of the thesis is to investigate the main sources of error and uncertainty affecting resource assessment, for example, spatial resolution. To that end, the model grid was developed such that submeshes of different density could be integrated to represent the Minas Passage without affecting the remainder of the grid (Figure 5.2). A total of 10 submeshes were produced for Minas Passage: 500, 400, 300, 250, 200, 150, 100, 75, 50 and 20 m resolution, accounting for the minimum recommended resolution of Feasibility and Layout Design assessments (Figure 5.3). The sensitivity analysis is conducted in Chapter 7.

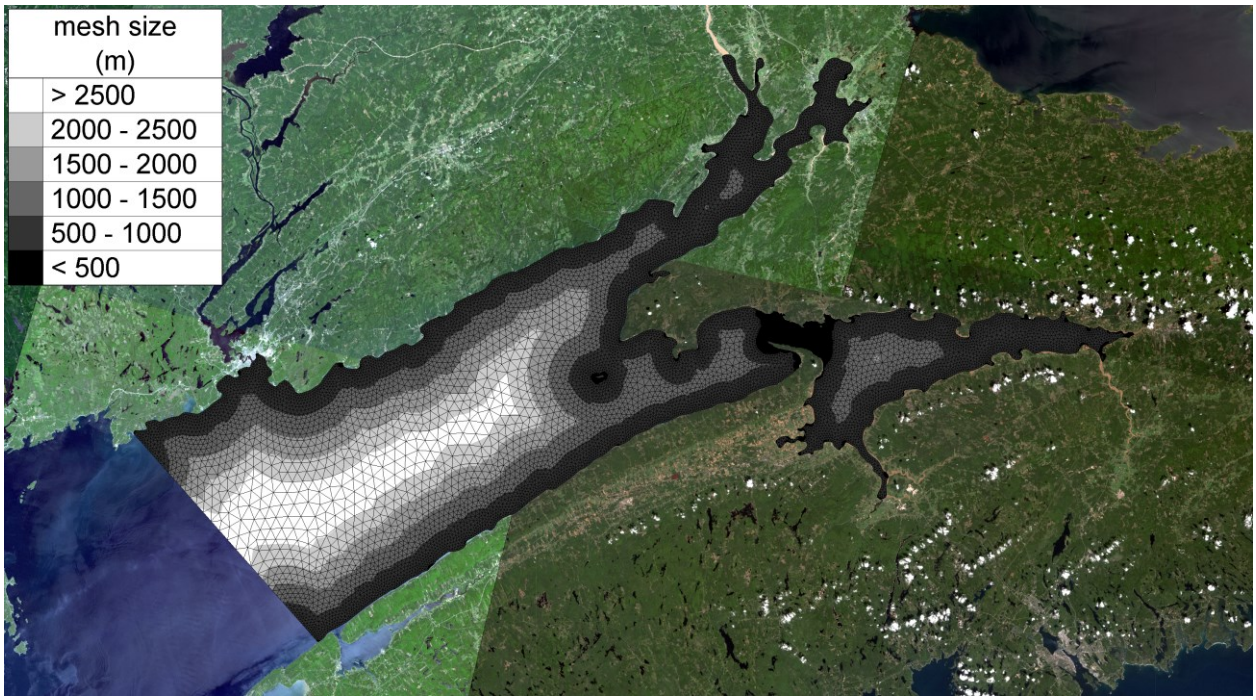

Figure 5.1. The standard mesh of the upper Bay of Fundy

The standard mesh for the purpose of calibration and validation was developed with 150 m resolution in Minas Passage. The grid consists of 16,026 nodes and 29,793 triangular elements which range in size from 100 m to 3 km. The computational domain covers an area of 8,485 km^2 from Saint John, New Brunswick, to the mudflats of Chignecto Bay and Cobequid Bay.

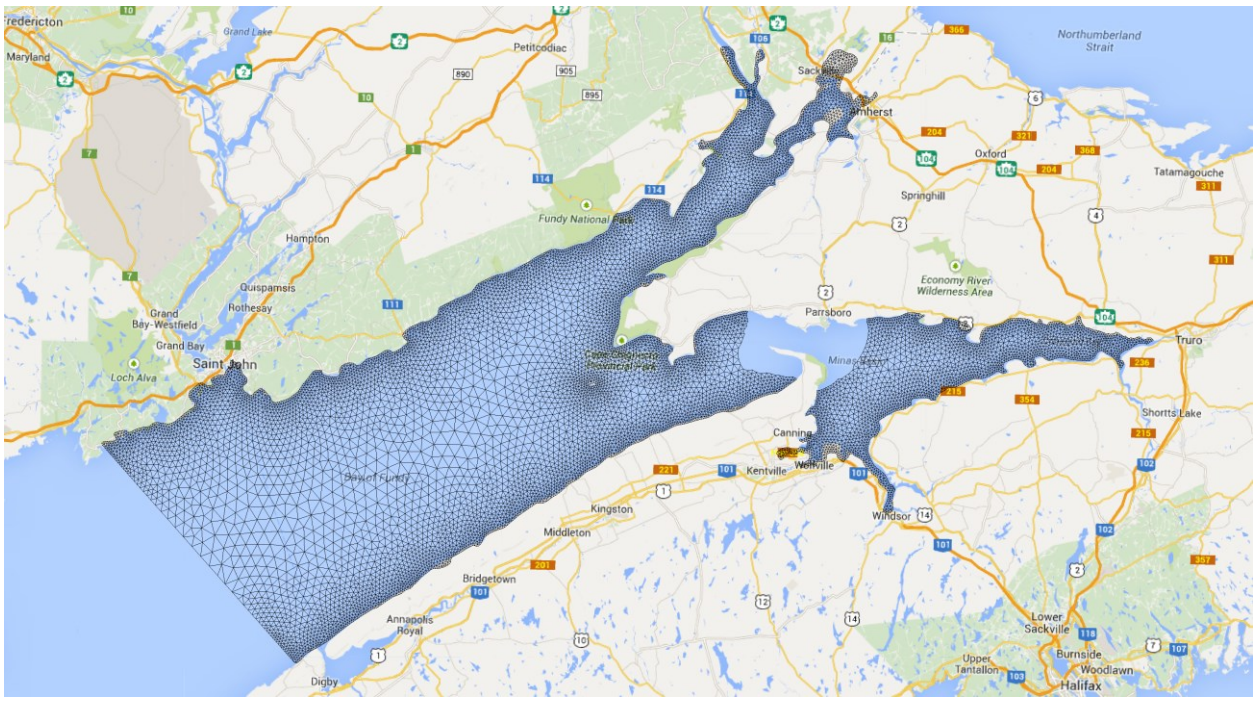

Figure 5.2. The standard mesh without a submesh

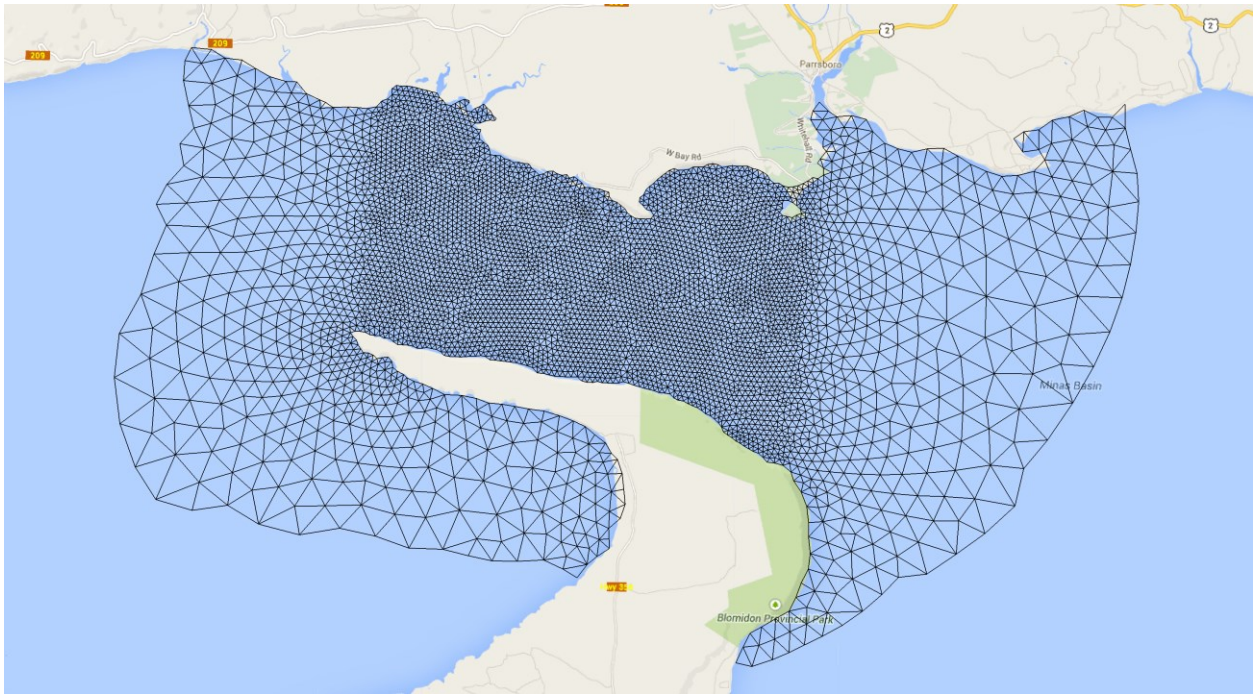

Figure 5.3. Minas Passage 150 m submesh

5.1.6. Topography / Bathymetry

The elevation of each node was interpolated, using Inverse Distance Weighting (IDW), from a Digital Elevation Model (DEM) assembled by Cousineau (2012). The DEM integrates bathymetric and topographic data from three sources: (1) Geobase Canadian Digital Elevation Data, (2) Natural Resource Canada Multibeam Bathymetry, and (3) CHS Nautical Charts (Figure 5.4). The first dataset defines the elevation of tidal flats whereas the second and third represent the sea floor. The three datasets were initially referenced to Universal Transverse Mercator (UTM) North American Datum (NAD) 83 Zone 19 in the horizontal plane and North American Vertical Datum of 1988 (NAVD 88) in the vertical plane. In this study, the horizontal reference was transformed to UTM NAD83 Zone 20. At a later point in time a more refined 5 m grid of the Minas Channel was made available by Natural Resources Canada (Figure 5.5). The elevation of nodes in Minas Passage covered by the 5 m grid was interpolated from that dataset.

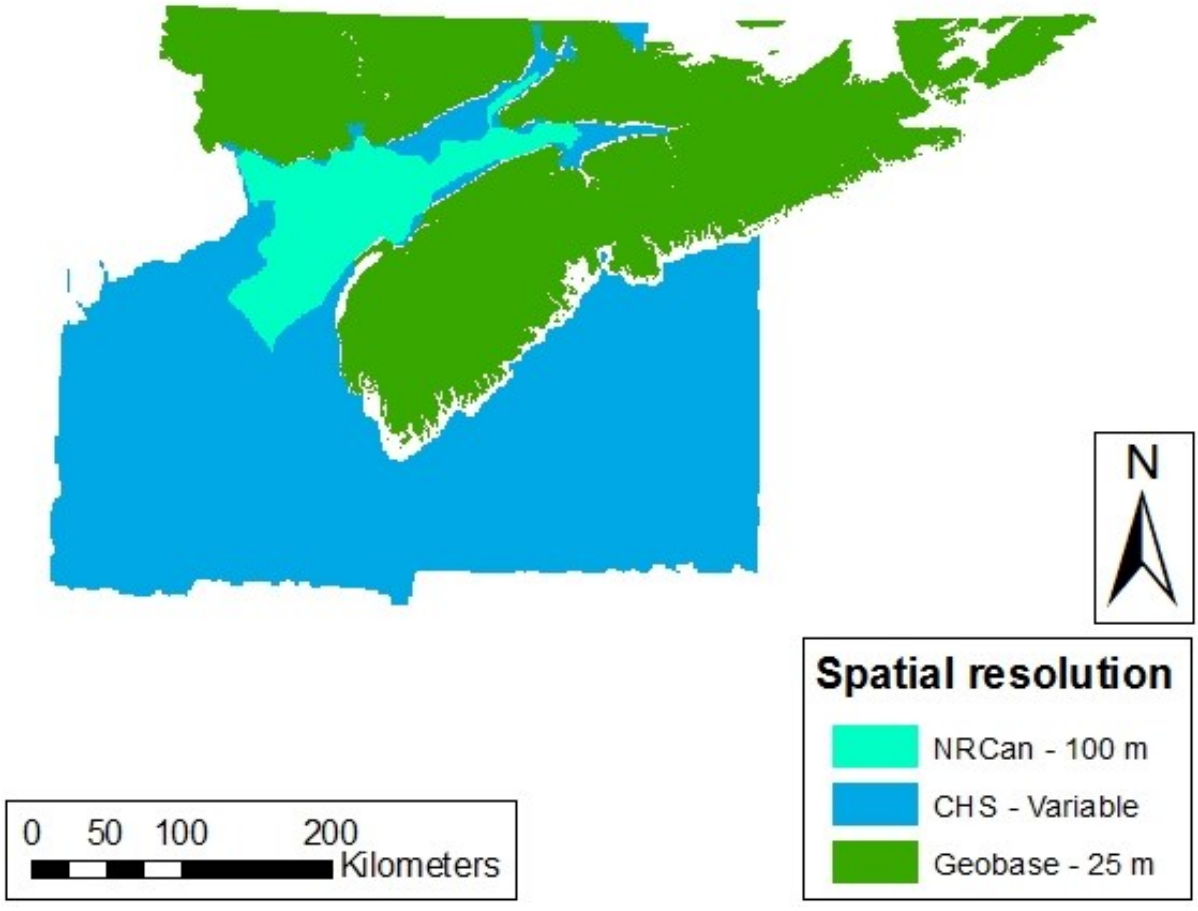

Figure 5.4. DEM data sources (Cousineau 2012)

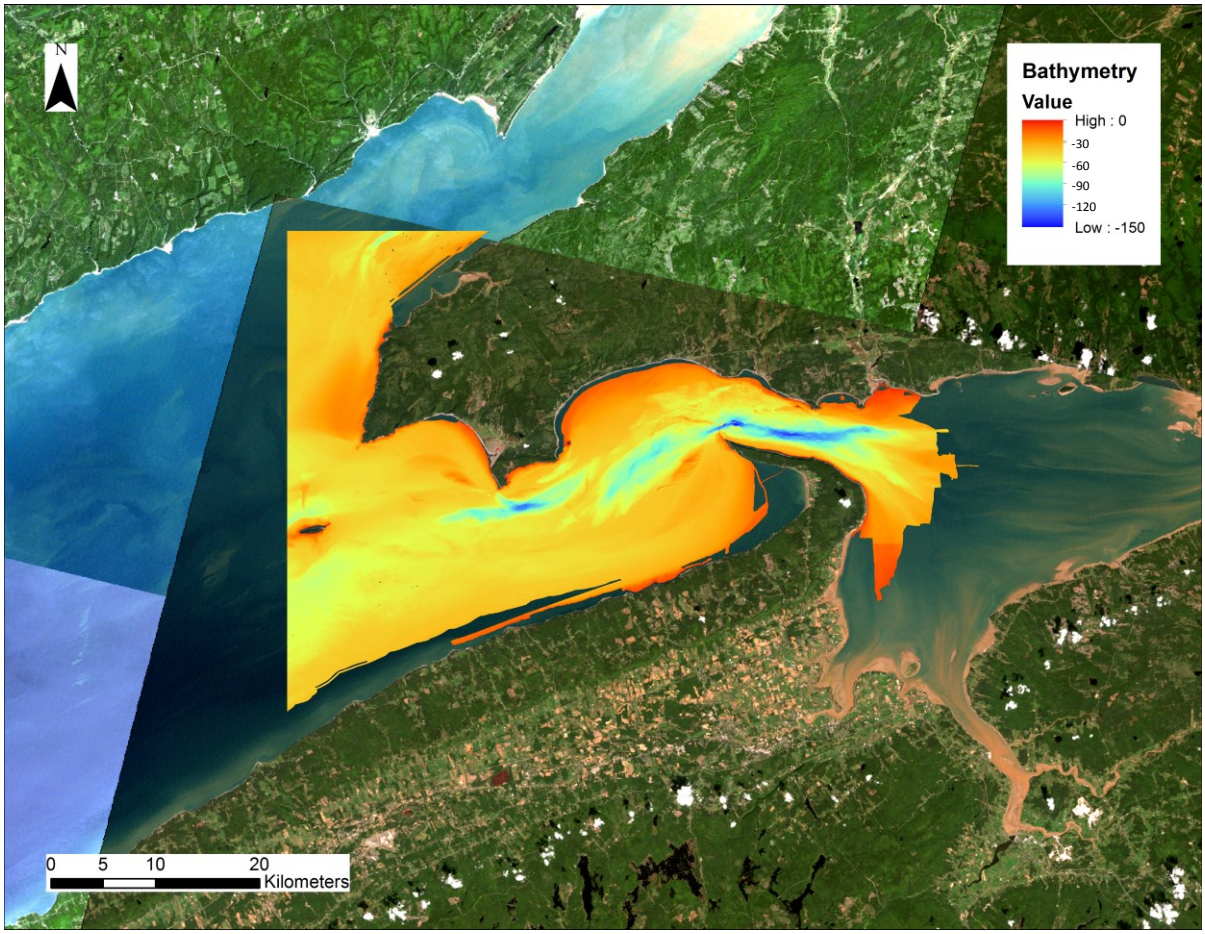

Figure 5.5. Minas Channel 5 m bathymetry survey

5.1.7. Boundary conditions

The model grid includes land and ocean boundaries. Freshwater inflows from rivers were presumed insignificant compared to the tidal flows and are therefore ignored. Land boundaries are considered solid boundaries where the energy flux is null. In this study, land boundaries were modelled to include tidal flats up to the Highest Astronomical tide (HAT). The HAT was calculated from a two-dimensional finite-element tidal circulation model of the upper Bay of Fundy developed by Dupont *et al.* (2005) with the help of the WebTide graphical user interface (http://www.bio.gc.ca/science/research-recherche/ocean/webtide/index-en.php).

Ocean boundaries, on the other hand, are open boundaries where the free surface elevation is specified at every time step. The ocean boundary was developed so as to draw a line between two Canadian Hydrographic Service (CHS) tidal stations: Dipper Harbour West and Deep Cove, located at the northwest and southeast ends of the boundary, respectively (Figure 5.7). Twenty of the harmonic constituents available at these stations are shown in Table 5.1. The draft standard recommends a

minimum of 4 - 8 harmonic constituents for modelling the driving boundary of a Feasibility study and 8 - 12 for Layout Design. In this study, eight leading constituents were selected for the purpose of calibration and validation (M2, N2, S2, K1, K2, NU2, O1, MU2). The modelled constituents were selected for the highest average amplitude at the open boundary. To specify the free surface elevation at each boundary node and time step, tidal height predictions are produced with T_TIDE and linearly interpolated along the ocean boundary between Dipper Harbour West and Deep Cove. An objective of the thesis is to investigate the main sources of error and uncertainty affecting resource assessment. Chapter 7 addresses the number of modelled constituents by specifying the boundary with 1 through 20 harmonics to evaluate the effect on resource assessment.

Table 5.1. CHS Tidal height constituents at Dipper Harbour West and Deep Cove

Tide	**Amplitude (m)** at Dipper Harbour West	**Amplitude (m)** at Deep Cove	**Average (m)** at ocean boundary
M2	**2.765**	**3.087**	**2.926**
N2	**0.536**	**0.568**	**0.552**
S2	**0.418**	**0.503**	**0.461**
K1	**0.159**	**0.172**	**0.166**
K2	**0.112**	**0.147**	**0.130**
NU2	**0.123**	**0.125**	**0.124**
O1	**0.112**	**0.110**	**0.111**
MU2	**0.015**	**0.144**	**0.080**
MM	0.083	0.056	0.070
P1	0.052	0.060	0.056
L2	0.053	0.034	0.044
MSF	0.040	0.033	0.037
MSN2	0.000	0.064	0.032
2N2	0.060	0.000	0.030
M6	0.023	0.032	0.028
ETA2	0.046	0.000	0.023
M4	0.038	0.006	0.022
Q1	0.020	0.023	0.022
OQ2	0.000	0.042	0.021
2SM2	0.000	0.035	0.018

5.2. Model calibration and validation

According to the IEC-TC-114 standard, model calibration is accomplished by adjusting bottom friction and turbulence parameters so that model results provide the most accurate numerical match to tidal height measurements with respect to harmonic constituents of amplitude and phase. In this study, the model was calibrated by adjusting bottom friction (*i.e.* Strickler's coefficient) in different parts of the computational domain (Figure 5.6) to minimise the error between modelled and observed tidal constituents at 15 Canadian Hydrographic Service stations (Figure 5.7). Table 5.2 shows the record length and available constituents at each station. The calibration stations were selected for their record length and available constituents, and to provide good spatial coverage of the domain. As for turbulence parameters, the model implements a constant ν_t of 0.0001. Values from 10^{-6} to 10^{0} were tried but had a negligible impact on flow statistics. A time step of 10 seconds was found to be appropriate (see Appendix C.1 for numerical parameters).

Calibration was carried out on the standard 150 m submesh in Minas Passage; for the M2 tide alone and then for all 8 included constituents together. Tides were simulated for a 127-day period so as to cover the ADCP deployments and allow for additional direct comparison. The first 24 hours of model output were discarded to allow the model to spin up. Harmonic constituents were derived from model results at each CHS station by performing a tidal analysis with T_TIDE and compared to the published values. The same set of 8 constituents (M2, N2, S2, K1, K2, NU2, O1, MU2) modelled at the open boundary are used to assess the performance of the model at the CHS locations. Constituents modelled at the boundary were sometimes unavailable at a CHS station and thus were not included in the calibration. Frequency-domain calibration is shown in Section 5.2.2 and time-domain comparisons are shown in Section 5.2.3.

According to the IEC-TC-114 standard, validation of model simulations is achieved with quantitative comparisons between the AEP computed from the stationary surveys of the measured current and from model simulations. However, additional statistical comparisons of both tidal height and current between the model output and measured field data are recommended. To maintain consistency with the calibration methodology this chapter highlights validation in terms of tidal height and currents. The Annual Energy Production is calculated and compared in Chapter 6. In this study, the model is validated by simulating the tides at the four FORCE berths for the span of the ADCP deployments. Modelled and observed tidal heights and currents were compared at every site. See Section 5.2.4 for frequency-domain and 5.2.5 for time-domain validation.

5.2.1. Friction domains

Strickler's roughness coefficient was adjusted between 20 and 40, corresponding to natural riverbeds (Arcement and Schneider 1989), in different parts of the computational domain to minimise calibration error. Initially, friction was adjusted uniformly across the domain to find an optimal value, then the Minas Passage friction domain was added and fine-tuned to produce the best results. **Figure 5.6** shows the calibrated Strickler's coefficients. While more numerous friction domains were previously defined, the simpler case of a coefficient for the Bay and another for Minas Passage was found to yield the best results.

Table 5.2. CHS boundary and calibration stations

ID	Station	Latitude (deg N)	Longitude (deg W)	Record length (days)	Available constituents
1	Saint John	45.267	66.067	365	42
2	St. Martins	45.350	65.533	29	10
3	Herring Cove	45.567	64.967	26	28
4	Cape d'Or	45.283	64.767	197	41
5	Port Greville	45.400	64.550	29	9
6	Cape Sharp	45.367	64.383	29	9
7	Parrsboro	45.367	64.333	29	9
8	Baxters Harbour	45.233	64.517	29	10
9	Ile Haute	45.250	64.967	90	27
10	Margretsville	45.050	65.067	62	27
11	Parkers Cove	44.800	65.533	218	53
12	Grindstone	45.717	64.600	87	46
13	Minas Basin	45.317	64.200	86	46
14	Economy	45.317	63.900	87	28
15	Cobequid Bay	45.367	63.733	87	46
B1	Dipper Harbour West	45.093	66.406	36	40
B2	Deep Cove	44.665	65.830	56	31

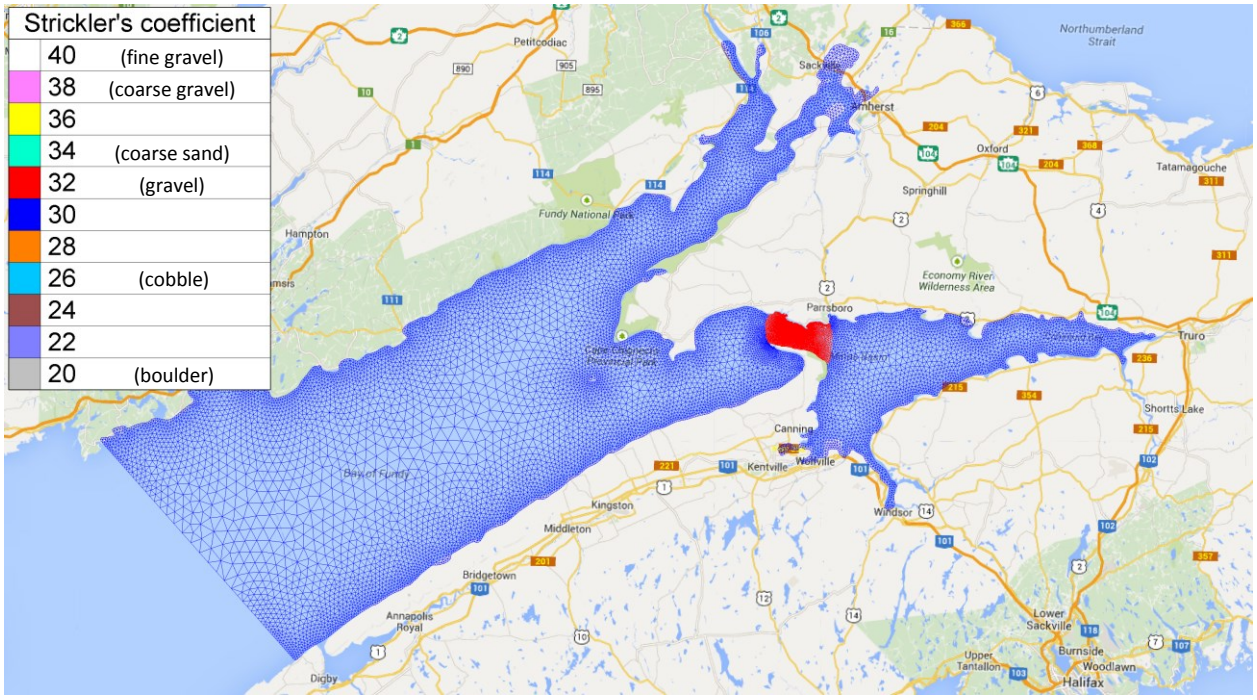

Figure 5.6. Strickler's coefficient in the computational domain

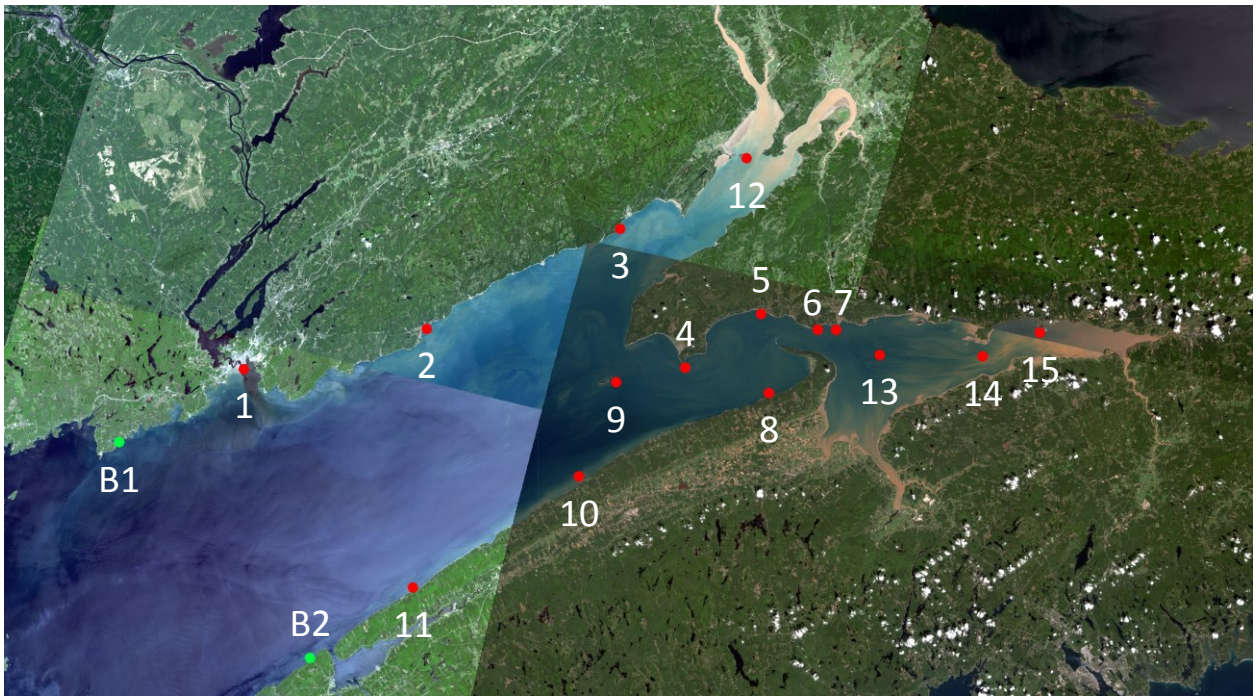

Figure 5.7. CHS boundary and calibration stations

5.2.2. Frequency-domain calibration

Table 5.3 shows the observed and modelled tidal height constituents of amplitude and phase, and discrepancies for the M2 tide at the 15 CHS stations. The *root-mean-square error* (RMSE) was calculated by:

$$\mathrm{RMSE} = \sqrt{\frac{1}{n}\sum_{i=1}^{n}(Y_i - X_i)^2} \tag{5.24}$$

where Y and X are the observed and modelled values, respectively. Table 5.4 and Table 5.5 compare observed and modelled amplitudes and phases for the next two leading constituents, N2 and S2, respectively. Figure 5.8 shows a scatterplot of observed and modelled amplitude and phase for the available constituents at Parrsboro, near the FORCE project site. The model predictions generally agree well with observations.

Table 5.3. Observed and modelled tidal height harmonics of amplitude (m) and phase (°) for M2 at CHS stations

Location	Observed		Modelled		Difference	
	Amp.	Phase	Amp.	Phase	Amp.	Phase
Saint John	3.014	98	3.138	98	-0.12	0.3
St. Martins	3.685	102	3.750	101	-0.06	0.3
Herring Cove	4.064	104	4.284	104	-0.22	-0.4
Cape d'Or	4.340	102	4.357	105	-0.02	-2.9
Port Greville	4.605	112	4.673	110	-0.07	1.6
Cape Sharp	4.803	121	4.974	117	-0.17	4.0
Parrsboro	5.050	121	5.083	117	-0.03	3.7
Baxters Harbour	4.615	103	4.629	105	-0.01	-2.3
Ile Haute	4.152	99	4.150	101	0.00	-1.7
Margretsville	3.864	93	3.972	96	-0.11	-2.9
Parkers Cove	3.434	90	3.405	90	0.03	-0.4
Grindstone	4.859	104	4.635	109	0.22	-4.4
Minas Basin	5.535	121	5.264	119	0.27	1.4
Economy	5.923	125	5.487	131	0.44	-5.4
Cobequid Bay	6.119	129	5.503	139	0.62	-9.4
				RMSE	**0.23**	**3.6**

Table 5.4. Observed and modelled tidal height harmonics of amplitude (m) and phase (°) for N2 at CHS stations

Location	Observations		Model		Difference	
	Amp.	Phase	Amp.	Phase	Amp.	Phase
Saint John	0.596	68	0.580	65	0.02	2.2
St. Martins	0.903	68	0.804	75	0.10	-6.5
Herring Cove	0.813	48	0.923	77	-0.11	-29.0
Cape d'Or	0.910	73	0.774	76	0.14	-2.6
Port Greville	0.862	78	0.978	87	-0.12	-9.6
Cape Sharp	0.905	99	1.036	96	-0.13	3.3
Parrsboro	0.847	91	1.059	96	-0.21	-5.4
Baxters Harbour	1.028	67	0.975	82	0.05	-14.8
Ile Haute	0.744	61	0.894	73	-0.15	-12.3
Margretsville	1.069	60	0.851	70	0.22	-10.2
Parkers Cove	0.658	61	0.624	60	0.03	1.2
Grindstone	0.897	76	0.824	81	0.07	-5.7
Minas Basin	0.977	95	0.916	95	0.06	0.0
Economy	1.006	91	1.126	109	-0.12	-18.6
Cobequid Bay	1.062	105	0.937	120	0.13	-14.8
				RMSE	**0.12**	**11.8**

Table 5.5. Observed and modelled tidal height harmonics of amplitude (m) and phase (°) for S2 at CHS stations

Location	Observations		Model		Difference	
	Amp.	Phase	Amp.	Phase	Amp.	Phase
Saint John	0.485	138	0.499	140	-0.01	-2.5
St. Martins	0.585	148	0.631	145	-0.05	2.7
Herring Cove	0.593	149	0.723	151	-0.13	-2.7
Cape d'Or	0.683	142	0.696	148	-0.01	-6.2
Port Greville	0.688	157	0.804	161	-0.12	-4.3
Cape Sharp	0.722	176	0.872	171	-0.15	4.7
Parrsboro	0.752	169	0.895	172	-0.14	-2.7
Baxters Harbour	0.729	151	0.798	155	-0.07	-3.6
Ile Haute	0.530	146	0.772	136	-0.24	10.1
Margretsville	0.417	143	0.658	139	-0.24	3.9
Parkers Cove	0.516	129	0.549	132	-0.03	-3.3
Grindstone	0.712	152	0.750	155	-0.04	-3.4
Minas Basin	0.778	175	0.839	170	-0.06	4.8
Economy	0.729	179	0.996	174	-0.27	4.8
Cobequid Bay	0.861	187	0.861	195	0.00	-8.2
				RMSE	**0.14**	**5.0**

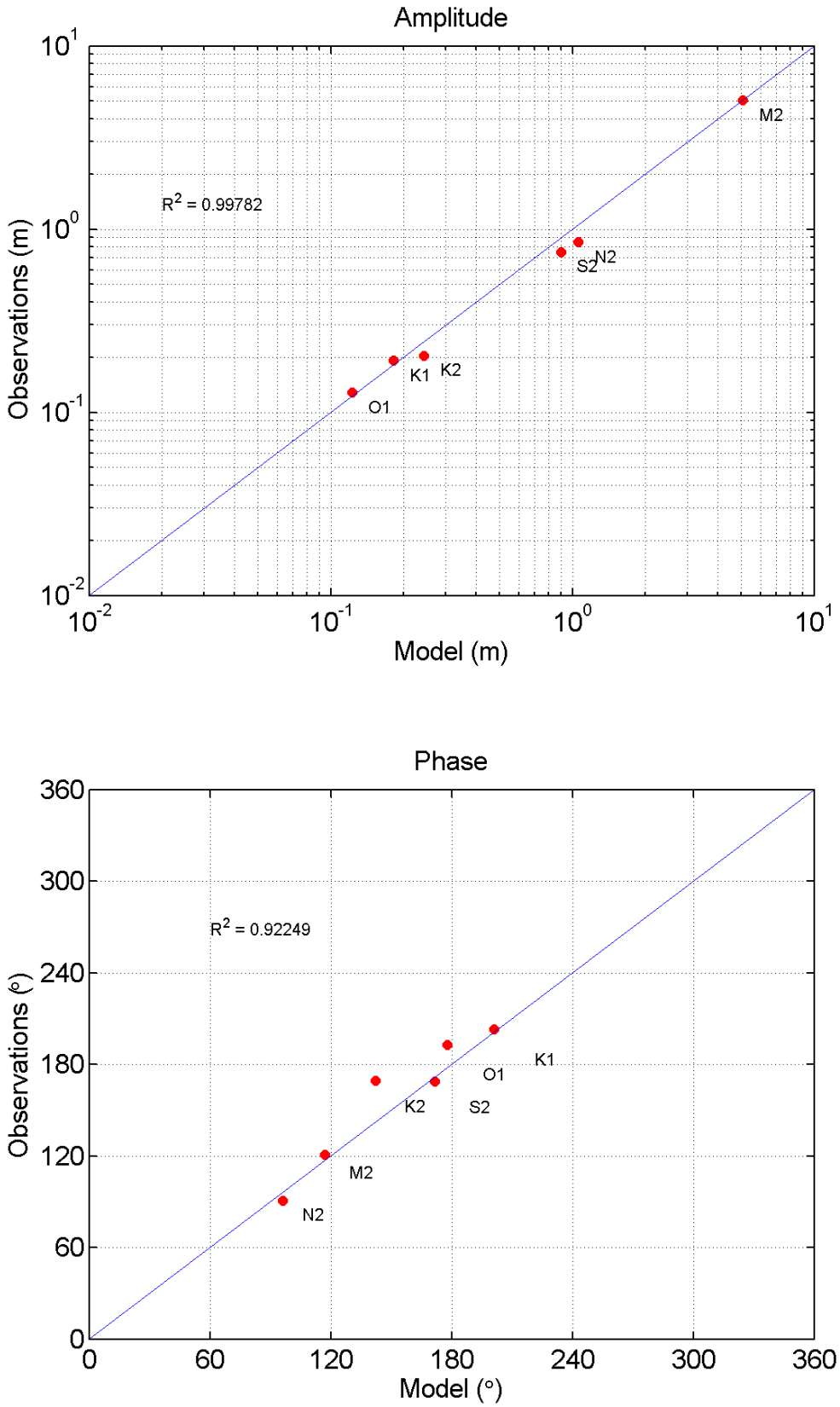

Figure 5.8. Scatterplot of the observed and modelled amplitude and phase at Parrsboro

5.2.3. Time-domain calibration

Figure 5.9 shows observed and modelled tidal height for the calibration period at the stations nearest to the FORCE project site. Only the last 7 days of simulation are shown for clarity. Table 5.6 shows the relative error and the phase difference (in minutes) of high and low tides at 15 CHS stations. The published constituents at each station were used to forecast tidal height for the calibration period with T_TIDE. Afterward the modelled high and low tides were compared with the predictions. The observed and modelled time-histories were restricted to 5 and 15 minute output time steps, respectively, therefore a second degree polynomial was fit to the data to calculate the height and timing of high or low water for an adequate comparison. The *relative error* was calculated by:

$$e = \frac{X - Y}{Y} \tag{5.25}$$

where Y and X are the observed and modelled values, respectively. There is generally good agreement between model predictions and Canadian Hydrographic Service projections.

Table 5.6. Relative error and phase difference of high and low tides at the CHS stations

Location	High tides		Low tides	
	RMS Relative error (%)	**RMS Phase difference (min)**	**RMS Relative error (%)**	**RMS Phase difference (min)**
Saint John	7.7	12	6.0	10
St. Martins	5.2	6	4.8	6
Herring Cove	10.3	12	11.5	12
Cape d'Or	6.1	16	5.3	12
Port Greville	5.1	6	5.1	12
Cape Sharp	5.5	8	10.4	15
Parrsboro	3.6	12	7.1	12
Baxters Harbour	5.2	9	5.2	9
Ile Haute	10.7	14	8.8	13
Margretsville	6.3	21	7.1	21
Parkers Cove	5.0	9	4.9	7
Grindstone	9.1	12	6.6	10
Minas Basin	9.4	12	7.7	11
Economy	11.0	15	9.7	25
Cobequid Bay	8.4	27	11.1	42
Average	**7.3**	**13**	**7.4**	**14**

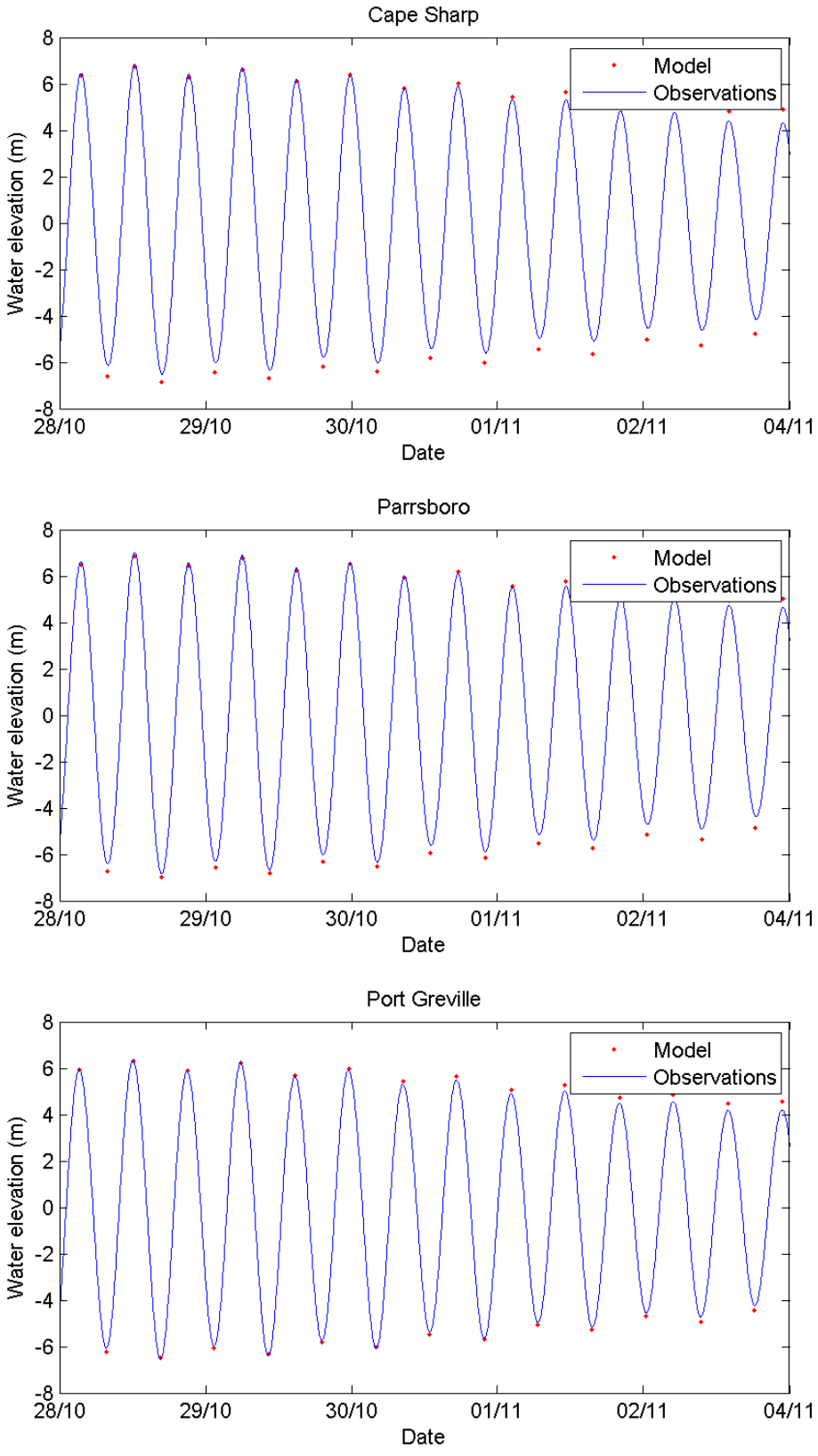

Figure 5.9. Observed and modelled tidal height at Cape Sharp, Parrsboro, and Port Greville

5.2.4. Frequency-domain validation

Table 5.7 shows the observed and modelled tidal height constituents of amplitude and phase, and discrepancies for the M2 tide at the four FORCE berths. Table 5.8 and 5.9 compare observed and modelled amplitudes and phases for the next two leading constituents, N2 and S2, respectively. Agreement between model predictions and observations is quite good particularly for the M2 tide. Figure 5.10 shows a scatterplot of observed and modelled amplitude and phase for the available constituents at Site C.

Table 5.7. Observed and modelled tidal height harmonics of amplitude (m) and phase (°) for M2 at FORCE berths

Site	Observed		Modelled		Difference	
	Amp.	Phase	Amp.	Phase	Amp.	Phase
A	4.877	115	4.854	114	0.02	0.5
B	4.818	116	4.842	114	-0.02	1.8
C	4.913	116	4.858	115	0.05	1.0
D	4.833	118	4.862	115	-0.03	2.6
				RMSE	**0.04**	**1.7**

Table 5.8. Observed and modelled tidal height harmonics of amplitude (m) and phase (°) for N2 at FORCE berths

Site	Observed		Modelled		Difference	
	Amp.	Phase	Amp.	Phase	Amp.	Phase
A	-	-	1.018	89	-	-
B	1.176	92	1.016	89	0.16	3.1
C	1.040	81	1.018	90	0.02	-9.4
D	1.173	95	1.019	90	0.15	4.4
				RMSE	**0.13**	**6.2**

Table 5.9. Observed and modelled tidal height harmonics of amplitude (m) and phase (°) for S2 at FORCE berths

Site	Observed		Modelled		Difference	
	Amp.	Phase	Amp.	Phase	Amp.	Phase
A	0.579	172	0.887	153	-0.31	19.0
B	0.838	149	0.884	153	-0.05	-3.5
C	0.736	151	0.887	153	-0.15	-2.1
D	0.812	152	0.887	154	-0.08	-1.6
				RMSE	**0.18**	**9.7**

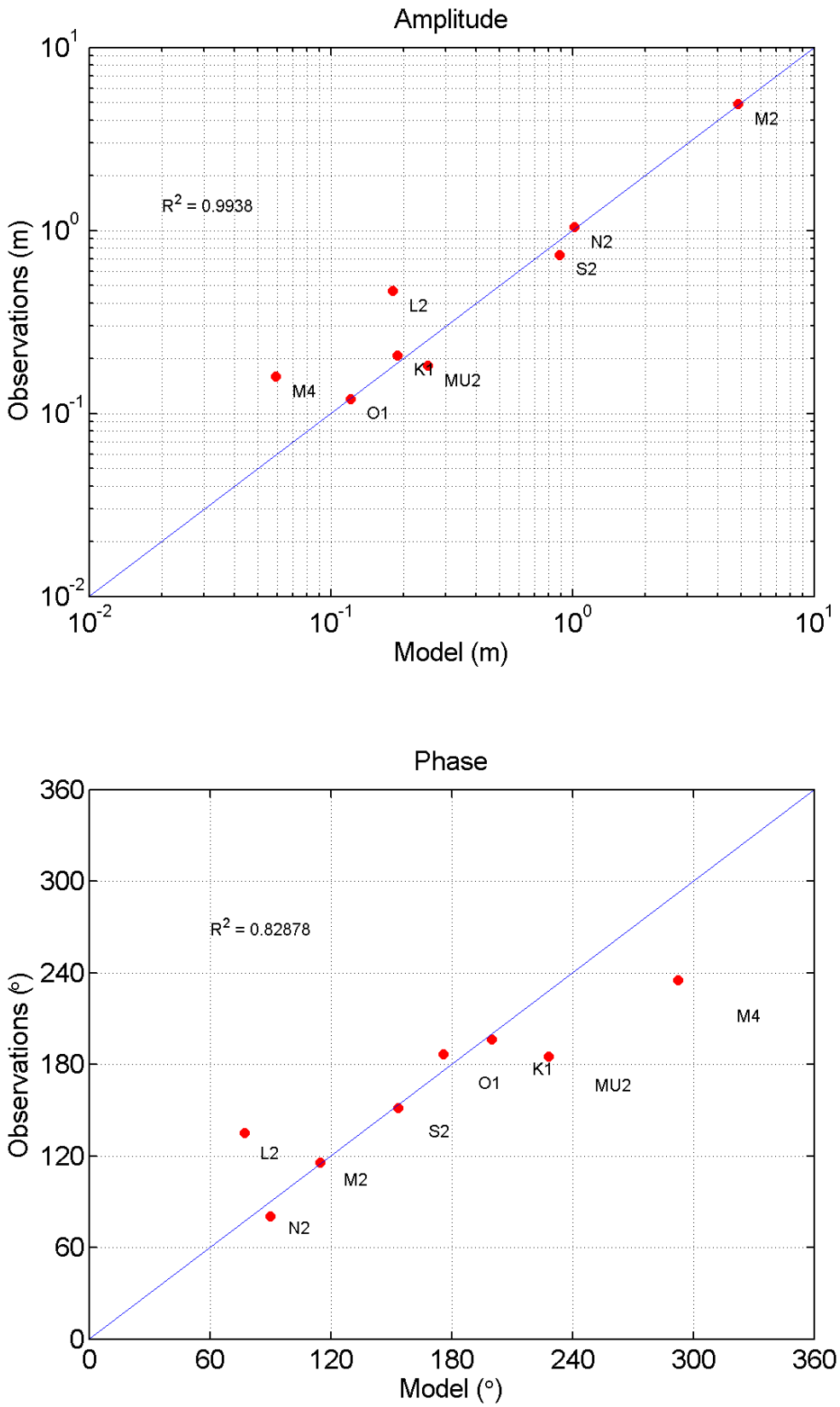

Figure 5.10. Scatterplot of the observed and modelled amplitude and phase at Site C

5.2.5. Time-domain validation

Table 5.10 shows the relative error and the phase difference (in minutes) of high and low tides at the four FORCE berths, similar to Section 5.2.3. Thanks to the ADCP surveys, it's possible to directly compare observed and modelled time-histories at these sites. Table 5.11 shows a statistical comparison of time-histories at the four FORCE berths for the survey periods.

Table 5.10. Relative error and phase difference of high and low tides at the FORCE berths

Site	High tide		Low tide	
	RMS Relative error (%)	RMS Phase difference (min)	RMS Relative error (%)	RMS Phase difference (min)
A	13.0	24	16.3	24
B	6.7	12	5.5	11
C	8.2	13	5.9	19
D	7.1	11	6.2	12
Average	**8.7**	**15**	**8.5**	**17**

Table 5.11. Statistical comparison of observed and modelled parameters at the FORCE berths

Parameter	Site	RMSE	RMAE	SI	Bias	R^2
Tidal height	A	0.349 m	0.106	0.112	0.144 m	0.990
	B	0.396 m	0.099	0.118	0.096 m	0.989
	C	0.380 m	0.099	0.114	0.112 m	0.990
	D	0.435 m	0.109	0.125	0.145 m	0.988
	F	-	-	-	-	-
East-west velocity	A	0.397 m/s	0.188	0.215	0.168 m/s	0.984
	B	0.341 m/s	0.164	0.197	0.038 m/s	0.984
	C	0.244 m/s	0.153	0.188	0.025 m/s	0.973
	D	0.485 m/s	0.208	0.243	0.168 m/s	0.980
	F	0.261 m/s	0.119	0.149	0.070 m/s	0.984
North-south velocity	A	0.187 m/s	0.196	0.239	-0.028 m/s	0.970
	B	0.290 m/s	0.846	0.936	0.061 m/s	0.938
	C	0.320 m/s	0.340	0.391	-0.088 m/s	0.958
	D	0.205 m/s	0.174	0.213	-0.059 m/s	0.969
	F	0.122 m/s	0.190	0.220	0.047 m/s	0.963
Tidal current speed	A	0.421 m/s	0.179	0.175	0.269 m/s	0.911
	B	0.283 m/s	0.129	0.140	0.142 m/s	0.929
	C	0.267 m/s	0.142	0.172	0.051 m/s	0.892
	D	0.499 m/s	0.188	0.178	0.331 m/s	0.897
	F	0.251 m/s	0.109	0.123	0.122 m/s	0.912

Here the *relative mean absolute error* (RMAE), *scatter index* (SI) and *bias* are calculated as follows:

$$\mathrm{RMAE} = \frac{\frac{1}{n}\sum_{i=1}^{n}|Y_i - X_i|}{\frac{1}{n}\sum_{i=1}^{n} X_i} \tag{5.26}$$

$$\mathrm{SI} = \frac{\frac{1}{n}\sqrt{\sum_{i=1}^{n}(E_i - \bar{E})^2}}{\frac{1}{n}\sum_{i=1}^{n} X_i} \tag{5.27}$$

$$\mathrm{Bias} = \frac{1}{n}\sum_{i=1}^{n} X_i - \frac{1}{n}\sum_{i=1}^{n} Y_i \tag{5.28}$$

where Y and X are the observed and modelled values, respectively, and $E_i = X_i - Y_i$ is the difference between the modelled and observed values. The following pages show 7-day plots of tidal height and tidal currents and a tidal ellipse of observed and modelled velocities during the ADCP deployment periods at Sites A, B, C, D and F.

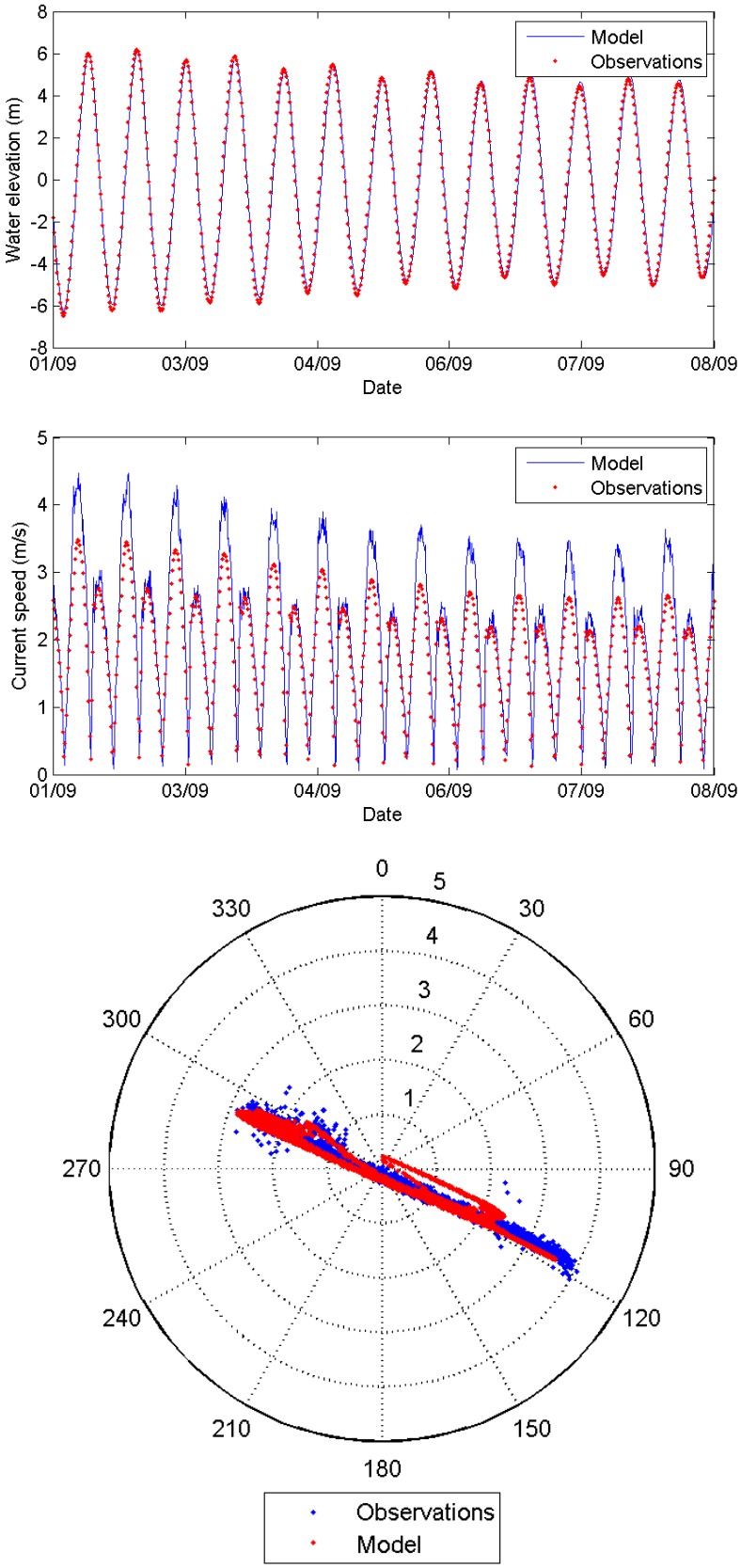

Figure 5.11. Tidal height, currents, and tidal ellipse at Site A

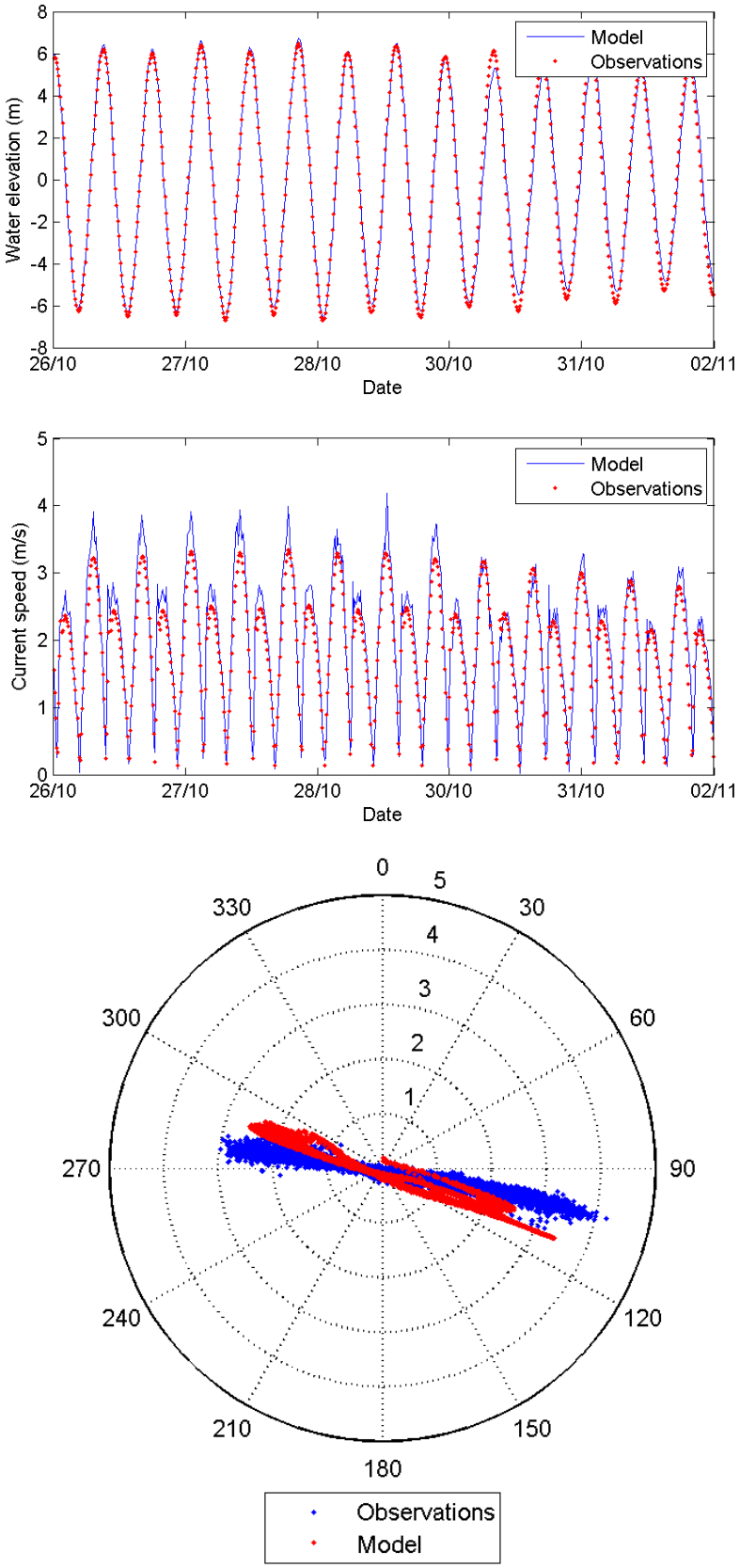

Figure 5.12. Tidal height, currents, and tidal ellipse at Site B

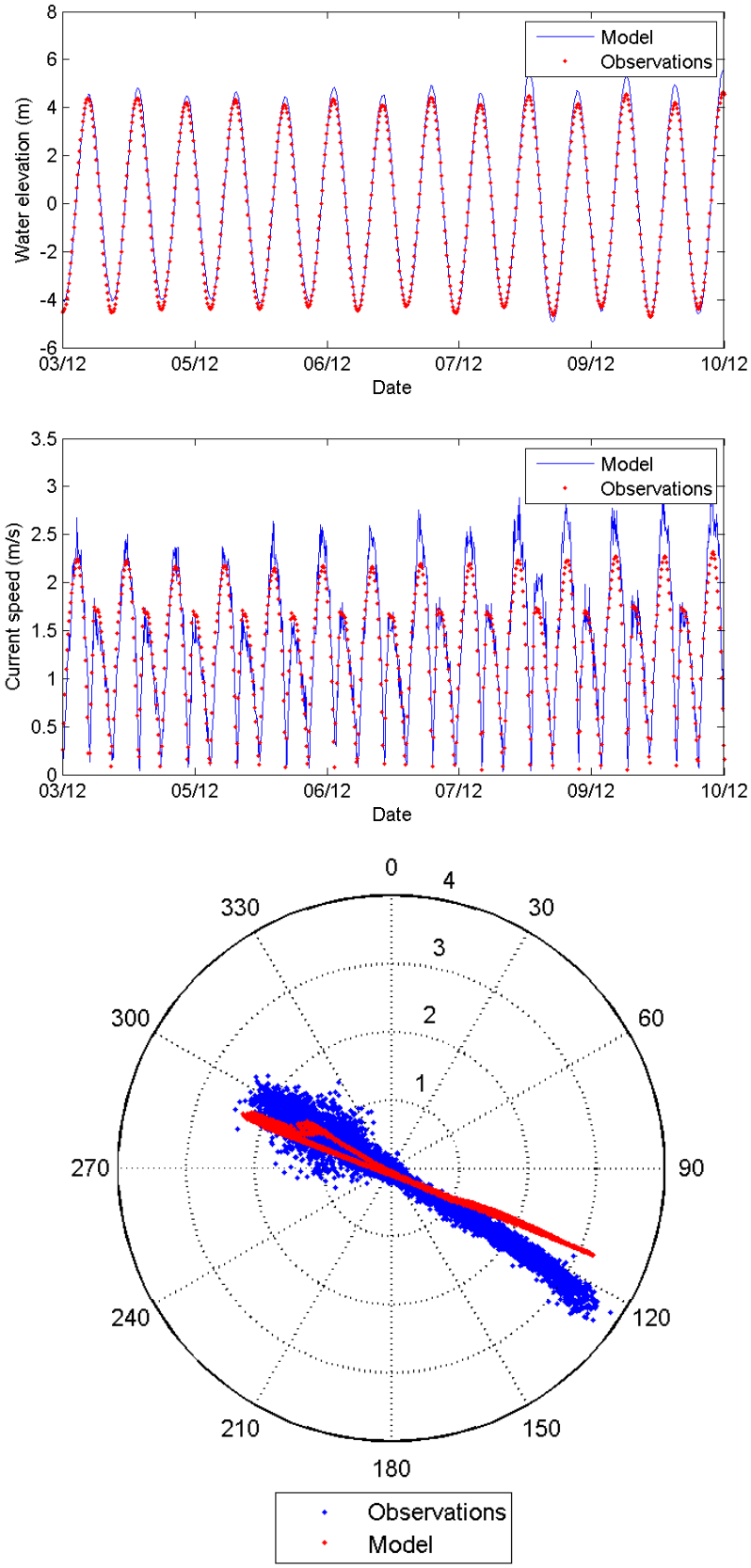

Figure 5.13. Tidal height, currents, and tidal ellipse at Site C

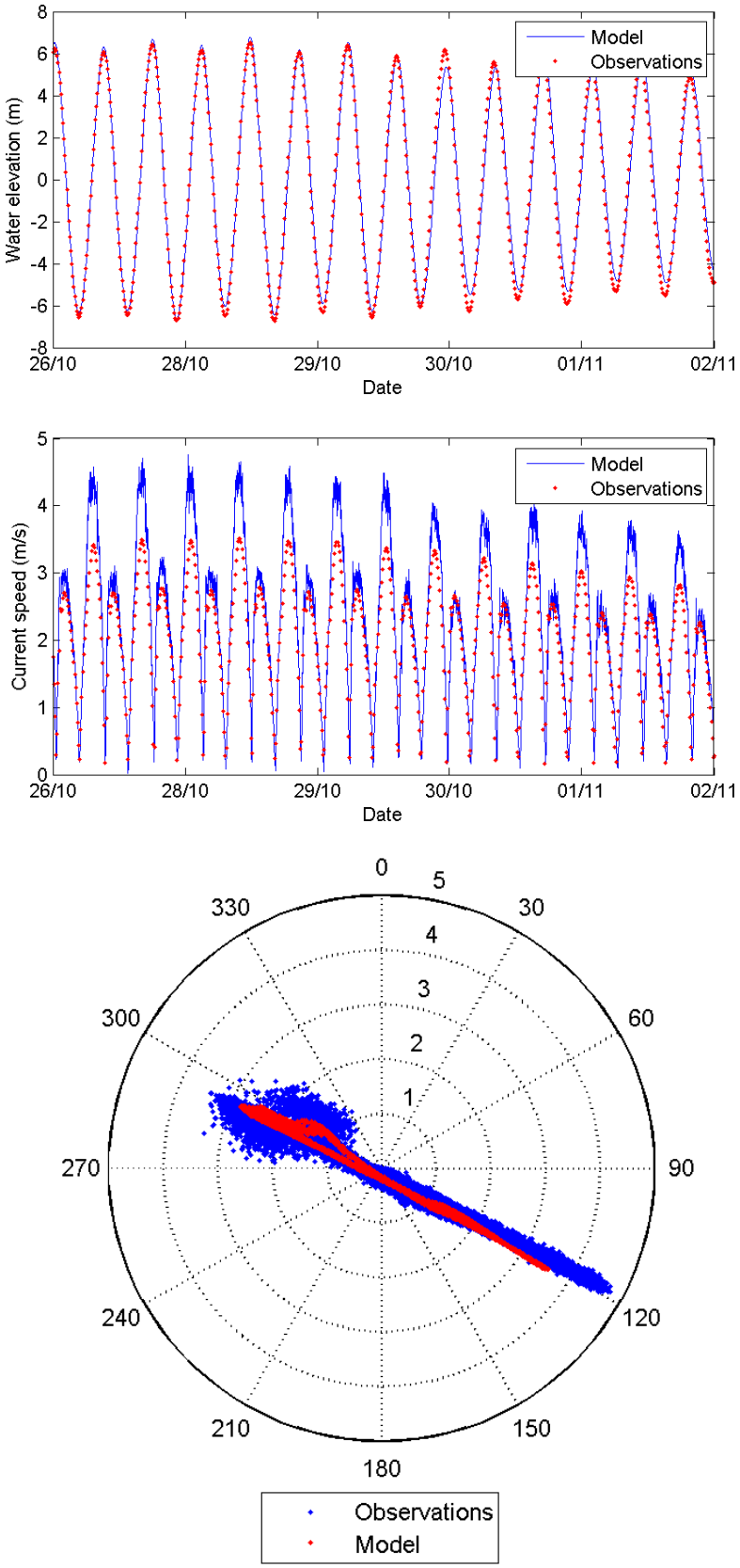

Figure 5.14. Tidal height, currents, and tidal ellipse at Site D

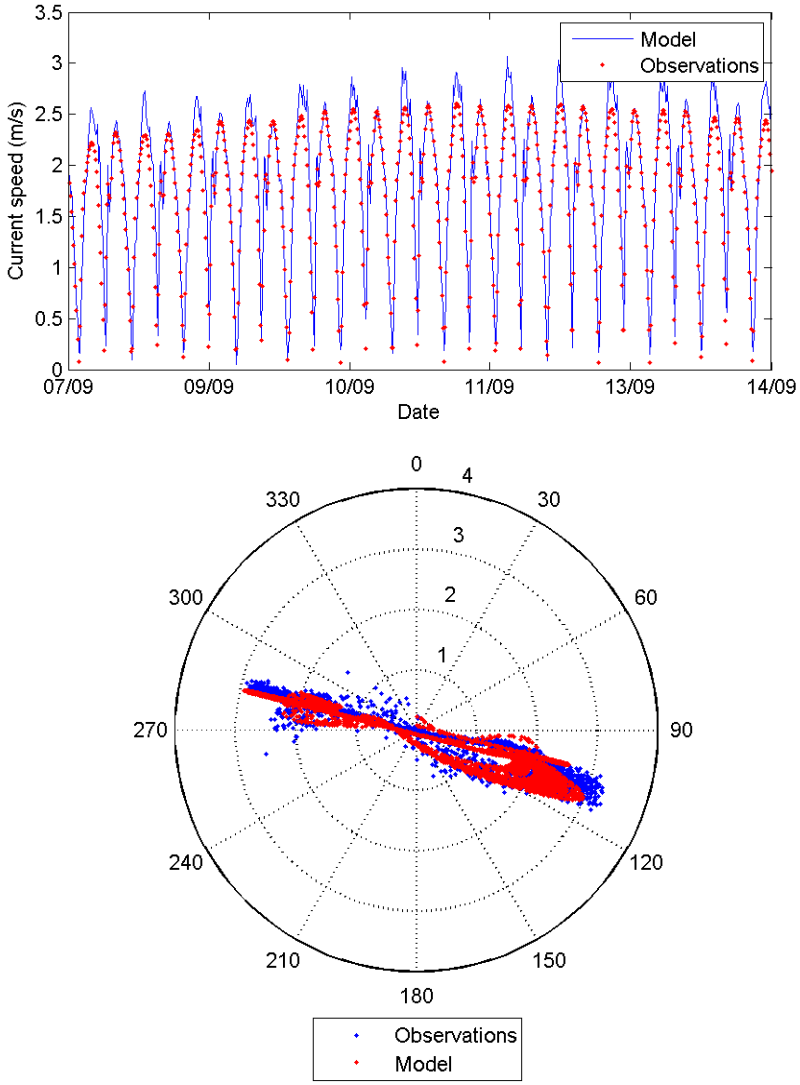

Figure 5.15. Tidal currents and tidal ellipse at Site F

5.3. Flow structures

A number of the flow structures described in Chapter 4 can be observed in the model predictions. For example, the pulse in flow at the beginning of ebb tide is captured at all four sites (Figure 5.16 and Figure 5.17). The eddies off of Cape Split and Cape Sharp, with the resulting tidal asymmetry, are illustrated as well (Figure 5.18).

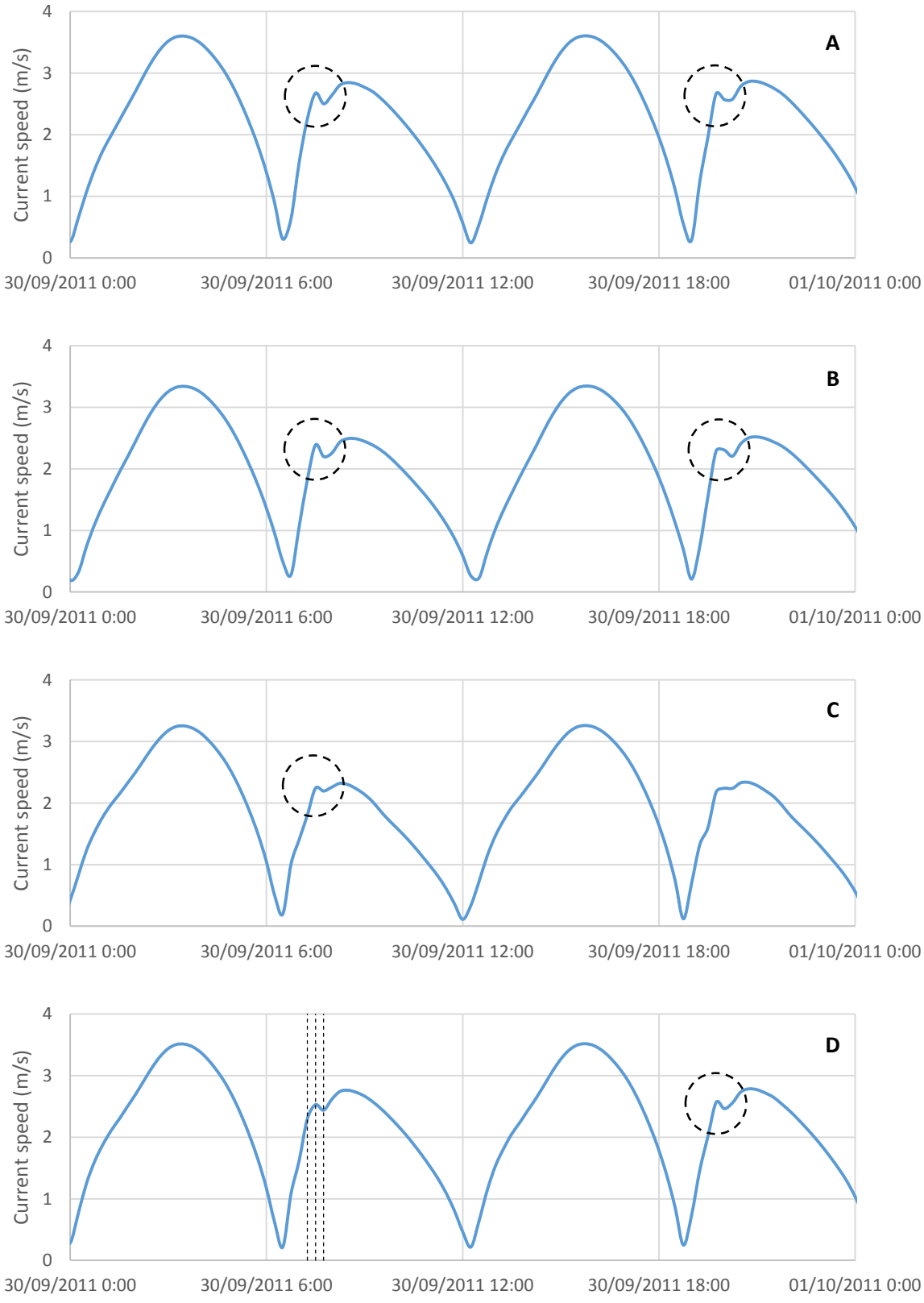

Figure 5.16. Modelled pulse at the beginning of ebb. The lines correspond to the snapshots in the following figure.

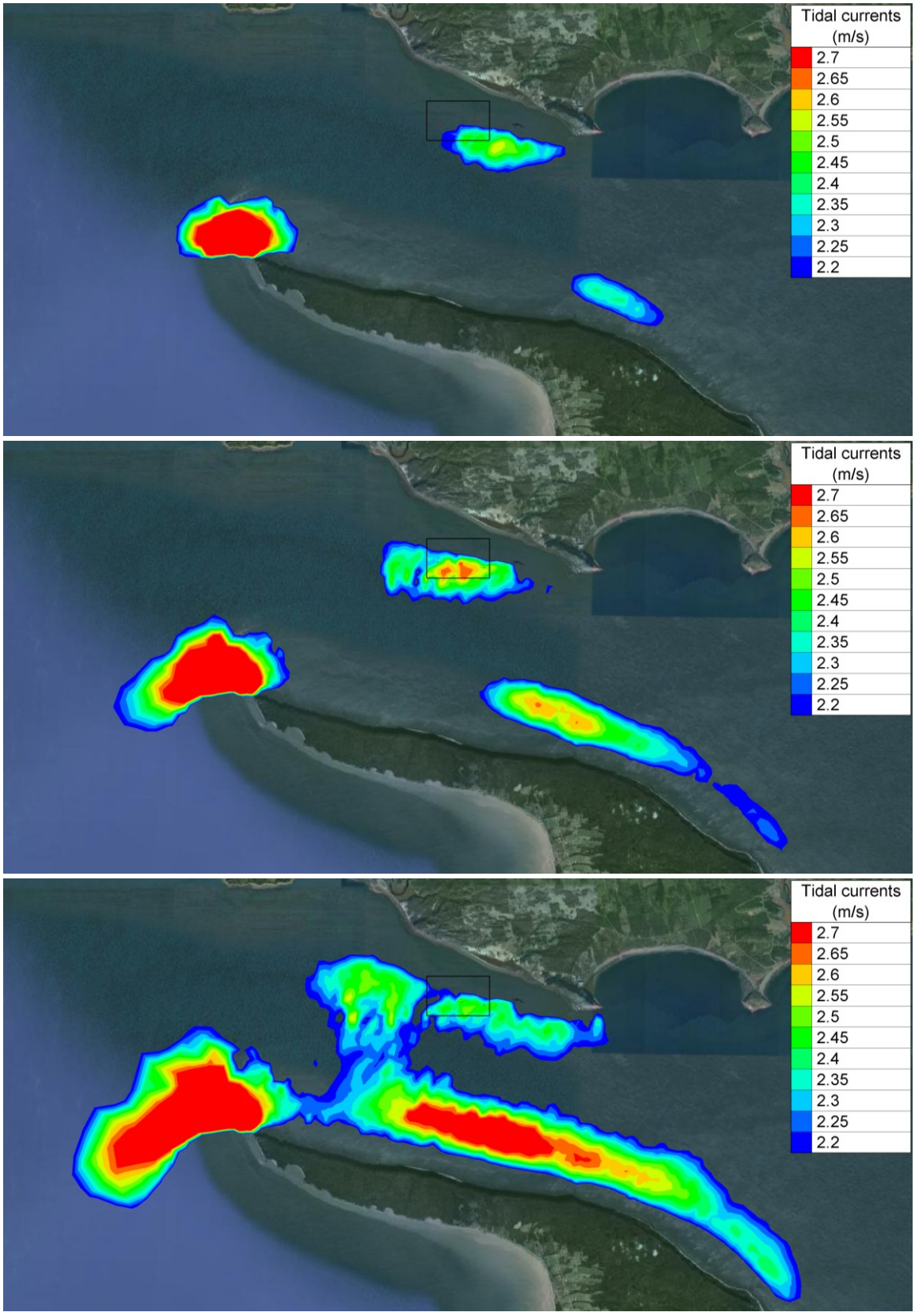

Figure 5.17. Modelled pulse at the beginning of ebb at 7:15, 7:30 and 7:45 AM on 30/09/2011

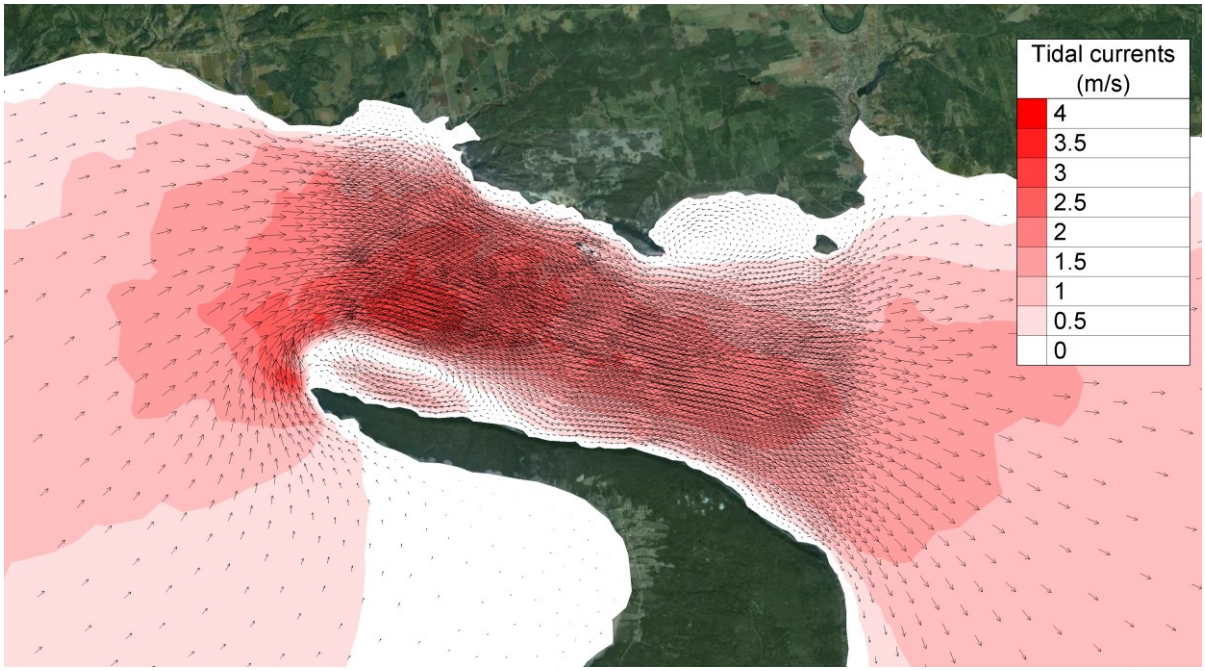

Figure 5.18. Modelled eddies off Cape Split and Cape Sharp

5.4. Harmonic analysis

The harmonic constituents are obtained by simulating a minimum of 35 days (see Appendix C.2) and conducting a tidal analysis with T_TIDE. Tables 5.12 and 5.13 show the ten most important tidal constituents for east-west and north-south velocity, respectively.

Table 5.12. East-west tidal current harmonics of amplitude (m) and phase (°) (modelled)

Tide	Site A		Site B		Site C		Site D	
	Amp.	Phase	Amp.	Phase	Amp.	Phase	Amp.	Phase
M2	2.344	33	2.170	36	2.026	27	2.208	30
N2	0.414	24	0.441	14	0.366	356	0.449	10
S2	0.457	92	0.407	78	0.274	68	0.413	73
M4	0.216	166	0.202	158	0.243	152	0.195	160
M6	0.158	301	0.127	313	0.150	292	0.148	288
MU2	0.134	128	0.132	142	0.121	138	0.145	133
L2	0.118	340	0.123	355	0.120	1	0.143	347
MN4	0.069	152	0.075	131	0.085	108	0.072	131
2MN6	0.085	298	0.078	295	0.065	251	0.092	272
MS4	0.073	221	0.066	199	0.061	188	0.064	200

Table 5.13. North-south tidal current harmonics of amplitude (m) and phase (°) (modelled)

Tide	Site A		Site B		Site C		Site D	
	Amp.	Phase	Amp.	Phase	Amp.	Phase	Amp.	Phase
M2	1.069	211	0.778	216	0.804	205	1.164	208
N2	0.187	202	0.156	194	0.144	174	0.236	188
S2	0.206	270	0.144	257	0.108	247	0.218	252
M4	0.168	339	0.139	336	0.135	327	0.152	328
M6	0.077	127	0.057	157	0.071	106	0.087	106
MU2	0.064	306	0.048	323	0.049	316	0.077	311
L2	0.057	160	0.044	178	0.050	179	0.077	165
MN4	0.049	328	0.048	312	0.044	282	0.052	303
2MN6	0.041	122	0.033	138	0.031	65	0.054	90
MS4	0.053	35	0.043	19	0.033	3	0.047	10

5.5. Discussion

According to the IEC-TC-114 standard, for projects over 10 MW the tidal energy resource is calculated using a hydrodynamic model validated against measured data. In keeping with the objectives of the project, Chapter 5 presented the development of a two-dimensional hydrodynamic model of the upper Bay of Fundy. Ultimately, the objective of Chapter 5 was to obtain the simulated tidal current constituents at the FORCE berths in order to proceed to the long-term current predictions and resource assessment in Chapter 6.

The ‘standard’ model for the purpose of calibration and validation includes Strickler’s law for the bottom shear stress, wetting and drying of tidal flats, a constant viscosity turbulence model, and Coriolis forcing. The model grid was developed with 500 m resolution at the shoreline, except for Minas Passage where elements were refined to 150 m. The elevation of each node in Minas Passage was interpolated from a 5 m grid of the Minas Channel prepared by Natural Resources Canada. The ocean boundary was modelled using eight leading tidal constituents from two Canadian Hydrographic Service posts at either end of the boundary: Dipper Harbour West and Deep Cove. The sensitivity of resource assessment to these parameters is evaluated in Chapter 7.

Model calibration was achieved by adjusting Strickler’s roughness coefficient in different parts of the computational domain to minimise the error between observed and modelled tidal height harmonics at 15 CHS posts. The model-predicted M2, N2 and S2 harmonics and corresponding errors are shown

in Tables 5.3, 5.4 and 5.5, respectively. The root-mean-square error for M2, N2 and S2 were 23, 12 and 14 cm in amplitude and 3.6, 11.8 and 5.0° in phase, respectively. At Cape Sharp, Parrsboro and Port Greville, the three CHS stations nearest to the Crown Lease Area, the model achieves a mean error of 9 cm in amplitude and 3° in phase for M2.

The errors are mostly small but reach a maximum in the upper reaches of the Bay, in Minas Basin, Cumberland Basin and Shepody Bay. The reason for these inaccuracies may be model grid discretisation: the grid was developed according to standard guidelines with a relatively coarse 500 m resolution at the shoreline except in Minas Passage, the area of interest. On the other hand, difficulties with modelling tidal circulation in Minas Basin are common. In Section 4.1.1 a number of hydrodynamic models of the Bay of Fundy were reviewed. Sankaranarayanan and McCay (2003) achieved errors < 20 cm in amplitude and 7° in phase for M2, except in the upper Bay where errors increased to 30 - 50 cm. Similarly, the errors for N2 were 10 - 30 cm in amplitude and as large as 20 degrees in phase for Minas Basin. Even the numerical model by Dupont *et al.* (2005), which included high resolution representation of the extensive tidal flats in Minas Basin only achieved RMSE of < 30 cm in amplitude for M2. The total water level in Minas Basin was replicated with a RMSE of 30 - 50 cm. In view of these results, the calibration of the model seems quite acceptable. The largest errors are seen in Minas Basin while tidal heights in Minas Passage, the area of interest, are well simulated.

Additional comparisons of the time series are shown in Section 5.2.3. The model simulated high water with a RMS relative error of 7.3% and a RMS phase difference of 13 minutes, and low water with a RMS relative error of 7.4% and RMS phase error of 14 minutes. At Cape Sharp, Parrsboro and Port Greville, the model achieves an average RMS relative error of 4.7 and 7.5% in tidal height and an average RMS phase error of 8.7 and 13 minutes at high and low tide, respectively.

There are many sources of error that contribute to these differences. First and foremost, in comparing the modelled time series to the CHS predictions, all of the available constituents at the tidal station were used to generate the prediction. There will inevitably be intricacies to the tidal signal that the hydrodynamic model, driven with only eight constituents, cannot replicate. Secondly, the open boundary is driven with published constituents at Dipper Harbour West and Deep Cove based on 36 and 56 day records, respectively. The constituents themselves may be inaccurate to some degree, but more importantly the water elevation along the boundary between the two stations was interpolated linearly, which is likely inaccurate. Freshwater inflows from rivers were presumed

insignificant compared to the tidal flows and were thus ignored. That assumption seems to be valid, considering the small calibration error seen at the Saint John CHS post. There was also considerable simplification of the shorelines, particularly in the upper Bay, *i.e.* Minas Basin, Cumberland Basin and Shepody Bay, due to the coarse resolution developed there. The same sources of error are applicable in the case of validation, with additional emphasis placed on the reliability (or lack thereof) of the current profiler measurements.

Model validation is achieved with quantitative comparisons between the Annual Energy Production computed from the static current profiler surveys and from model simulations. However, additional comparisons of both tidal height and currents are recommended. To maintain consistency with the calibration procedure, this chapter highlights validation in terms of tidal height and currents. Annual Energy Production is calculated and compared in Chapter 6. Simulated tidal heights and currents are compared to observations at the four FORCE berths for the span of the static current profiler surveys.

Observed and modelled constituents of tidal height were compared at the project site. Table 5.7 shows the model-predicted harmonics and corresponding errors at Sites A, B, C and D. Tables 5.8 and 5.9 show the results for the next two leading harmonics, N2 and S2. The model-predicted M2 agrees quite well with the measurements: the root-mean-square error is 4 cm in amplitude and 1.7° in phase. For N2 and S2, the RMS errors are 13 and 18 cm in amplitude and 6.2 and 9.7° in phase, respectively. Readers should take note that the N2 constituent could not be resolved at Site A with only 20 days of useable data. By the same token, notice that the model overpredicts S2 by 31 cm and 19° at Site A – the largest error by a considerable margin. In fact, these errors may not reflect modelling error but rather the limitations of harmonic analysis with poor quality data and a short record length. In recent tidal current energy resource assessments (see Section 3.3, Table 3.2), the average reported RMSE in M2 and S2 were 8 and 5 cm in amplitude and 5 and 6° in phase, respectively. In view of these results, the modelled harmonics at the project site are excellent.

Additional comparisons of the time series are shown in Section 5.2.5. The model simulated high water with a RMS relative error of 8.7% and a RMS phase difference of 15 minutes, and low water with a RMS relative error of 8.5% and RMS phase error of 17 minutes. The biggest discrepancies by far are at Site A where the observed harmonics are unreliable.

Statistical comparisons of the observed and modelled tidal height and current time-histories are shown in Table 5.11. A few trends can be untangled from these numbers. The root-mean-square errors are by and large high. Compared to the mean absolute error, RMSE amplifies and rigorously

punishes large errors. Hence, the model's inability to replicate peak tidal velocities yields a high RMSE. The relative mean absolute error (RMAE) at Sites A, B, C, D and F is about 10% for tidal height and 15% for tidal current speed. Concerns with respect to the integrity of the field measurements led to the inclusion of Site F for extra comparisons. On that note, the lowest errors in tidal velocity are seen at Sites F, C and B, in that order. Readers will recall that Site C had the most reliable measurements, with only the first 24 h discarded. Site B required a sudden shift in MSL to be corrected but the tidal velocities were left as is. The positive bias values indicate, again, the model's inability to replicate the peak tidal flows. Statistical comparisons of this nature are typically not available in the literature, hence it's difficult to judge the validation. Hashemi *et al.* (2015) reported a mean absolute error of < 0.20 m/s in depth-averaged tidal currents, which is roughly equivalent to the RMAE of 15% seen at the project site. According to Dupont *et al.* (2005) and Sankaranarayanan and McCay (2003), velocity errors are commonly larger than elevation errors, thus 20% is considered a good match. However, for the purpose of tidal current energy resource assessment – where the resource is literally the velocity probability distribution – models should be held to a high standard. The last observation relating to Table 5.11 is that the error in east-west and north-south velocities are often higher than those of tidal current speed, indicating a discrepancy between modelled and measured flow direction.

Graphical comparisons of tidal height and currents are shown for Sites A, B, C, D and F in Figures 5.11, 5.12, 5.13, 5.14 and 5.15, respectively. It's plain from these figures that the model underpredicts peak tidal velocities, especially on the stronger flood tide. Sites B, C and F seem to better simulate the flows. Recall that these sites required fewer corrections in the previous chapter. Surprisingly, the model-predicted flow direction matches the observations at Sites A and D, in spite of the fact that velocities at those locations had to be rotated in Section 4.3. Conversely, the model-predicted flow direction at Sites B and C diverge from the measurements. At Site B, the modelled currents are rotated slightly clockwise and at Site C, counterclockwise. Tidal current speed and direction are both very well replicated at Site F. The model's inability to simulate peak tidal currents and direction, particularly at Sites B and C, may be due to coarse model grid disretisation. Flow direction at Sites A and D, which lay atop a flat shelf, is accurately reproduced. At Sites B and C, which are a short distance off and away from the shelf, the 150 m grid resolution may be too coarse to accurately represent the complex geometry of the shelf and replicate flow dynamics (Figure 4.18). Similarly, Site F is surrounded by relatively smooth bathymetry and is well modelled.

As a final check of sorts, the model results were scanned for flow structures described in the literature. For example, the model is able to show the pulse in flow through the Crown Lease Area at the beginning of ebb tide described by Karsten *et al.* (2011). The pulse is shown in Figures 5.16 and 5.17. In addition, the major eddie formed off Cape split on the flood tide and the lesser eddie in West Bay are illustrated in Figure 5.18. With the 'standard' model calibrated and validated, the tidal current harmonics were analysed using T_TIDE, fulfilling the objective of Chapter 5 (Tables 5.12 and 5.13).

6. Resource assessment

Chapter 6 is the last step in conducting a comprehensive assessment of the tidal current energy resource at the project site. Long-term current predictions are produced from the observed and modelled harmonic constituents to define the velocity probability distribution and subsequently calculate: (1) Annual Energy Flux, based on the kinetic energy flux, and (2) Annual Energy Production as defined by the IEC-TC-114 draft standard.

6.1. Annual Energy Flux

Long-term current predictions are produced via T_TIDE for 2015 at 15 min resolution using observed (see Section 4.5) and modelled tidal current harmonics. The modelled constituents are obtained by simulating a minimum of 35 days (see Appendix C.2) and conducting a harmonic analysis with T_TIDE. Tidal current predictions for the first week of January 2015 are shown as an example in Figure 6.1. Using Eq. (2.2) the kinetic energy flux is calculated (Figure 6.2) and numerical integration provides the Annual Energy Flux (Table 6.1). The Annual Energy Flux will serve as the point of comparison to test the sensitivity of tidal current energy resource assessment to a number of parameters in Chapter 7.

Table 6.1. Annual Energy Flux for 2015 from observed and modelled tidal constituents

Site	Observed		Modelled		Relative error (%)
	Average P_f (kW/m^2)	AEF (MWh/m^2)	Average P_f (kW/m^2)	AEF (MWh/m^2)	
A	6.515	57.1	4.792	42.0	26.4
B	4.667	40.9	3.506	30.7	24.9
C	3.222	28.2	2.872	25.2	10.9
D	7.636	66.9	4.418	38.7	42.1
F	5.103	44.7	4.344	38.1	14.9

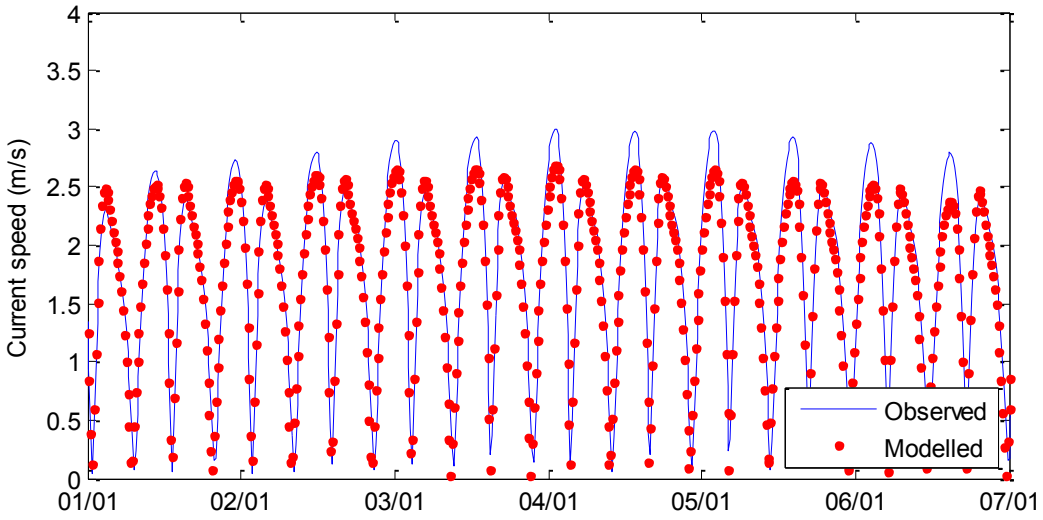

Figure 6.1. Current predictions for Jan 1-7 2015 (Site C)

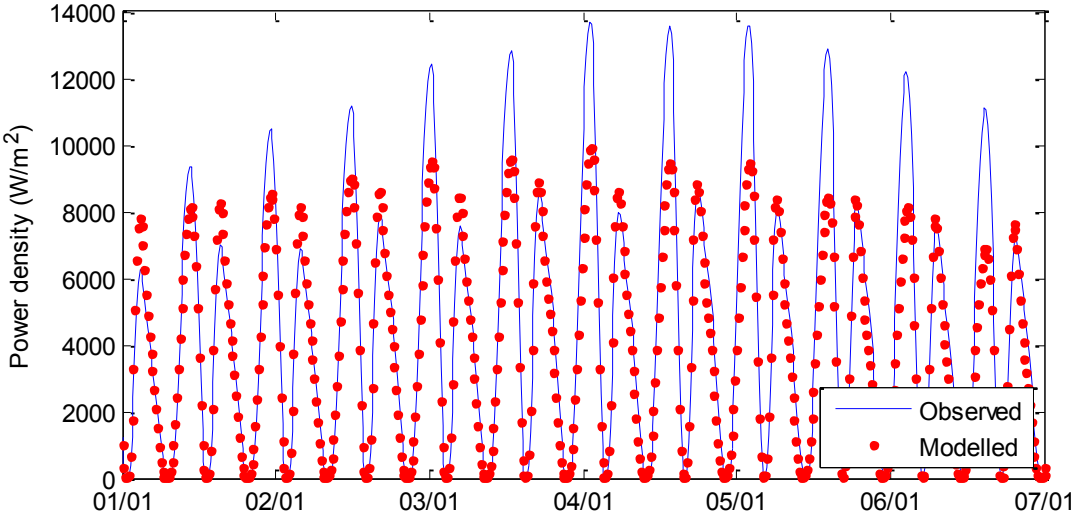

Figure 6.2. Kinetic energy flux for Jan 1-7 2015 (Site C)

6.2. Annual Energy Production

In order to calculate the Annual Energy Production the velocity probability distribution is required. The long-term current predictions are organised into 0.1 m/s bins to produce histograms and exceedance curves. The observed and modelled exceedance curves for Site C are compared below (Figure 6.3). A few assumptions enable calculation of the Annual Energy Production from Eq. (3.1). First of all, the measured power curve of the SeaGen S turbine is adopted (available online at http://www.marineturbines.com/). Developed by Marine Current Turbines, the SeaGen S is already operating and grid-connected in Strangford Lough, UK. The SeaGen curve exhibits asymmetry between the ebb and flood phases of the tidal cycle and therefore for the task at hand an average

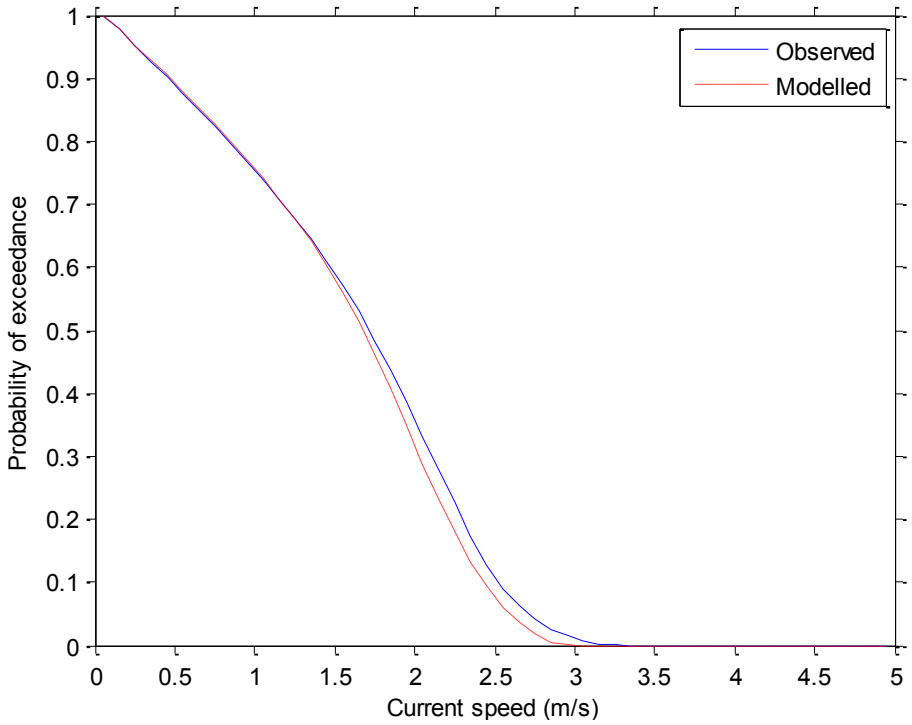

Figure 6.3. Exceedance curve of tidal currents for 2015 (Site C)

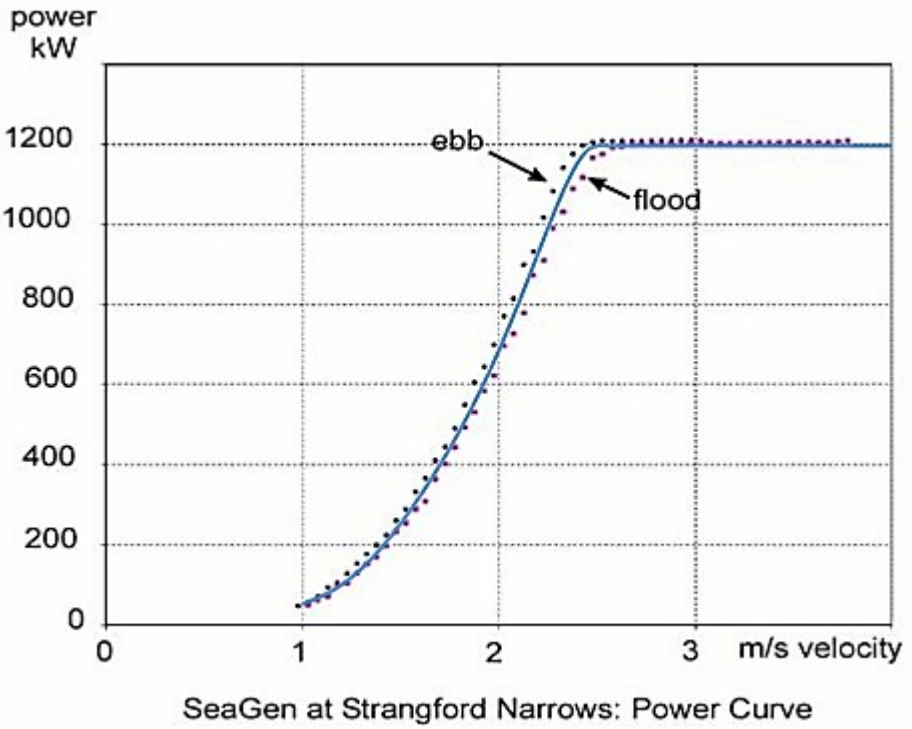

Figure 6.4. The measured power curve of the SeaGen S tidal turbine (available online at http://www.marineturbines.com/)

power curve has been fit to the data (Figure 6.4). Secondly, turbine availability of 94% is assumed from the literature (Douglas *et al*. 2008). Taking 8760 hours in the year and the computed tidal current histogram, the Annual Energy Production is calculated (Figure 6.5). Table 6.2 summarises and compares the Annual Energy Production estimates from observed and modelled tidal constituents.

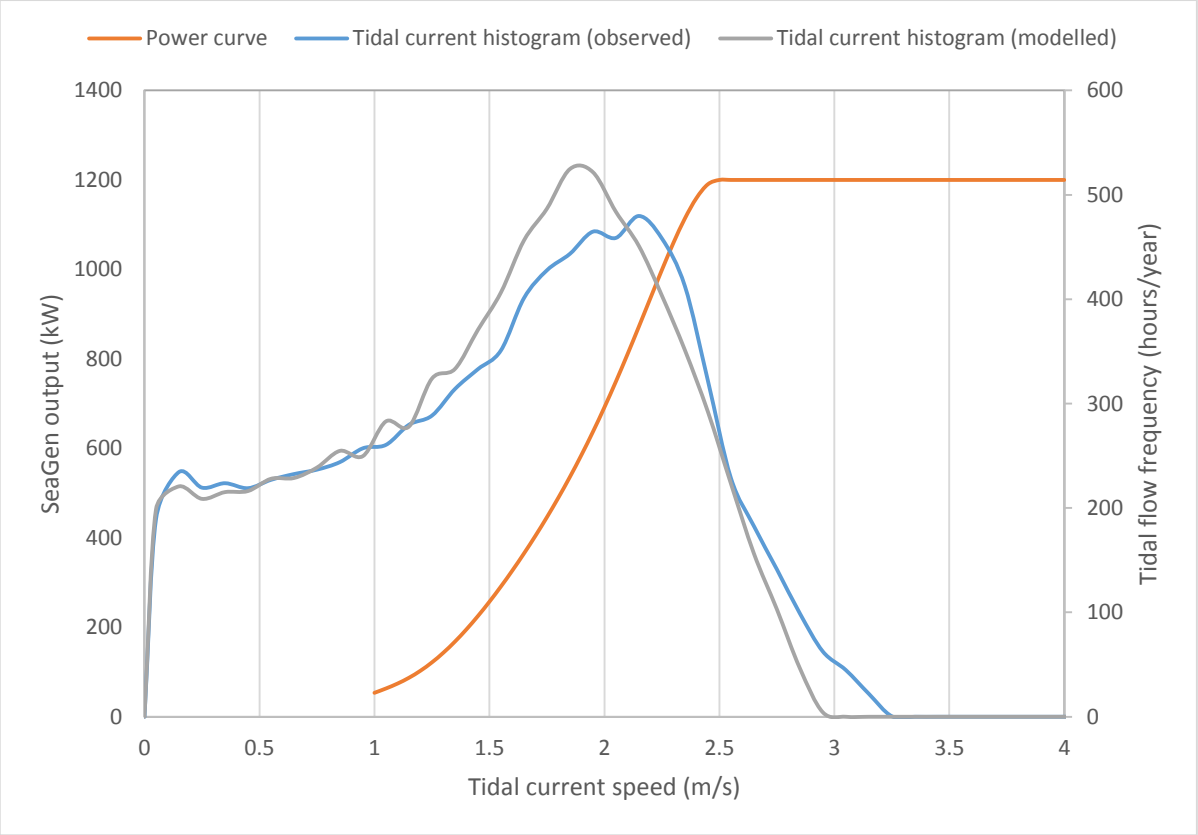

Figure 6.5. Tidal current histograms for Site C and SeaGen power curve

Table 6.2. Annual Energy Production for 2015 from observed and modelled tidal constituents

Site	Observed AEP (GWh)	Modelled AEP (GWh)	Relative error (%)
A	5.982	5.093	14.9
B	4.874	4.174	14.4
C	3.927	3.643	7.2
D	5.994	4.874	18.7
F	5.056	5.052	0.1

6.3. Discussion

Chapter 6 completes the assessment of the tidal current energy resource at the four FORCE berths. With the help of the observed and modelled harmonic constituents from Chapters 4 and 5, respectively, long-term current predictions are produced in order to define the velocity probability distribution and calculate the Annual Energy Flux and Annual Energy Production.

Long-term current predictions were produced for 2015 at 15 minute resolution with the help of T_TIDE. The observed tidal constituents were derived from the static current profiler surveys analysed in Chapter 4 (see Section 4.5). The modelled tidal current constituents were derived from output of the standard numerical model developed in Chapter 5 (see Section 5.4). Based on the predicted currents the kinetic energy flux is calculated with Eq. (2.2) and numerical integration yields the Annual Energy Flux. The measured and modelled Annual Energy Flux are compared in Table 6.1.

The resource is modelled most accurately at Sites C and F with relative errors of 10.9 and 14.9%, respectively. Sites B and A are less than ideal with relative errors of 24.9 and 25.4%, respectively. Lastly, Site D has a relative error of 42.1% with respect to direct measurement. The accuracy of the Annual Energy Flux follows more or less the same trend as the relative mean absolute error in tidal current speed (Table 5.11). In other words, the error in tidal velocity is communicated and amplified by the cubic velocity term in the Annual Energy Flux formula. Probable sources of error have already been discussed with regard to tidal velocity (see Section 5.5): model grid discretisation, the number of modelled tidal constituents, and the measurement errors. Those discussions apply here as well, the relative error has just been amplified by the cubic velocity term in the kinetic energy equation. To reiterate, the measured Annual Energy Flux at Site A is expected to contain errors because the long-term predictions were based on a tidal analysis of poor quality data with a short record length. Sites C and F have the lowest relative error in Annual Energy Flux and had the cleanest datasets, while there are doubts as to the integrity of the data at Sites B and D.

Figure 6.2 demonstrates the calculation of the power flux and the amplification of error that occurs. Model-predicted tidal velocities are underpredicted at peak flood whereas peak ebb appears to be well reproduced. These differences are exaggerated in the kinetic energy flux, which is drastically underpredicted at peak flood and a touch overpredicted at peak ebb.

In order to calculate Annual Energy Production the long-term current predictions are organised into 0.1 m/s bins to produce histograms and exceedance curves. Figure 6.3 shows the observed and

modelled exceedance curves for Site C. The curves clearly illustrate how the model successfully replicates tidal velocities below 1.5 m/s but then diverges from the observations. Although not shown here, model-predicted velocities at Sites A, B, D and F similarly deviate from observed values at higher magnitudes. Annual Energy Production is calculated by combining the velocity probability distribution, the measured power curve of the SeaGen S 16 m diameter twin 600 kW rated turbine and an availability of 94%. Table 6.2 summarises and compares the Annual Energy Production estimates from observed and modelled harmonics. The model-predicted Annual Energy Production is between 3.6 and 5.1 GWh depending on the site. According to Marine Current Turbines Ltd, the SeaGen S has an annual energy output of ~5.09 GWh. Therefore, the modelled estimate is within reason depending on flow conditions at the location.

The relative error in Annual Energy Production is lower than the relative error in Annual Energy Flux at the same site by an average 13%. Although unexpected, there is a logical explanation. In the calculation of Annual Energy Flux, the kinetic energy equation is applied to the velocity distribution whereas for Annual Energy Production, the SeaGen power curve was applied. The difference between these relationships is that the power curve terminates in a plateau when the rated velocity is attained: the kinetic energy equation has no such upper limit. Therefore, the power curve or 'per-generator' method limits the impact that poorly replicated peak velocities have on the relative error of the Annual Energy Production.

According to IEC-TC-114 protocols, model validation is achieved with quantitative comparisons between the Annual Energy Production computed from the static current profiler surveys and from model simulations. The observations noted above should deter from validation with respect to Annual Energy Production. The tidal current energy resource is literally the velocity probability distribution: the ability of a numerical model to replicate the flow dynamics and thus the velocity distribution is critical to resource assessment. As shown by Table 6.2, the Annual Energy Production calculated in this manner says very little about a model's ability to accurately simulate tidal velocities. For example, because of the transforming effect of the SeaGen power curve, Site F has a relative error of ~0% in Annual Energy Production. However, its relative error in Annual Energy Flux is 15%, and the model-predicted tidal current time series has a root-mean-square error of 0.251 m/s and a relative mean absolute error of 11%. At this location, with this power curve, averaged over a year, the model has been validated with a relative error of nearly 0%. But adopting a different power curve would produce very different results. Likewise, moving from Site F to Site D changes the relative error in Annual

Energy Production from 0 to almost 20%. Validating against Annual Energy Production is inappropriate. Models should instead be validated against measured tidal velocities to ensure accurate simulation of the velocity probability distribution. A successful validation of the tidal currents will lead to accurate resource assessment.

For these reasons, Annual Energy Production is unsuitable to conduct a sensitivity analysis of tidal current energy resource assessment (*e.g.* Lewis *et al.* 2015). Because of the transforming effect of the designated power curve, Annual Energy Production is not directly proportional to tidal velocity and may misrepresent the influence of numerical parameters on resource assessment. Therefore, Annual Energy Flux was adopted as a metric for the sensitivity analysis conducted in Chapter 7. The results should accurately represent the sensitivity of resource assessment to numerical parameters while remaining device agnostic. Although the relative error in Annual Energy Flux is high at some sites, for the purpose of sensitivity analysis the accuracy of the resource assessment is not the primary concern: the trends shown are still valid. The model was developed to 'standard' Feasibility specifications, thus if the model-predicted resource is insufficiently accurate, that result is noteworthy. If the inaccuracies of the assessment are due to numerical parameters and not measurement error, that will be uncovered in Chapter 7. Readers may have noticed that neither a device hub height nor a velocity profile were assumed in order to extrapolate the 2D model output. The decision was made to use depth-averaged values so as to avoid introducing new errors into the modelled resource and making comparisons in Chapter 7 less direct.

7. Sensitivity analysis

Chapter 7 tackles an important objective of the thesis, conducting a sensitivity analysis to determine the main sources of error and uncertainty affecting resource assessment. A number of parameters for which recommendations are ambiguous or uncertain are investigated, such as minimum spatial resolution and the number of harmonic constituents for modelling the driving boundary. In so doing, Chapter 7 touches on two more objectives of the thesis: establishing and confirming a solid scientific basis for the IEC-TC-114 standard and developing suggestions for improving and extending future revisions of the standard.

7.1. Harmonic analysis

Tidal analysis and prediction are essential components of the methodology proposed by IEC-TC-114 at many stages of resource assessment: hydrodynamic model calibration, long-term model current predictions and model boundary condition specification. Numerous tools are available to conduct these analyses, including T_TIDE (Pawlowicz *et al.* 2002), IOS Tidal Package (Foreman *et al.* 2009) and UTide (Codiga 2011). Each of these introduces its own set of limitations and uncertainties to the tidal current energy resource assessment. The objective of this section is to conduct a sensitivity analysis of T_TIDE, the main harmonic analysis tool throughout the thesis, to determine the sensitivity of the solutions to length of record (*i.e.* observation/simulation period) and temporal resolution (*i.e.* sampling interval/output time step).

T_TIDE employs an algorithm based on the Rayleigh criterion to select which package of harmonic constituents to include in its analysis. The Rayleigh criterion determines whether two neighbouring constituents can be separated from each other in an analysis depending on the difference in their frequency and the length of record. A series of experiments on the Site B survey shows how many and which constituents are included in the analysis as record length increases (Table 7.1).

Table 7.1. Number of constituents extracted based on record length

Record length (days)	**1**	**2 – 7**	**8 – 13**	**14**	**15 – 27**	**28 – 31**	**32 – 42**
Number of constituents	**4**	**8**	**9**	**10**	**17**	**29**	**35**
Tide	K1	K1	K1	O1	MSF	MSF	MM
	M2	M2	M2	K1	O1	2Q1	MSF
	2MK5	M3	M3	M2	K1	Q1	ALP1
	3MK7	M4	M4	M3	M2	O1	2Q1
		2MK5	2MK5	M4	S2	NO1	Q1
		M6	2SK5	2MK5	M3	K1	O1
		3MK7	M6	2SK5	SK3	J1	NO1
		M8	3MK7	M6	M4	OO1	K1
			M8	3MK7	MS4	UPS1	J1
				M8	S4	N2	OO1
					2MK5	M2	UPS1
					2SK5	S2	EPS2
					M6	ETA2	MU2
					2MS6	MO3	N2
					2SM6	M3	M2
					3MK7	MK3	L2
					M8	SK3	S2
						MN4	ETA2
						M4	MO3
						MS4	M3
						S4	MK3
						2MK5	SK3
						2SK5	MN4
						2MN6	M4
						M6	SN4
						2MS6	MS4
						2SM6	S4
						3MK7	2MK5
						M8	2SK5
							2MN6
							M6
							2MS6
							2SM6
							3MK7
							M8

The next step is to investigate how record length affects the reliability of the amplitudes and phases. For that purpose, Site B was selected for its lengthy record (46 days) and uniform sampling interval (15 minutes). Harmonic analysis was performed on subsets of the Site B data with T_TIDE, allowing the tool to select which constituents to include in the analysis following Table 7.1. Depending on which (for example) 7-day interval of data was analysed, the solution would be different. Therefore, a script was written to select a random subset of the data of the required length. Harmonic analysis was performed on 100 randomly selected subsets of 1 through 42 days of Site B data (*i.e.* 100 7-day intervals, 100 8-day intervals, *et cetera*). The tidal height constituents of amplitude and phase for the M2 tide and 3 leading constituents are shown in Figure 7.1 and 7.2**.** As record length (and the number of constituents included in the analysis) increases T_TIDE converges on a solution.

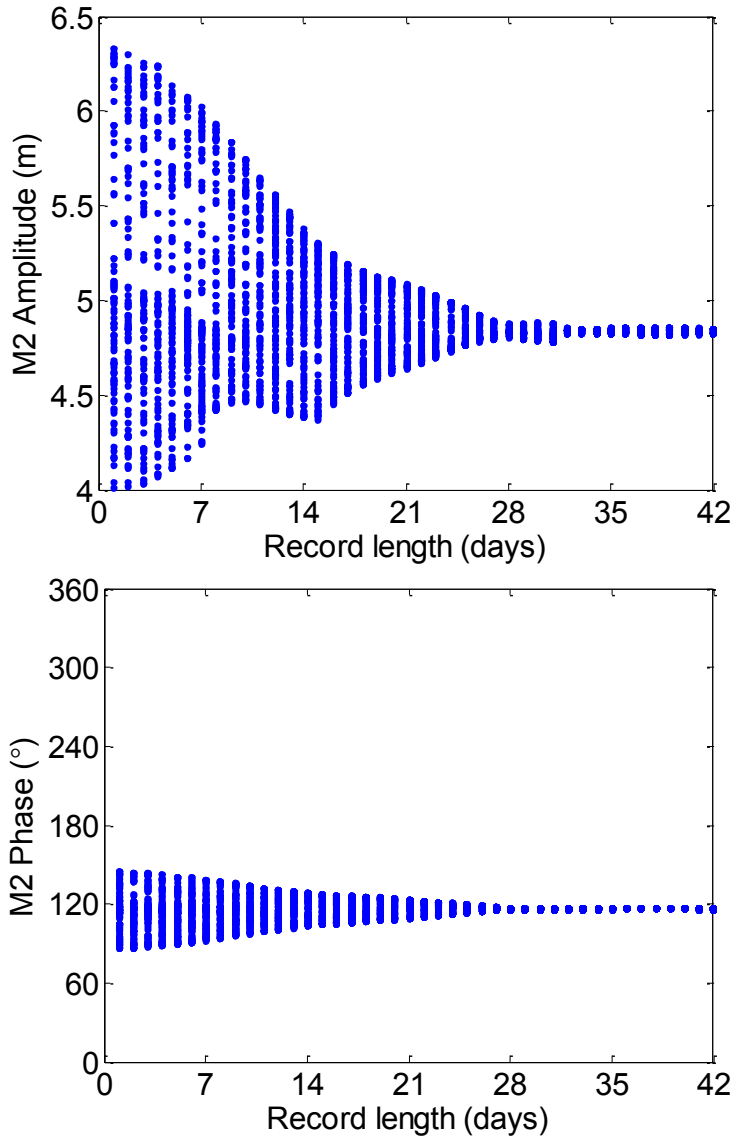

Figure 7.1. Tidal height constituents of amplitude and phase for M2 versus record length

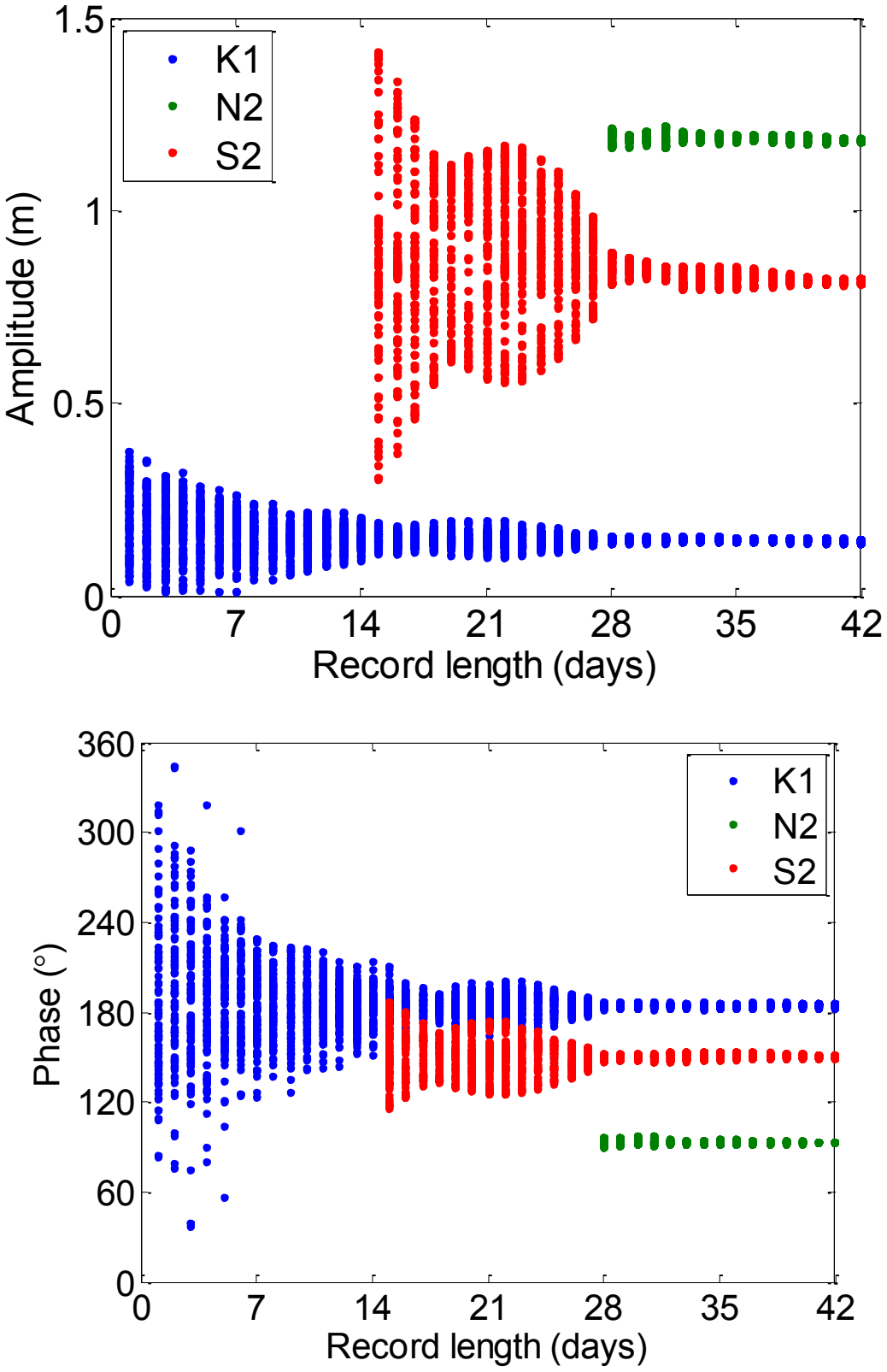

Figure 7.2. Tidal height constituents of amplitude and phase for N2, S2 and K1 versus record length

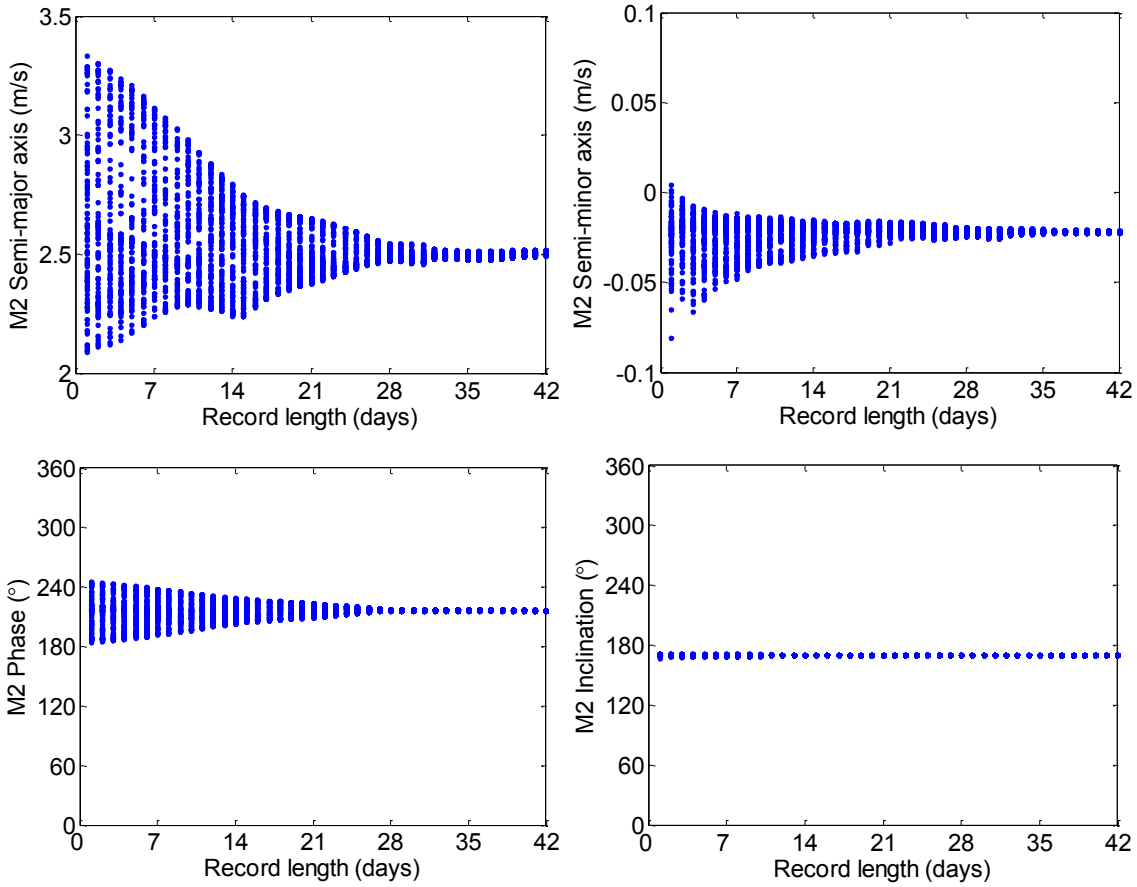

Figure 7.3. Tidal current constituents for M2 versus record length

The trends observed in tidal current constituents are essentially the same, with perhaps slightly more variability in the result (Figure 7.3). The next series of experiments looked at the number of constituents fit to the data. Rather than allow T_TIDE to select which constituents to include in the analysis based on the record length, three analyses were conducted: with the standard 8, 17 and 35 constituent packages. For each set of constituents and record length, 100 randomly selected subsets of Site B data were analysed. Figure 7.4 shows tidal height constituents of amplitude and phase for the M2 tide based on the record length and number of constituents included in the analysis.

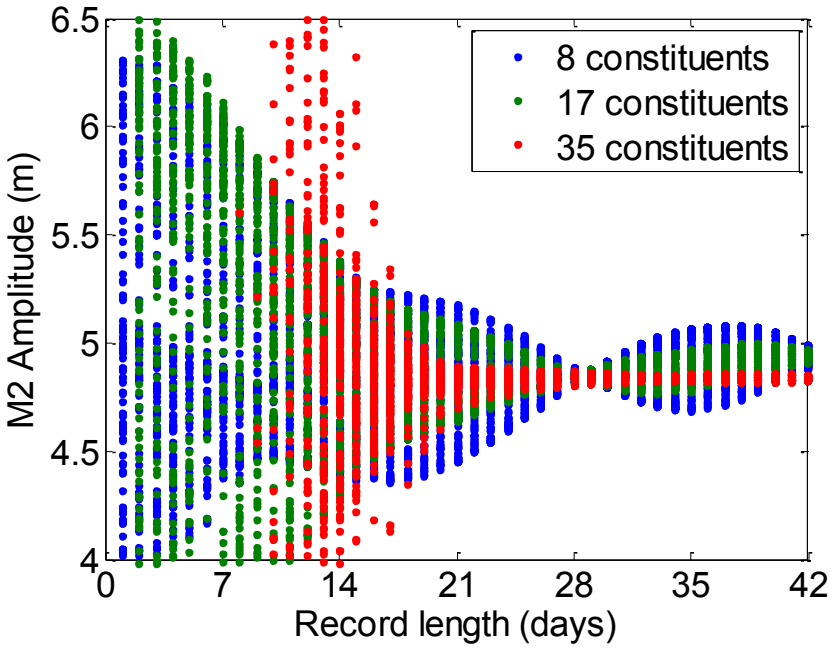

Figure 7.4. Tidal height constituents of amplitude and phase for M2 versus record length and analysed constituents

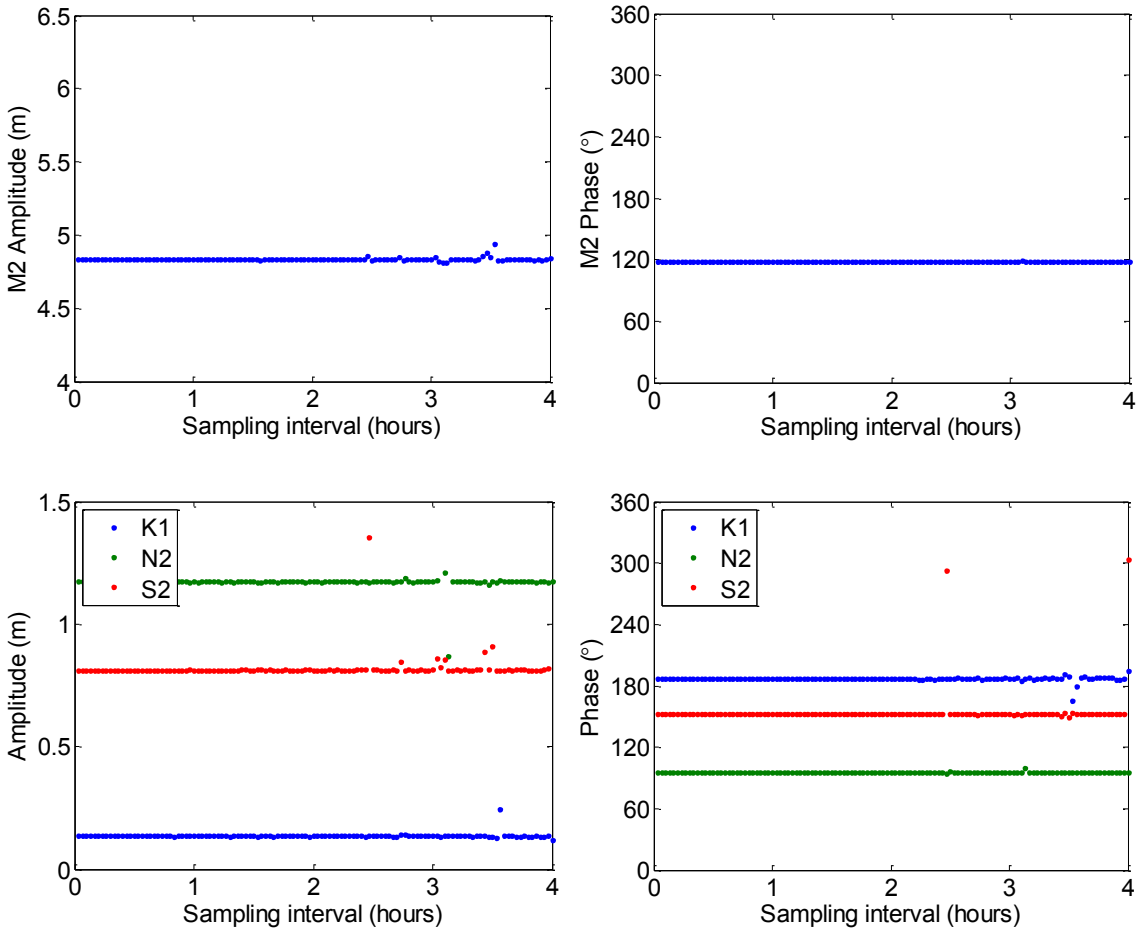

Figure 7.5. Tidal height constituents for M2, N2, S2 and K1 versus sampling interval

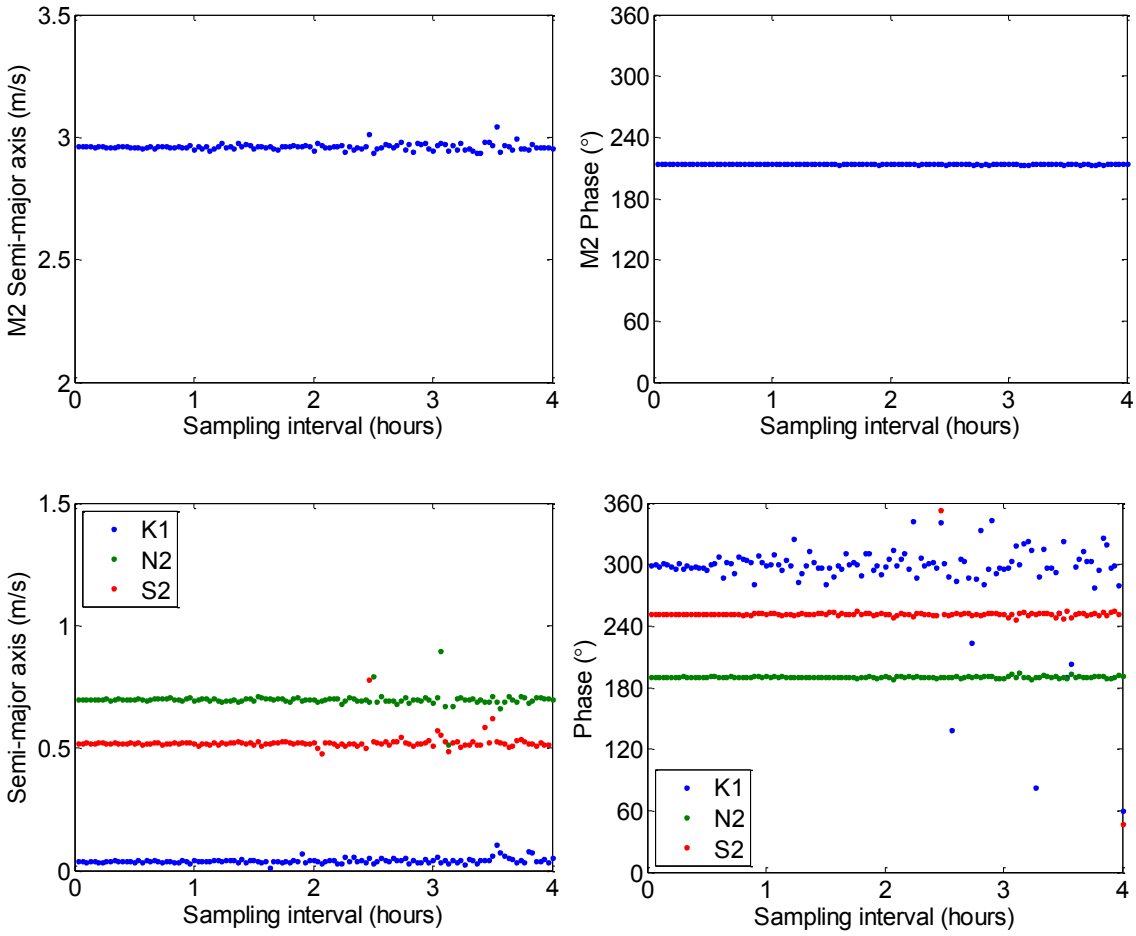

Figure 7.6. Tidal current constituents for M2, N2, S2 and K1 versus sampling interval

The last series of experiments looked at sampling interval/output time step. The Site D survey has nearly the same record length as Site B (44 days) and a higher resolution sampling interval (2 minutes). This presented an opportunity to verify the sensitivity of harmonic analysis to the temporal resolution of input data. A harmonic analysis was performed on the record as such, then the time-series was resampled to a lower frequency and the analysis was repeated. The record length of the survey was unchanged. Figure 7.5 shows tidal height constituents of amplitude and phase for M2, N2, S2 and K1. The solution is stable even up to large sampling intervals, though that may not be the case with a shorter record length. Figure 7.6 shows tidal current constituents for M2, N2, S2 and K1. The solution appears less stable at lower sampling intervals for tidal currents than tidal height. Based on these figures a sampling interval/output time step of no more than two hours would be recommended.

To test the sensitivity of the Annual Energy Flux calculation to temporal resolution (*i.e.* tidal analysis), simulations were performed with an increasingly long output time step. Table 7.2 shows the Annual Energy Flux computed with each output time step. As previously suggested, harmonic analysis cannot produce accurate tidal current constituents if the temporal resolution of the input data is > 2 hours. See Appendix C.7 for a log of the simulations.

Table 7.2. Annual Energy Flux versus numerical output time step

Output time step (min)	Annual Energy Flux (MWh/m^2)			
	Site A	**Site B**	**Site C**	**Site D**
5	42.0	30.7	25.2	38.7
10	42.0	30.7	25.2	38.7
15	42.0	30.7	25.2	38.7
20	42.0	30.7	25.2	38.7
30	42.0	30.7	25.2	38.7
60	41.9	30.7	25.2	38.7
120	41.8	30.7	25.1	38.7
240	7.4E+35	1.1E+36	7.6E+35	6.1E+35
360	1.3E+38	3.0E+37	9.2E+36	5.3E+37
480	2.0E+37	5.0E+36	1.0E+37	1.1E+37
720	3.4E+40	6.8E+39	1.7E+39	7.3E+39

7.2. Boundary specification (tidal amplitude)

The draft standard recommends a minimum of 4 - 8 harmonic constituents for modelling the driving boundary of a Feasibility study and 8 - 12 for Layout Design. In this study, eight leading constituents were selected for the purpose of calibration and validation (M2, N2, S2, K1, K2, NU2, O1, MU2). The modelled constituents were selected for the highest average amplitude at the open boundary (**Table 5.1**). In this section, the boundary is specified with 1 - 20 constituents to evaluate the impact on tidal current energy resource assessment. The modelled constituents were selected, as before, based on the average amplitude at the ocean boundary (Table 5.1). See Appendix C.4 for a log of the simulations and included constituents.

The simplest starting point is to plot the Annual Energy Flux (AEF), calculated as shown in Chapter 6, as a function of the fraction of the tidal amplitude modelled at the ocean boundary (Figure 7.7). There is a trend of increasing AEF as more constituents are modelled, but the relationship is not simple. It would be more useful to plot the proportion of the AEF contributed by each added constituent so as to be able to compare between the sites. An example of the calculation of fractional AEF is shown in Table 7.3. Firstly, the Annual Energy Flux is computed for each simulation. Secondly, the contribution of each constituent to the AEF is calculated by subtracting the AEF of the previous simulation without it. Thirdly, the contribution is expressed as a percentage of the total AEF by assuming that 20 constituents would model nearly 100% of the energy.

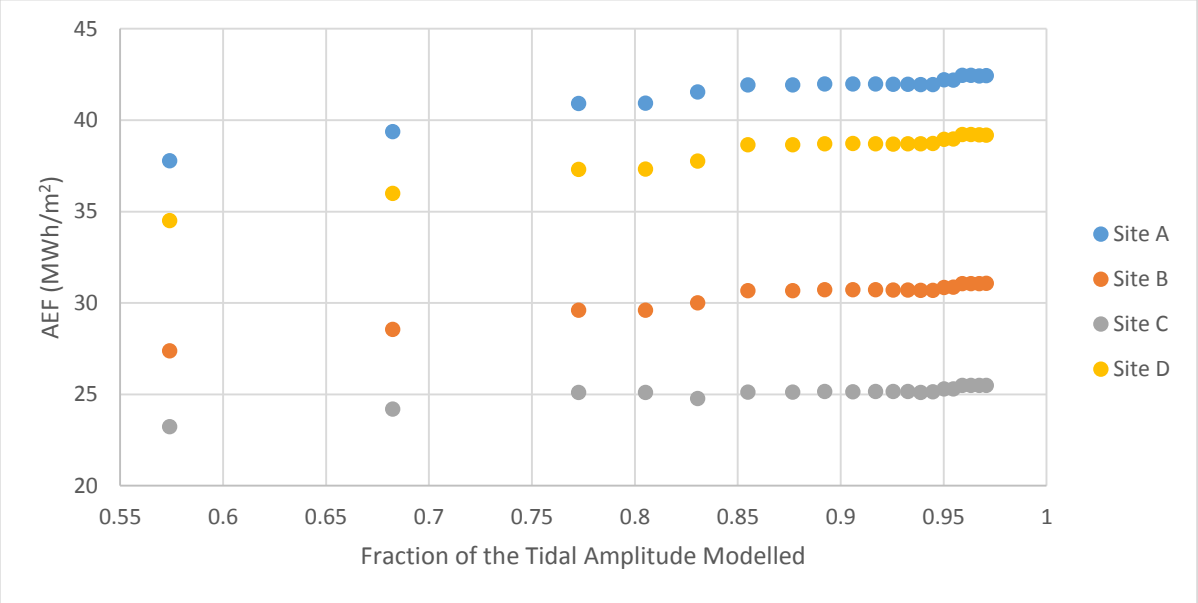

Figure 7.7. Annual Energy Flux as a function of the tidal amplitude modelled at the open boundary

Table 7.3. Contribution of each constituent to the Annual Energy Flux at Site A

# of constituents modelled	Added constituent	AEF (MWh/m^2)	Contribution to AEF (MWh/m^2)	Contribution to AEF (%)
1	M2	37.8	37.8	89
2	N2	39.4	1.6	4
3	S2	40.9	1.5	4
4	K1	40.9	0.0	0
5	K2	41.5	0.6	1
6	NU2	41.9	0.4	1
7	O1	41.9	0.0	0
8	MU2	42.0	0.1	0
9	MM	42.0	0.0	0
10	P1	42.0	0.0	0
11	L2	42.0	0.0	0
12	MSF	42.0	0.0	0
13	MSN2	41.9	0.0	0
14	2N2	41.9	0.0	0
15	M6	42.2	0.2	1
16	ETA2	42.2	0.0	0
17	M4	42.4	0.3	1
18	Q1	42.4	0.0	0
19	OQ2	42.4	0.0	0
20	2SM2	42.4	0.0	0

A pattern emerges whereby a few constituents appear to be responsible for the majority of the AEF. Figure 7.8 shows the fraction of the total Annual Energy Flux modelled as each new constituent is introduced to the simulation. It's an average of the values for Sites A, B and D. Note that M2, N2, S2, K2, NU2, M6 and M4 mark new plateaus in the computed AEF. Although the pattern is the same at all four locations, Site C was excluded because K2 had an equal but opposite impact there: its contribution to the AEF at Site C was to reduce it by about 1 per cent (Figure 7.9). In absolute values, the contribution of each of these 7 constituents would be approximately the same at the four sites.

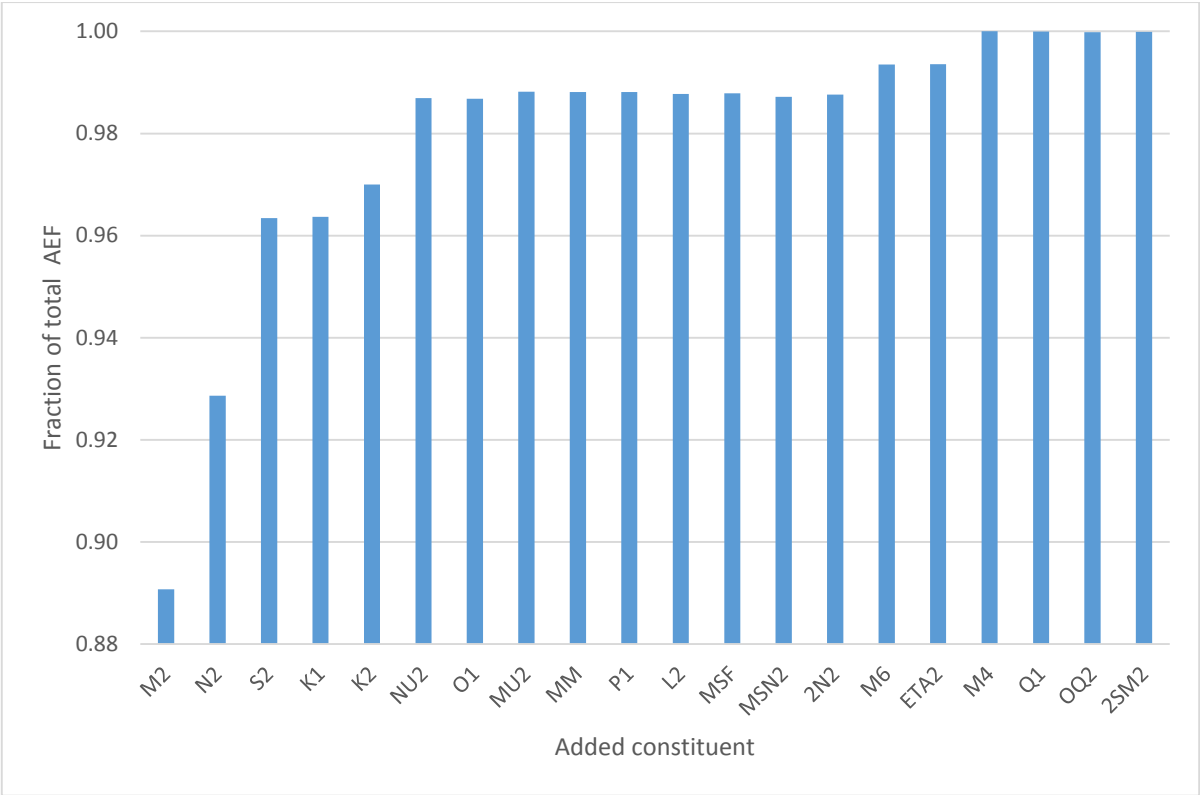

Figure 7.8. Fraction of the Annual Energy Flux modelled versus number of modelled constituents (Sites A, B and D)

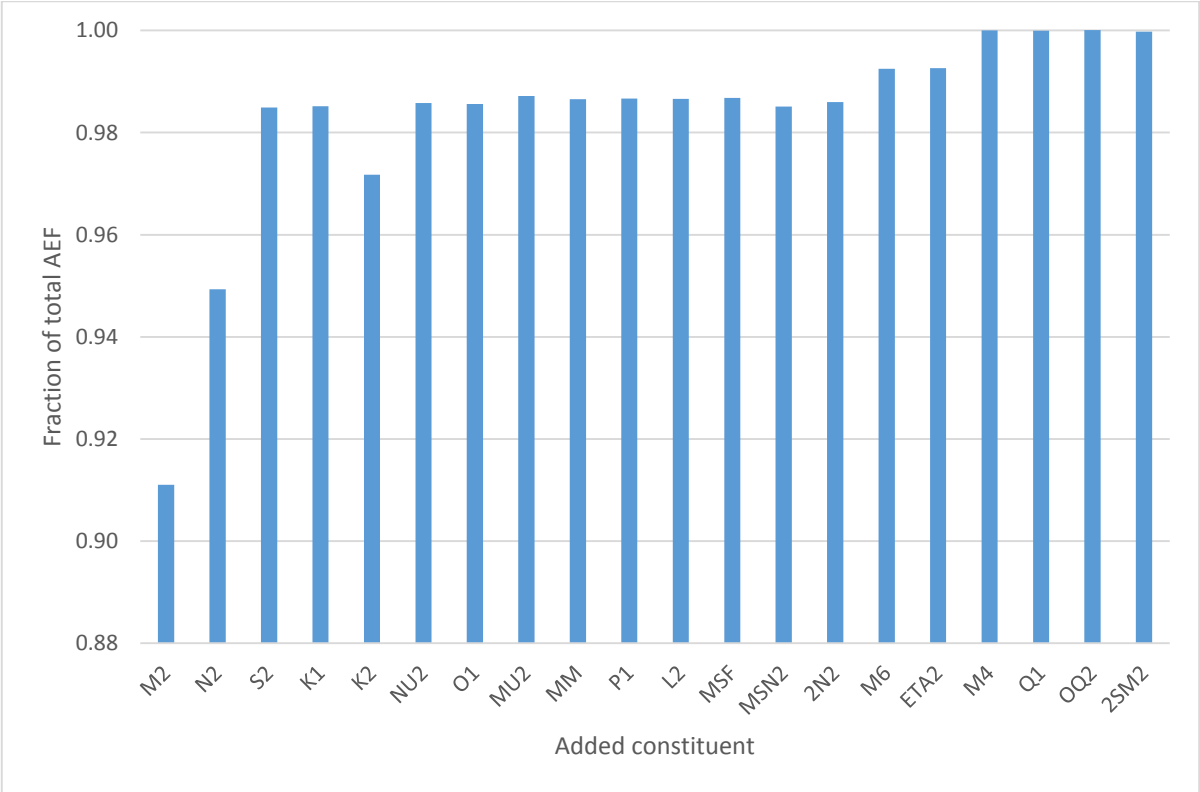

Figure 7.9. Fraction of the Annual Energy Flux modelled versus number of modelled constituents (Site C)

Table 7.4 shows the average contribution of the 7 constituents to the Annual Energy Flux of Sites A, B, C, and D. Together, these constituents represent 83% of the tidal amplitude at the ocean boundary and 99.9% of the Annual Energy Flux at the FORCE berths. Interestingly, when a simulation was run with only the 7 'key' constituents modelled, the calculated Annual Energy Flux was almost identical to the runs with 20 constituents (Table 7.5). The relative error is about 0.08%. Compared with the standard 8 constituent simulations there is a ~1% difference in AEF because most of the 7 'key' constituents were included among the eight.

Table 7.4. Average Annual Energy Flux contributed by 7 constituents at the FORCE berths

Tide	% of Tidal amplitude	% of Annual Energy Flux
M2	57	89
N2	11	3.8
S2	9.0	3.5
K2	2.5	0.63
NU2	2.4	1.7
M6	0.54	0.59
M4	0.43	0.65
TOTAL	**83**	**99.9**

Table 7.5. Annual Energy Flux predicted by 7 key constituents compared to the maximum of 20

Site	Annual Energy Flux (kWh/m^2)		Relative error (%)
	20 constituents modelled	7 'key' constituents modelled	
A	42437	42429	0.02
B	31073	31037	0.11
C	25486	25482	0.02
D	39183	39121	0.16

7.3. Spatial resolution

The recommendations of the IEC-TC-114 draft standard with respect to grid resolution are < 500 m for a Feasibility stage assessment, refined to 200 m in regions of bathymetric complexity or < 50 m for Layout Design. The standard mesh for the purpose of calibration and validation was developed with 150 m resolution in the Minas Passage, however, the model grid was developed such that submeshes of different density could be integrated to represent Minas Passage without affecting the remainder of the grid. A total of 10 submeshes were produced for Minas Passage: 500, 400, 300, 250, 200, 150, 100, 75, 50 and 20 m resolution, accounting for the minimum recommended resolution of Feasibility and Layout Design assessments. Note that, for all simulations conducted in Section 7.3, the numerical time step was reduced to 2.5 seconds. See Appendix C.5 for a log of the simulations.

Table 7.6 shows the properties of the developed grids: number of nodes and elements, minimum and maximum mesh size, and resolution in Minas Passage. Figure 7.10 and 7.11 show the 20 and 100 m grids, respectively. For grids < 150 m, only the Crown Lease Area itself is covered by the nominal resolution because of the maximum growth rate of elements and spatial restrictions. Grids of 150 m resolution upward cover the entire Minas Passage, for example the 250 m submesh (Figure 7.12). It can be seen that grids coarser than 250 m were unable to model the perimeter of Black Rock Island. Figure 7.13 shows the largest submesh with a resolution of 500 m.

Table 7.6. Properties of the developed grids

Nominal size (m)	Nodes	Elements	Min mesh size (m)	Max mesh size (m)
500	11754	21429	216.5	4575
400	12109	22120	150.5	4575
300	12675	23215	167.5	4575
250	13129	24092	85.3	4575
200	14191	26181	71.1	4575
150	16026	29793	66.3	4575
100	15848	29429	44.1	4575
75	16623	30979	48.8	4575
50	18353	34421	22.5	4575
20	27476	52573	12.3	4575

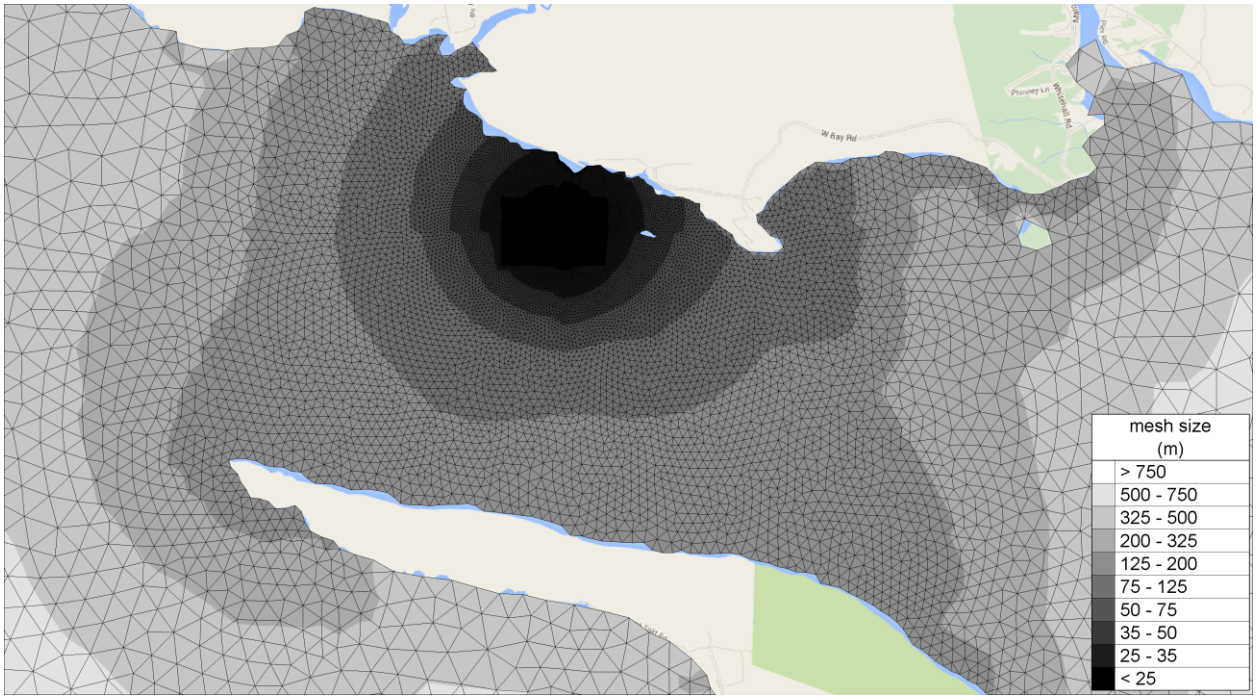

Figure 7.10. 20 m submesh

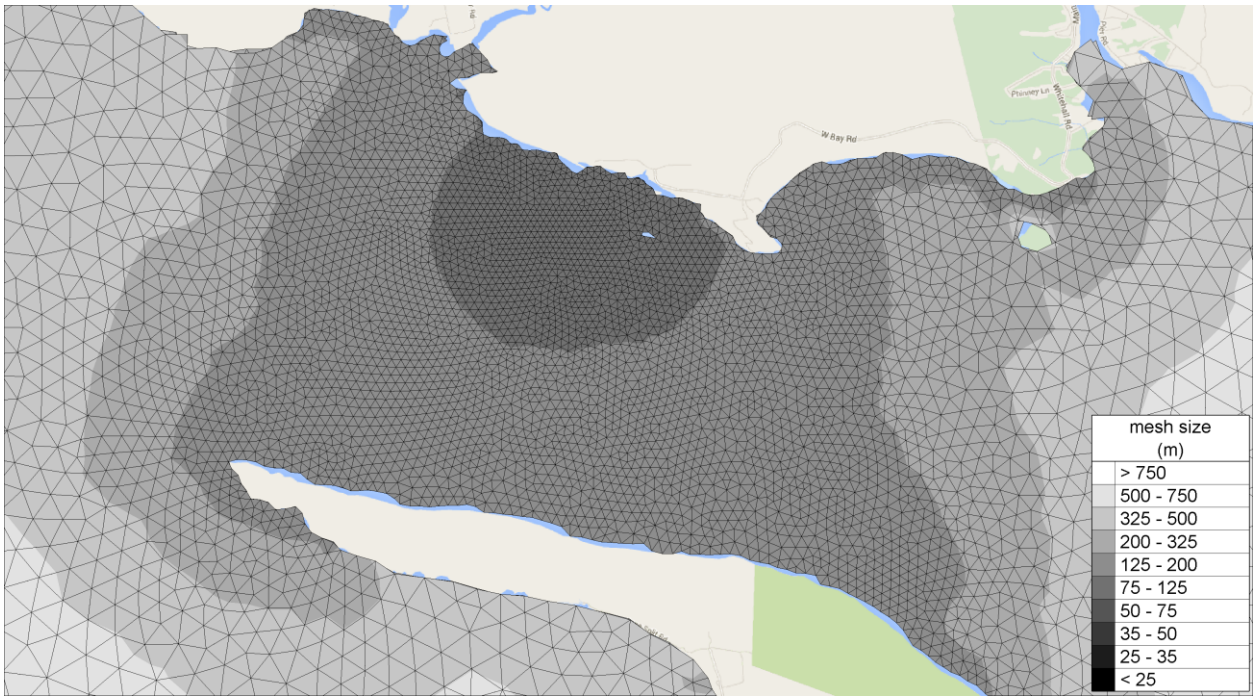

Figure 7.11. 100 m submesh

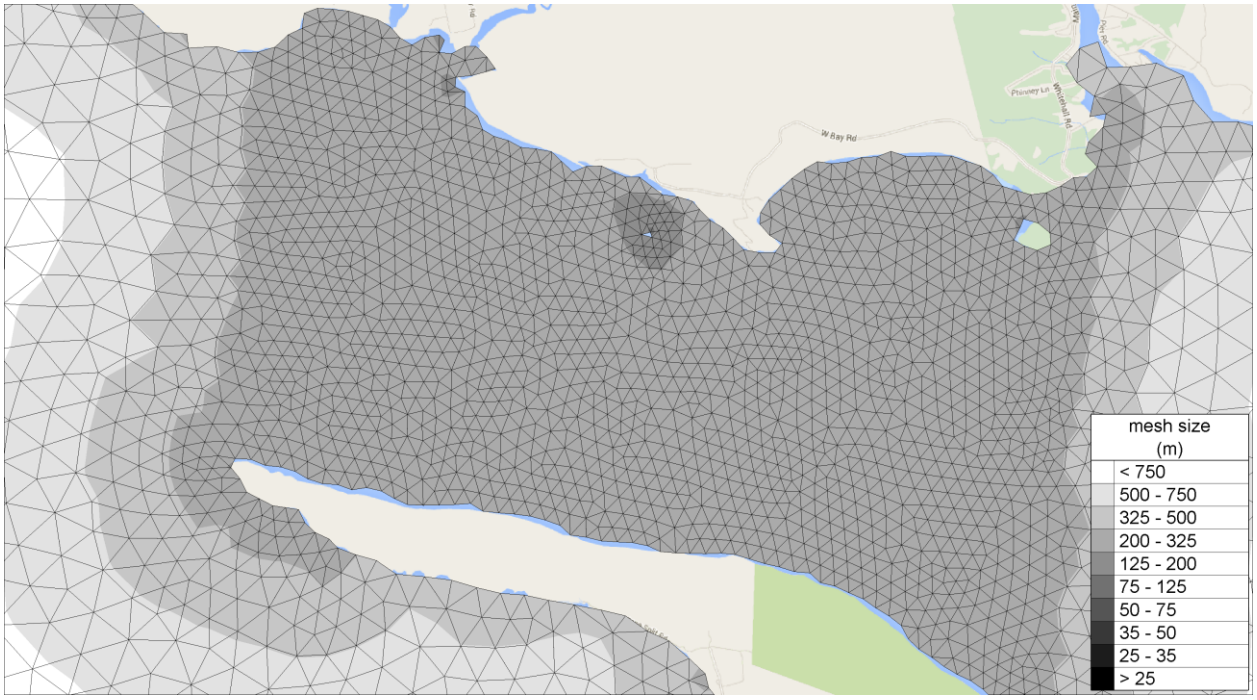

Figure 7.12. 250 m submesh

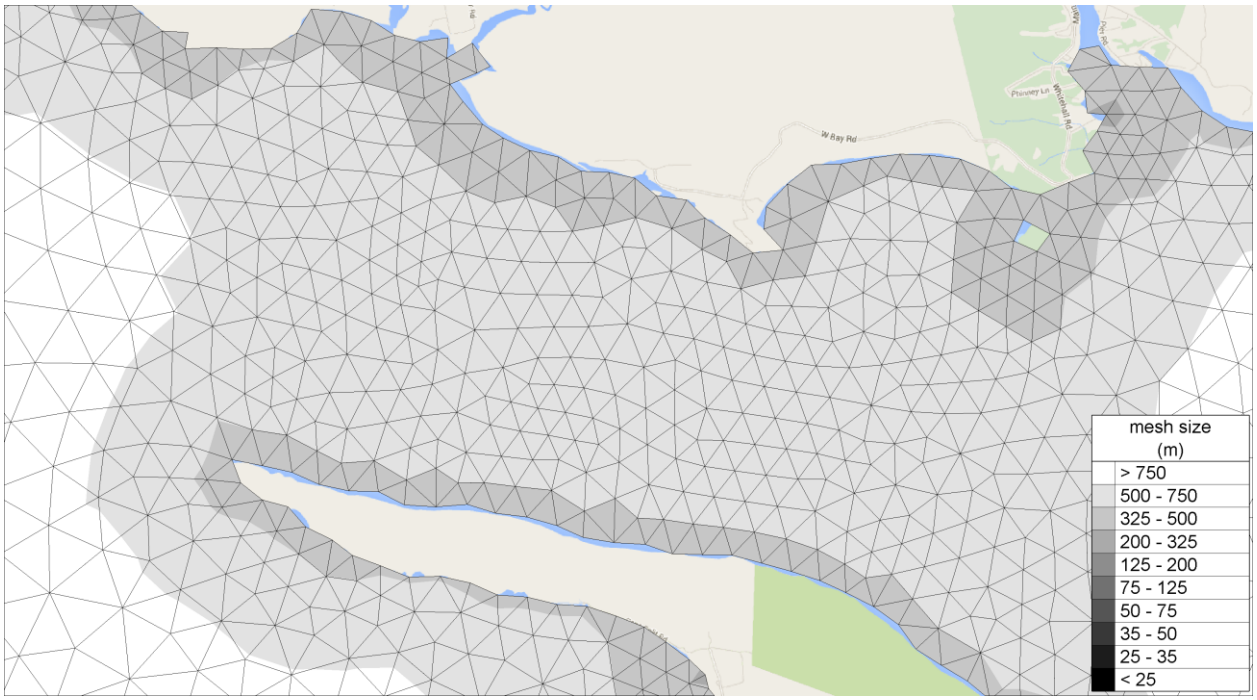

Figure 7.13. 500 m submesh

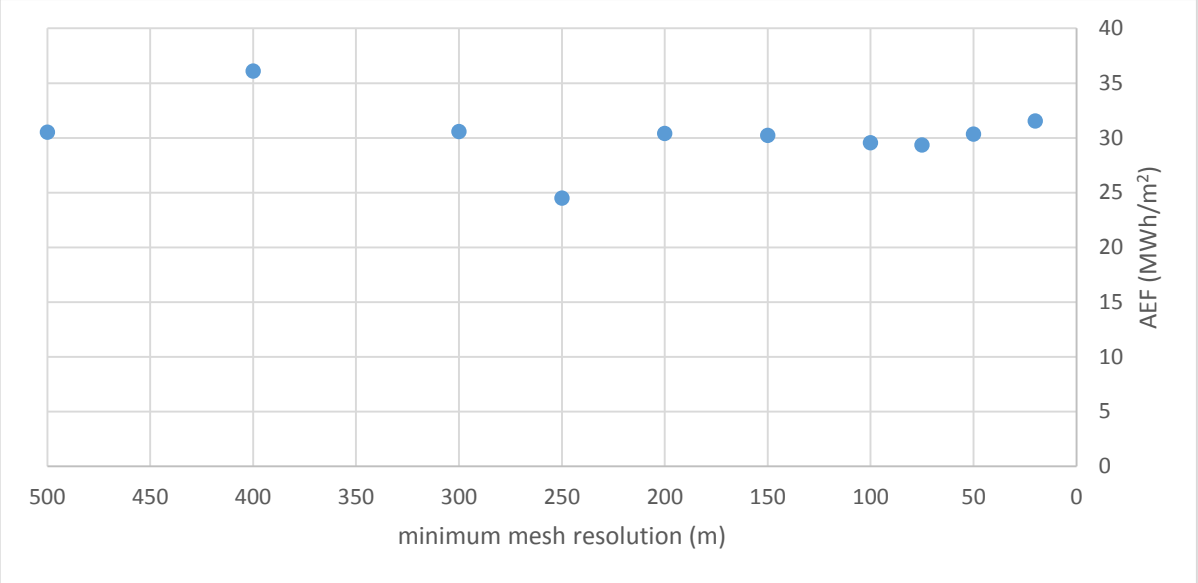

Figure 7.14. Annual Energy Flux as a function of local mesh resolution (Site B)

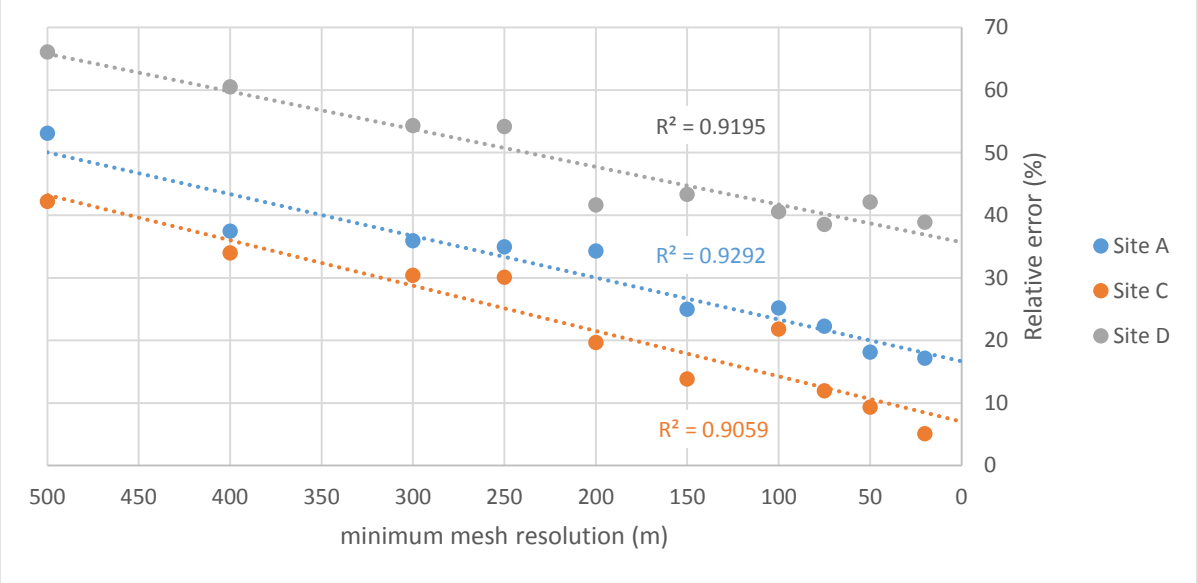

Figure 7.15. Relative error in Annual Energy Flux as a function of local mesh resolution (Sites A, C and D)

The way to proceed is to plot the Annual Energy Flux as a function of local mesh resolution in the Crown Lease Area. Site B, it should be said, does not show any trend in Annual Energy Flux with increasing grid resolution (Figure 7.14). Sites A, C and D, however, demonstrate a linear relationship between Annual Energy Flux and local mesh resolution. The relationship is illustrated in Figure 7.15 as the relative error in Annual Energy Flux at these sites with respect to the observed estimates. The slope is quite similar at all three sites, suggesting that a refinement in resolution of 50, 100 and 150 m would yield a 3.3, 6.6 and 10% improvement in relative error, respectively.

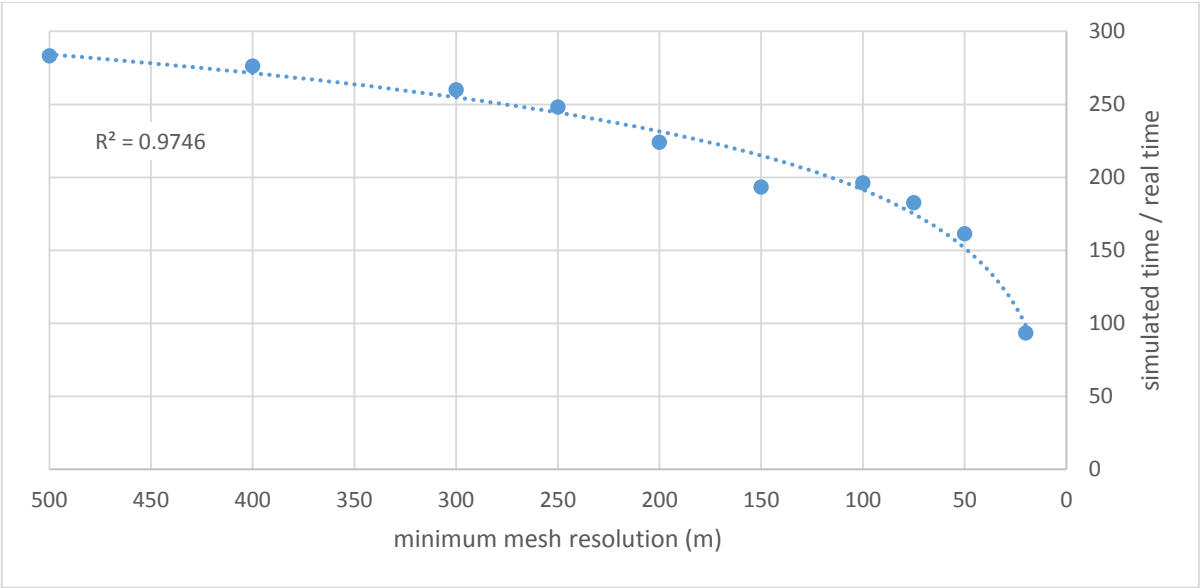

Figure 7.16. Computational time versus minimum mesh resolution

However, the improved accuracy comes with added computational cost. Figure 7.16 shows the logarithmic relationship between minimum mesh resolution and simulation speed. Figure 7.17 demonstrates the improvement of the modelled velocity probability distribution with increasing grid resolution at Site C. By the same token, Figure 7.18 shows the increasingly accurate modelled tidal ellipses at Site D with refinement of the local grid.

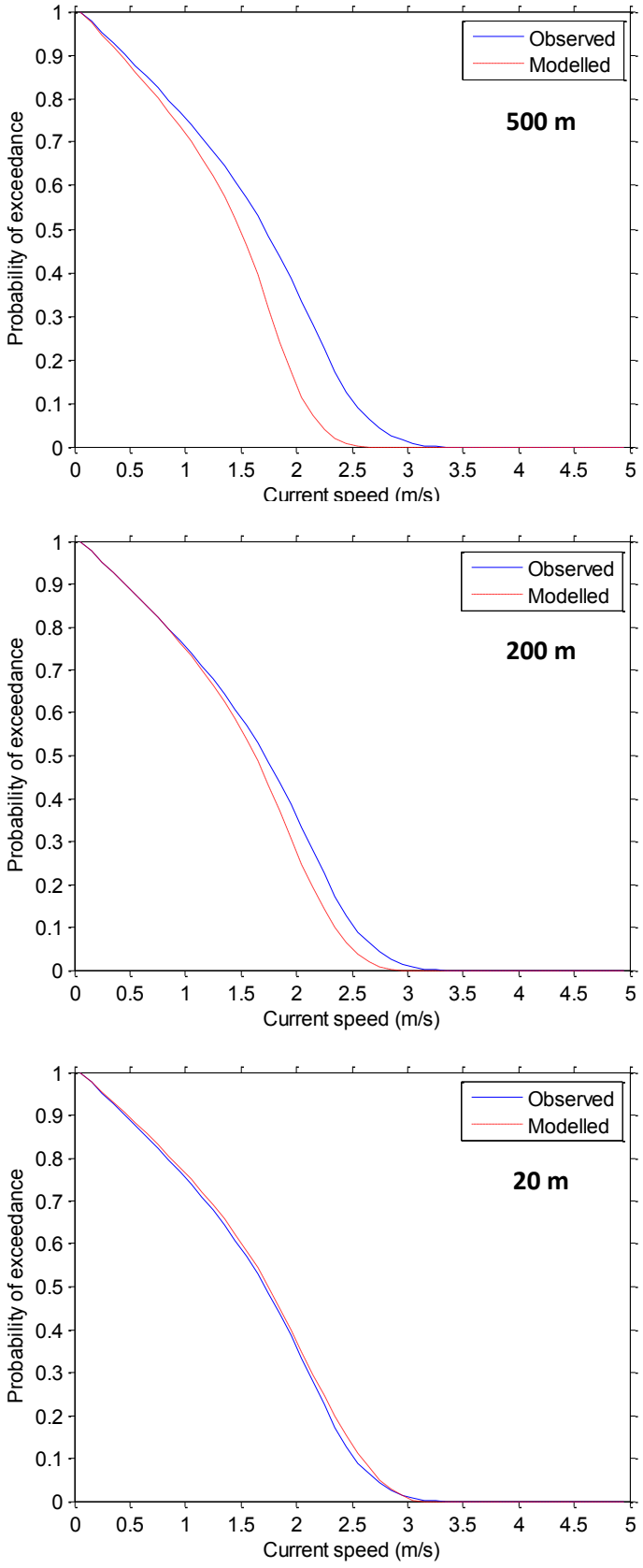

Figure 7.17. Tidal current speed probability of exceedance at 500, 200 and 20 m resolution (Site C)

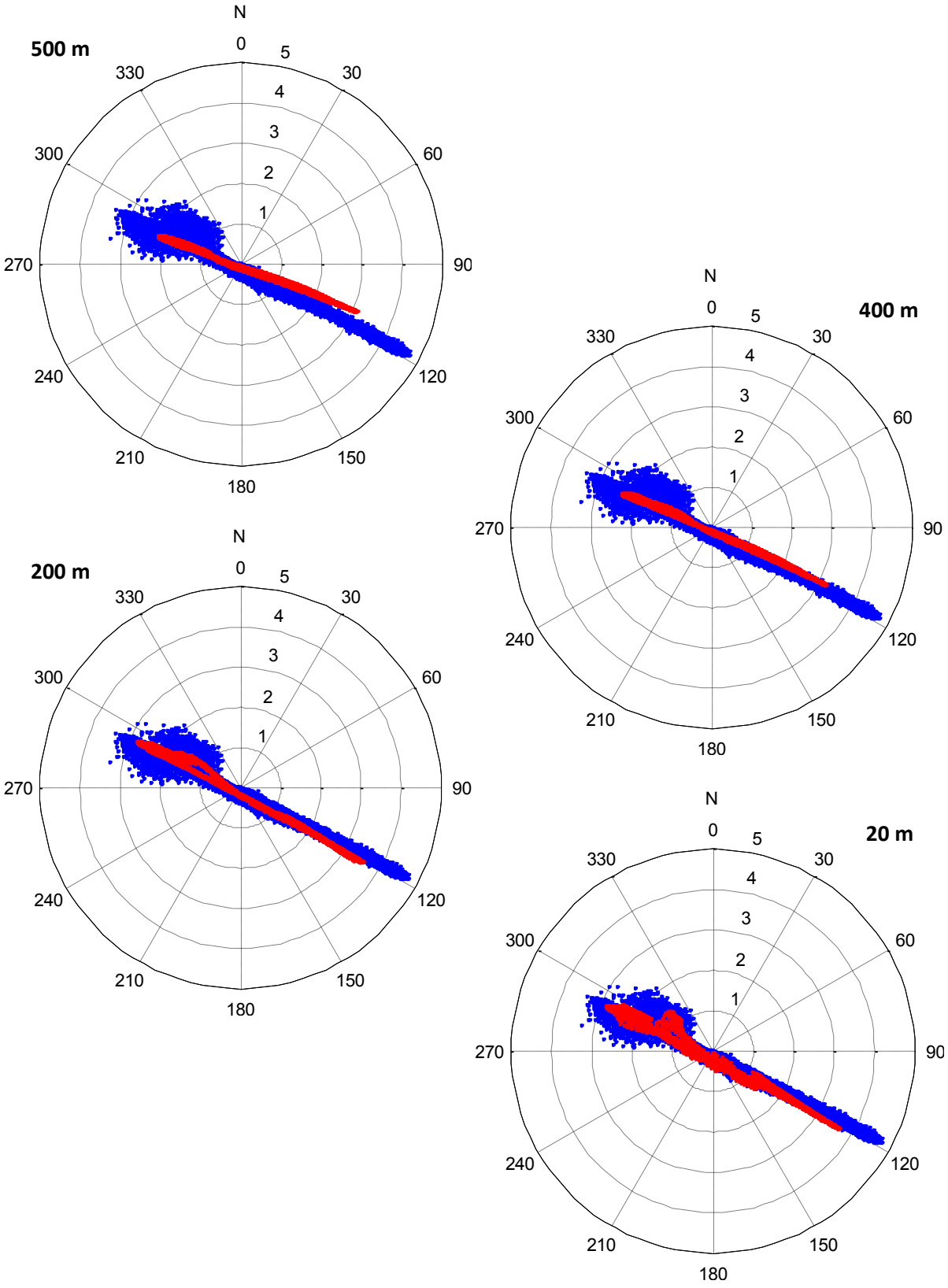

Figure 7.18. Observed (blue) and modelled (red) tidal ellipse at 500, 400, 200 and 20 m resolution (Site D)

7.4. Coriolis force

The Coriolis force is due to the rotation of the Earth on its own axis and the inertia of the mass experiencing the effect. The Earth rotates slowly, hence the Coriolis force is quite small, and its effects generally become noticeable only for motions occurring over large spatial and temporal scales. In this study, the model applies Coriolis forcing with a constant Coriolis parameter calculated by:

$$f = 2\omega \sin(\lambda) = 2(7.292 \times 10^{-5}) \sin(45.365°) = 0.0001$$

where the latitude corresponds to the Crown Lease Area. The Coriolis coefficient may be considered constant across small areas. In this section, simulations were run without including the Coriolis effect to investigate the impact on tidal current energy resource assessment. The Annual Energy Flux changed, on average, by 3.9% compared to simulations including the Coriolis force. The relative error of the Annual Energy Flux with respect to the observed estimates decreased by an average of 2.9%. The root-mean-square error (RMSE) and relative mean absolute error (RMAE) in tidal current speed were reduced by 0.01 m/s and 0.01, respectively, at the four deployment berths.

7.5. Bathymetry resolution

The quality and resolution of bathymetric data will directly influence the ability of a numerical model to replicate flow dynamics. According to the IEC-TC-114 draft standard, the resolution of the bathymetric data should reflect that of the model grid. Therefore, the resolution should be < 500 m for a Feasibility stage assessment, refined to 200 m in regions of bathymetric complexity or < 50 m for Layout Design. In this study, the elevation of nodes in the Minas Channel was interpolated onto the standard 150 m mesh from a 5 m grid prepared by Natural Resources Canada (see Section 5.1.6). Sectional 7.3 already investigated the impact of spatial resolution on tidal current energy resource assessment, however, that represented the simultaneous refinement of model and bathymetric resolution as the 5 m grid was mapped onto the finer mesh. In this section, the aim is to evaluate the impact of the quality/resolution of bathymetric data on resource assessment. For that purpose, the 5 m NRCan grid was resampled to 20, 40, 60, 80, 100, 125 and 150 m and interpolated onto the 20 m mesh to conduct a series of simulations. See Appendix C.10 for a log of the simulations. Note that, for all simulations performed in Section 7.5, the numerical time step was reduced to 2.5 s.

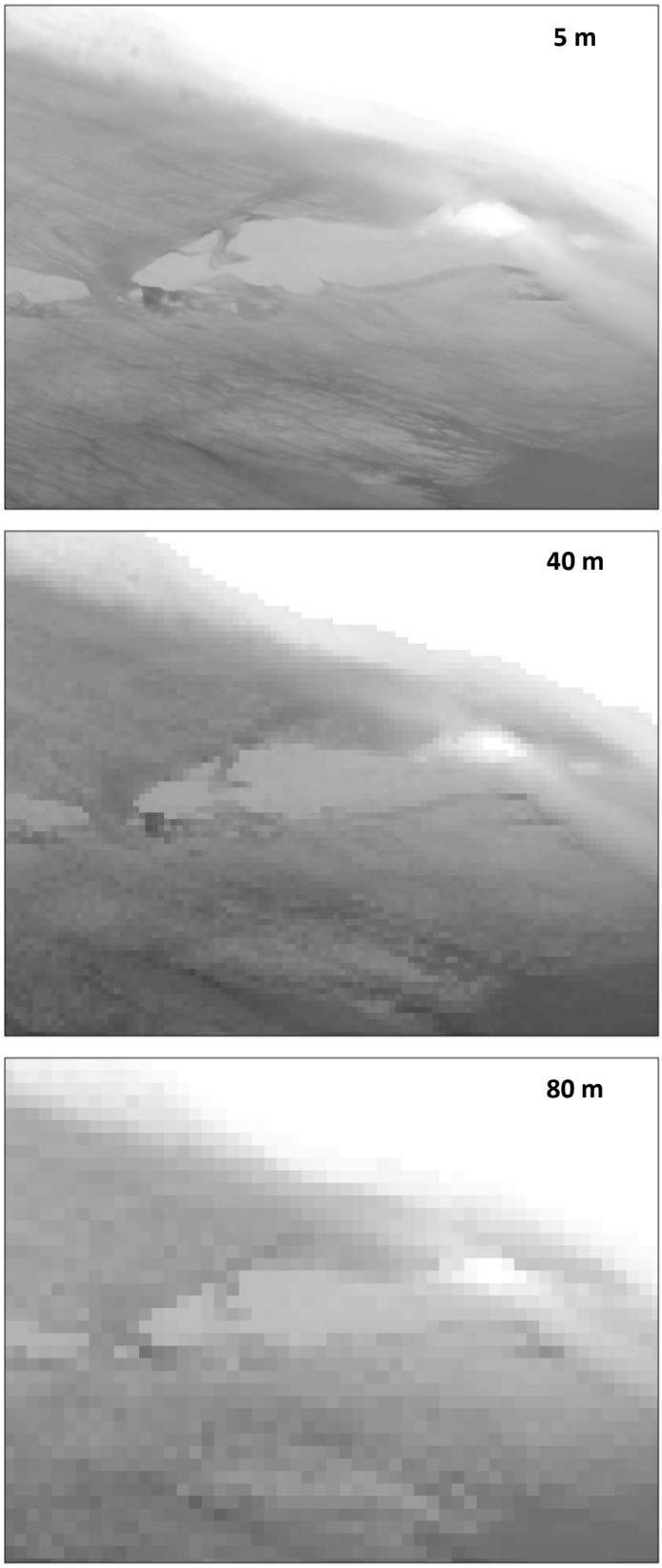

Figure 7.19. Resampled 5, 40 and 80 m bathymetric data

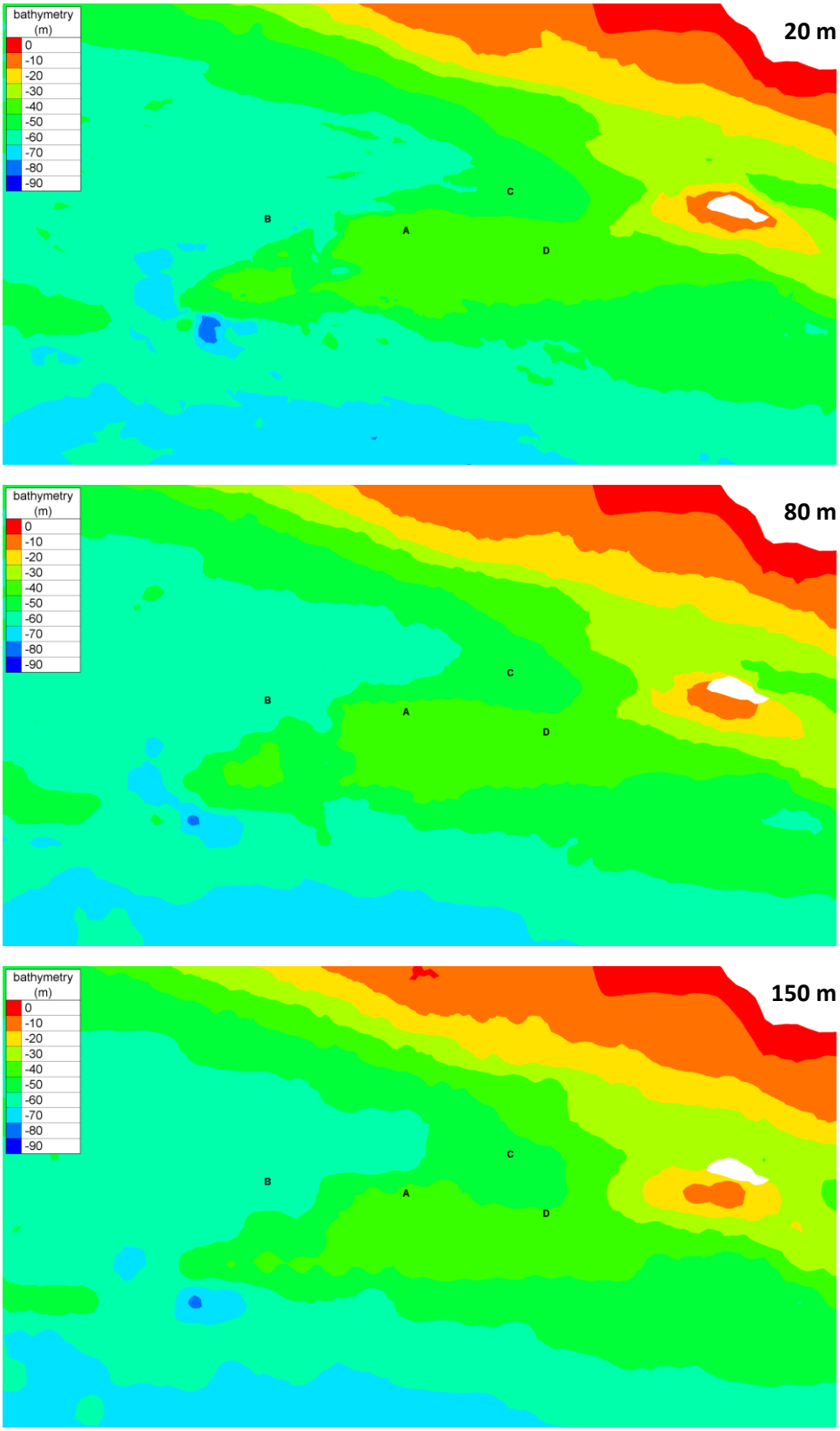

Figure 7.20. Resampled 20, 80 and 150 m bathymetric data mapped onto the 20 m mesh

Figure 7.19 shows examples of the resampled bathymetric data and Figure 7.20 provides examples of the resampled data interpolated onto the 20 m mesh. Sites A, B and D do not show a trend in Annual Energy Flux with improved bathymetric resolution (Figure 7.21). Site C, on the other hand, demonstrates a clear relationship between Annual Energy Flux and local bathymetric resolution. The relationship is illustrated in Figure 7.22 as the relative error in Annual Energy Flux with respect to the observed value. Based on this trend, the relative error in Annual Energy Flux begins by decreasing rapidly and then reaches a plateau: refining bathymetry from 150 to 100 and 100 to 50 m decreases the error by 16.5 and 10.0%, respectively. At that point, diminishing returns are evident as improving bathymetric resolution from 50 to 5 m only reduces the error by 3.3%.

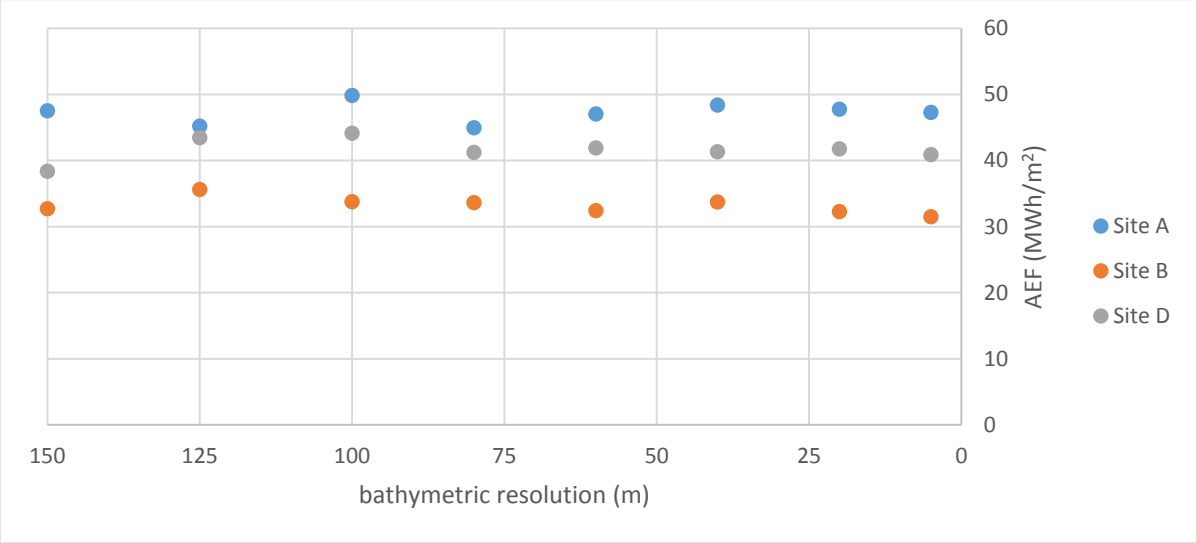

Figure 7.21. Annual Energy Flux as a function of local bathymetric resolution (Site A, B and D)

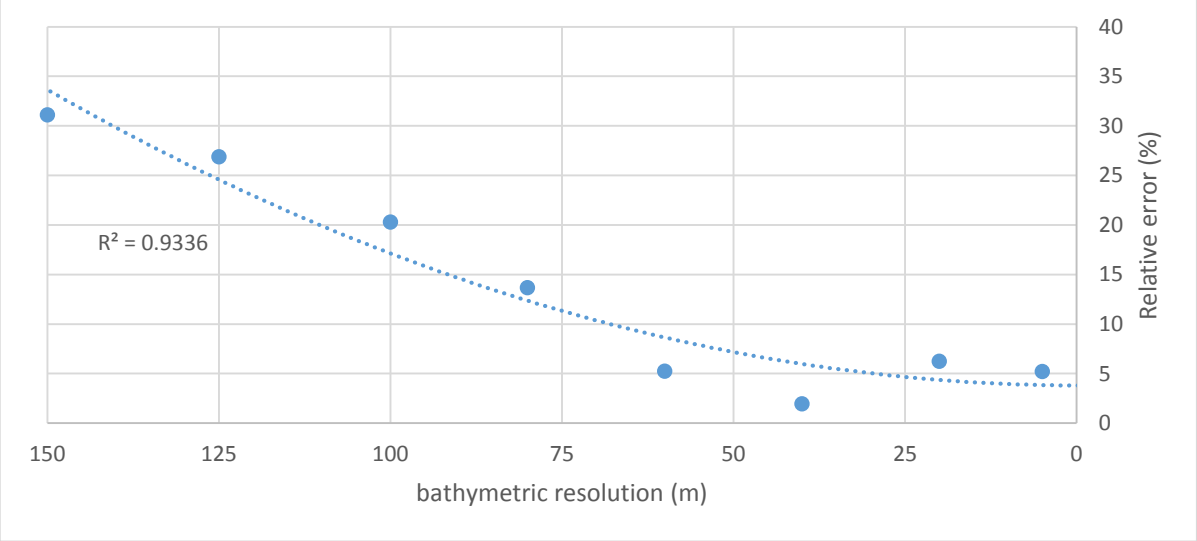

Figure 7.22. Relative error in Annual Energy Flux as a function of local bathymetric resolution (Site C)

7.6. Turbulence model

According to the IEC-TC-114 draft standard, model calibration should include the adjustment of turbulence parameters. Four turbulence models of differing complexity are available to TELEMAC users: constant viscosity, Elder, K-epsilon, and Smagorinsky. In this study, a constant viscosity turbulence model is implemented with an eddy viscosity of 0.0001. Values from 10^{-6} to 10^{0} were tried but had a negligible impact on flow statistics. In this section, simulations were performed on the 150 m mesh with the four available turbulence models to investigate the impact on tidal current energy resource assessment. When the results showed little to no change, the turbulence models were tried on the 50 and 20 m meshes. The simulations used a 2.5 second time step with the exception of the Elder model on the 20 m mesh which necessitated a one second time step. See Appendix C.6 for a log of the simulations.

Table 7.7. Relative error in Annual Energy Flux for the four turbulence models (150 m mesh)

Site	Relative error (%)	Difference (%)		
	Constant viscosity	Elder	K-epsilon	Smagorinsky
A	25.0	+1.3	+0.1	+0.2
B	26.1	+0.9	+0.1	+0.2
C	13.8	+1.8	+0.2	+0.5
D	43.3	+0.8	+0.1	+0.2

Table 7.8. Relative error in Annual Energy Flux for the four turbulence models (50 m mesh)

Site	Relative error (%)	Difference (%)		
	Constant viscosity	Elder	K-epsilon	Smagorinsky
A	18.1	+0.8	+0.1	+0.1
B	25.8	+0.5	+0.1	+0.1
C	9.3	+0.7	-0.1	+0.1
D	42.1	+0.4	+0.0	+0.1

Table 7.9. Relative error in Annual Energy Flux for the four turbulence models (20 m mesh)

Site	Relative error (%)	Difference (%)		
	Constant viscosity	Elder	K-epsilon	Smagorinsky
A	17.2	+3.0	+0.5	+0.1
B	22.8	+2.2	+0.5	+0.2
C	5.1	-3.6	-0.7	-0.3
D	38.9	+2.2	+0.6	+0.2

Tables 7.7, 7.8 and 7.9 show the relative error in Annual Energy Flux for the four available turbulence models on the 150, 50 and 20 m mesh, respectively. The difference compared to the constant viscosity model is < 1% in most cases, and where differences do exist, the more complex turbulence model generally does not improve upon the estimate. Only the results of the Elder model on the 20 m mesh deviate significantly from those of the constant viscosity model and only the prediction at Site C is improved. While more complex turbulence models may not have a significant impact on the Annual Energy Flux as it's computed here, there is still an associated computational cost. Table 7.10 shows the ratio of simulated to real time for these runs. Table 7.11 normalises the ratio with respect to the constant viscosity scheme, which is the most efficient. Compared to the constant viscosity model, the Elder and Smagorinsky models run at 95% speed while the K-epsilon model is slowest at 80%.

Table 7.10. Ratio of simulated to real time in the turbulence model simulations

Mesh	Turbulence model			
	Constant ν_t	Elder	K-epsilon	Smagorinsky
150 m	193	185	156	186
50 m	161	153	129	157
20 m	93	–	73	89

Table 7.11. Relative computational efficiency of the constant viscosity, Elder, K-epsilon and Smagorinsky turbulence models

Mesh	Turbulence model			
	Constant ν_t	Elder	K-epsilon	Smagorinsky
150 m	1.00	0.96	0.81	0.96
50 m	1.00	0.95	0.80	0.97
20 m	1.00	-	0.78	0.95
Average	**1.00**	**0.95**	**0.79**	**0.96**

7.7. Boundary specification (tidal database)

The ocean boundary can be specified with tidal height data from tidal stations, larger-scale hydrodynamic models, and satellite-derived data. In this study, the boundary was specified with published constituent data from two Canadian Hydrographic Service (CHS) tidal stations located at either end of the open boundary. In this section, the boundary is specified with satellite-derived data and regional hydrodynamic models to evaluate the impact on tidal current resource assessment. See Appendix C.8 for a log of the simulations.

- WebTide is a graphical user interface for a tidal prediction program. Predictions can be obtained for any point inside a selected model domain and are based on analyses of ocean model output. Among the available datasets are the *Scotia-Fundy-Maine* (Dupont et al. 2005) and *Global* (Lyard et al. 2006) models.
- *Eastcoast 2001* (Mukai et al. 2002) is a tidal constituent database for the Western North Atlantic, Caribbean and Gulf of Mexico available online at http://adcirc.org/products/adcirc-tidal-databases/. FORTRAN source code extracts all constituents at user-specified locations.
- *TOPEX/Poseidon* (Egbert and Erofeeva 2002) is a global model of ocean tides which assimilates satellite altimetry data. Predictions can be obtained at any point with the MATLAB Tidal Model Driver. The TPXO Global Tidal Solution is available online at http://volkov.oce.orst.edu/tides/global.html.

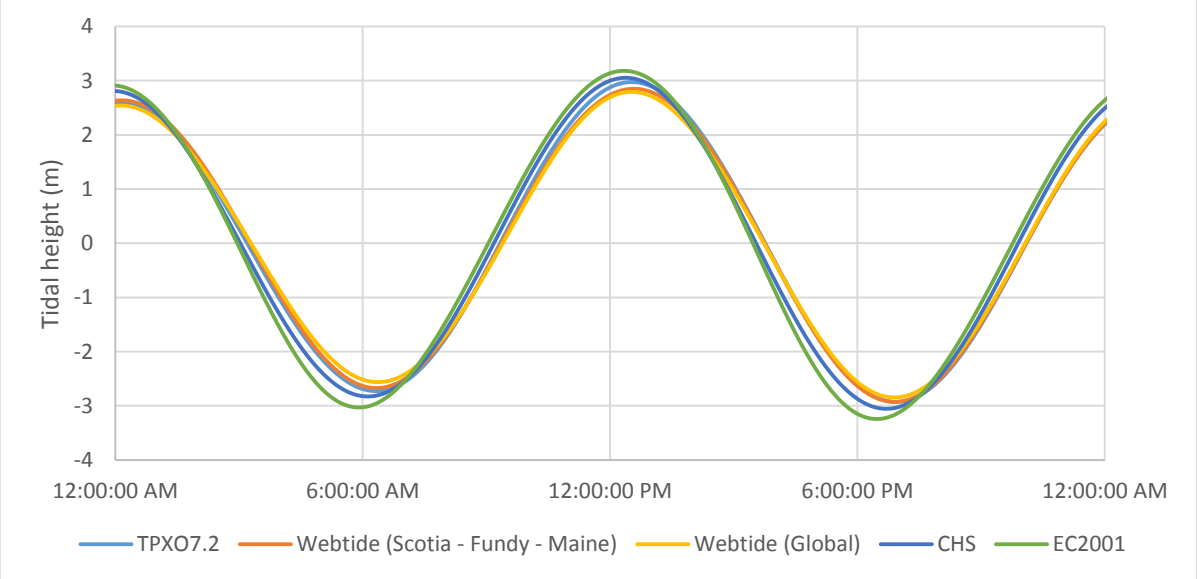

Figure 7.23. Tidal height prediction at Dipper Harbour West on 1st Jan. 2015

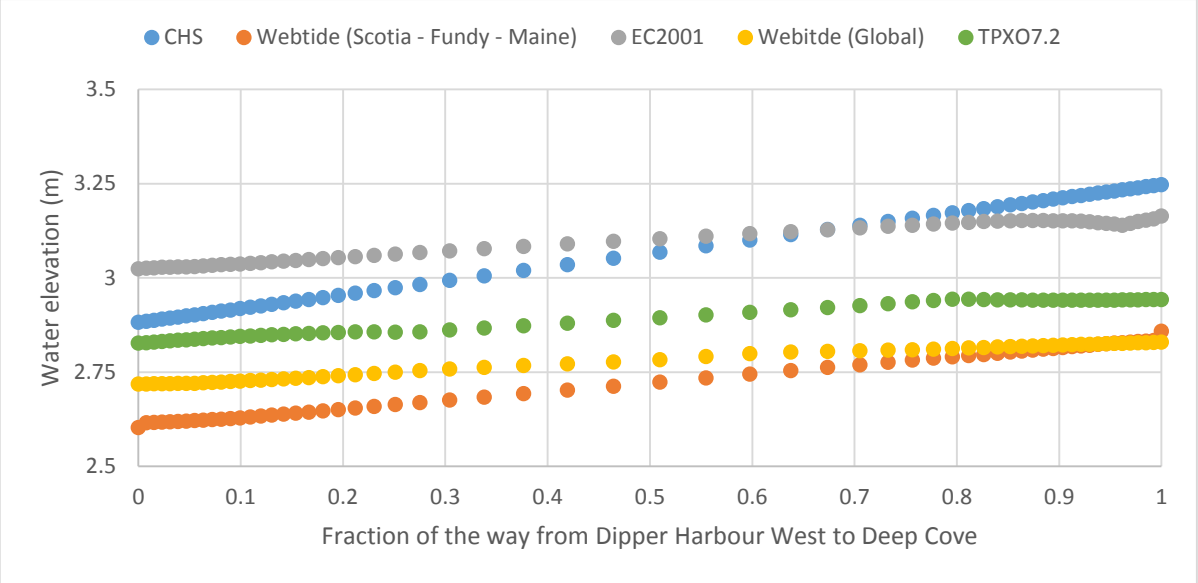

Figure 7.24. Tidal height prediction at the ocean boundary on 1st January 2015

Figure 7.23 illustrates how these tidal databases differ in a tidal height prediction at Dipper Harbour West for January 1st 2015. Similarly, Figure 7.24 shows tidal height predictions along the ocean boundary between Dipper Harbour West and Deep Cove at midnight on January 1st 2015. Differences of up to half a metre are observed. The relative error in Annual Energy Flux modelled with these datasets is compared with that of the standard 8 CHS constituents in Table 7.12. The CHS tidal stations provide the lowest relative error followed by Eastcoast 2001, WebTide (Scotia-Fundy-Maine), TPXO7.2 and WebTide (Global).

Table 7.12. Relative error in Annual Energy Flux for the five tidal databases

Site	Relative error (%)	Difference (%)			
	CHS	EC2001	WebTide (S-F-M)	TPXO7.2	WebTide (Global)
A	26.4	+3.1	+5.7	+11.0	+31.2
B	24.9	+3.6	+5.8	+11.0	+33.1
C	10.9	+3.4	+6.5	+11.4	+35.9
D	42.1	+3.1	+4.3	+8.1	+24.8

7.8. Uncertainty

The last product of Chapter 7 summarises the ~200 simulations comprising the sensitivity analysis. For every simulation presented in this chapter, the measured and modelled time series were directly compared to calculate the mean relative error in tidal current speed with Eq. (5.25). Only tidal velocities > 0.5 m/s were included in the calculation, and model-predicted tidal currents were interpolated using a quadratic polynomial fit for comparison. Figure 7.25 plots the relative error in Annual Energy Flux against the mean relative error in tidal current speed for these ~200 simulations. Table 7.13 recaps key values.

Table 7.13. Relative error in Annual Energy Flux versus relative error in tidal current speed

Tidal current speed Relative error (%)	**Annual Energy Flux** Relative error (%)
0	0
2.5	8
5	15
7.5	22
10	28

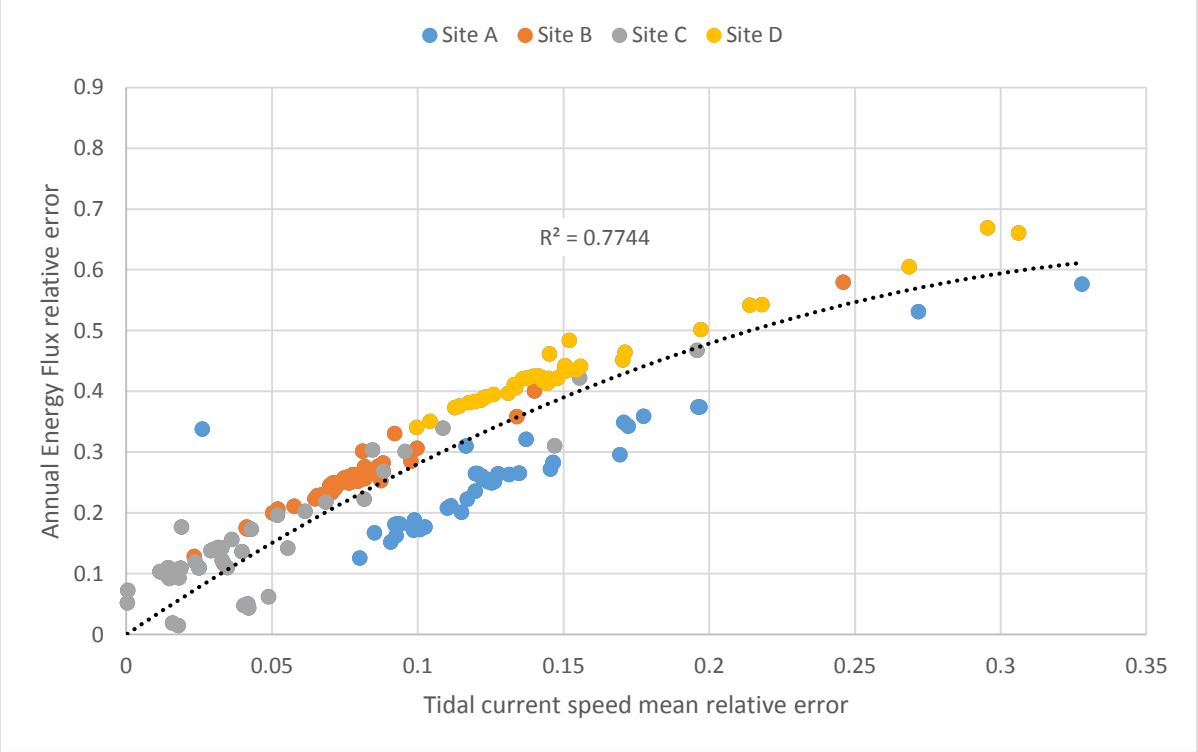

Figure 7.25. Relative error in Annual Energy Flux versus mean relative error in tidal current speed

7.9. Discussion

Chapter 7 tackles an important objective of the thesis, conducting a sensitivity analysis to determine the main sources of error and uncertainty affecting resource assessment, a topic which has yet to be addressed in the literature. In so doing, Chapter 7 touches on two more objectives of the thesis: to establish a firm scientific basis for the IEC-TC-114 draft standard and to develop suggestions for improving and extending future revisions of the standard. Throughout this chapter, it is assumed that while fundamental elements of the hydrodynamic model are being changed, the calibration remains valid. Many of the conclusions and recommendations derived in this chapter are site-specific, but efforts are made toward providing general guidance.

The sensitivity analysis began by investigating T_TIDE, the main harmonic analysis tool throughout the research. Figures 7.1 and 7.2 show the tidal height constituents of amplitude and phase for the M2 tide and 3 leading constituents, respectively, as a function of record length. As record length increases, the range of values returned by T_TIDE narrows. It's important to recognise that the Site B survey on which these tests were performed consists of 46 days of data, therefore, as record length increases the number of unique intervals that can be selected for analysis decreases. While that may be a contributing factor to the narrowing solution it is unlikely to be the only factor, because convergence occurs at ∼28 days for the four constituents shown. Figure 7.3 shows the same experiment performed on tidal current harmonics. A stable solution is reached at ∼28 days as well.

The next set of experiments looked at record length along with the number of constituents fit to the data (Figure 7.4). The results show excessive scatter with a record length of less than 21 days. Readers will recall that Site A was left with only 20 days of useable data. Based on Figure 7.4, tidal height constituents at Site A may have a relative error of about 10%. With a short record length including too many constituents in the analysis produces worse results than including fewer. The record is just not long enough for harmonics of the same species to be parsed. Similarly, with a long record including too few constituents can produce worse results.

The last series of experiments looked at sampling interval/output time step. Figure 7.5 shows tidal height constituents of amplitude and phase for M2, N2, S2 and K1. The solution is stable even up to large sampling intervals, though that may not be the case with a shorter record length. Figure 7.6 shows tidal current constituents for M2, N2, S2 and K1. Tidal current harmonics require a shorter sampling interval for accurate results. Based on these figures, a sampling interval/ output time step

of no more than 2 hours would be recommended. The sensitivity of the Annual Energy Flux to temporal resolution, *i.e.* sampling interval/output time step is shown in Table 7.2. The tidal current energy resource is consistent until the output time step exceeds two hours, at which point the estimates are many orders of magnitude outside the realm of possibility.

Two recommendations can be made based on the results thus far. The standard imposes an observation/simulation period of at least 35 days for the purpose of extracting the requisite 20 harmonic constituents. The experiments performed here indicate that the harmonic constituents of amplitude and phase returned by T_TIDE stabilise at ~28 days. Hence, an observation/simulation period of 28 days would be the recommended minimum. Likewise, Robins *et al.* (2015) indicate that robust estimates of the long-term power generation potential of a site require an observation/simulation period of at least 30 days. European Marine Energy Centre (EMEC) guidelines indicate that for later stages of site characterisation at least 20 tidal constituents should be resolved, which should be possible with a month of data (Legrand 2009). As for temporal resolution, the model output time step should never exceed 2 hours.

The next section of the sensitivity analysis investigated the number of harmonic constituents modelled at the boundary. With Figure 7.7 the author was looking for a relationship between the Annual Energy Flux and the fraction of the tidal amplitude modelled at the boundary. While there is a positive trend, the relationship was found to be more complex than that. Instead, the fraction of the Annual Energy Flux modelled by each successive constituent added at the boundary was calculated (Table 7.3). A pattern emerged whereby seven constituents appeared to be responsible for the majority of the Annual Energy Flux: M2, N2, S2, K2, NU2, M6 and M4. Figure 7.8 shows the cumulative fraction of the Annual Energy Flux modelled at Sites A, B and D as harmonics are added at the boundary. The pattern is identical at all four sites, but in the case of Site C, K2 decreases the Annual Energy Flux by 1% instead of the increase seen at Sites A, B and D. Table 7.4 shows the average contribution of the 7 'key' constituents to the Annual Energy Flux. Together, they represent 83% of the tidal amplitude at the ocean boundary and 99.9% of the Annual Energy Flux at the FORCE berths. The M2 tide alone accounts for an average 89% of the Annual Energy Flux. It is likely inaccurate to say that the remaining 13 constituents have no impact. Their influence may be more evident in tidal height, or elsewhere in the Bay of Fundy. It's also possible that over a year, the net effect of these constituents on the Annual Energy Flux is null. However, at finer time scales, they may have an important impact on accurate predictions of tidal currents.

Comparisons may be drawn to other studies in this matter. Robins *et al.* (2015) found that, in the northwest European shelf seas, the contribution from M2 and S2 accounts for 75% or more of the annual practical power predicted by the 5 primary harmonics, with an average contribution of 93%. In this study, M2 and S2 account for an average contribution of 92.5% of the Annual Energy Flux predicted by the 20 primary harmonics. Sutherland *et al.* (2007) found that by including the 8 major constituents for the Johnston Strait, the power estimates from the M2 tide are multiplied by 1.12. In this study, by including the 7 'key' harmonics the Annual Energy Flux from M2 is multiplied by 1.12. Blanchfield *et al.* (2008b) showed that by including the 3 dominant constituents in Haida Gwaii the extractable power increased by 9%. In this study, by including the 3 dominant constituents the predicted Annual Energy Flux increased by 8%.

In Section 4.5, the observed tidal current harmonics were derived. It's interesting to note that of the seven 'key' constituents, five were among the top ten tidal current constituents derived from measurements. The two which are not – NU2 and K2 – are not included in analyses by T_TIDE without greater record lengths. Instead, the L2 constituent (of the same species) is present.

Recommendations may be drawn from these results. Firstly, tidal amplitude at the open boundary by itself is not a reliable indicator of the importance of a constituent for modelling tidal currents within the domain. Secondly, while the draft standard recommends that a minimum number of constituents be modelled at the boundary, this research indicates that it is not a matter of how many, but of which. As recommended by Robins *et al.* (2015), it would be reasonable for Feasibility studies to model only M2 and S2, adding more constituents at later stages. Early in the resource assessment, field data could be used in conjunction with harmonic analysis of tidal currents in order to determine which constituents are significant to model Annual Energy Flux at the project site. Take note that while only a limited number of constituents may be important to model Annual Energy Flux, accurate modelling of the resource at finer time scales likely necessitates more. For instance, Robins *et al.* (2015) showed that the contribution from M2 and S2 to the annual practical power can be as low as 75%. Future research should investigate the contribution of constituents to the kinetic energy flux at finer time scales than annual, in order to determine which are necessary to accurately predict power output on a daily, weekly or monthly basis.

The importance of hydrodynamic model spatial resolution is unknown for tidal current energy resource assessment. Section 7.3 of the sensitivity analysis seeks to address that knowledge gap.

Although the Annual Energy Flux at site B does not show any trend with increasing mesh resolution (Figure 7.14), Sites A, C and D demonstrate a strong, linear relationship.

At any point within a hydrodynamic model, there is a relationship between model grid discretisation and model-predicted flow properties. As local geometry is modelled more accurately, flow dynamics are better replicated. This continues until an equivalent geometry is reached which replicates the flow properties most accurately. In other words, improvement followed by a plateau. If the relative error in Annual Energy Flux at Site B does not improve with finer spatial discretisation, that implies that the model-predicted tidal currents are not improving. If the flow properties are not improving then the plateau has already been reached. If errors are still present, then either the measurements are responsible or the model is. For example, the forcing functions or bathymetry may be inaccurate.

Sites A, C and D, on the other hand, show considerable improvement with refinement of the mesh. Interestingly, the linear trend has nearly identical slopes at the three sites. The relationship suggests that a refinement in resolution of 50, 100 and 150 m would yield 3.3, 6.6, and 10% improvements of the relative error in Annual Energy Flux, respectively. Evidently, the linear trend cannot continue indefinitely. If refinement of the grid were to continue on to resolutions finer than 20 m a plateau would be attained eventually. It's important to keep in mind that the improved accuracy comes at a computational cost, illustrated in Figure 7.16. Figure 7.17 demonstrates why the Annual Energy Flux estimates are improving at these sites. As the local grid resolution is refined, the model's ability to simulate the peak tidal current speeds is improving. Likewise, Figure 7.18 illustrates how the higher resolution grid allows for finer variations in flow direction and magnitude to be replicated. At 20 m resolution, the scatter on the ebb tide is captured.

Although the relationship shown is sure to be site-specific, the need for fine grid resolution in resource assessments of dynamic tidal regions has been illustrated. Areas of interest for tidal current energy often feature complex bathymetries responsible for the powerful tidal flows. As suggested by O'Rourke *et al.* (2010), the importance of model grid discretisation in tidal current energy resource assessment has been underestimated. An appropriately fine mesh is important to simulate momentum/advection processes and accurately model currents. The draft standard recommends a model grid resolution refined to 200 m in regions of bathymetric complexity for a Feasibility study. According to Figure 7.15, the corresponding relative error in Annual Energy Flux for a 200 m grid would be as low as 20%. In order to achieve a relative error below 10%, 20 m resolution is required, which the standard only recommends for Layout Design studies. In addition, IEC-TC-114 protocols do

not require any comparisons of tidal current speed during model calibration. It is suggested, but not required. Mode calibration should include mandatory checks of modelled tidal velocity in the event that model grid refinements are needed before proceeding with the resource assessment.

The impact of the Coriolis force on resource assessment was evaluated. No guidance is provided in the draft standard as to whether Coriolis forcing should be included in the modelling. The root-mean-square and relative mean absolute errors in tidal current speed were changed by 0.01 m/s and 1%, respectively, at the four FORCE berths by excluding the Coriolis force. Hence, the influence of the Coriolis effect is judged to be negligible. The result was expected because the effects of the Coriolis force generally become noticeable only for motions occurring over large spatial and temporal scales. The domain of the upper Bay of Fundy is too small to see a significant impact. Resource assessments in domains of a similar scale can choose to neglect the Coriolis effect.

The next section looked at the impact of bathymetry resolution independent of mesh resolution. The impact was expected to be significant due to the prominence of the Crown Lease Area shelf in local bathymetry, but Sites A, B and D did not show any trend between Annual Energy Flux and bathymetric resolution (Figure 7.21). In spite of any measurement errors that may be present in the observed data, the trends in Annual Energy Flux should be valid. Just as with spatial resolution, the expected trend is improvement followed by a plateau. It may be that due to the positioning of the three sites, 150 m is bathymetry is not coarse enough to see a decline in model accuracy at those locations: the shelf is still sufficiently well-defined that flows through B, A and D are represented in an equivalent manner. Additionally, the present research uses depth-averaged velocities to assess the resource. Bathymetry may have played a more important role at these sites in 3D flow with an assumed device hub height. Future research on Layout Design stage resource assessment should reinvestigate the impact of bathymetry resolution in a 3D model.

At Site C, there exists a clear relationship between Annual Energy Flux and local bathymetric resolution (Figure 7.22). The sensitivity of Site C to bathymetry may have to do with its location in a depression to the west of Black Rock Island. The definition of Black Rock Island changes considerably with bathymetric resolution and flow dynamics at Site C change accordingly on the ebb. Based on the relationship at Site C, refining bathymetric resolution from 150 to 100 and 100 to 50 m decreases the relative error in Annual Energy Flux by 16.5 and 10.0%, respectively. At that point, diminishing returns are evident as improving bathymetric resolution from 50 to 5 m only reduces the relative error in Annual Energy Flux by 3.3%. Again, the relationship shown is sure to be site-specific. If the results at

Site C are applicable to other similarly complex dynamic tidal regions, it would be possible to conclude that a 10% relative error in Annual Energy Flux requires bathymetric data with approximately 75 m resolution (if grid resolution is not limiting). Considering the site-specific nature of the relationship shown at Site C, bathymetric surveys should start by collecting relatively coarse data. Refined datasets can be acquired over time to improve hydrodynamic modelling in regions of bathymetric complexity.

The impact of turbulence modelling on resource assessment was evaluated. Elder, K-epsilon and Smagorinsky models were compared with the default constant viscosity scheme. In most cases, the difference in Annual Energy Flux is < 1% and where differences do exist the more complex turbulence model does not improve upon the assessment. Only the results of the Elder model on the 20 m mesh deviate significantly from those of the constant viscosity model and only the prediction at Site C is improved (Table 7.9). Although the more sophisticated turbulence models don't have a significant impact on the Annual Energy Flux, they do have a significant impact on computational cost (Table 7.11). Compared to the constant viscosity model, the Elder and Smagorinsky models run at 95% speed while the K-epsilon model is slowest at 80%. The draft standard does not provide any suggestions with regard to turbulence modelling. In view of the sensitivity analysis, there is no reason to recommend the more complex and computationally expensive turbulence models over the constant viscosity scheme: the tidal current resource was unaffected. Future research on Layout Design stage resource assessment should reinvestigate the impact of turbulence modelling in a 3D model with compatibly fine spatial and temporal resolution.

The ocean boundary can be specified with tidal height data from tidal stations, larger-scale hydrodynamic models, and satellite-derived data. In this study, the boundary was specified with published constituent data from two Canadian Hydrographic Service posts located at either end of the ocean boundary. For the sensitivity analysis, the boundary was specified with satellite-derived data (TOPEX/Poseidon) and regional hydrodynamic models (EC2001, WebTide) to evaluate the impact on resource assessment. Figure 7.24 shows tidal height predictions along the ocean boundary between Dipper Harbour West and Deep Cove at midnight on January 1st 2015. In Section 5.5, linear interpolation of water elevation between the boundary stations was listed as a source of error. However, Figure 7.24 shows that most of the solutions produce a more or less linear surface. The Annual Energy Flux modelled with these databases is compared to that of the standard 8 CHS constituents in Table 7.12. The CHS tidal stations provide the lowest relative error, followed by Eastcoast2001, WebTide (Scotia-Fundy-Maine), TPXO, and WebTide (Global). Thus, wherever possible

models should be forced with local measurements rather than large-scale hydrodynamic models. It's acknowledged that for hydrodynamic models extending out to deep ocean water depths, the reliability and accuracy of satellite-derived data is increased.

Throughout Chapter 7, the sensitivity of tidal current energy resource assessment to various numerical parameters has been tested. The tidal energy resource, it's been said many times, is the velocity probability distribution. All of the parameters evaluated throughout Chapter 7 have been affecting the velocity probability distribution. Bearing that in mind, Figure 7.25 was produced so as to summarise the ∼200 simulations comprising the sensitivity analysis. The figure shows relative error in Annual Energy Flux as a function of mean relative error in tidal current speed. For example, a model with 5% mean relative error in tidal current speed can expect a relative error of about 15% in Annual Energy Flux. This is stated, but not elaborated upon, in the draft standard. Furthermore, if that model reduces its mean relative error in tidal current speed to 2.5%, regardless of the means by which that's achieved, the relative error in Annual Energy Flux should be reduced to about 8%.

8. Conclusions

The present research sought to appraise the IEC-TC-114 technical specification for tidal energy resource assessment and characterisation in terms of ease of use, accuracy, scientific basis, and sources of error. To that end the FORCE test site in the Bay of Fundy was adopted for pilot application of the draft standard. The desired outcomes of this work are user guidance, suggestions to improve and extend future revisions of the draft standard, and a comprehensive assessment of the tidal energy resource at the FORCE project site.

The draft standard can be applied with moderate expenses and computational effort. However, the text is quite dense and often references supplemental materials. This research has highlighted the need for a user-friendly, all-in-one, plain language guide to facilitate use of the IEC-TC-114 methodology. Accuracy varies significantly from site to site. The model developed according to standard specifications for a Feasibility assessment yielded relative errors in Annual Energy Flux from 11 to 42%. At locations where the field data did not require correction the relative errors were from 11 to 15%. A review of the state of the art in Chapter 2 showed that the velocity probability distribution and 'per-generator' method of resource assessment prescribed by the draft standard is well grounded in the scientific literature.

A sensitivity analysis was carried out in Chapter 7 to identify the main sources of error and uncertainty affecting resource assessment:

- Accurate and precise tidal analysis requires an observation/simulation period of ≥ 28 days and a sampling interval/output time step of < 2 hours.
- Feasibility assessments may model only M2 and S2 which account for ∼93% of the Annual Energy Flux.
- Specifying the ocean boundary with local data products (*e.g.* tidal height stations) produced more accurate assessments than regional/global solutions.
- The required model spatial resolution for tidal energy resource assessment has thus far been underestimated. There was a linear relationship between model spatial resolution and relative error in Annual Energy Flux at 3 of 4 sites: 50 m refinement in spatial resolution decreased relative error by 3.3%.

- The relationship between bathymetry resolution and relative error in Annual Energy Flux was significant at 1 of 4 sites. Therefore, 150 m bathymetry may be sufficient for Feasibility assessments.
- Relative error in Annual Energy Flux correlates with mean relative error in tidal current speed (*e.g.* 5% MRE in tidal current speed = 15% RE in Annual Energy Flux). Validating against tidal velocity thus quantifies the error in resource assessment.

Chapter 3 developed recommendations to improve and extend future revisions of the standard in view of the preceding literature review. First and foremost, the draft standard is vague. No specific recommendations are made with respect to: bathymetry resolution, meteorological phenomena, turbulence, horizontal density gradients, suspended sediment load, and wave-current interactions. When specific requirements are provided they are overly broad, *e.g.* model spatial resolution < 500 m or 4 - 8 constituents for modelling the driving boundary. Although this gives users more flexibility it fails to standardise resource assessment. It may be that there is a lack of evidence to support specific guidance. Where science-based recommendations are unclear or unavailable the standard should adopt a best practice. For example, the standard does not provide targets for model calibration or validation: to support evidence-based practice and standardisation, it could include a review of values from published tidal energy resource assessments (*e.g.* Table 3.2).

The flaws and limits discussed here are sometimes indicative of areas of ongoing research. For example, new studies on the impact of wave-current interactions on the tidal energy resource necessitate updating the relevant clause. A linear relationship between kinetic energy flux and average wave height proposed by Lewis *et al.* (2014) may provide a simple method to incorporate wave-current interactions in resource assessments.

The technical specification is only appropriate for individual or sparsely arrayed TECs extracting a negligible fraction of the theoretical resource. And yet, it's believed that commercial deployments of TECs will occur in arrays, where the proposed methods are inappropriate. The draft standard must include a comprehensive procedure for modelling energy extraction to overcome these limitations, for instance, an augmented drag method.

The end product of the IEC-TC-114 methodology is Annual Energy Production. Although useful, this metric is insufficient. The key advantage of tidal power over established renewable is its

predictability. The standard should require users to quantify the average monthly, weekly, and daily energy production in addition to the range.

An assessment of the tidal energy resource at the four FORCE berths was carried out in Chapter 6. The average observed and modelled Annual Energy Flux were 48 and 34 MWh/m^2 respectively. The average observed and modelled Annual Energy Production were 5.2 and 4.4 GWh respectively. It was concluded that Annual Energy Production as defined by the IEC-TC-114 technical specification is inappropriate for model validation or sensitivity analysis. It is device-specific and does not reflect the ability of the model to replicate flow properties.

The research presented here is a case study: the findings of the sensitivity analysis are site-specific. However, a few generalisations can be made. Numerous studies around the world (Robins *et al.* 2015; Sutherland *et al.* 2007; Blanchfield *et al.* 2008b) corroborate that M2 and S2 account for 93% of the tidal energy resource. Although the relationship between model spatial resolution and relative error in Annual Energy Flux does not extend to all sites, the case of a narrow channel accelerating tidal flows is common among sites targeted for tidal power development. Thus, similar relationships may apply elsewhere. Similarly, 150 m bathymetry may be sufficient for Feasibility stage resource assessments at comparable locations. Though not all lessons learned here may apply elsewhere, this research is intended to promote evidence-based practices in tidal energy resource assessment.

9. Recommendations for future work

The present research has enabled the author to recognise the shortcomings of the IEC-TC-114 standard and of the literature on tidal current energy resource assessment. As a result, the following directions for future work are provided:

- With the present work, the feasibility stage (regional scale) resource assessment has been addressed. The next step is to carry out a similar sensitivity analysis at the **design stage** (local scale). The design stage model should resolve the vertical dimension.
- Lewis *et al.* (2015) suggested that the assumption of **rectilinear flow** may overestimate the tidal current energy resource by ~6%, but the study was conducted at a large scale with the farm method and used the undisturbed kinetic energy flux as a metric for comparison. A case study following the 'per-generator' method and calculating the annual energy production would offer a more practical understanding of the losses to expect.
- Evans *et al.* (2015) showed that **depth-averaging** tidal velocity data across the entire water column instead of over the depth span of the turbine misrepresents the tidal current resource by 12.9 to 23.4%. An interesting idea would be to compare resource assessments at a site using measured data, 2D modelling with power laws, and 3D modelling.
- Lewis *et al.* (2014) and Hashemi *et al.* (2015) showed that **wave-current interactions** can decrease the tidal current resource by > 15%. However, both studies used depth-averaged velocities to compute the change in kinetic energy flux. It would be interesting to conduct an assessment looking at the magnitude of the effect on annual energy production at different depths in the water column.
- Creating a **site selection** assistance tool could be of benefit to potential developers and to Canada's marine renewable energy sector. The software would take input from a hydrodynamic model and account for the factors outlined in Section 2.10 to identify suitable development sites. The program could then estimate annual energy production for an isolated turbine and display useful location information (*e.g.* wave climate, tidal data). User should have the option to input device parameters (*e.g.* dimensions, power curve, maximum bed slope).
- **Wind**, **storm surge, suspended sediment load, stratification,** and **drag on support structures** are not currently addressed in the literature.

- Although research has shown the importance of **tidal asymmetry** in quantifying the tidal current resource (*e.g.* Neill *et al.* 2014; Robins *et al.* 2015), there is currently no appropriate metric to aid in decision-making. Ramos and Iglesias (2013) have taken steps in this direction with the Tidal Stream Exploitability index which accounts for mid-flood and mid-ebb velocities. Specifications for a number of devices are now publicly available, it should be possible to identify an appropriate metric and a threshold at which a site is no longer economically viable.

10. References

Adcock, T. A. A., Draper, S., Houlsby, G. T., Borthwick, A. G. L., & Serhadlioğlu, S. (2013). The available power from tidal stream turbines in the Pentland Firth. *Proceedings of the Royal Society A: Mathematical, Physical and Engineering Science*, *469*(2157), 1471–2946.

Arcement, G. J., & Schneider V.R. (1989). Guide for selecting Manning's roughness coefficients for natural channels and flood plains. United States Geological Survey Water-supply Paper 2339.

Aretxabaleta, A. L., McGillicuddy, D. J., Smith, K. W., & Lynch, D. R. (2008). Model simulations of the Bay of Fundy Gyre: 1. Climatological results. *Journal of Geophysical Research: Oceans*, *113*(10), 1–16.

Atwater, J. F., & Lawrence, G. A. (2011). Regulatory, design and methodological impacts in determining tidal-in-stream power resource potential. *Energy Policy*, *39*(3), 1694–1698.

Bahaj, A. S., & Myers, L. E. (2003). Fundamentals applicable to the utilisation of marine current turbines for energy production. *Renewable Energy*, *28*(14), 2205–2211.

Bahaj, A. S., & Myers, L. (2004). Analytical estimates of the energy yield potential from the Alderney Race (Channel Islands) using marine current energy converters. *Renewable Energy*, *29*(12), 1931–1945.

Bai, G., Li, J., Fan, P., & Li, G. (2013). Numerical investigations of the effects of different arrays on power extractions of horizontal axis tidal current turbines. *Renewable Energy*, *53*, 180–186.

Black and Veatch Consulting Ltd. (2004). *UK, Europe and global tidal stream energy resource* assessment. Peer review issue 107799/D/2100/05/1, Carbon Trust, London.

Black and Veatch Consulting Ltd. (2005). *Phase I UK tidal stream energy resource assessment.* Technical report 107799/D/2200/03, Carbon Trust, London.

Blanchfield, J., Garrett, C., Wild, P., & Rowe, A. (2008a). The extractable power from a channel linking a bay to the open ocean. *Proceedings of the Institution of Mechanical Engineers, Part A: Journal of Power and Energy*, *222*(3), 289–297.

Blanchfield, J., Garrett, C., Rowe, A., & Wild, P. (2008b). Tidal stream power resource assessment for Masset Sound, Haida Gwaii. *Proceedings of the Institution of Mechanical Engineers, Part A: Journal of Power and Energy*, *222*(5), 485–492.

Blunden, L. S., & Bahaj, A. S. (2007). Tidal energy resource assessment for tidal stream generators, *221*, 137–146.

Blunden, L. S. (2009). New approach to tidal stream energy analysis at sites in the English Channel. Retrieved from http://eprints.soton.ac.uk/73610/

Blunden, L. S., Bahaj, A. S., & Aziz, N. S. (2013). Tidal current power for Indonesia? An initial resource estimation for the Alas Strait. *Renewable Energy*, *49*, 137–142.

Boehlert G. W., & Gill, A. B. (2010). Environmental and ecological effects of ocean renewable energy development. *Oceanography*, *23*(2), 68–81.

Brière, C., Abadie, S., Bretel, P., & Lang, P. (2007). Assessment of TELEMAC system performances, a hydrodynamic case study of Anglet, France. *Coastal Engineering*, *54*(4), 345–356.

Brooks, D. A. (2006). The tidal-stream energy resource in Passamaquoddy-Cobscook Bays: A fresh look at an old story. *Renewable Energy*, *31*(14), 2284–2295.

Bryden, I. G., Naik, S., Fraenkel, P., & Bullen, C. R. (1998). Matching tidal current plants to local flow conditions. *Energy*, *23*(9), 699–709.

Bryden, I. G., Grinsted, T., & Melville, G. T. (2004). Assessing the potential of a simple tidal channel to deliver useful energy. *Applied Ocean Research*, *26*(5), 198–204.

Bryden, I. G., Couch, S. J., Owen, A., & Melville, G. (2007). Tidal current resource assessment. *Proceedings of the Institution of Mechanical Engineers, Part A: Journal of Power and Energy*, *221*(2), 125–135.

Carballo, R., Iglesias, G., & Castro, A. (2009). Numerical model evaluation of tidal stream energy resources in the R??a de Muros (NW Spain). *Renewable Energy*, *34*(6), 1517–1524.

Chanson, H. (2011). Current knowledge in tidal bores and their environmental, ecological and cultural impacts. *Environmental Fluid Mechanics*, *11*(1), 77–98.

Charlier, R. H. (2007). Forty candles for the Rance River TPP tides provide renewable and sustainable power generation. *Renewable and Sustainable Energy Reviews*, *11*(9), 2032–2057.

Charlier, R. H., & Finkl, D.W. (2009). *Ocean energy.* New York, NY: Springer

Chen, Y., Lin, B., & Lin, J. (2014). Modelling tidal current energy extraction in large area using a three-dimensional estuary model. *Computers & Geosciences*, *72*, 76–83.

Clark, R. H. (2007). *Elements of tidal-electric engineering*. Hoboken, NJ: Wiley.

Codiga, D. L. (2011). Unified Tidal Analysis and Prediction Using the UTide Matlab Functions, 59.

Coles, D. S., Blunden, L. S., & Bahaj, A. S. (2013). Resource Assessment of Large Marine Current Turbine Arrays.

Couch, S. J., & Bryden, I. (2006). Tidal current energy extraction: hydrodynamic resource characteristics. *Proceedings of the Institution of Mechanical Engineers, Part M: Journal of Engineering for the Maritime Environment*, *220*(4), 185–194.

Cousineau, J. (2012). *Hydrodynamic impacts of tidal lagoons in the upper Bay of Fundy*. PhD Thesis, University of Ottawa.

Cousineau, J., Nistor, I., & Cornett, A. (2012). Hydrodynamic impacts of tidal power lagoons in the Bay of Fundy. *Coastal Engineering Proceedings*, *1*(33*)*.

Crowe, C. T., Elger, D. F., Williams, B. C., & Roberson, J. A. (2009). *Engineering fluid mechanics*. Hoboken, NJ: Wiley.

Cummins, P. F. (2013). The extractable power from a split tidal channel: An equivalent circuit analysis. *Renewable Energy*, *50*, 395–401.

Defant, A. (1961). *Physical Oceanography.* New York, NY: Pergamon Press.

Douglas, C. A., Harrison, G. P., & Chick, J. P. (2008). Life cycle assessment of the Seagen marine current turbine. *Proceedings of the Institution of Mechanical Engineers, Part M: Journal of Engineering for the Maritime Environment*, *222*(1), 1–12.

Dupont, F., Hannah, C. G., & Greenberg, D. (2005). Modelling the sea level of the upper Bay of Fundy. *Atmosphere-Ocean*, *43*(1), 33–47.

Egbert, G. D., & Erofeeva, S. Y. (2002). Efficient inverse modeling of barotropic ocean tides. *Journal of Atmospheric and Oceanic Technology*, *19*(2), 183–204.

Elghali, S. E. Ben, Benbouzid, M. E. H., & Charpentier, J. F. (2007). Marine Tidal Current Electric Power Generation Technology: State of the Art and Current Status. *2007 IEEE International Electric Machines & Drives Conference*, *2*, 1407–1412.

Esteban, M., Leary, D., Zhang, Q., Utama, A., Tezuka, T., & Ishihara, K. N. (2011). Job retention in the British offshore sector through greening of the North Sea energy industry. *Energy Policy*, *39*(3), 1543–1551.

Esteban, M., & Leary, D. (2012). Current developments and future prospects of offshore wind and ocean energy. *Applied Energy*, *90*(1), 128–136.

Etemadi, A., Emami, Y., AsefAfshar, O., & Emdadi, A. (2011). Electricity generation by the tidal barrages. *Energy Procedia*, *12*, 928–935.

Evans, E. M. (1987). Tidal stream energy. PhD Thesis, Plymouth Polytechnic.

Evans, P., Mason-Jones, A., Wilson, C., Wooldridge, C., O'Doherty, T., & O'Doherty, D. (2015). Constraints on extractable power from energetic tidal straits. *Renewable Energy*, *81*, 707–722.

Fairley, I., Evans, P., Wooldridge, C., Willis, M., & Masters, I. (2013). Evaluation of tidal stream resource in a potential array area via direct measurements. *Renewable Energy*, *57*, 70–78.

Fischer, H. B. (1979). *Mixing in inland and coastal waters*. Waltham, MA: Academic Press.

Foreman, M. G. G., Cherniawsky, J. Y., & Ballantyne, V. A. (2009). Versatile harmonic tidal analysis: Improvements and applications. *Journal of Atmospheric and Oceanic Technology*, *26*(4), 806–817.

Forrester, W. D. (1983). *Canadian tidal manual*. Ottawa, ON: Department of Fisheries and Oceans.

Fraenkel, P. L. (2002). Power from marine currents. *Proceedings of the I MECH E Part A Journal of Power and Energy*, *216*(1), 1–14.

Fraenkel, P. L. (2007). Marine current turbines: pioneering the development of marine kinetic energy converters. *Proceedings of the Institution of Mechanical Engineers, Part A: Journal of Power and Energy*, *221*(2), 159–169.

Frid, C., Andonegi, E., Depestele, J., Judd, A., Rihan, D., Rogers, S. I., & Kenchington, E. (2012). The environmental interactions of tidal and wave energy generation devices. *Environmental Impact Assessment Review*, *32*(1), 133–139.

Garrett, C. (1972). Tidal Resonance in the Bay of Fundy and Gulf of Maine. *Nature*, *238*(5365), 441–443.

Garrett, C. (1974). Normal Modes of the Bay of Fundy and Gulf of Maine. *Canadian Journal of Earth Sciences*, *11*(4), 549–556.

Garrett, C. (1984). Tides and tidal power in the Bay of Fundy. *Endeavour*, *8*(2), 58–64.

Garrett, C., & Cummins, P. (2004). Generating Power from Tidal Currents. *Journal of Waterway, Port, Coastal, and Ocean Engineering*, *130*(3), 114–118.

Garrett, C., & Cummins, P. (2005). The power potential of tidal currents in channels. *Proceedings of the Royal Society A: Mathematical, Physical and Engineering Sciences*, *461*(2060), 2563–2572.

Garrett, C., & Cummins, P. (2007). The efficiency of a turbine in a tidal channel. *Journal of Fluid Mechanics*, *588*, 243–251.

Gill, A. B. (2005). Offshore renewable energy: Ecological implications of generating electricity in the coastal zone. *Journal of Applied Ecology*, *42*(4), 605–615.

Gooch, S., Thomson, J., Polagye, B., & Meggitt, D. (2009). Site Characterization for Tidal Power. *OCEANS 2009, MTS/IEEE Biloxi - Marine Technology for Our Future: Global and Local Challenges*, 1–10.

Grabbe, M., Lalander, E., Lundin, S., & Leijon, M. (2009). A review of the tidal current energy resource in Norway. *Renewable and Sustainable Energy Reviews*, *13*(8), 1898–1909.

Greenberg, D. A. (1979). A numerical model investigation of tidal phenomena in the Bay of Fundy and Gulf of Maine. *Marine Geodesy*, *2*(2), 161–187.

Güney, M. S., & Kaygusuz, K. (2010). Hydrokinetic energy conversion systems: A technology status review. *Renewable and Sustainable Energy Reviews*, *14*(9), 2996–3004.

Gunn, K., & Stock-Williams, C. (2013). On validating numerical hydrodynamic models of complex tidal flow. *International Journal of Marine Energy*, *3-4*, 82–97.

Hagerman, G., & Polagye, B. (2006). Methodology for estimating tidal current energy resources and power production by tidal in-stream energy conversion (TISEC) devices. EPRI North American Tidal In Stream Power Feasibility Demonstration Project.

Hammons, T. J. (1993). Tidal power. *Proceedings of the IEEE*, *81*(3).

Hashemi, M. R., Neill, S. P., Robins, P. E., Davies, A. G., & Lewis, M. J. (2015). Effect of waves on the tidal energy resource at a planned tidal stream array. *Renewable Energy*, *75*, 626–639.

Haskoning (2011) SeaGen Environmental Monitoring Programme. Final Report.

Hervouet, J. M. (2007). *Hydrodynamics of free surface flows: Modelling with the finite element method.* Hoboken, NJ: Wiley.

Hicks, S.D. (2006). *Understanding Tides*. National Oceanic and Atmospheric Administration.

Johnstone, C. M., Pratt, D., Clarke, J. A., & Grant, A. D. (2013). A techno-economic analysis of tidal energy technology. *Renewable Energy*, *49*, 101–106.

Kamphuis, J. W. (2010). *Introduction to coastal engineering and management.* Hackensack, NJ: World Scientific.

Karsten, R. H., McMillan, J. M., Lickley, M. J., & Haynes, R. D. (2008). Assessment of tidal current energy in the Minas Passage, Bay of Fundy. *Proceedings of the Institution of Mechanical Engineers, Part A: Journal of Power and Energy*, *222*(5), 493–507.

Karsten, R., Culina, J., Swan, A., O'Flaherty-Sproul, M., Corkum, A., Greenberg, D., & Tarbottom, M. (2011). Assessment of the potential of tidal power from Minas Passage and Minas Basin. Final Report.

Kirke, B. (2005). Developments in ducted water current turbines. Retrieved July 15, 2015, from http://www.cyberiad.net/tide.htm

Khan, M. J., Bhuyan, G., Iqbal, M. T., & Quaicoe, J. E. (2009). Hydrokinetic energy conversion systems and assessment of horizontal and vertical axis turbines for river and tidal applications: A technology status review. *Applied Energy*, *86*(10), 1823–1835.

Langhamer, O., Haikonen, K., & Sundberg, J. (2010). Wave power-Sustainable energy or environmentally costly? A review with special emphasis on linear wave energy converters. *Renewable and Sustainable Energy Reviews*, *14*(4), 1329–1335.

Lawton, F. L. (1972). *Tidal power*. New York, NY: Plenum Press.

Legrand, C. (2009). Assessment of tidal energy resource. The European Marine Energy Centre, London.

Lewis, M. J., Neill, S. P., Hashemi, M. R., & Reza, M. (2014). Realistic wave conditions and their influence on quantifying the tidal stream energy resource. *Applied Energy*, *136*, 495–508.

Lewis, M., Neill, S. P., Robins, P. E., & Hashemi, M. R. (2015). Resource assessment for future generations of tidal-stream energy arrays. *Energy*, *83*, 403–415.

Lyard, F., Lefevre, F., Letellier, T., & Francis, O. (2006). Modelling the global ocean tides: Modern insights from FES2004. *Ocean Dynamics*, *56*(5-6), 394–415.

Mukai, A. Y., Westerink, J. J., Luettich Jr, R. A., & Mark, D. (2002). Eastcoast 2001: A tidal constituent database for the western North Atlantic, Gulf of Mexico and Caribbean Sea. Coastal and Hydraulics Laboratory Tech. Rep. ERDC. *US Army Corps of Engineers, ERDC/CHL TR-02-24*, (September), 25.

Myers, L. E., & Bahaj, A. S. (2012). An experimental investigation simulating flow effects in first generation marine current energy converter arrays. *Renewable Energy*, *37*(1), 28–36.

Nature Publishing Group (1933). The Severn Barrage Scheme. London: Macmillan.

Neill, S. P., Hashemi, M. R., & Lewis, M. J. (2014). The role of tidal asymmetry in characterizing the tidal energy resource of Orkney. *Renewable Energy*, *68*, 337–350.

Ocean Renewable Power Company LLC (2013). Cobscook Bay Tidal Energy Project. Available from http://www.orpc.co/permitting_doc/P-12711_Report_w_Appendices_FINAL2.pdf.

O'Rourke, F., Boyle, F., & Reynolds, A. (2010). Tidal current energy resource assessment in Ireland: Current status and future update. *Renewable and Sustainable Energy Reviews*, *14*(9), 3206–3212.

O'Rourke, F., Boyle, F., & Reynolds, A. (2014). Ireland's tidal energy resource; An assessment of a site in the Bulls Mouth and the Shannon Estuary using measured data. *Energy Conversion and Management*, *87*(2014), 726–734.

Pawlowicz, R., Beardsley, B., & Lentz, S. (2002). Classical tidal harmonic analysis including error estimates in MATLAB using T_TIDE. *Computers and Geosciences*, *28*(8), 929–937.

Ragheb, M., & Ragheb, A. M. (2011). Wind Turbines Theory - The Betz Equation and Optimal Rotor Tip Speed Ratio. *Fundamental and Advanced Topics in Wind Power*, *1*(1).

Ramos, V., & Iglesias, G. (2013). Performance assessment of Tidal Stream Turbines: A parametric approach. *Energy Conversion and Management*, *69*, 49–57.

Retiere, C. (1994). Tidal power and the aquatic environment of La Rance. *Biological Journal of the Linnean Society*, *51*, 25–36.

Robins, P. E., Neill, S. P., Lewis, M. J., & Ward, S. L. (2015). Characterising the spatial and temporal variability of the tidal-stream energy resource over the northwest European shelf seas. *Applied Energy*, *147*, 510–522.

Sankaranarayanan, S., & McCay, D. F. (2003). Three-Dimensional Modeling of Tidal Circulation in Bay of Fundy. *Journal of Waterway, Port, Coastal, and Ocean Engineering*, *129*(3), 114–123.

Serhadlioğlu, S., Adcock, T. A. A., Houlsby, G. T., Draper, S., & Borthwick, A. G. L. (2013). Tidal stream energy resource assessment of the Anglesey Skerries. *International Journal of Marine Energy*, *3-4*, 98–111.

Shaw, J., Todd, B. J., Li, M. Z., & Wu, Y. (2012). Anatomy of the tidal scour system at Minas Passage, Bay of Fundy, Canada. *Marine Geology*, *323-325*, 123–134.

Sucsy, P. V., Pearce, B. R., & Panchang, V. G. (1993). Comparison of Two- and Three-Dimensional Model Simulation of the Effect of a Tidal Barrier on the Gulf of Maine Tides. *Journal of Physical Oceanography*.

Sustainable Energy Ireland (2004). Tidal & Current Energy Resources in Ireland. Available from http://www.seai.ie/Publications/Renewables_Publications_/Ocean/Tidal_Current_Energy_Resources_in_Ireland_Report.pdf.

Sutherland, G., Foreman, M., & Garrett, C. (2007). Tidal current energy assessment for Johnstone Strait, Vancouver Island. *Proceedings of the Institution of Mechanical Engineers, Part A: Journal of Power and Energy*, *221*(2), 147–157.

Tousif, S. M. R., & Taslim, S. M. B. (2011). Tidal Power : An Effective Method of Generating Power. *International Journal of Scientific & Engineering Research*, *2*(5), 1–5.

Triton Consultants Ltd. (2006). Canada Ocean Energy Atlas (Phase 1) Potential Tidal Current Energy Resources Analysis Background.

Vennell, R. (2011). Estimating the power potential of tidal currents and the impact of power extraction on flow speeds. *Renewable Energy*, *36*(12), 3558–3565.

Verdant Power LLC (2010). Roosevelt Island Tidal Energy Project. Available from http://www.theriteproject.com /uploads/VPRITE-FLAVol2-Part1of2.pdf.

Appendices

A. Theory of tides

A.1 Introduction

Tides are the rise and fall of sea levels due to gravitational and centrifugal forces acting on individual water particles. These forces are gravitational attraction of the Earth, Moon, and Sun, and the centrifugal force generated by the rotation of the Earth-Moon system. While tides are usually the defining short-term sea level fluctuation, sea levels are also subject to storm surge, barometric surge, seasonal, and climatic fluctuations.

A.2 Equilibrium tide

Neglect – for now – the gravitational attraction of the Sun and consider the Earth covered with water. The resultant force on the water particles generates two bulges of high water: toward the Moon and away from the Moon (Defant 1961). As the Earth rotates about its axis through this deformed sphere of water it sees two high water levels and two low water levels per day (Figure A.1). The resulting tidal period is about 12.42 hours, exactly half a lunar (tidal) day, which is the time required for the Earth to rotate once relative to the moon. The lunar day is longer than the solar day because the Moon orbits in the same direction the Earth spins.

The tide described above is called *equilibrium tide* because it carries the assumption that the system has reached steady state. However, as the Earth rotates, the magnitude and direction of the tide-generating force at any given point on the Earth's surface change constantly. The ocean never reaches equilibrium – there is never time for the fluid to "catch up" to the state it would ultimately reach if the tide-generating force were constant.

The Earth-Sun system forms a similar, smaller set of bulges toward the Sun and away from the Sun. The tide-raising force of the Sun is approximately 46% that of the Moon because of its distance from the Earth. The resulting tidal period is 12 hours, which is half the time required for the Earth to rotate once relative to the Sun. The equilibrium tides are not separate phenomena. Both occur simultaneously and overlap.

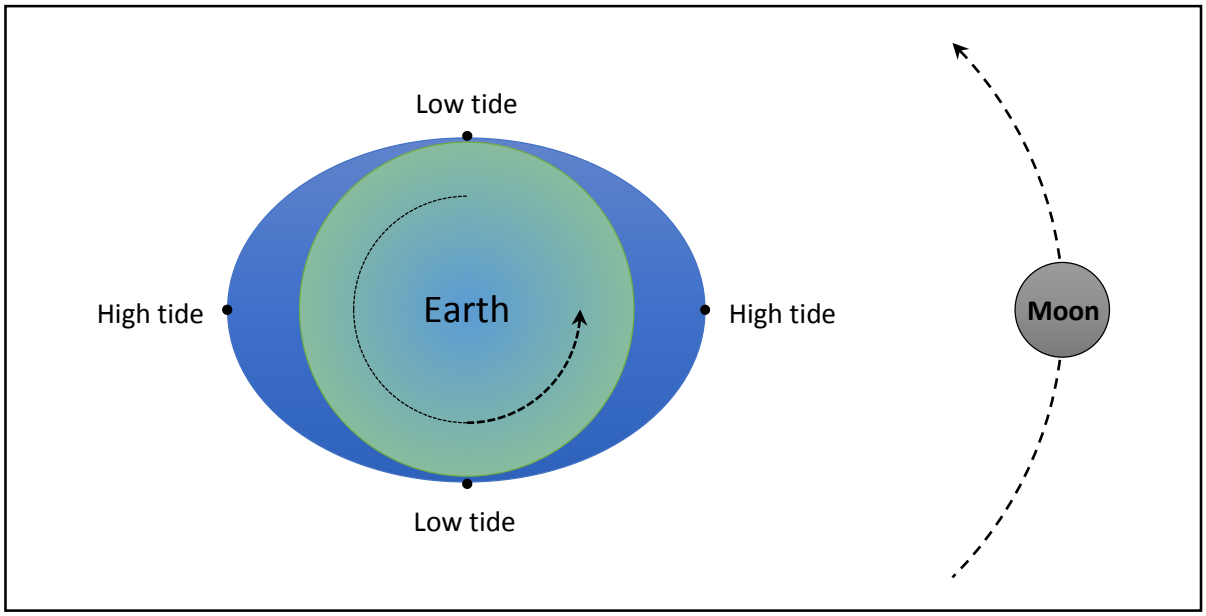

Figure A.1. Equilibrium tide

When the Sun and Moon are aligned (at new Moon and full Moon) the equilibrium tides are in phase and tides are higher than average. At quarter Moon, the tide-generating forces of the Sun and Moon are 90 degrees out of phase and destructive interference yields tides of diminished range. The former are called *spring tides* and the latter are called *neap tides* (Figure A.2). Since the period of the Moon's revolution relative to the Sun is 29.5 days, or a lunar month, the spring-neap cycle occurs with a period half of that, or approximately two weeks.

A.3 Daily inequality

Figure A.1 was drawn looking down on the North Pole. It's expected from this representation that an observer traveling along a constant latitude would experience two tides of equal height per day. However, the Sun or Moon is seldom in the plane of the equator. The declination of the Sun or Moon with respect to the equator will generate one bulge of the equilibrium tide above the equator and one below the equator (Figure A.3). Thus, an observer traveling along a constant latitude would experience two tides of unequal height per day. This is called the *daily inequality*. The daily inequality is null at the equator and increases with latitude. The daily inequality cycle generated by the Moon's forces repeats itself every 27.3 days, or tropical month, which is the period of the Moon's revolution relative to the background stars. The lunar month is longer than the tropical month because the Earth-Moon system is orbiting the Sun in the same direction as the Moon is orbiting the Earth. The daily inequality cycle generated by the Sun's forces has a period of a year.

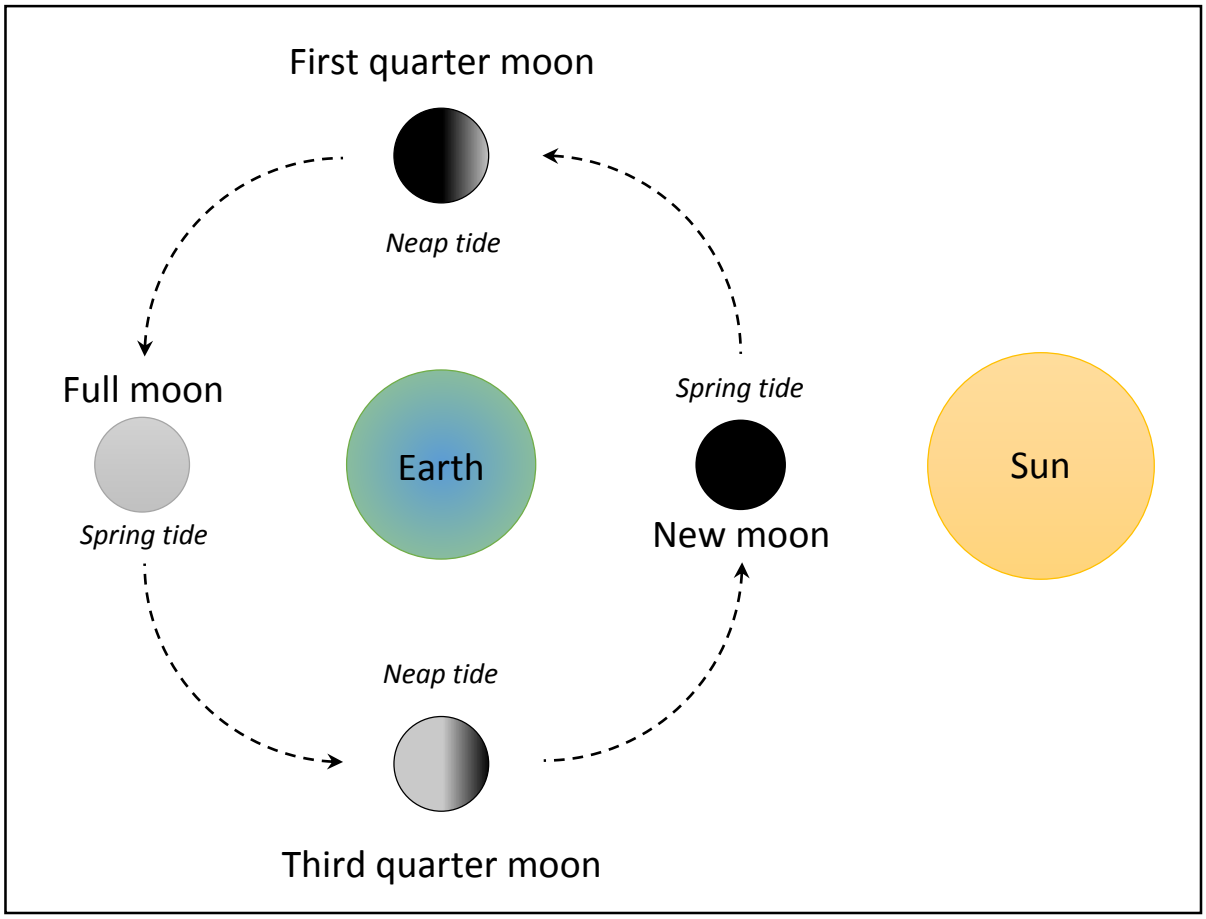

Figure A.2. Spring and neap tide

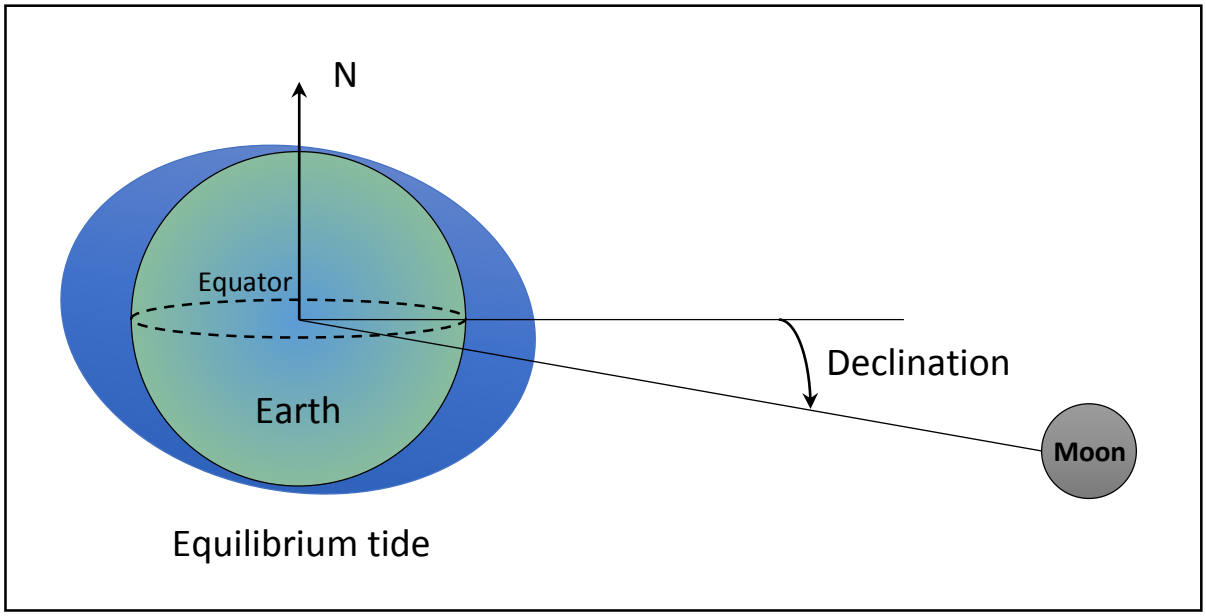

Figure A.3. Daily inequality

The simple picture drawn thus far has traced the origin of tides to the gravitational attraction of the Earth-Moon-Sun system and the declination of the Moon and Sun. In truth, there are many other effects that contribute to the observed tides. For example, it has been implied up to this point that the Moon and Sun travel along circular orbits relative to the Earth. These orbits are actually elliptical and thus the distances between the Earth and the Sun and Moon change in cyclical fashion, as do the tide-generating forces. For instance, the Moon's tide-generating force is 30 to 48% greater at perigee than at apogee. Each separate effect can be viewed as a tide generator with its own amplitude, frequency, and phase angle with respect to the others. The tide may therefore be understood as a sum of the effects of the Sun, the Moon, and many secondary causes. Each component is called a *tidal constituent*.

A.4 Tidal constituents

The most important tidal constituents have already been discussed; they are the semi-diurnal constituents generated by the Sun (S2) and Moon (M2) with periods of 12 and 12.42 hours, and the daily inequality (or diurnal) constituents. There are many other tidal constituents to be considered such as the ellipticity of the earth and lunar orbits, as well as shallow-water constituents (superharmonics and compound tides). The name and period of important constituents are shown in Table A.1.

Table A.1. Important tidal constituents

Tide	Period (h)	Description	Nature
M2	12.42	Principal lunar	semi-diurnal
S2	12.00	Principal solar	semi-diurnal
N2	12.66	Larger lunar elliptic	semi-diurnal
K2	11.97	Luni-solar	semi-diurnal
K1	23.93	Luni-solar diurnal	diurnal
O1	25.82	Principal lunar diurnal	diurnal
P1	24.07	Principal solar diurnal	diurnal
Q1	26.87	Larger lunar elliptic	diurnal
MF	327.90	Lunar fortnightly	long-term
MM	661.30	Lunar monthly	long-term
SSA	4383.00	Solar semi-annual	long-term
M4	6.21		compound
MS4	6.10		compound

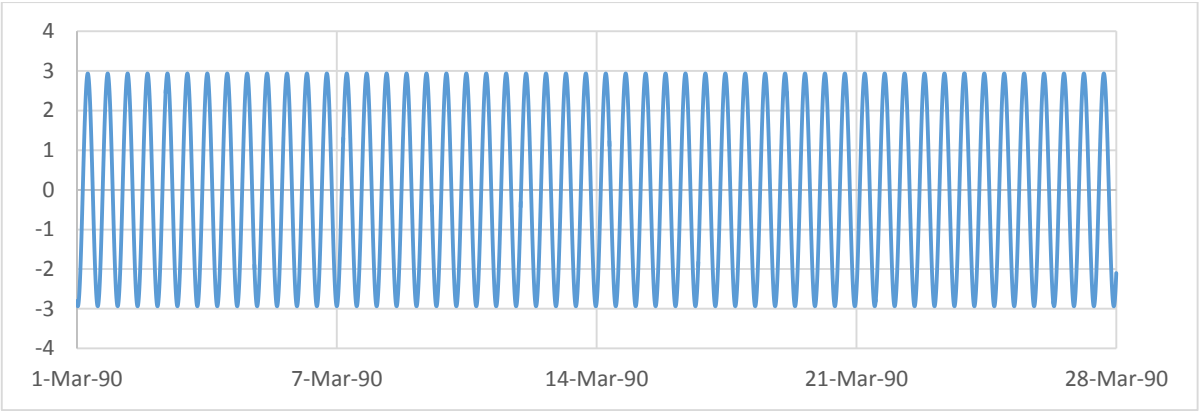

Figure A.4. M2 for Saint John NB, March 1-28, 1990

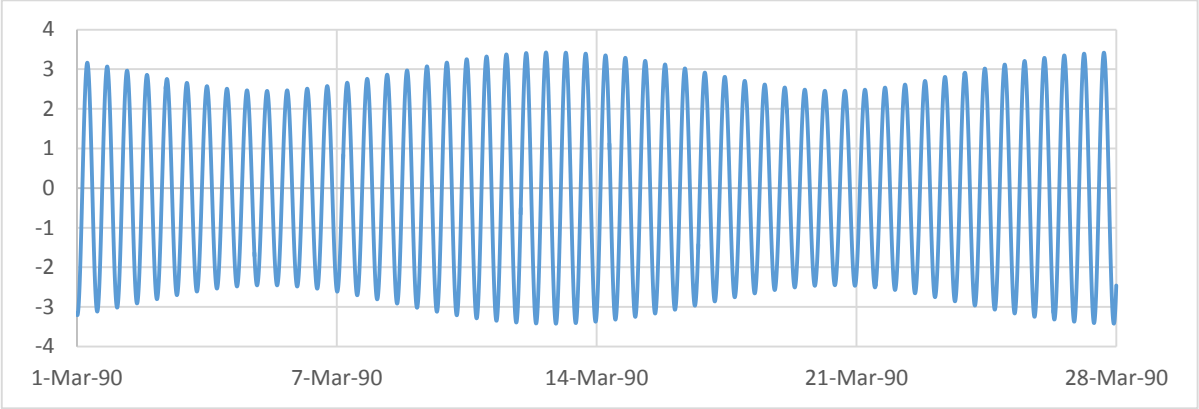

Figure A.5. M2 + S2 for Saint John NB, March 1-28, 1990

The M2 constituent is by far the most important. If the Sun could be neglected, and if the Moon orbited in a perfect circle in the plane of the Earth's equator, this term alone would give the tide. Figure A.4 shows the M2 tide for Saint John. In the same way, the S2 constituent would give the solar tide if the Sun were always in the Earth's equatorial plane and if the Earth's orbit were a perfect circle. The plot of M2 + S2 (Figure A.5) shows the combined tide of this ideal Sun and Moon. Note the spring and neap tides repeating on a fortnightly cycle. The diurnal constituents K1, O1, and P1 account for the Moon's declination (among other effects). During a month the Moon spends about two weeks above the equator and then two weeks below, effecting the daily inequality. Twice a month, when the Moon crosses the equator, the two tides are roughly equal. The plot of M2 + K1 (Figure A.6) illustrates the daily inequality cycle. The N2 constituent involves the ellipticity of the Moon's orbit. Tides are higher when the Moon approaches perigee (nearest the Earth) and lower when it is near its apogee (farthest from Earth). Figure A.7 illustrates the impact of the Moon's elliptical orbit.

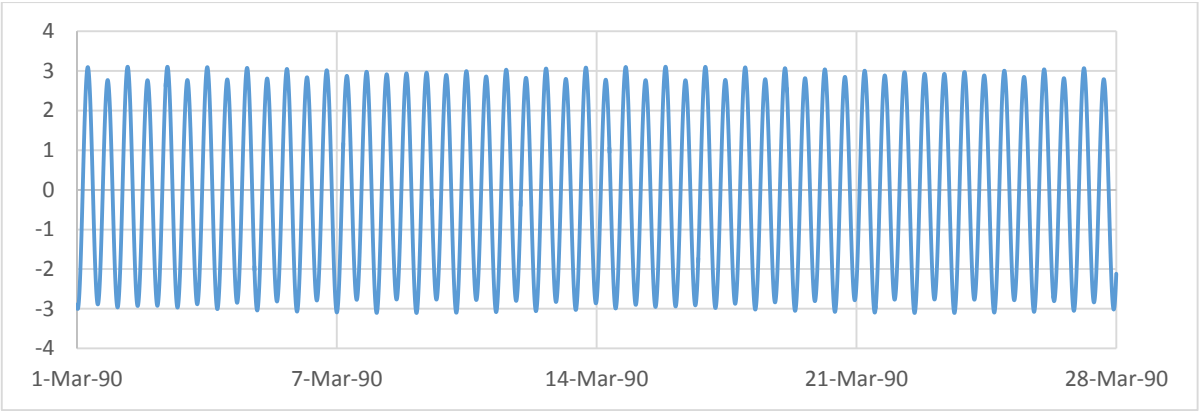

Figure A.6. M2 + K1 for Saint John NB, March 1-28, 1990

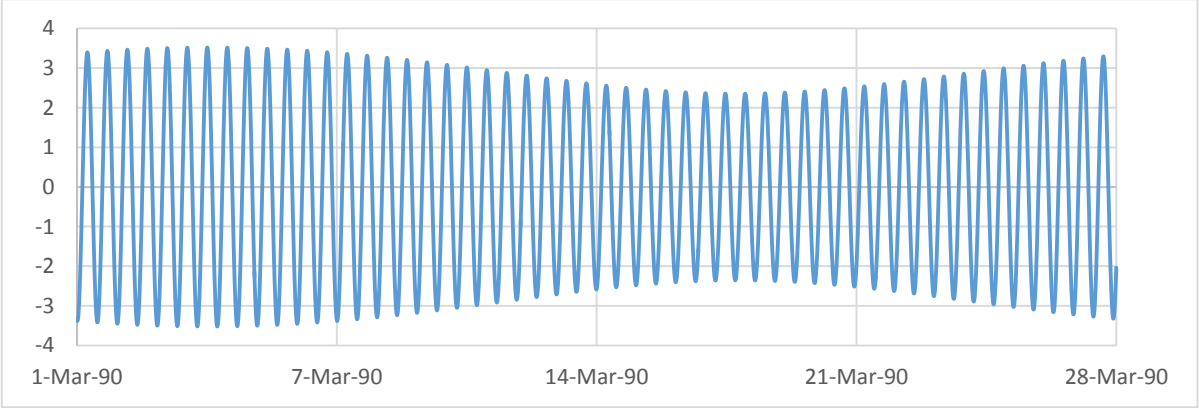

Figure A.7. M2 + N2 for Saint John NB, March 1-28, 1990

Tides entering waters where the tidal range is no longer insignificant with respect to the depth undergo a transformation that yields added waves called overtides (or superharmonics). These are analogous to the overtones produced by a musical instrument. Overtides do not arise directly from the tide-generating forces, they are introduced as a mathematical convenience to represent distortion of the tidal wave (i.e. shoaling). The frequency (or speed) of an overtide is always an exact multiple of the fundamental frequency – the frequency of the parent wave that underwent transformation. Therefore, the overtide waveform is stationary with respect to the parent waveform. The function of overtides is to modulate the parent wave, thereby giving rise to permanent tidal asymmetries. As an example, M6 is the second harmonic of the fundamental tidal constituent M2, with three times its frequency. The most common shallow-water constituents are the quarter-diurnals M4 and MS4, with frequencies twice that of M2 and the sum of those of M2 and S2, respectively. Besides overtides, other constituents called compound tides also arise in shallow water. Compound tides, for example MS4, arise from the shallow-water interaction of its two parent waves, in this case M2 and S2.

To simplify the concept of the equilibrium tide it was stipulated that the Earth is completely covered with water. The surface of the Earth not only confines and displaces water, but it also causes certain tidal constituents to resonate locally in the various oceans, seas, bays, and estuaries. This effect, whereby some constituents are magnified while others disappear, confers a unique character on the tide at each location. For example, the daily inequality is often amplified by geography, increasing the difference between the larger and smaller daily tides such that the smaller tides practically disappear. Thus, tides at that location are *diurnal* rather than *semi-diurnal*.

A.5 Tide analysis and prediction

Tide analysis (or harmonic analysis) consists of separating a measured tide into as many of its constituents as can be identified from the length of record available. Tide prediction consists of calculating water levels in the future from the relevant constituents. The tide is assumed to be represented by the harmonic summation

$$\eta(t) = a_0 + \sum_{i=1}^{n} a_i \cos(\omega_i t + \alpha_i) \qquad (A.1)$$

where $\eta(t)$ is the sea level at time t, a_0 is the mean sea level, a_i and α_i are the amplitudes and phase angles of the tidal constituents and ω_i are the angular frequencies of the tide generators behind the constituents. For example, M2 has a period of 12.42 hours and thus a frequency of $\omega_{M2} = 2\pi/(3600 \times 12.42) = 1.405 \times 10^{-4}$ Hz. Tidal analysis, therefore, is a matter of determining values of a_i and α_i by Fourier series analysis of recorded water levels.

The following works are recommended to readers interested in learning more about tides: Understanding Tides (Hicks 2006), Canadian Tidal Manual (Forrester 1983), and Introduction to Coastal Engineering and Management (Kamphuis 2010).

B. Field study

B.1 Site A

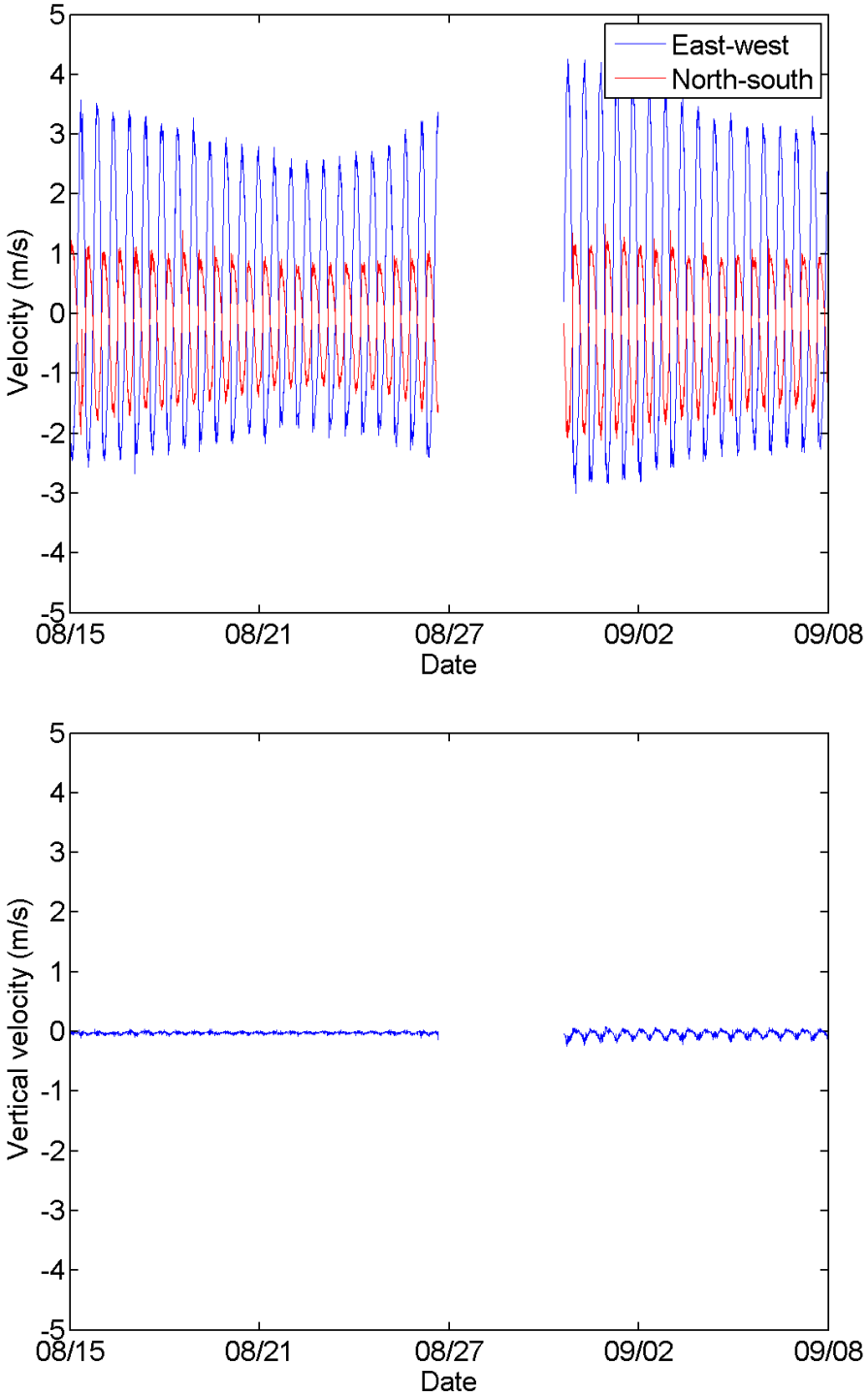

Figure B.1. East-west, north-south, and vertical velocities (Site A)

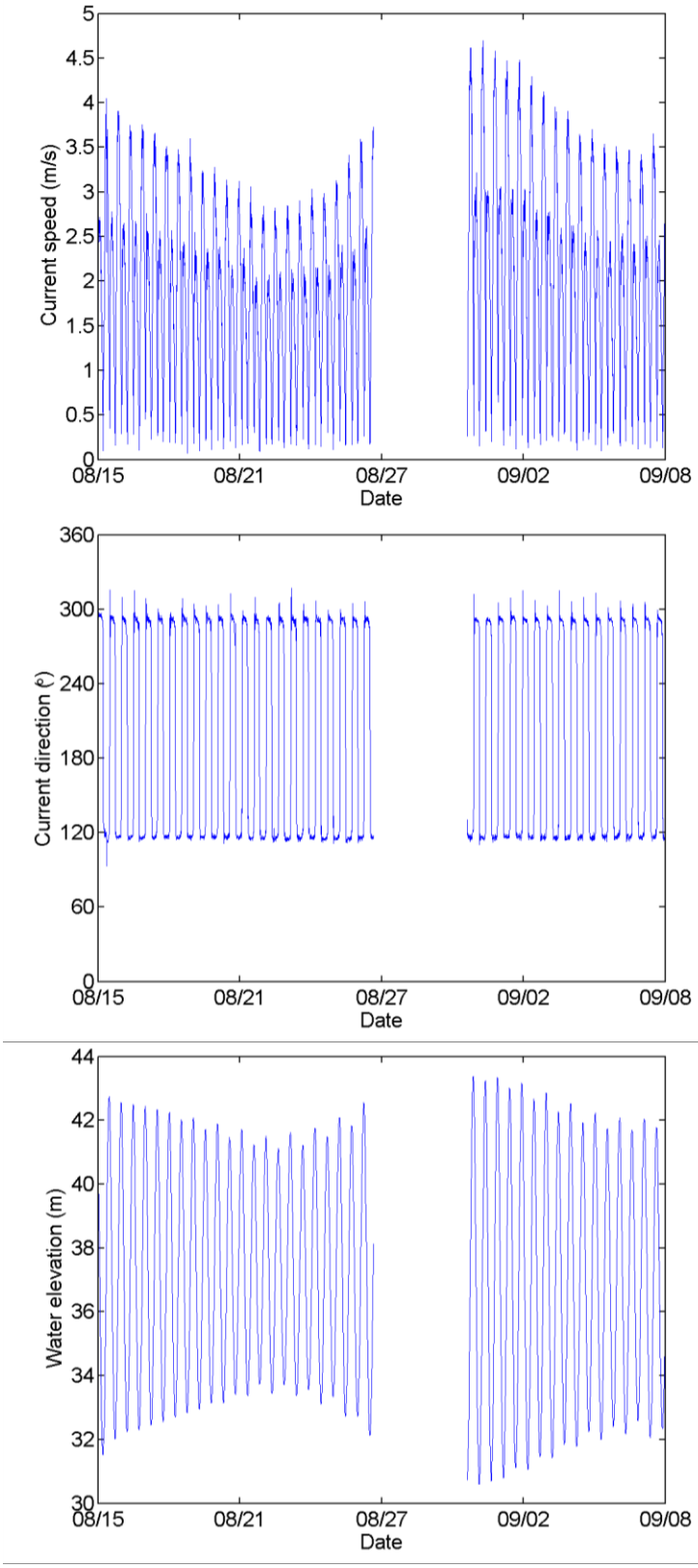

Figure B.2. Current speed, direction, and water elevation (Site A)

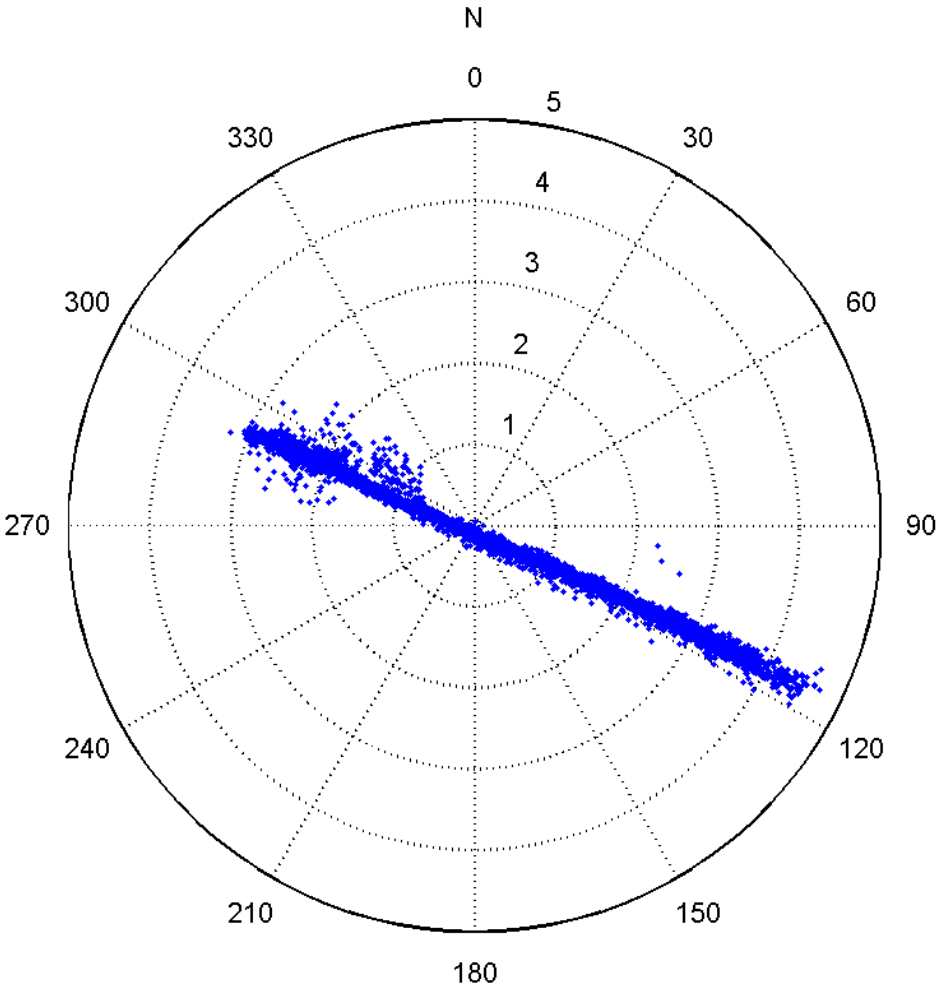

Figure B.3. Tidal ellipse (Site A)

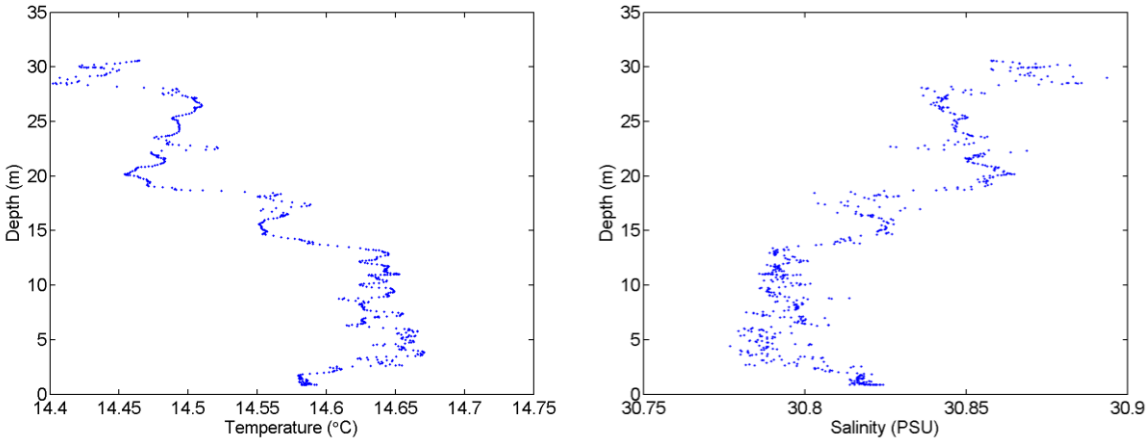

Figure B.4. Temperature and salinity depth profiles (Site A)

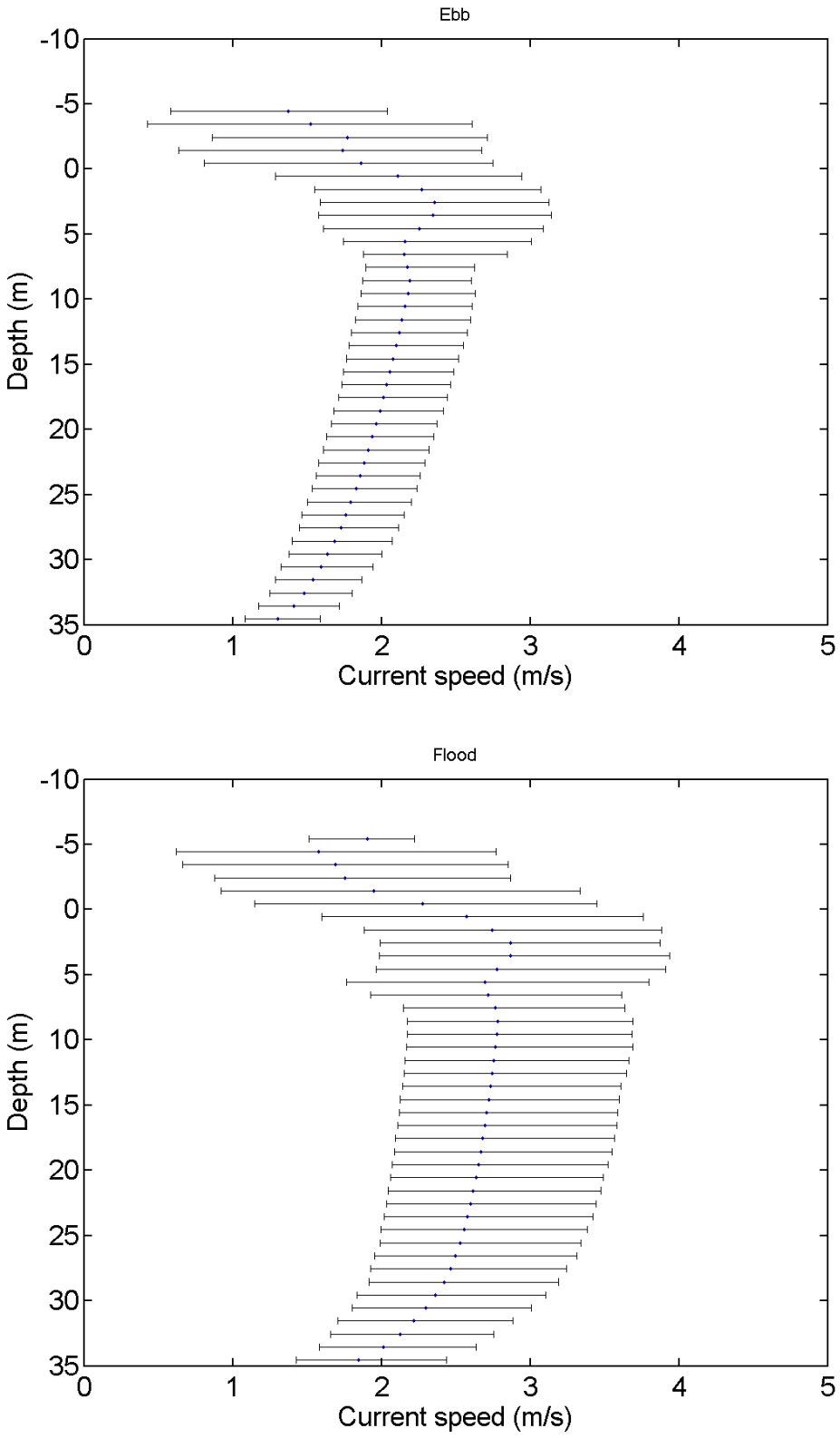

Figure B.5. Average ebb and flood current profiles (Site A)

B.2 Site B

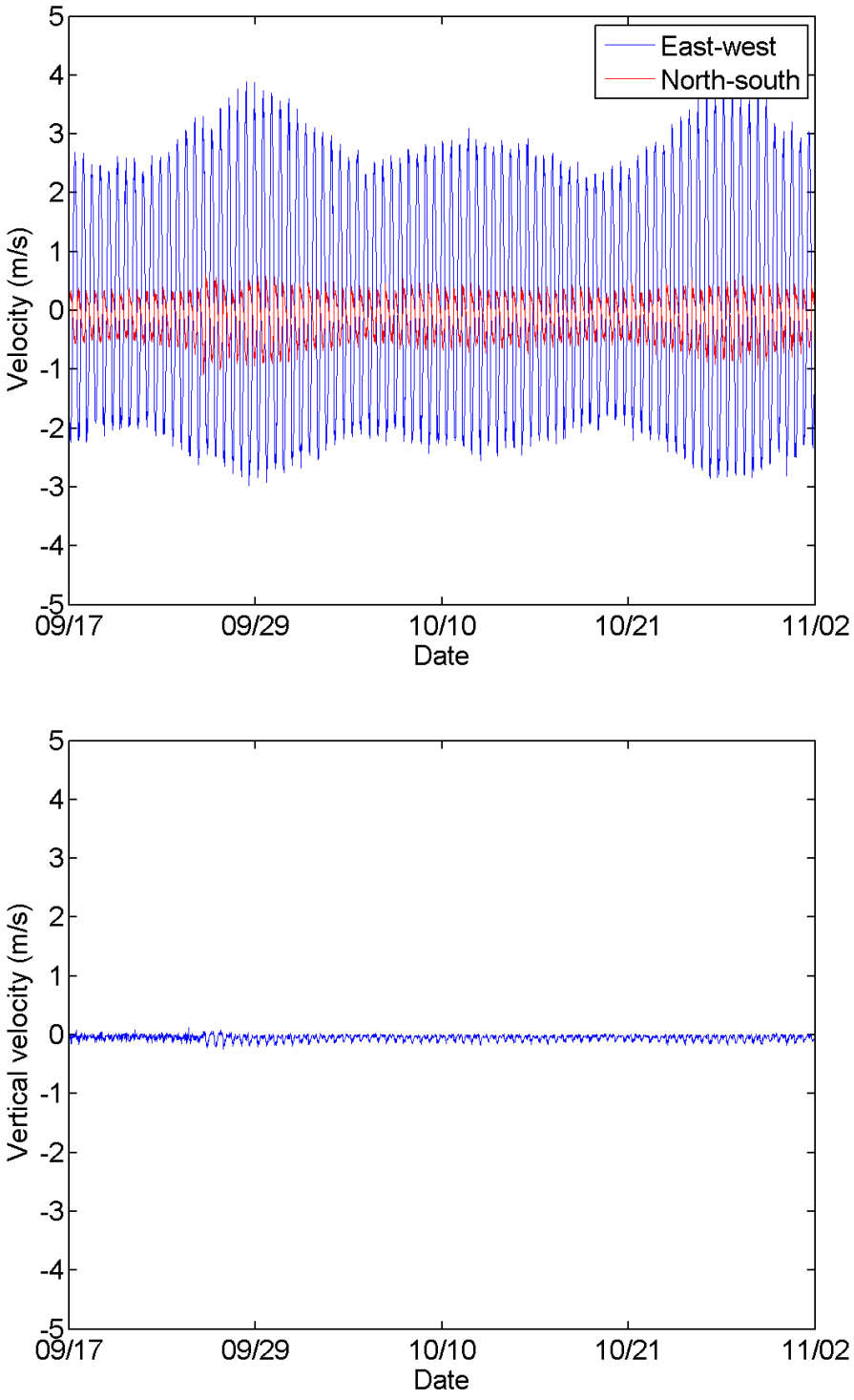

Figure B.6. East-west, north-south, and vertical velocities (Site B)

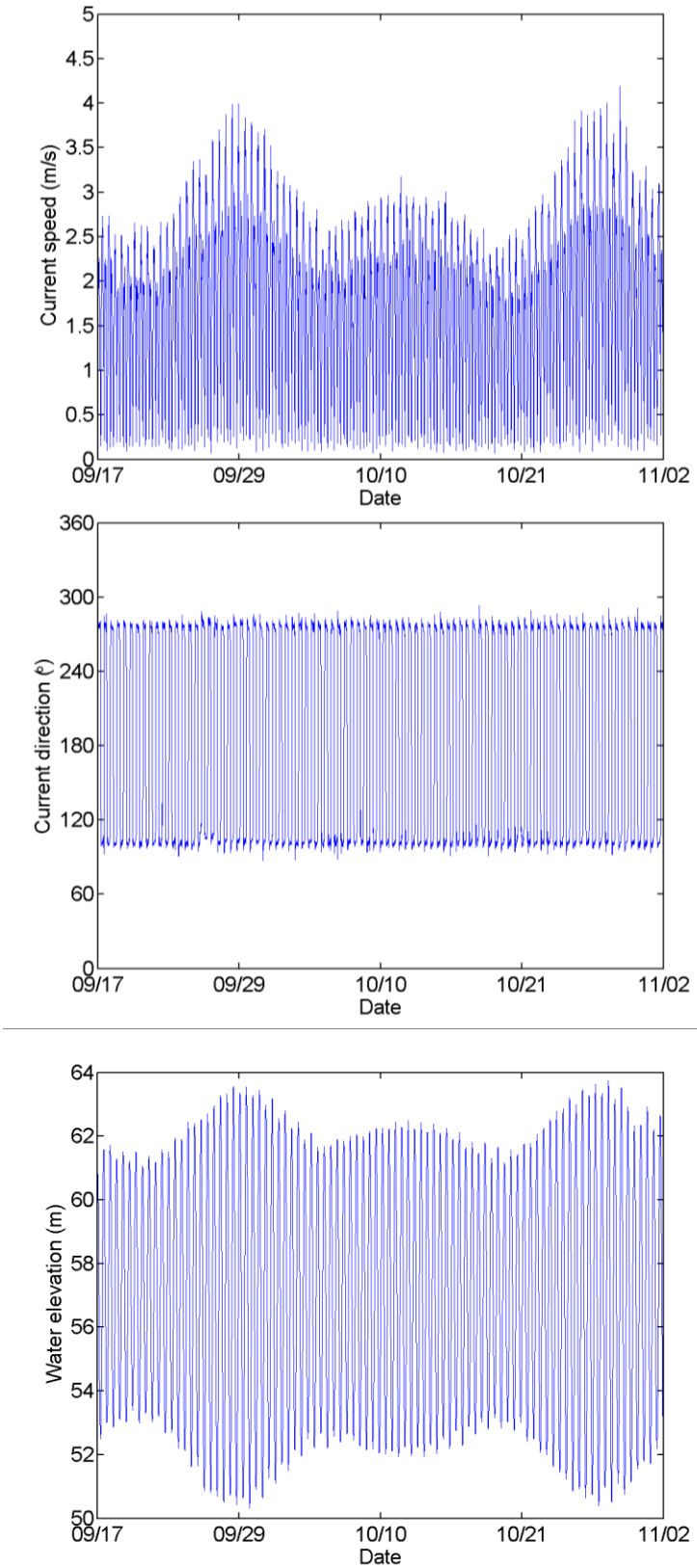

Figure B.7. Current speed, direction, and water elevation (Site B)

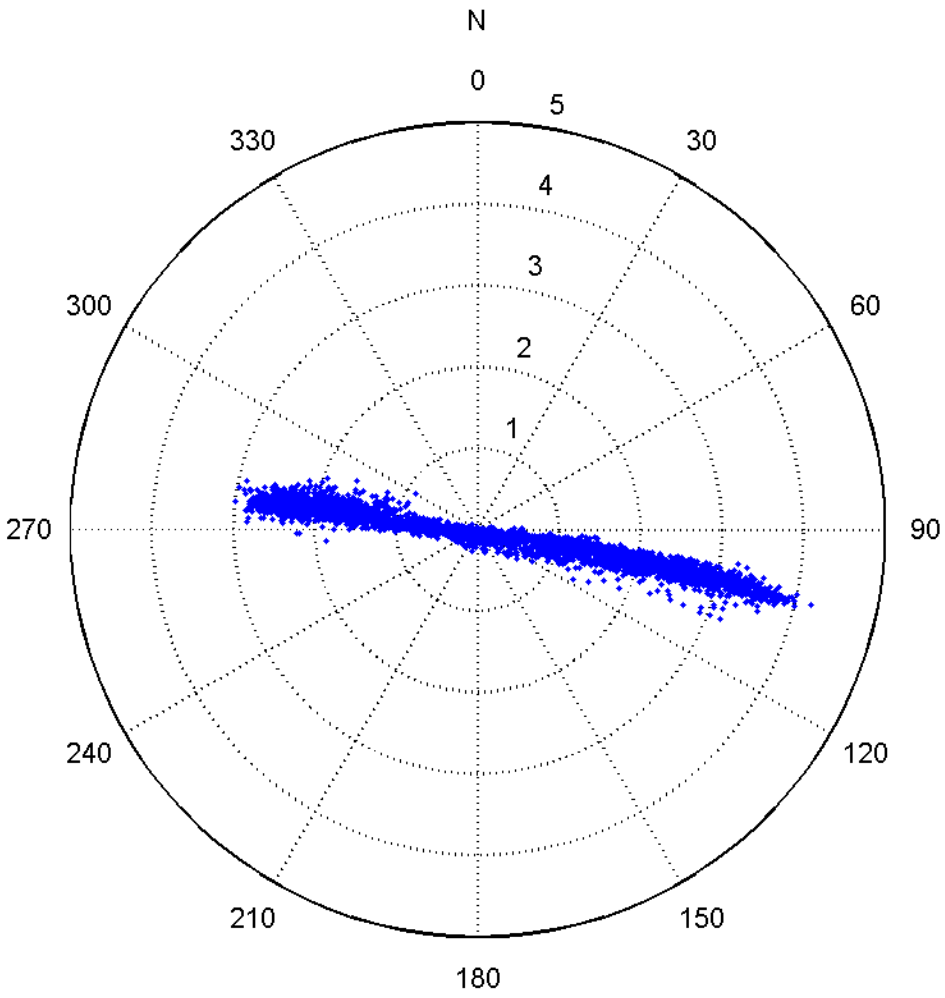

Figure B.8. Tidal ellipse (Site B)

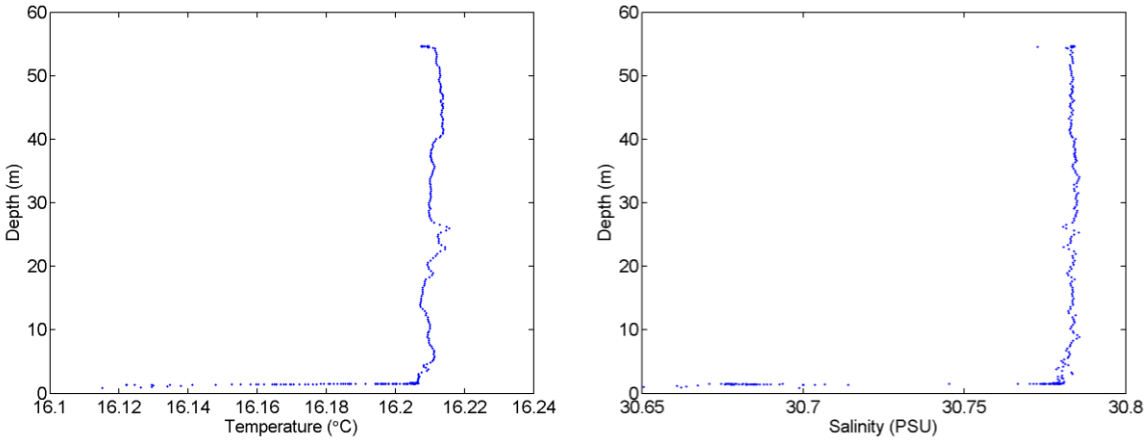

Figure B.9. Temperature and salinity depth profiles (Site B)

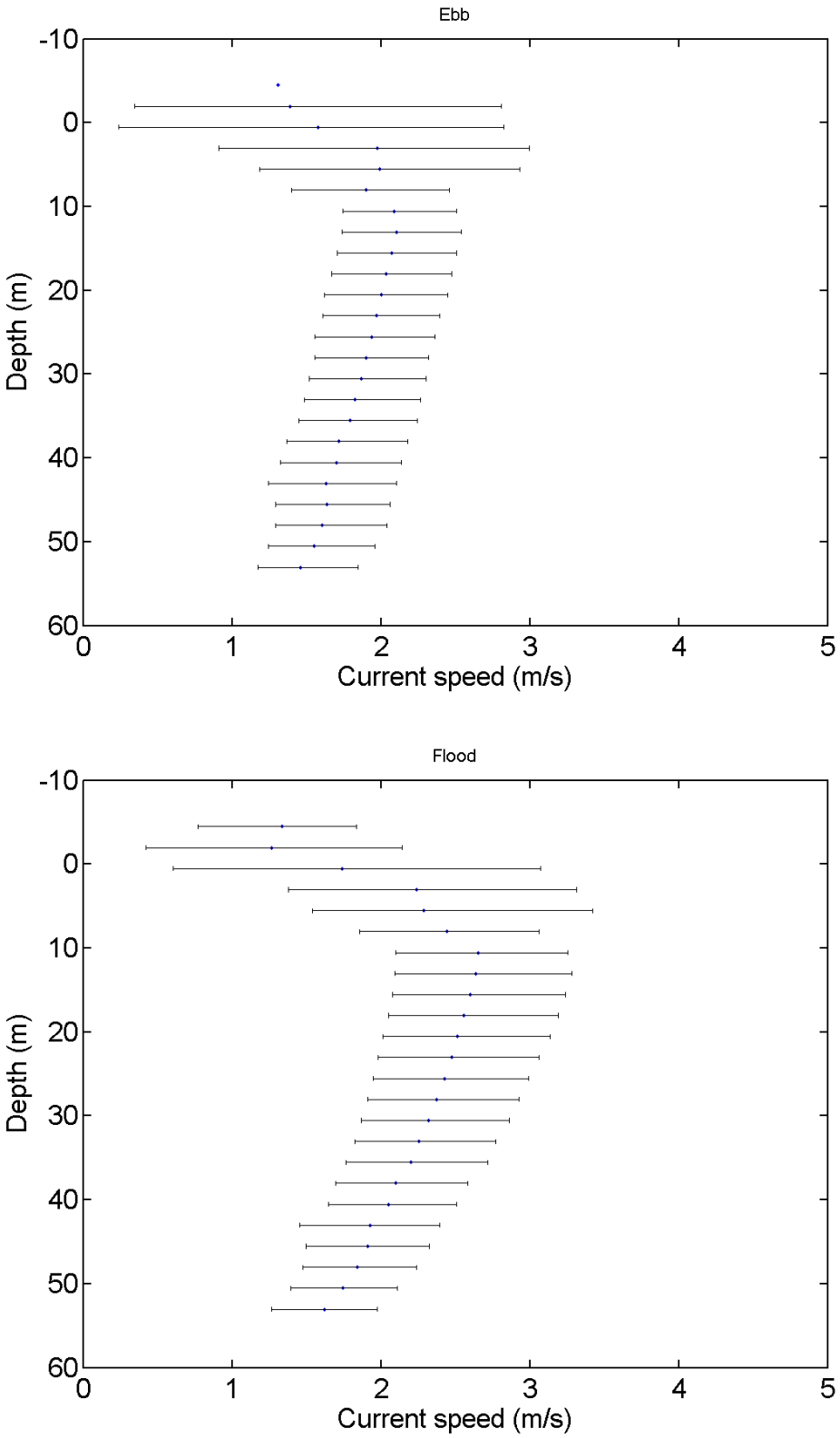

Figure B.10. Average ebb and flood current profiles (Site B)

B.3 Site C

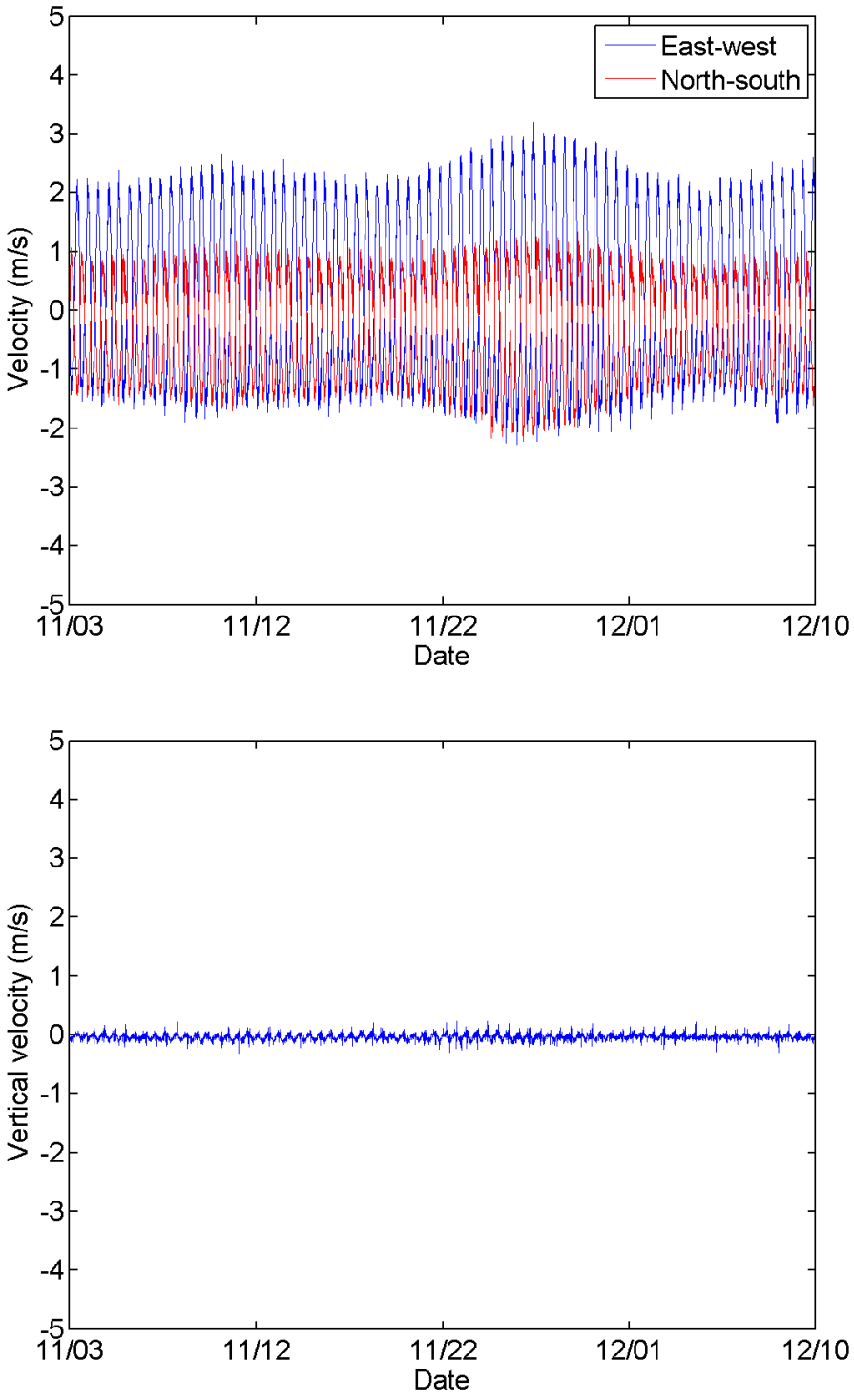

Figure B.11. East-west, north-south, and vertical velocities (Site C)

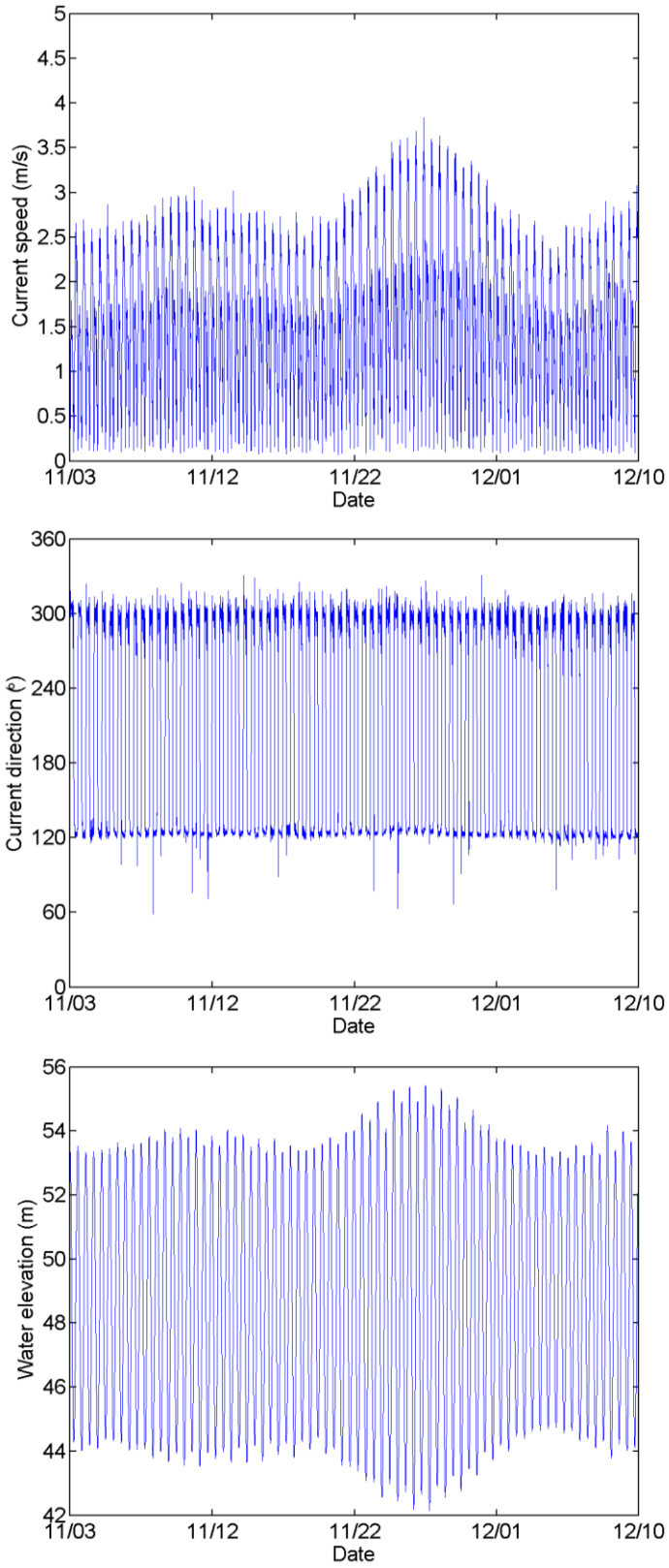

Figure B.12. Current speed, direction, and water elevation (Site C)

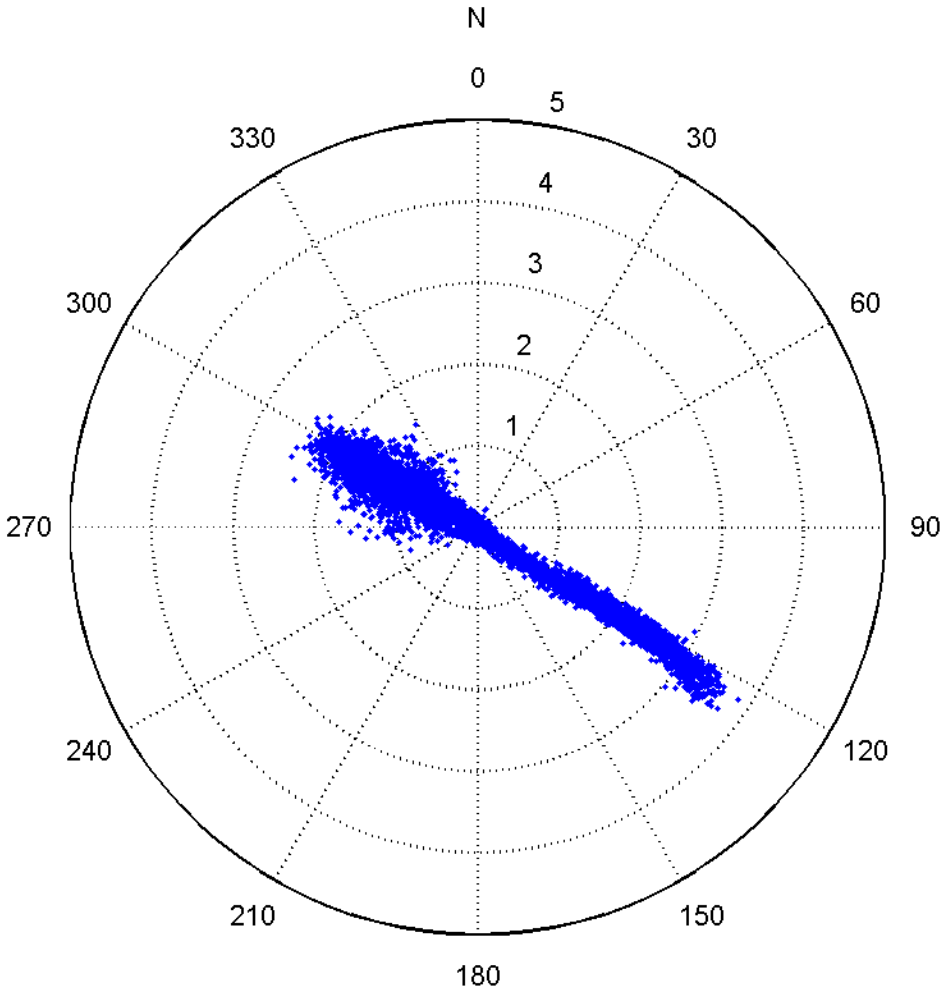

Figure B.13. Tidal ellipse (Site C)

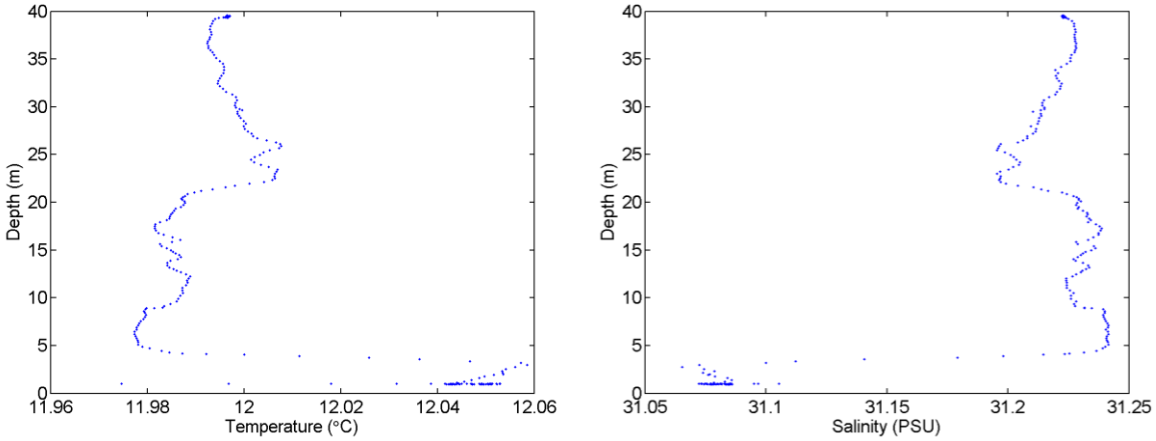

Figure B.14. Temperature and salinity depth profiles (Site C)

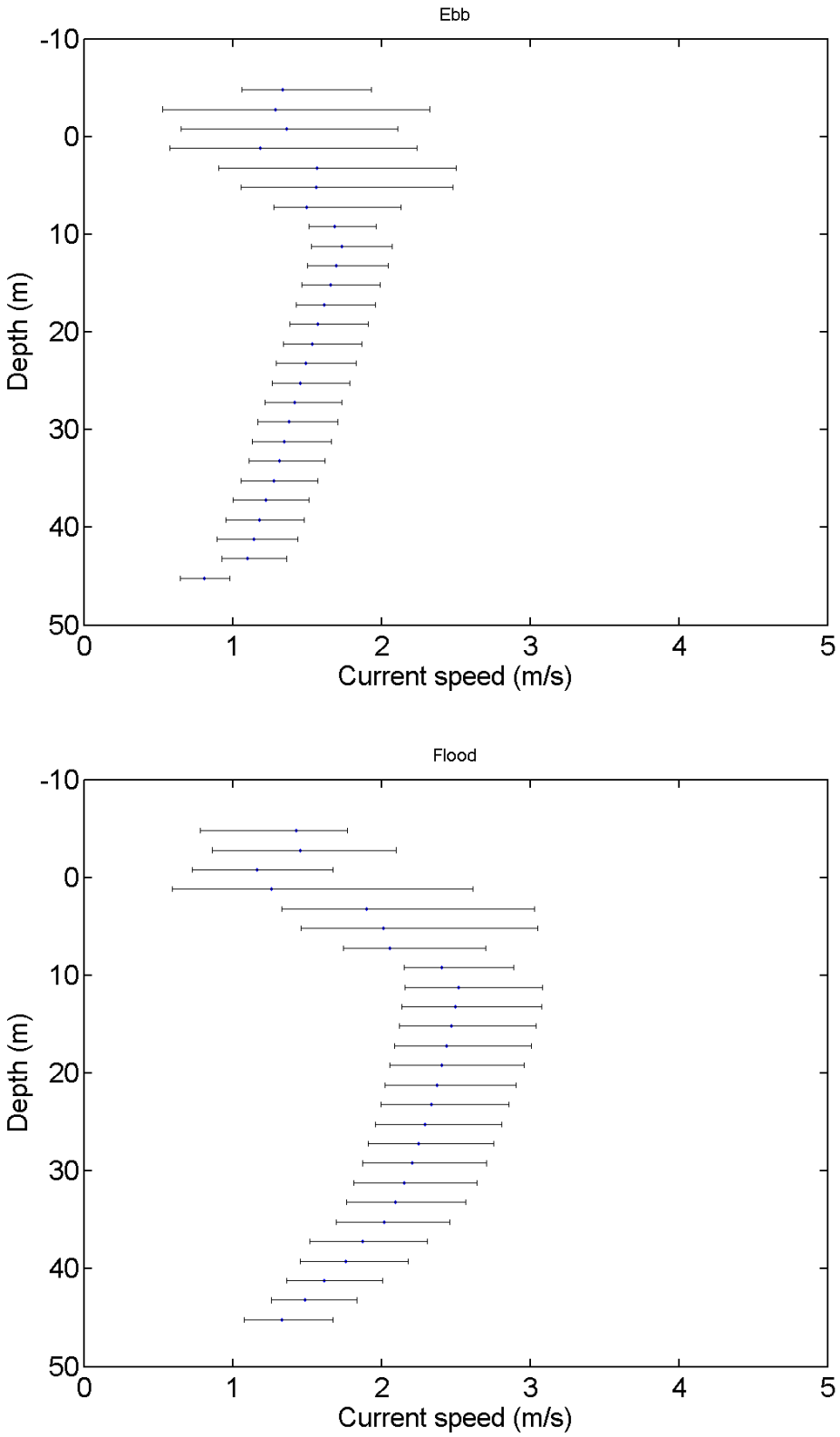

Figure B.15. Average ebb and flood current profiles (Site C)

B.4 Site D

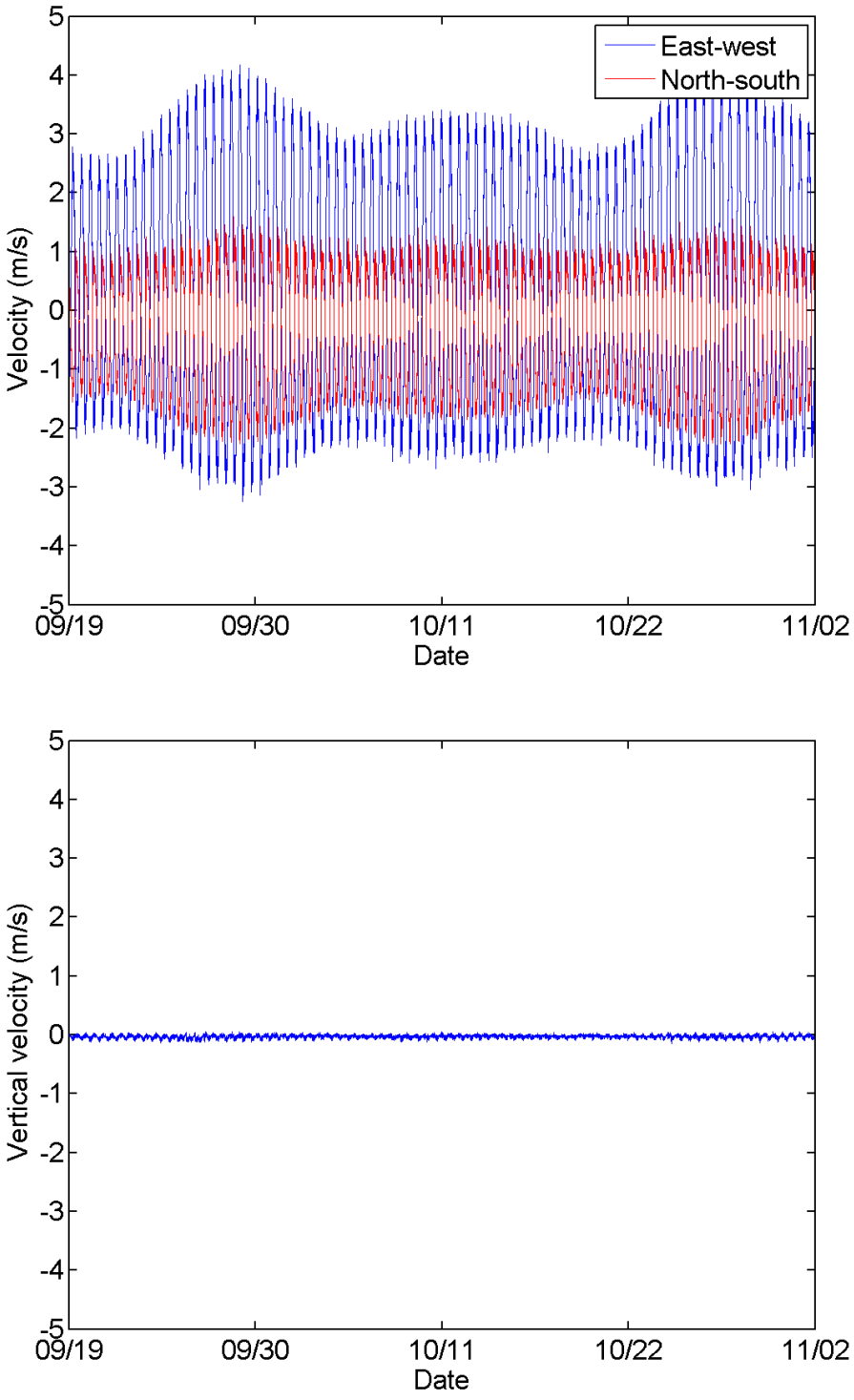

Figure B.16. East-west, north-south, and vertical velocities (Site D)

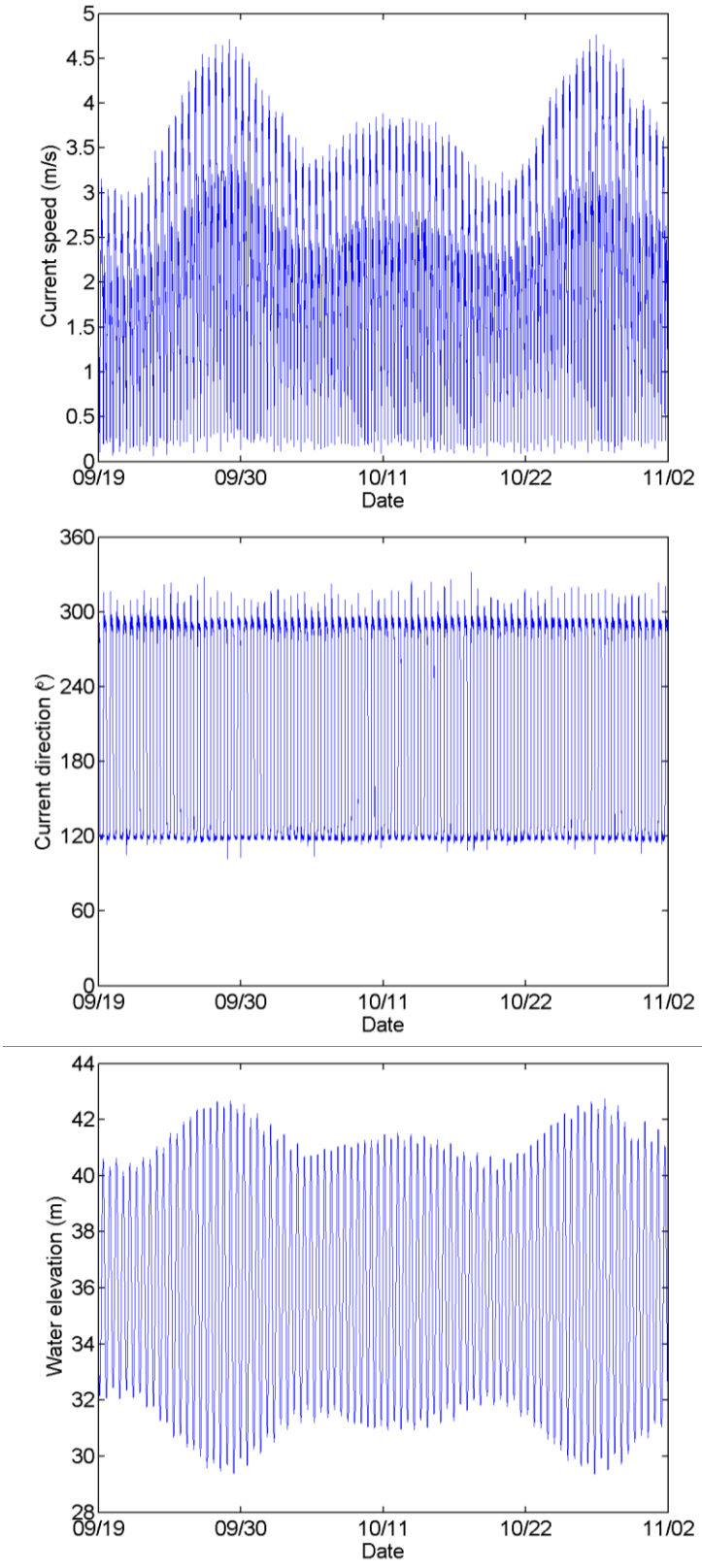

Figure B.17. Current speed, direction, and water elevation (Site D)

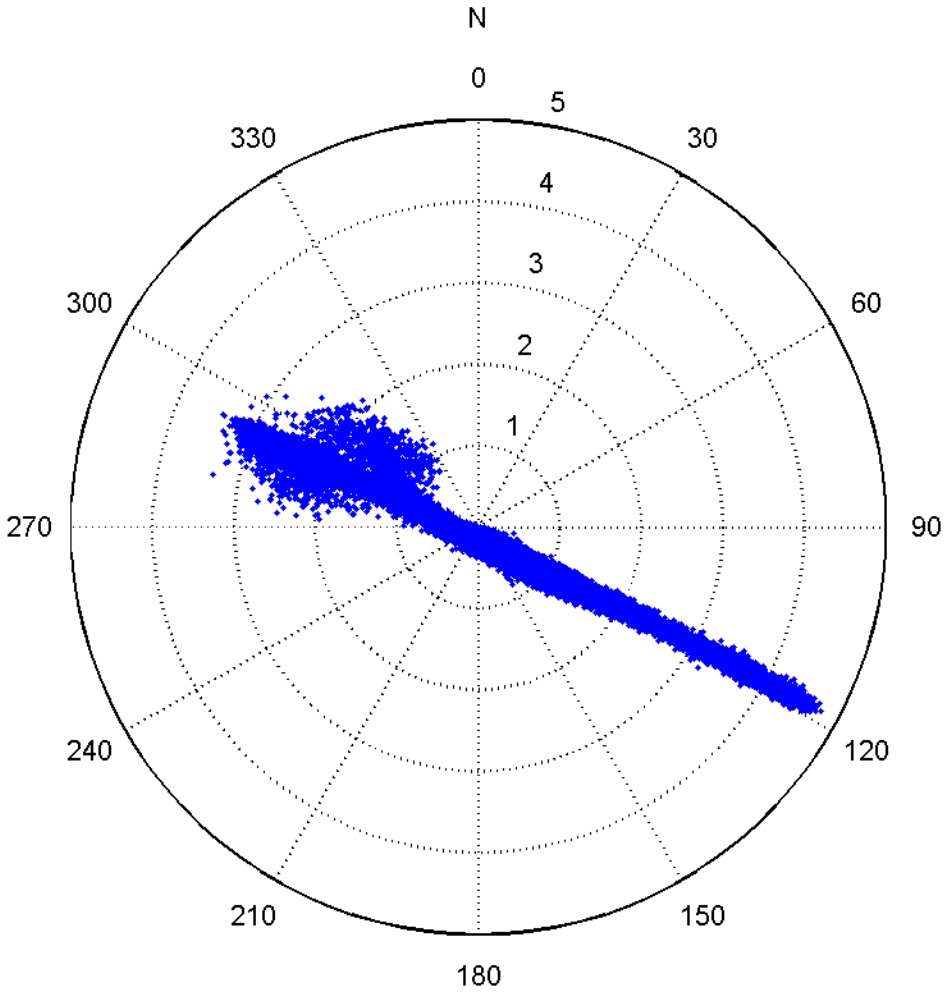

Figure B.18. Tidal ellipse (Site D)

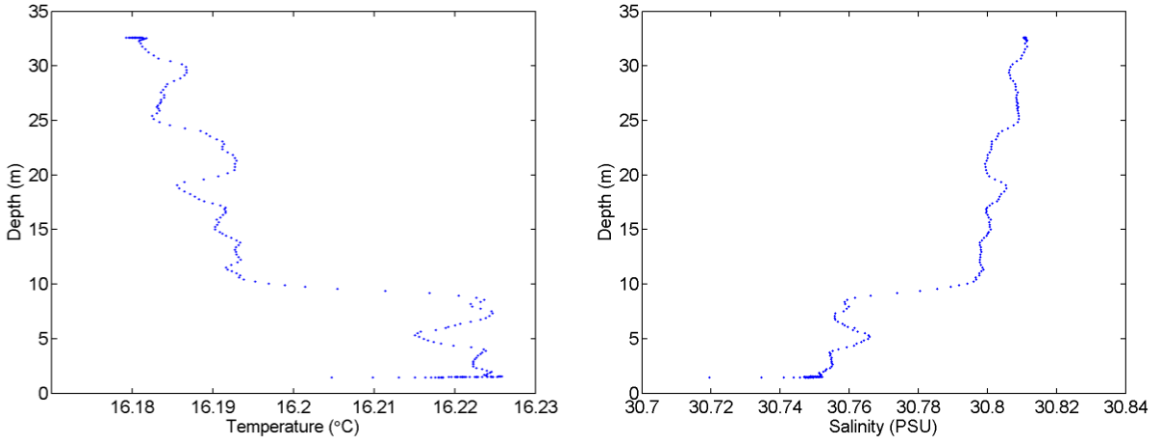

Figure B.19. Temperature and salinity depth profiles (Site D)

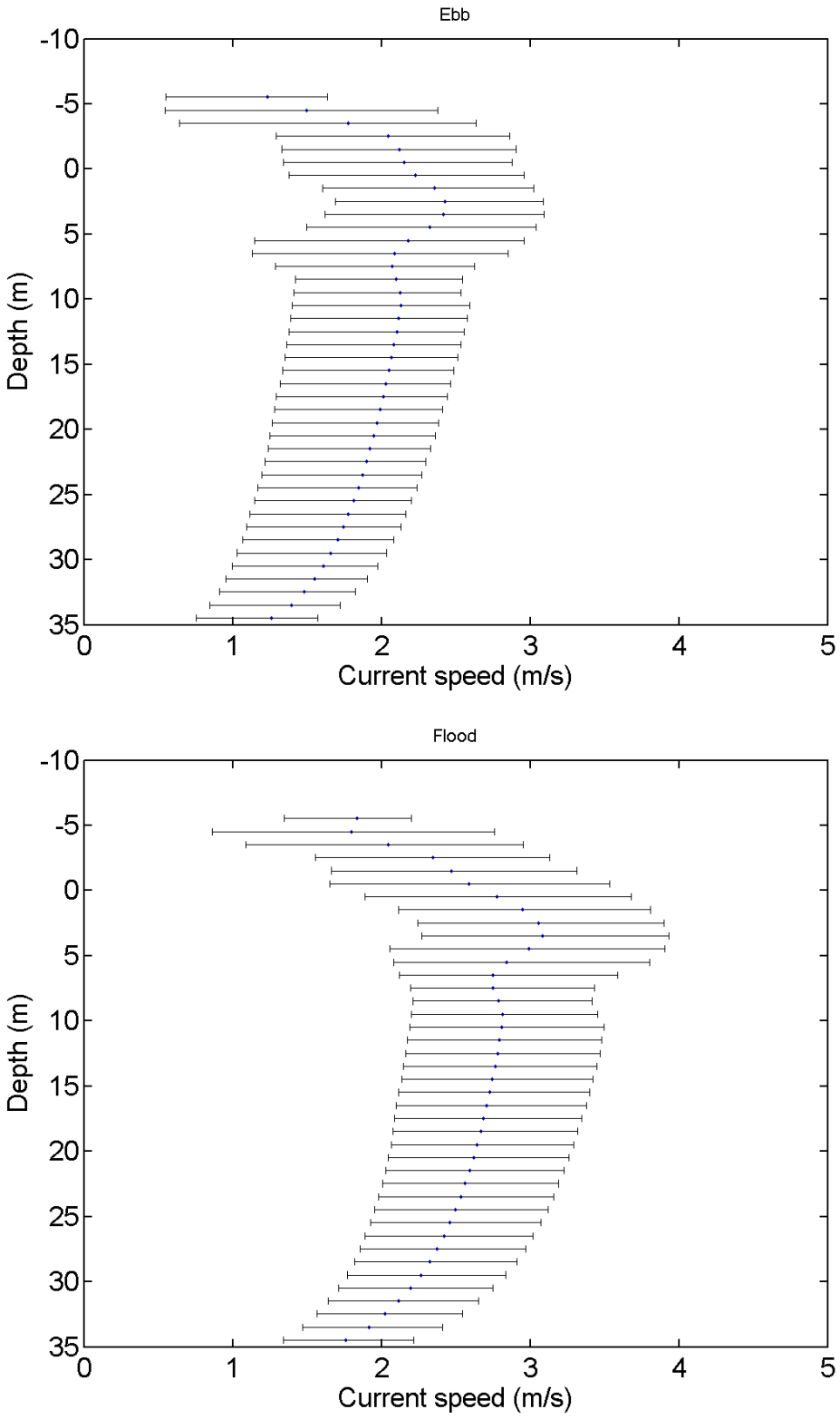

Figure B.20. Average ebb and flood current profiles (Site D)

C. Simulation log

C.1 Numerical parameters

Coriolis coefficient	10^{-4}
Eddy viscosity	10^{-4} m^2/s
Time step	10 s
Water density	1020 kg/m^3

C.2 Simulation period

Simulation	**Period of run**
Validation/Sensitivity A	10th Aug. 2011 – 16th Sept. 2011 (37 days)
Validation/Sensitivity B	12th Sept. 2011 – 4th Nov. 2011 (53 days)
Validation/Sensitivity C	28th Oct. 2011 – 12th Dec. 2011 (45 days)
Validation/Sensitivity D	14th Sept. 2011 – 4th Nov. 2011 (51 days)
Calibration	10th Aug. 2011 – 15th Dec. 2011 (127 days)

C.3 Viscosity coefficient

Viscosity coefficient	**Survey**	**ID**	**Computing time (s)**
10^0	A	V0A	4272
	B	V0B	5864
	C	V0C	5166
	D	V0D	5725
10^{-1}	A	V1A	4234
	B	V1B	5836
	C	V1C	5166
	D	V1D	5786
10^{-2}	A	V2A	4163
	B	V2B	5824
	C	V2C	5052
	D	V2D	5797
10^{-3}	A	V3A	4195
	B	V3B	5837
	C	V3C	5158
	D	V3D	5731
10^{-4}	A	V4A	4065
	B	V4B	5907
	C	V4C	4984
	D	V4D	5694
10^{-5}	A	V5A	4078
	B	V5B	5870
	C	V5C	5241
	D	V5D	5867

10^{-6}	A	V6A	4224
	B	V6B	5957
	C	V6C	5034
	D	V6D	5831

C.4 Boundary specification (tidal amplitude)

Number of harmonic constituents	Added constituent	Survey	ID	Computing time (s)
1	M2	A	N01A	4190
		B	N01B	5986
		C	N01C	4987
		D	N01D	5748
2	N2	A	N02A	4167
		B	N02B	6118
		C	N02C	5069
		D	N02D	5728
3	S2	A	N03A	4122
		B	N03B	5810
		C	N03C	5331
		D	N03D	5659
4	K1	A	N04A	4307
		B	N04B	5871
		C	N04C	5026
		D	N04D	5647
5	K2	A	N05A	4287
		B	N05B	6126
		C	N05C	5169
		D	N05D	6528
6	NU2	A	N06A	4289
		B	N06B	6146
		C	N06C	5209
		D	N06D	6060
7	O1	A	N07A	4211
		B	N07B	5863
		C	N07C	5082
		D	N07D	6347
8	MU2	A	N08A	4130
		B	N08B	5935
		C	N08C	5044
		D	N08D	5694
9	MM	A	N09A	4202
		B	N09B	5823
		C	N09C	5120
		D	N09D	5706
10	P1	A	N10A	4116
		B	N10B	5977
		C	N10C	5025
		D	N10D	5856

11	L2	A	N11A	4285
		B	N11B	5933
		C	N11C	5910
		D	N11D	5783
12	MSF	A	N12A	4224
		B	N12B	6042
		C	N12C	5159
		D	N12D	6092
13	MSN2	A	N13A	4171
		B	N13B	5947
		C	N13C	5043
		D	N13D	5718
14	2N2	A	N14A	4115
		B	N14B	5899
		C	N14C	5003
		D	N14D	5851
15	M6	A	N15A	4374
		B	N15B	6043
		C	N15C	5187
		D	N15D	5917
16	ETA2	A	N16A	4138
		B	N16B	5900
		C	N16C	5011
		D	N16D	5666
17	M4	A	N17A	4066
		B	N17B	5906
		C	N17C	5024
		D	N17D	5680
18	Q1	A	N18A	4200
		B	N18B	6010
		C	N18C	5175
		D	N18D	5809
19	OQ2	A	N19A	4275
		B	N19B	6083
		C	N19C	5225
		D	N19D	5905
20	2SM2	A	N20A	4298
		B	N20B	6148
		C	N20C	5188
		D	N20D	5884

C.5 Spatial resolution

Nominal mesh resolution (m)	**Survey**	**ID**	**Computing time (s)**
20	A	R020A	34416
	B	R020B	48372
	C	R020C	41276
	D	R020D	47926

50	A	R050A	19548
	B	R050B	28834
	C	R050C	24345
	D	R050D	26949
75	A	R075A	17273
	B	R075B	24568
	C	R075C	21673
	D	R075D	24579
100	A	R100A	16240
	B	R100B	23465
	C	R100C	19548
	D	R100D	22748
150	A	R150A	16262
	B	R150B	23307
	C	R150C	20534
	D	R150D	23064
200	A	R200A	13828
	B	R200B	20961
	C	R200C	17598
	D	R200D	19531
250	A	R250A	12895
	B	R250B	18188
	C	R250C	15785
	D	R250D	17849
300	A	R300A	12172
	B	R300B	17248
	C	R300C	15280
	D	R300D	17145
400	A	R400A	11242
	B	R400B	17209
	C	R400C	14311
	D	R400D	15570
500	A	R500A	11491
	B	R500B	16034
	C	R500C	13750
	D	R500D	15401

C.6 Turbulence model

Turbulence model	**Nominal mesh resolution (m)**	**Survey**	**ID**	**Computing time (s)**
Constant viscosity	150	A	EV150A	-
		B	EV150B	-
		C	EV150C	-
		D	EV150D	-
Elder	150	A	EL150A	17273
		B	EL150B	24646
		C	EL150C	21033
		D	EL150D	23748

K-epsilon	150	A	KE150A	20627
		B	KE150B	29293
		C	KE150C	24877
		D	KE150D	28297
Smagorinsky	150	A	SM150A	17411
		B	SM150B	24577
		C	SM150C	20733
		D	SM150D	23686
Constant viscosity	50	A	EV050A	-
		B	EV050B	-
		C	EV050C	-
		D	EV050D	-
Elder	50	A	EL050A	21147
		B	EL050B	29652
		C	EL050C	25252
		D	EL050D	28706
K-epsilon	50	A	KE050A	24965
		B	KE050B	35490
		C	KE050C	29837
		D	KE050D	33948
Smagorinsky	50	A	SM050A	20695
		B	SM050B	28746
		C	SM050C	24745
		D	SM050D	27911
Constant viscosity	20	A	EV020A	-
		B	EV020B	-
		C	EV020C	-
		D	EV020D	-
Elder	20	A	EL020A	89165
		B	EL020B	128705
		C	EL020C	110925
		D	EL020D	127520
K-epsilon	20	A	KE020A	43790
		B	KE020B	62843
		C	KE020C	53742
		D	KE020D	60869
Smagorinsky	20	A	SM020A	35960
		B	SM020B	51492
		C	SM020C	43697
		D	SM020D	49354

C.7 Temporal resolution

Output time-step (min)	**Survey**	**ID**	**Computation time (s)**
5	A	TS005A	4244
	B	TS005B	6220
	C	TS005C	5115
	D	TS005D	5872

10	A	TS010A	4281
	B	TS010B	6145
	C	TS010C	5180
	D	TS010D	5916
15	A	TS015A	-
	B	TS015B	-
	C	TS015C	-
	D	TS015D	-
20	A	TS020A	4239
	B	TS020B	6072
	C	TS020C	5133
	D	TS020D	5820
30	A	TS030A	4210
	B	TS030B	6040
	C	TS030C	5199
	D	TS030D	5818
60	A	TS060A	4234
	B	TS060B	6057
	C	TS060C	5135
	D	TS060D	5785
120	A	TS120A	4200
	B	TS120B	6045
	C	TS120C	5118
	D	TS120D	5805
240	A	TS240A	4106
	B	TS240B	5748
	C	TS240C	4949
	D	TS240D	5575
360	A	TS360A	4095
	B	TS360B	5789
	C	TS360C	4964
	D	TS360D	5608
480	A	TS480A	4058
	B	TS480B	5889
	C	TS480C	4949
	D	TS480D	5582
600	A	TS600A	4138
	B	TS600B	5936
	C	TS600C	5083
	D	TS600D	5755
720	A	TS720A	4087
	B	TS720B	5934
	C	TS720C	5003
	D	TS720D	5683

C.8 Boundary specification (tidal database)

Tidal database	**Survey**	**ID**	**Computation time (s)**

WebTide (Scotia - Fundy - Maine)	A	SSA	4128
	B	SSB	5764
	C	SSC	5111
	D	SSD	5863
TPXO7.2	A	TPXOA	4246
	B	TPXOB	5898
	C	TPXOC	5029
	D	TPXOD	5653
WebTide (Global)	A	GLA	4171
	B	GLB	5907
	C	GLC	5010
	D	GLD	5684
EC2001	A	ECA	4138
	B	ECB	5824
	C	ECC	4921
	D	ECD	5607

C.9 Coriolis force

Coriolis force	**Survey**	**Coriolis coefficient**	**ID**	**Computation time (s)**
Included	A	0.0001	C1A	4106
	B		C1B	5837
	C		C1C	5010
	D		C1D	5665
Excluded	A	–	C0A	4197
	B		C0B	5982
	C		C0C	5021
	D		C0D	5784

C.10 Bathymetry resolution

Bathymetry resolution (m)	**Survey**	**ID**	**Computation time (s)**
5	A	B005A	35625
	B	B005B	50311
	C	B005C	43178
	D	B005D	49070
20	A	B020A	34988
	B	B020B	50268
	C	B020C	42617
	D	B020D	48551
40	A	B040A	33827
	B	B040B	48417
	C	B040C	41610
	D	B040D	47213

60	A	B060A	34906
	B	B060B	50168
	C	B060C	42658
	D	B060D	48465
80	A	B080A	34157
	B	B080B	48852
	C	B080C	41856
	D	B080D	47566
100	A	B100A	36477
	B	B100B	48960
	C	B100C	41463
	D	B100D	47191
125	A	B125A	34383
	B	B125B	49198
	C	B125C	41649
	D	B125D	47210
150	A	B150A	34635
	B	B150B	49632
	C	B150C	42662
	D	B150D	48448